

**Morphodynamic equilibria in double-inlet systems
Their existence, multiplicity and stability**

Deng, X.

DOI

[10.4233/uuid:afad2560-3e7b-4b43-9997-17b4e24e9e02](https://doi.org/10.4233/uuid:afad2560-3e7b-4b43-9997-17b4e24e9e02)

Publication date

2023

Document Version

Final published version

Citation (APA)

Deng, X. (2023). *Morphodynamic equilibria in double-inlet systems: Their existence, multiplicity and stability*. [Dissertation (TU Delft), Delft University of Technology]. <https://doi.org/10.4233/uuid:afad2560-3e7b-4b43-9997-17b4e24e9e02>

Important note

To cite this publication, please use the final published version (if applicable).
Please check the document version above.

Copyright

Other than for strictly personal use, it is not permitted to download, forward or distribute the text or part of it, without the consent of the author(s) and/or copyright holder(s), unless the work is under an open content license such as Creative Commons.

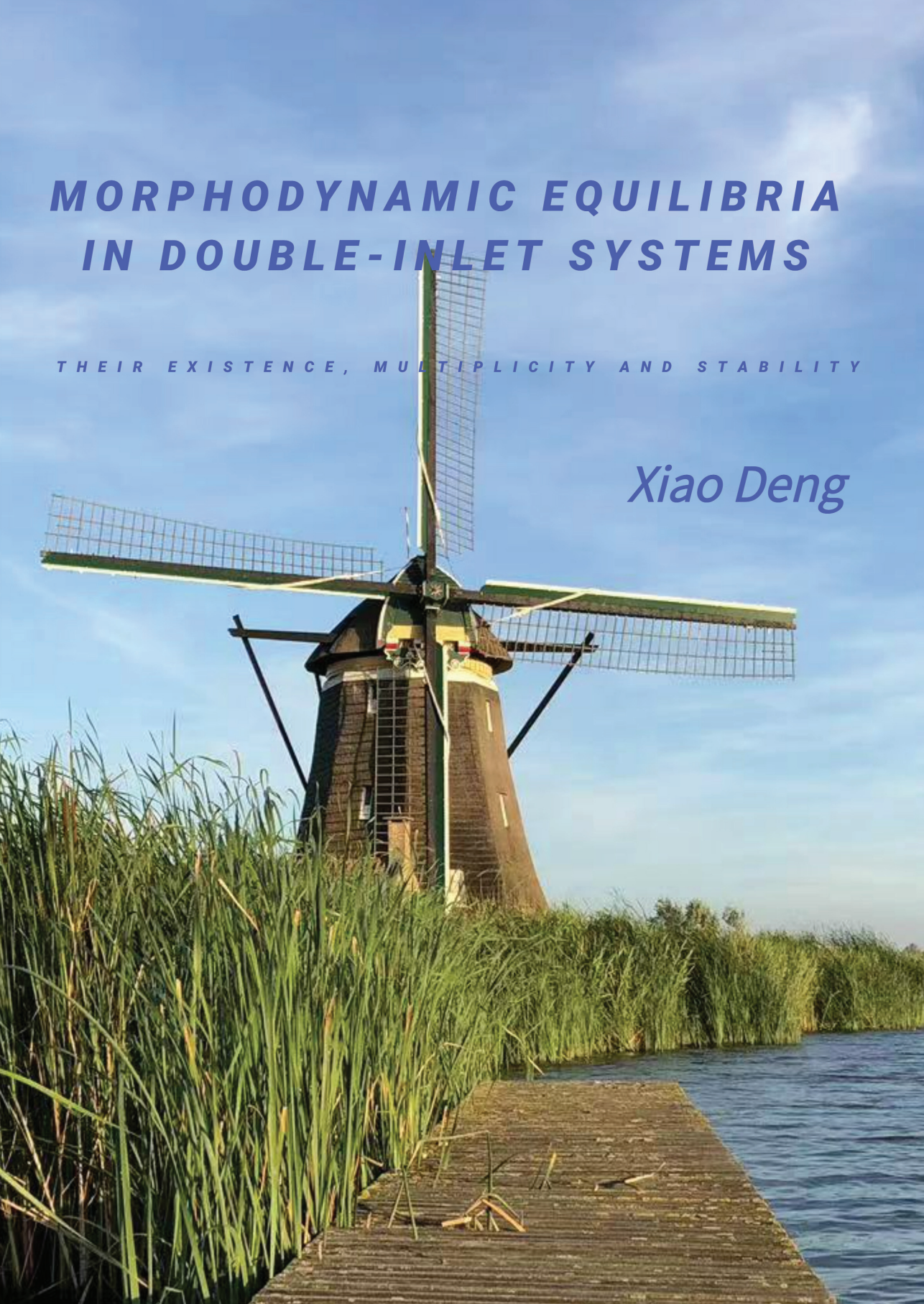
Takedown policy

Please contact us and provide details if you believe this document breaches copyrights.
We will remove access to the work immediately and investigate your claim.

MORPHODYNAMIC EQUILIBRIA IN DOUBLE-INLET SYSTEMS

THEIR EXISTENCE, MULTIPLICITY AND STABILITY

Xiao Deng



MORPHODYNAMIC EQUILIBRIA IN DOUBLE-INLET SYSTEMS

THEIR EXISTENCE, MULTIPLICITY AND STABILITY

MORPHODYNAMIC EQUILIBRIA IN DOUBLE-INLET SYSTEMS

THEIR EXISTENCE, MULTIPLICITY AND STABILITY

Proefschrift

ter verkrijging van de graad van doctor
aan de Technische Universiteit Delft,
op gezag van de Rector Magnificus Prof. dr. ir. T.H.J.J. van der Hagen
voorzitter van het College voor Promoties,
in het openbaar te verdedigen op maandag, 6 Maart 2023 om 15:00 uur

door

Xiao DENG

Master of Science in Applied Mathematics in College of Sciences,
Shanghai University, Shanghai, China,
geboren te Wuzhou, China.

Dit proefschrift is goedgekeurd door de promotoren.

Samenstelling promotiecommissie:

| | |
|-------------------------------|---|
| Rector Magnificus, | voorzitter |
| prof. dr. H. M. Schuttelaars, | Technische Universiteit Delft, promotor |
| prof. dr. ir. T. De Mulder, | Universiteit Gent, België, promotor |

Onafhankelijke leden:

| | |
|-----------------------------|---|
| prof. dr. S. Lanzoni | Università degli Studi di Padova, Italy |
| prof. dr. A. Doelman | Universiteit Leiden |
| dr. ir. P. C. Roos | Universiteit Twente |
| prof. dr. ir. Z. B. Wang | Technische Universiteit Delft |
| prof. dr. ir. A. W. Heemink | Technische Universiteit Delft |



Keywords: Tidal embayment, Process-based model, Idealized model, Double-inlet systems, Morphodynamic equilibria, Bifurcations

Printed by: Proefschrift specialist

Front & Back: Xiao Deng

Copyright © 2023 by Xiao Deng

ISBN 978-94-6366-661-9

An electronic version of this dissertation is available at
<http://repository.tudelft.nl/>.

To my family

CONTENTS

| | |
|--|-------------|
| Summary | xi |
| Samenvatting | xiii |
| 1 Introduction | 1 |
| 1.1 Tidal inlet systems | 2 |
| 1.2 Marsdiep–Vlie inlet system | 4 |
| 1.3 Morphodynamic models–General overview | 5 |
| 1.3.1 Classification of morphodynamic models | 6 |
| 1.3.2 Process-based morphodynamic models | 7 |
| 1.4 Morphodynamic models: Selected approach | 9 |
| 1.4.1 Single-inlet systems | 9 |
| 1.4.2 Double-inlet systems | 13 |
| 1.5 Research questions | 13 |
| 1.6 Methodology | 14 |
| 1.7 Outline | 14 |
| References | 14 |
| 2 Morphodynamic equilibria in double inlet systems: their existence and stability | 23 |
| 2.1 Introduction | 24 |
| 2.2 Model description | 26 |
| 2.3 Solution method | 30 |
| 2.3.1 Scaling and Expansion | 30 |
| 2.3.2 Morphodynamic equilibria and linear stability | 33 |
| 2.4 Results | 34 |
| 2.4.1 Constant-width system subjected to an M_2 tidal forcing | 35 |
| 2.4.2 Constant-width system subjected to all forcings | 41 |
| 2.4.3 Varying-width system subjected to all forcings | 43 |
| 2.5 Discussion | 44 |
| 2.5.1 Morphodynamic equilibria | 44 |
| 2.5.2 Comparison with results of a complex numerical model | 45 |
| 2.6 Conclusions | 47 |
| References | 49 |
| 3 Initial formation of channel–shoal patterns in double-inlet systems | 53 |
| 3.1 Introduction | 54 |
| 3.2 Model description | 55 |
| 3.3 Solution method | 59 |
| 3.3.1 Scaling and Expansion | 59 |

| | | |
|----------|---|------------|
| 3.3.2 | Basic state and linear stability | 62 |
| 3.4 | Results | 64 |
| 3.4.1 | M_2 tidal forcing | 65 |
| 3.4.2 | All forcings included | 72 |
| 3.5 | Discussion and Conclusions | 72 |
| | References | 76 |
| 4 | The channel and shoal patterns in short double-inlet systems | 81 |
| 4.1 | Introduction | 82 |
| 4.2 | Model description | 83 |
| 4.2.1 | Geometry | 83 |
| 4.2.2 | Hydrodynamic equations | 84 |
| 4.2.3 | Concentration equation | 85 |
| 4.2.4 | Bed evolution equation | 86 |
| 4.3 | Solution method | 87 |
| 4.3.1 | Dimensionless equations | 87 |
| 4.3.2 | Morphodynamic equilibria and linear stability | 89 |
| 4.4 | Results | 91 |
| 4.4.1 | Laterally uniform morphodynamic equilibria and their linear stability | 91 |
| 4.4.2 | Laterally varying morphodynamic equilibria. | 96 |
| 4.5 | Discussions | 102 |
| 4.6 | Conclusion | 105 |
| | References | 107 |
| 5 | Conclusions | 111 |
| 5.1 | General conclusions | 111 |
| 5.2 | Discussion of the research questions | 112 |
| 5.3 | Outlooks | 113 |
| | References | 113 |
| A | Supporting Information for "Morphodynamic equilibria in double-inlet systems: their existence and stability" | 115 |
| A.1 | Velocity scale | 115 |
| A.2 | Details concerning the Numerical Implementation | 116 |
| A.2.1 | Element order | 116 |
| A.2.2 | Numerical bifurcation approach | 116 |
| A.2.3 | Time-integration method | 118 |
| A.3 | Sensitivity of Morphodynamic Equilibria to inlet depth and prescribed tidally-averaged water transport | 118 |
| A.3.1 | Varying inlet depths | 118 |
| A.3.2 | Varying residual water transport at inlet II | 118 |
| A.4 | Advective Transport contributions | 121 |
| | References | 121 |

| | | |
|----------|--|------------|
| B | Morphodynamic equilibria in systems with diffusively dominated transport | 125 |
| B.1 | Morphodynamic equilibria of diffusion without topographical variations . . . | 125 |
| B.2 | Morphodynamic equilibria of diffusion with topographical variations . . . | 128 |
| | References | 128 |
| C | Initial formation of channel–shoal patterns in double–inlet systems:Diffusively dominated transport | 131 |
| | References | 136 |
| D | Bifurcation diagram for morphodynamic equilibria by varying friction parameter | 137 |
| E | The operator G | 139 |
| | Acknowledgements | 141 |
| | Curriculum Vitae | 143 |
| | List of Publications | 145 |

SUMMARY

Tidal inlet systems, which consist of back-barrier basins connected to the open sea by one or multiple inlets, are found at many places along sandy coasts. They are valuable for ecology (breeding and feeding areas), economy (gas-mining and sand-mining) and recreation, and are important for coastal safety. But they are also sensitive to external forcings like prevailing currents, tides, winds, sea level rise and human interferences. Therefore, it is important to investigate the morphodynamic behaviour of these tidal inlet systems, especially the formation of the channels and shoals. In this thesis, idealized models will be developed to study so-called double-inlet systems, which are tidal basins with two inlets connecting to the open sea.

To assess the morphodynamic behaviour of double-inlet systems, a one-dimensional idealized model is developed. In this model, the water motion is governed by cross-sectionally averaged shallow water equations, forced by tides prescribed at the seaward boundaries. Sediment transport is governed by a width-averaged and depth-integrated advection diffusion equation, with sink and source terms. The bed evolution is described by the cross-sectionally averaged equation for the concentration of mass in a sediment layer. A system is said to be in morphodynamic equilibrium if the bed does not evolve on a long (morphodynamic) timescale anymore.

The model is first analysed without the presence of externally prescribed overtides, so the water motion is only forced by the M_2 tidal constituents. To systematically analyse the sensitivity of the resulting morphodynamic equilibria to the characteristics of the M_2 forcing, a continuation approach is employed to obtain these equilibria in the parameter space spanned by the relative phase and amplitude of the M_2 tidal constituent. In this parameter space, it was found that there are regions where no morphodynamic equilibrium, one equilibrium or multiple equilibria can exist. When there is no morphodynamic equilibrium, the double-inlet system is reduced to two single-inlet systems. For a certain parameter setting, four morphodynamic equilibria are found. The water depth of these four equilibria are further analysed, as well as the sediment transport contributions.

The influence of the depth variations, the presence of externally generated overtides and width variations of this model are then further analysed for the stable morphodynamic equilibria. The model finally allows a qualitative comparison with observations in the Marsdiep-Vlie inlet system at the Dutch Wadden Sea. Using characteristic values of this system, one stable equilibria is obtained, suggesting that this double-inlet system can be stable on the long morphodynamic timescales.

Next, the morphodynamic model is extended to include dynamics in the lateral direction. The model consists of depth-averaged shallow water equations neglecting the effects of earth rotation, a depth-integrated concentration equation and a tidally-averaged bottom evolution equation. Since the equations are still averaged over depth, a 2DH model is obtained. With this idealized model the initial formation of channel-shoal

patterns in a double-inlet system with a rectangular geometry was systematically investigated. Utilizing infinitesimally small perturbations with a lateral structure, the initial formation of channels and shoals can be expected if the laterally uniform morphodynamic equilibria are linearly unstable with respect to these perturbations.

When the water motion is only forced by an M_2 tidal constituent, restricting only attention to that part of the parameter space spanned by the relative phase and amplitudes of M_2 tidal forcing where laterally uniform morphodynamic equilibria exist, it is found that these equilibria can be either stable against two-dimensional perturbations, or linearly unstable. When linearly unstable, the instabilities can be either due to diffusive mechanisms, or due to advective mechanisms.

When the morphodynamic equilibria become unstable due to diffusive processes, the classical diffusive mechanism has a destabilizing effect, while the topographically induced diffusive mechanism has a stabilizing effect. The associated eigenvalues are all real, implying an exponential growth/decay in time. When the advective mechanism results in linear instabilities, the eigenvalues are complex, implying that bedforms do not only grow/decay in time, but also migrate.

When external overtides and a residual discharge are included, the laterally uniform morphodynamic equilibria can be unstable due to the convergences and divergences of both (interally and externally) advective and diffusive transport.

Finally, we study channels and shoals in double-inlet systems, using a scaled depth-averaged model. This model consists of scaled shallow water motion equations, a scaled depth-integrated concentration equation and a scaled bottom evolution equation. By focusing on a short rectangular tidal basin, laterally uniform morphodynamic equilibria can be found. These equilibria are either linearly stable or linearly unstable due to diffusive processes.

When varying one or more parameters, such as the friction parameter and the width of the system, bifurcations can be found where the stabilities of morphodynamic equilibria change. Using associated eigenfunctions as a load vector, arclength method allows to switch branches. At different branches, morphodynamic equilibria are characterized by lateral variations with different mode numbers. When default parameters are used, the resulting bifurcation diagrams reveal that multiple morphodynamic equilibria exist.

SAMENVATTING

Barrièrekusten en de bijbehorende zeegat systemen komen op veel plaatsen langs zandige kusten voor. Ze bestaan uit getijdebekkens die met de open zee verbonden zijn door één of meerdere zeegaten. Deze kustgebieden zijn erg waardevol voor de ecologie (broed- en voedselgebieden), economie (gaswinning en zandwinning) en recreatie en zijn belangrijk voor de kustveiligheid. Deze systemen en hun stabiliteit zijn erg gevoelig voor (veranderingen in) externe krachten zoals stromingen, getijden, winden, zeespiegelstijging en menselijk ingrijpen. Daarom is het belangrijk om het morfodynamisch gedrag van deze zeegat systemen te onderzoeken, met name de vorming van de geul en plaatsystemen. In dit proefschrift zullen geïdealiseerde modellen worden ontwikkeld voor het bestuderen van zogenaamde dubbele zeegat systemen, waarbij de getijdebekkens met twee zeegaten zijn verbonden met de open zee.

Om beter inzicht te krijgen in het morfodynamisch gedrag van dubbel zeegat systemen, is eerst een één-dimensionaal geïdealiseerd model ontwikkeld. In dit model wordt de waterbeweging bepaald door doorsnee gemiddelde vergelijkingen voor ondiep water, geforceerd door getijden voorgeschreven aan de zeewaartse randen. Sedimenttransport wordt beschreven door een breedte-gemiddelde en diepte-geïntegreerde advection-diffusievergelijking, die bron- en puttermen voor sediment bevat. De bodem evolutie wordt beschreven door de doorsnee gemiddelde vergelijking voor behoud van massa in de bodem. Een systeem is in morfodynamisch evenwicht als de bodem niet meer verandert op de lange (morfodynamische) tijdschaal.

Het model wordt eerst geanalyseerd als de waterbeweging alleen geforceerd wordt door het M_2 getij. De morfodynamische evenwichten worden verkregen door gebruik te maken van een continueringsmethode in de parameterruimte die wordt opgespannen door de relatieve fase en amplitude van de voorgeschreven M_2 forcering. Uit deze analyse volgt dat er in deze parameterruimte gebieden zijn waar geen morphodynamisch evenwicht is, gebieden waar één zo'n evenwicht bestaat en gebieden waar meervoudige evenwichten bestaan. Als er geen morfodynamisch evenwicht bestaat, reduceert het dubbele zeegat systeem tot een systeem dat bestaat uit twee enkele zeegat systemen. Voor bepaalde parameterinstellingen worden vier verschillende morfodynamische evenwichten gevonden. De bodems van deze vier evenwichten en het bijbehorende sediment transport worden verder geanalyseerd.

De invloed van de voorgeschreven dieptes aan de zeewaartse randen, de aanwezigheid van extern voorgeschreven hogere getijcomponenten en geometrische breedtevariëaties wordt vervolgens verder geanalyseerd door specifiek naar stabiele morphodynamische evenwichten te kijken. De modelresultaten worden tenslotte kwalitatief vergeleken met waarnemingen van het Marsdiep-Vlie zeegat systeem (Nederlandse Waddenzee). Gebruikmakend van waarden representatief voor dit systeem wordt één stabiel morfodynamisch evenwicht gevonden. Dit suggereert dat dit dubbele zeegat systeem stabiel kan zijn op de lange morfodynamische tijdschaal.

Vervolgens wordt het morfodynamische model uitgebreid door laterale dynamica toe te voegen. Dit betekent dat nu de diepte-gemiddelde ondiepwatervergelijkingen worden opgelost om de waterbeweging te verkrijgen. Hierbij worden effecten van aardrotatie verwaarloosd. De andere vergelijkingen zijn een diepte-geïntegreerde concentratievergelijking voor het modelleren van de concentratie van het zwevend sediment en een getij-gemiddelde bodem-evolutie vergelijking voor het berekenen van bodemveranderingen. Met dit geïdealiseerde model wordt de initiële vorming van geulen en platen in een dubbel zeegat systeem in een rechthoekige geometrie systematisch onderzocht door het temporele gedrag van oneindig kleine verstoringen met een laterale structuur te bestuderen: als de amplituden van (sommigen van de) kleine verstoringen gaan groeien in de tijd, ofwel als de onderliggende lateraal uniforme bodem lineair instabiel is ten opzichte van deze verstoringen, zien we de eerste vorming van geulen en platen. We beperken ons bij deze analyse tot dat deel van de parameter ruimte opgespannen door de relatieve fase en amplitude van het M_2 getij waar morfodynamische evenwichten bestaan die niet variëren in de laterale richting.

Wanneer de waterbeweging alleen wordt geforceerd door een M_2 getij kunnen de lateraal uniforme morfodynamische evenwichten lineair stabiel of instabiel zijn. Wanneer de evenwichten lineair instabiel zijn, kunnen deze instabiliteiten het gevolg zijn van diffusieve of advectieve mechanismen. Wanneer de morfodynamische evenwichten instabiel worden ten gevolge van diffusieve processen, dan blijkt dat het klassieke diffusiemechanisme destabiliserend werkt, terwijl het topografisch geïnduceerd diffusiemechanisme een stabiliserend effect heeft. De bijbehorende eigenwaarden zijn allemaal reëel, wat een exponentiële groei/demping in de tijd impliceert. Wanneer advectieve processen resulteren in lineaire instabiliteiten zijn de eigenwaarden complex, wat impliceert dat de bodemvormen niet alleen groeien of dempen in de tijd, maar ook migreren. Ook wanneer hogere getijcomponenten of een netto watertransport wordt voorgeschreven, wordt de lateraal uniforme morfodynamische evenwichtsbodem lineair instabiel ten gevolge van de convergenties en divergenties van zowel (intern als extern) advectief en diffusief transport.

Ten slotte bestuderen we de eindige amplitude oplossingen in morfodynamisch evenwicht van geul-plaat patronen in dubbele zeegat systemen. De vergelijkingen bestaan weer uit de diepte-gemiddelde ondiep-water vergelijking, de concentratie vergelijking en de bodem evolutie vergelijking. We focussen op korte rechthoekig dubbel zeegat systeem, waarbij het lateraal uniforme morfodynamisch evenwicht lineair instabiel wordt door diffusieve mechanismen,

Door één of meerdere parameters (zoals de bodemwrijvings parameter of de breedte) langzaam te variëren, kunnen we de evenwichten volgen met behulp van een continueringmethode. Met deze methode kunnen we bifurcaties detecteren waarbij het aantal morfodynamische equilibria kan veranderen: dit betekent dat er verschillende takken van oplossingen kunnen bestaan, waarop de morfodynamische evenwichten worden gekarakteriseerd door hun lineaire stabiliteit en de patronen door de bijbehorende laterale mode getallen.

1

INTRODUCTION

In this thesis, the morphodynamic behaviour of double-inlet systems is investigated by developing and solving a depth-averaged morphodynamic model and analysing the model results. As a first step, the existence of morphodynamic equilibria and their sensitivity to parameter variations is studied. The multiplicity and bifurcation structure of these double-inlet systems are analysed by focussing on tidal forcing variations. Whenever possible, the model results are compared to field observations. The second main objective is to determine the key mechanisms that generate the observed channel-shoal patterns in these inlet systems. To understand the initial formation of such channels and shoals, a linear stability with respect to two-dimensional perturbations of laterally uniform morphodynamic equilibria in a rectangular basin is analysed.

In the first section of this chapter, the characteristic features of tidal inlet systems connected to an open sea by one or multiple inlets are presented. In section 1.2 a closer look is taken into the Marsdiep-Vlie inlet system (Dutch part of the Wadden Sea), which is a typical example of a double-inlet system. In section 1.3, different types of morphodynamic models are discussed. Results of previous studies are highlighted in Section 1.4, while the research questions are formulated in Section 1.5. In Section 1.6 the methodology is presented, and the following chapters are outlined in the last section.

1.1. TIDAL INLET SYSTEMS

Tidal inlet systems, defined as semi-enclosed basins with one or more tidal inlets connecting back-barrier basins to the open sea, are found along many sandy coasts around the world and account for some 12 percent of the world's coastline (Glaeser [2]). Examples are the Venice Lagoon in Italy (Seminara *et al.* [3], Amos *et al.* [4]), the Wadden Sea in North-Western Europe (Oost and De Boer [5], Oost *et al.* [6], Roos *et al.* [7]), the Georgia Bight barrier system in the United States (Hayes [8]) and the Jiaozhou Bay in China (Gao *et al.* [9], Yang *et al.* [10]).

An idealized tidal inlet system, connected to the open sea by a single inlet, is shown in Fig. 1.1. It consists of three morphodynamically active elements—the tidal inlet connecting the back-barrier basin to the open sea, the ebb tidal delta on the seaward side of the tidal inlet and the back-barrier basin at the landward side (de Swart and Zimmerman [1]).

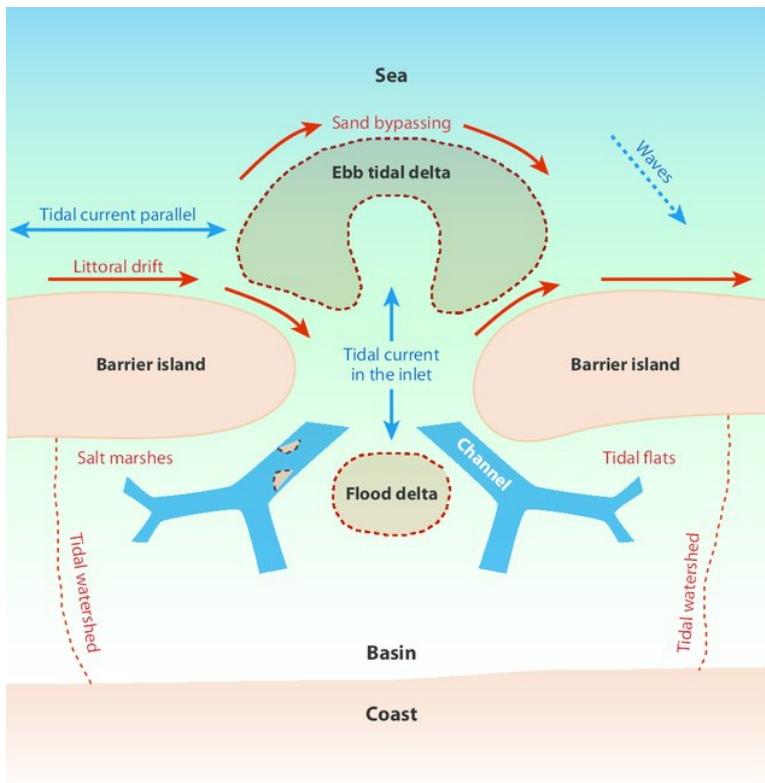


Figure 1.1: A sketch of an idealized tidal basin by de Swart and Zimmerman [1]. It shows an idealized basin consisting of a back-barrier basin separated by barrier islands from the open sea and by tidal watersheds from other basins, a tidal inlet connecting the tidal basin to the open sea, an ebb tidal delta on the seaward side of the tidal inlet. In the tidal basin, a flood tidal delta is usually found, and in the intertidal zone of the tidal basin tidal flats and salt marshes may be found.

Ebb tidal deltas are shallow sandy features at the seaward side of tidal inlets, which are formed by the interaction between the ebb tidal currents and the incoming waves (Hayes [11], Lenstra *et al.* [12]). The evolution of many ebb tidal deltas is cyclic, demonstrating a rotation of channels and formation of sandy shoals that migrate and attach to the downdrift coastal area (Sha [13], FitzGerald [14], FitzGerald *et al.* [15], Ridderinkhof *et al.* [16]). Ebb tidal deltas often serve as a sediment reservoir for the back-barrier basin at the landward side of tidal inlets. Apart from that, they also act as a filter for offshore incident wave energy: waves propagate and dissipate their energy by means of shear stresses related to bottom friction and wave breaking on ebb tidal deltas, which thus protects the coasts and back-barrier basins (FitzGerald [17], WestHuysen [18], Elias and Hansen [19]). Wave energy dissipation strongly depends on the relative wave height (wave height divided by water depth) and waves can refract over the shoals. It is therefore expected that the changes of channels and shoals influence the wave energy patterns not only on ebb tidal deltas but also in tidal inlets. Furthermore, waves can drive flows and are able to entrain bottom materials as suspended sediment which can be transported by currents. Therefore, waves are an important element for the sediment transport near tidal inlets (Ridderinkhof *et al.* [16], Nahon *et al.* [20]).

The tidal inlets are the major channels transporting large amounts of water and sediment from the open sea to the tidal basin and back. Their hydrodynamics and morphodynamics are dominated by tides and modified by the incoming waves. Many tidal inlets are considered to be shielded from waves, for the major dissipation of wave energy usually occurs at the seaward sides of the inlet, especially at the ebb tidal deltas (Hayes [21]).

The back-barrier basin is, apart from the inlets connecting it to the open sea, either completely encircled by land or by land and tidal watersheds. Tidal watersheds are locations where the exchange of water and/or sediment between various subbasins is minimal. If there is no or little transport at the watersheds, the basins on either side of the watersheds can be studied separately. If there is a strong water and/or sediment exchange between adjacent basins (Duran-Matute *et al.* [22], Sassi *et al.* [23]), the interactions between these basins have to be taken into account, i.e., the basins on either side of the tidal watersheds have to be regarded as integral parts of one system.

Similar to the water motion in tidal inlets, the hydrodynamics of back-barrier basins is usually dominated by tides. In case of microtidal conditions flood deltas are observed in the basins (Hayes [21]), while for mesotidal conditions with fractal characteristic channel networks are found, in which the depth generally decreases from the sea towards the land (Oost and De Boer [5], Hayes [21]). In the case of macrotidal conditions, which are mainly found in estuaries (Dalrymple and Rhodes [24]), the water motion is characterised by high current speeds and migrating large scale bedforms are often observed. In the intertidal zone of the back-barrier basin tidal flats and salt marshes can be found.

Tidal inlet systems are important in many respects. These inlet systems are very significant for the ecology, for they provide a habitat for many aquatic and terrestrial species and other ecosystem services, resulting in a high biodiversity. They are also important for the local economy because activities such as gas-mining, sand-mining and recreation are common in these regions. Furthermore, tidal inlet systems play a very significant role in coastal safety, since they strongly influence the sediment budget of the coast which

could strengthen or undermine nearby beaches and barrier island shorelines (Glaeser [2], Mulhern *et al.* [25]).

Field measurements and observations indicate that these tidal inlet systems are highly sensitive to changes in external forcings. The changes in tidal forcings, sea level, extreme weather conditions, and human interferences like land reclamation and inlet deepening can affect the morphology of a tidal inlet system in a significant way (McBride *et al.* [26], Van der Spek [27]).

Motivated by their ecological and economical importance and their sensitivity to external forcing conditions, a proper understanding and management of these tidal inlet systems is needed. In this thesis, morphodynamic models will be developed and analysed. These models are important tools for investigating the impacts of anthropogenic interventions on the morphodynamic evolution, as well as the natural development in these tidal basins. Among tidal inlet systems, the so-called double-inlet systems, which consist of a back-barrier basin with two tidal inlets connected to the open sea, are the simplest multiple-inlet systems and are the focus of this thesis. A typical example of a double-inlet system is the Marsdiep–Vlie system, which will be briefly discussed in the next section.

1.2. MARSDIEP–VLIE INLET SYSTEM

The Wadden Sea, which stretches along the Dutch, German and Danish coast in the North–West of Europe, covers an area of approximately 8000 km². It consists of a series

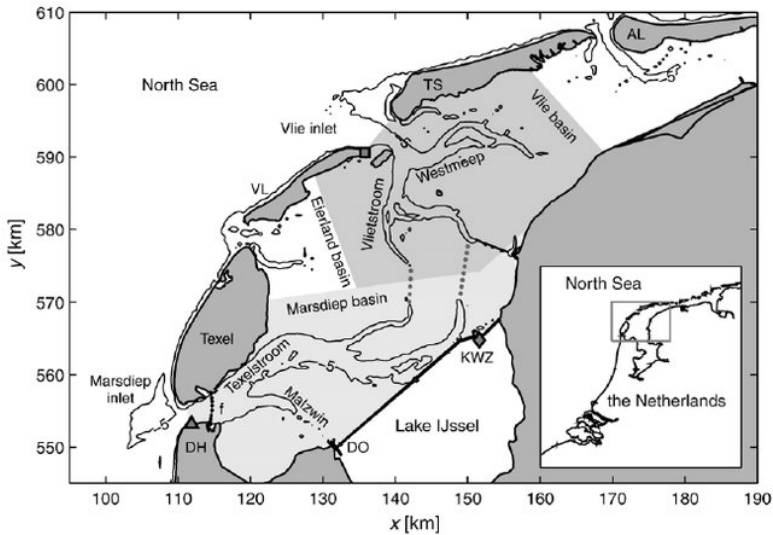


Figure 1.2: The western part of the Dutch Wadden Sea (a figure adopted from Buijsman and Ridderinkhof [28]). The Marsdiep and Vlie basins are shaded with light-grey and darker-grey, respectively. The town Den Helder is indicated by DH, while the Lake IJssel sluices at Den Oever and Kornwerderzand by DO and KWZ. The back-barrier islands of Vlieland, Terschelling, and Ameland are indicated by VL, TS, and AL, respectively. The connections between the Marsdiep and Vlie tidal basins are marked by the grey dotted lines.

of tidal back-barrier basins, separated from the North Sea by a series of barrier islands, and connected to the North Sea by many tidal inlets (Oost *et al.* [6]). Since the Wadden Sea is one of the major intertidal areas on earth and has a unique biodiversity, it is listed as a World Heritage site by UNESCO in 2009 (the Danish part was added in 2014).

The Marsdiep–Vlie inlet system, consisting of the Marsdiep basin and the Vlie basin, is a double inlet system in the Wadden Sea. The Marsdiep basin (see Fig. 1.2), located in the most western part of the Wadden Sea, has a length of approximately 50 km and an area of around 680 km² (Buijsman and Ridderinkhof [28, 29, 30]). The Marsdiep basin borders to the northeast on the Vlie basin, and to the northwest on the Eijerlandse Gat basin. To the north the Marsdiep inlet is bounded by the island of Texel, to the south the sea dike of the mainland town of Den Helder. To the west seaward of the Marsdiep inlet, an ebb-tidal delta is observed, consisting of the subtidal sand shoal Noorderhaaks that shields the Marsdiep inlet from waves coming from the (north)west. The main channel of the Marsdiep inlet bifurcates in two channels, the northern channel called Texelstroom and the southern channel the Malzwin. The seafloor of the Marsdiep basin consists of medium to fine sized sands and features large bedforms with wavelengths of 100–200 m and heights of several meters.

The currents in the Marsdiep inlet are primarily governed by the semi-diurnal tides. These tides co-oscillate with the tides in the adjacent North Sea, and enter the Marsdiep channel from the south near Den Helder, propagating northward towards Texel and eastward into the inlet. The mean tidal range at the mouth near Den Helder is 1.4 m, while that at the head near Harlingen is over 2 m because of tidal amplification.

The Vlie basin (see Fig. 1.2) is the third (from the west) sub-basin in the Dutch Wadden Sea, having an area of around 660 km² (van Prooijen and Wang [31]). The Vlie basin borders the Marsdiep basin to the south, and the Eijerlandse Gat basin to the southwest. To the north, the back-barrier basin is bounded by the islands of Vlieland and Terschelling, to the east the watershed with the Amelander basin is found and to the southeast the mainland of Frisia. The inlet channel bifurcates in the east channel Westmeep and the southern channel Vliestroom.

When studying the behaviour of the Wadden Sea, the Marsdiep basin together with the Vlie basin is considered as a double-inlet system. This is because the Marsdiep basin is strongly connected to the Vlie basin through the Texelstroom channel in the Marsdiep basin and Vliestroom channel in the Vlie basin (Buijsman and Ridderinkhof [30]). Indeed, Duran-Matute *et al.* [22], Sassi *et al.* [23] clearly showed that there are strong exchanges of water and sediment between these two basins.

1.3. MORPHODYNAMIC MODELS—GENERAL OVERVIEW

Morphodynamics, as defined by Wright and Thom [32], is the complex mutual adjustments of topography and fluid dynamics, including sediment transport. In other words, it is the dynamic behaviour of alluvial boundaries caused by waves, currents and sediment transport (de Vriend [33]). This interaction occurs at very different length and time scales, which can be used to classify these processes. Here, the classification proposed by de Vriend [33] is presented:

- **Micro-scale (process-scale)** phenomena concern mainly the constituent processes

(waves, currents and sediment transport), whose length and time scales are essentially smaller than the length and time scales associated with the "primary" morphological behaviour. Examples of micro-scale phenomena are the water motion in channels and on shoals, the turbidity dynamics, and the sediment diffusion and advection.

- **Meso-scale (dynamic scale)** phenomena describe the "primary" morphodynamic behaviour caused by the interaction of the above mentioned processes and the sea bed. The scales involved are of the order of magnitude of processes inherent to this interaction. Examples are bed forms and bed patterns which are relevant to currents and navigation, shoaling and migration of natural channels which are important for coastal defence, and the response of these patterns to human interferences which is important to manage and protect the system as a whole.
- **Macro-scale (trend-scale)** phenomena are related to trends at scales much larger than the meso-scale phenomena described above. These slow trends can be caused by secular effects in the behaviour inherent to the system, or by gradual changes in the extrinsic forcing or the system parameters. Examples are the evolution of channel-shoal patterns in basins and outer deltas, and the evolution of the intertidal zone. These phenomena are in general important for the ecosystem and coastal defence.

The above phenomena are generally coupled in a complex nonlinear way. One has to decide which processes and forcing conditions are essential to consider for the phenomenon under study, and which processes need to be included in a parameterized way. Examples of such parameterization are sediment erosion and transport formulas.

1.3.1. CLASSIFICATION OF MORPHODYNAMIC MODELS

Due to the great variety and complexity of the morphodynamic interactions, even when only considering tidal basins and processes observed in them, as well as the different fields of interest that can be addressed, many different approaches have been used to study morphodynamics of tidal inlets. These approaches are generally classified into five different ones, proposed by de Vriend [34], de Vriend and Ribberink [35]:

- **Data-based models** only utilize observed data to describe and predict the behaviour of barrier coasts. Examples are geostatistical models and models based on empirical orthogonal function analysis (Fairley *et al.* [36], Alvarez and Pan [37]), which typically apply to macro-scale phenomena. These models are able to make predictions without analyzing the complex morphodynamic behaviour of the system, and are especially effective in simple cases for which it is easy to predict whether the relevant processes remain unaltered. These models are impotent to determine which mechanisms play a key role and what are the key parameters, and whether these mechanisms and parameters will be altered if the forcing conditions change.
- **Empirical relationships and empirical models** use measured data to establish relationships between different variables. An example is the relation between the

cross-sectional area of an inlet and the tidal prism proposed by O'Brien [38] (see de Vriend [34] for other examples). They can be used to validate process-based and idealized models (see below), because the empirical knowledge is based on large data sets observed in many inlets around the world.

- **Semi-empirical long-term models** describe the dynamic interactions between macro-scale phenomena by using basic physical principles and empirical relationships to represent the effects of smaller scale processes. They are able to describe the evolution of a tidal inlet to its equilibrium state, but do not give any small-scale information.
- **Process-based models** are mathematical (numerical) models based on first physical principles. They are used to get detailed insight into the physical processes and are typically based on complex state-of-the-art model formulations. These models are able to simulate the morphodynamic evolution, such as the development of channels and shoals. They are often too complex to determine the essential mechanisms controlling the phenomena under consideration. Because these models are very cpu intensive, they usually are not employed for extensive sensitivity analyses.
- **Idealized models (formally integrated long-term models)** are mathematical models aimed at retaining only those processes that are relevant for the phenomena under investigation. They are derived from process-based models by formal integration over space and time, with possible empirical or parametric closure relations. Since this approach aims at strongly reducing cpu time (compared to process-based models), it enables us to gain insight into the processes which are essential for the observed phenomena, and allows for extensive sensitivity studies.

1.3.2. PROCESS-BASED MORPHODYNAMIC MODELS

The latter two types of models are based on physical laws, and typically consist of three basic modules. The first module concerns the water motion, which is usually governed by the shallow water equations, resulting in the sea surface elevation and water velocities for a given bathymetry. The second module, using the information of the first module, calculates the sediment transport, which generally includes both suspended load and bed load transport. The third module uses sediment transport to calculate a new bed profile from the mass balance of the sediment layer. The new bed profile is then used to recalculate the water motion, thus completing one step of the morphodynamic loop (see Fig.1.3, left panel). Alternatively, if one focuses on morphodynamic equilibria (see Fig.1.3, right panel), the three modules are not solved sequentially, but an asymptotic solution, consisting of velocities, a concentration and a bed profile, is directly looked for (see Dijkstra *et al.* [39]). The most simple asymptotic solution is a morphodynamic steady state, for which the sediment transport has no spatial convergence or divergence. In what follows, the three modules will be discussed in detail.

- **The hydrodynamic module** describes the water motion driven by various physical processes, possibly including wind, waves, tides, density differences and rotational (Coriolis) accelerations. In this thesis, the hydrodynamics will be described

by the depth-averaged shallow water equations (Csanady [40]), also called the Saint-Venant equations (Vreugdenhil [41]). Indeed, the tidal basins under consideration are assumed to be shallow, such that the vertical scale of the fluid flow is much smaller than typical horizontal scales (Nihoul and Runday [42]). Moreover, the width scale is assumed to be much smaller than the Rossby deformation radius. Hence, the Coriolis effects are not important and are neglected.

- **The sediment module** describes the transport of sediment particles from one place to another. This transport only happens if the bed shear stress acting on the particles exceeds a certain threshold value. Since the shear stress is related to the flow velocity just above the bed, the flow velocity must exceed a critical (friction) velocity before the particles begin to move. This critical value is determined by the gravitational force exerted on these sediment particles. The lift and drag force created by the water flow need to overcome this gravitational force and the associated friction force in the contact points with the neighbouring particles.

Sediment transport is usually decomposed into bed load transport and suspended load transport (Dyer [43], Dyer and Soulsby [44], Fredsøe and Deigaard [45], van Rijn [46], Soulsby [47]). Bed load transport describes the sediment particles transported by rolling, gliding and jumping within a thin layer close to the bed. The suspended load transport describes the sediment particles suspended into and transported in the water column; hence these sediment particles are not in contact with the bed when they are transported. For bed load transport, the local friction velocity is larger than the critical friction velocity, but smaller than the settling velocity, i.e., the velocity of a sediment particle sinking to the bottom in stagnant water. For suspended load transport the local flow velocity exceeds both the critical friction velocity and the settling velocity. The sum of bed load and suspended

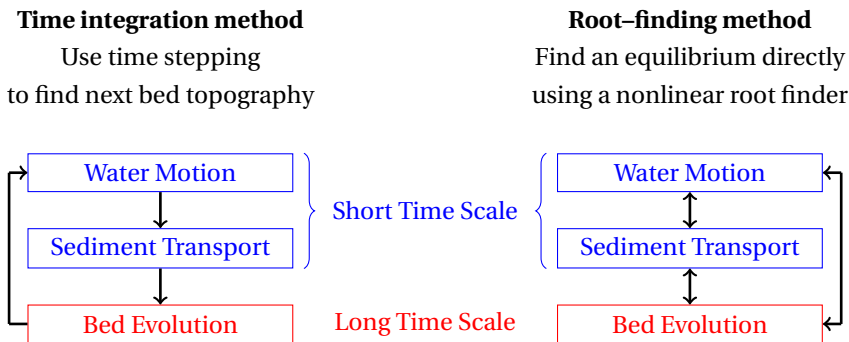


Figure 1.3: Typical schematisation of morphodynamic models. Left scheme shows how the three modules are used in the time integration method: the water motion is calculated depending on bottom topography which changes only on a longer time scale (morphodynamic time scale); the sediment transport is calculated using the water motion; the bed evolution is calculated by implementing the sediment transport into the Exner sediment balance equation. Finally, the new bed topography is fed back to the water motion module. When morphodynamic equilibria are sought for directly, the three modules are regarded as mutually influencing each other, as shown in the right scheme.

load transport is called the total load transport.

Various physical mechanisms control the tidally averaged (i.e., averaged over a tidal period) sediment transport. One important mechanism in tidal basins is tidal asymmetry, which leads to a non-zero tidally averaged transport of sediment if one or more higher harmonics of the basic frequency are prescribed as an external forcing or are generated by nonlinear hydrodynamics. Pingree and Griffiths [48] showed that the net bed load transport induced by tidal asymmetry is in the direction of the peak current. Furthermore, depth-dependent bottom friction has been found to favour flood-dominant transport, whereas hypsometric effects caused by tidal flats favour ebb-dominant transport (Friedrichs and Aubrey [49], Dronkers [50]). Another mechanism is related to spatial settling lag effects, i.e., due to the time needed for sediment particles suspended in the water to settle at slack water. Postma [51] and van Straaten and Kuenen [52] showed that this effect results in net sediment transport in the direction of decreasing tidal current and/or decreasing water depth. Dronkers [53] and Groen [54] showed that tidal asymmetry together with the effects of local inertia results in a net sediment transport that is controlled by the difference in time from maximum ebb (flood) to maximum flood (ebb), referred to as the temporal settling lag effect. Diffusive processes can also result in tidally averaged transport, driven by spatial variations in tidally averaged suspended sediment concentration. These variations can be, amongst others, the result of variations in flow velocities, sediment availability and bed topography.

- **The bed evolution module** describes the bottom changes over time due to erosion and deposition of sediment, which is described by the mass balance equation in the sediment layer. If one is interested in bottom changes at long time scales, tidal averaging is an effective approach (Sanders and Verhulst [55], Krol [56], Schuttelaars and de Swart [57]).

1.4. MORPHODYNAMIC MODELS: SELECTED APPROACH

In this thesis, idealized models will be developed to study the morphodynamics of double-inlet systems. This type of models is chosen because they allow for a quick assessment of morphodynamic equilibria and their sensitivity to parameters (see for instance Schuttelaars [58], Ter Brake [59], van Leeuwen and de Swart [60]). Insight in the existence and multiplicity of possible morphodynamic equilibria of these systems is important as these attractors are the states towards which the systems tend to evolve.

The majority of studies with idealized models focuses on single inlet systems rather than double inlet systems. In this thesis, I will extend the techniques and insights gained from single inlet systems to double inlet system. Hence, in this section, previous studies of idealized and, for completeness, process-based models are briefly discussed for single inlet systems (Sect. 1.4.1), followed by a discussion of existing studies of double inlet systems (Sect. 1.4.2).

1.4.1. SINGLE-INLET SYSTEMS

In this subsection, previous studies of cross-sectionally averaged models are first presented, followed by results concerning the initial formation of channels and shoals in

depth-averaged models. Finally, studies on the development of finite amplitude channel-shoal systems are discussed.

CROSS-SECTIONALLY AVERAGED MODELS

In order to determine the fundamental mechanisms resulting in the morphological evolutions of tidal inlets, Schuttelaars and de Swart [57] developed an analytical cross-sectionally averaged (i.e., one-dimensional) morphodynamic model for a tidal embayment connected by a single inlet to the open sea. In this model, the geometry of the tidal embayment consists of a semi-enclosed rectangular planform, with a width much smaller than the length of the basin and the Rossby deformation radius. The water motion is governed by a simplified version of the cross-sectionally averaged shallow water equations, forced by sea surface elevations at the seaward boundary. Sediment, assumed to be fine sand with a uniform grain size, is transported as suspended load by advective and diffusive processes. The bottom evolution equation is derived from the mass balance in the sediment layer. It was found that for all parameter settings, there is only one morphodynamic equilibrium, which is in qualitative agreement with observed bottom profiles in the short embayments of the Dutch Wadden sea (de Swart and Blaas [61]). Moreover, these bed profiles were shown to be stable against one-dimensional perturbations.

De Jong and Heemink [62] and De Jong [63] developed a similar model for short basins with either a rectangular planform or a converging geometry, and extended their model to long basins. In this model, the water motion was forced by externally prescribed M_2 and M_4 tidal constituents, while the M_4 tidal constituent generated internally by the nonlinear terms was neglected. They found that the inlet length and geometry can strongly influence the morphodynamic equilibrium, which is also sensitive to boundary conditions and friction. Moreover, they found a significant difference between the models for short, medium and long embayments: results obtained for short basins could not be extrapolated to long basins, while the medium-sized basins could shorten themselves to a short basin, depending on the parameter settings. Motivated by these results, Schuttelaars and de Swart [64] extended the model to simulate the morphodynamic evolution of a tidal basin of arbitrary length. The equilibria found were in qualitative agreement with field observations. Furthermore, when the external M_4 constituent of the tidal forcing prescribed at the seaward entrance was important enough, the model allowed for multiple morphodynamic equilibria.

Lanzoni and Seminara [65] also focused on the width-averaged morphodynamic evolution, using a different approach from Schuttelaars and de Swart [57], allowing for a quadratic bottom stress and basin hypsometry. Their model predictions compared well with the observed bed levels in various channels in the Venice Lagoon.

The model of Schuttelaars and de Swart [57] was extended by van Leeuwen *et al.* [66] by making the sediment deposition formula dependent on the local water depth. For a short basin, they found that by adding this depth-dependency the equilibrium bed profile becomes convex. In van Leeuwen [67], width variations of the tidal basin were also taken into account. They found that a converging width has little impact on the resulting morphodynamic equilibria when the convergence is not too strong. When a rectangular basin with tidal flats is considered, the bed profile becomes slightly concave. The influence of geometry on the morphodynamic equilibria was later extended by Meerman *et al.* [68].

Hibma *et al.* [69, 70] extensively compared the results obtained with numerical process-based models with those found using idealized models. The comparison of both types of models is not straightforward, due to the differences in model assumptions and formulations. Hibma *et al.* [70] adapted a complex process-based model, Delft3D, and compared the numerical results with those obtained from cross-sectionally averaged models. They found that qualitative differences between the model approaches were mainly due to a different boundary condition at the entrance of the estuary. The sea bed was allowed to vary at the entrance in the process-based model while it was fixed in the idealized model.

In idealized models, the diffusive sediment transport induced by topographic variations (topographically induced sediment transport) was usually assumed to be balanced by transport due to wind effects (Schuttelaars and de Swart [57], van Leeuwen *et al.* [66]). In order to study this transport, Ter Brake and Schuttelaars [71] extended the model developed by Schuttelaars and de Swart [57]. They found that topographically induced sediment transport leads to a concavity of the equilibrium bed profile which depends on the sediment properties and the length of the embayment.

THE INITIAL FORMATION OF CHANNEL-SHOAL PATTERNS

Bed forms with scales ranging from meters to kilometers are usually observed in tidal basins. The initial formation and development of such bed forms has been reproduced in the laboratory by Tambroni *et al.* [72], Leuven and Kleinhans [73] and has been simulated with complex process-based models (see for example Van der Wegen and Roelvink [74]).

To study the initial formation of sandbars using an idealized model approach, Seminara and Tubino [75] developed a local three-dimensional model for a narrow and frictionally dominated tidal channel. In their model, sediment was transported as suspended load and only advective processes were taken into account. They showed the initial formation of tidal sand bars. Schramkowski *et al.* [76] also investigated these local bed forms with a depth-averaged model, qualitatively reproducing the results found by Seminara and Tubino [75]. Garotta *et al.* [77] also found the same sand bars by depth-averaged approaches, but in their model, a more advanced forcing was included. The bars found in their model show a net migration in the direction of the peak current. Hepkema [78] extended the model of Schramkowski *et al.* [76], and found that when horizontal turbulent exchange processes (parameterized by horizontal eddy viscosities and diffusivities) are included the spatial and temporal scales of tidal bar patterns were in good agreement with observed ones, with the tidal bar wavelength dependent on channel width.

Hibma *et al.* [79] also compared the initial formation of channels and shoals computed through a complex process-based model and an idealized model of a schematised estuary. The initial formation of these bed profiles were obtained by short-term simulations with the process-based model Delft3D and compared well to the results of the linear stability analysis of Schramkowski *et al.* [76].

Schuttelaars and de Swart [80] studied the initial growth of large-scale bed forms using linear stability theory in an idealized model. They considered a short semi-enclosed rectangular basin and included in the model only diffusive processes. The water motion

was forced by an M_2 tide at the seaward side and a simplified bottom friction formulation was used. They found that the one-dimensional constantly sloping bed profile characterising the morphodynamic equilibrium obtained in their earlier cross-sectionally averaged model (Schuttelaars and de Swart [57]), became unstable and two-dimensional perturbations began to grow when the bottom friction exceeded a critical value. In particular, the most preferred perturbation had an along-channel spatial scale of the order of the basin length, thus leading to global scale bottom patterns.

To bridge the gap between the global bed forms found in Schuttelaars and de Swart [80] and the local bed forms found in Seminara and Tubino [75], van Leeuwen and de Swart [81] included advective transport into the model of Schuttelaars and de Swart [80]. They varied the relative strength of diffusive and advective processes and found both small- and large-scale bed forms. When the advective transport dominated, the local bedforms that started to grow resemble those found in local models. When diffusive transport was dominant or of the same order as advective transport, the bottom patterns resembled those found in Schuttelaars and de Swart [80]. Using a complex processed-based model, Van der Wegen and Roelvink [74] pointed out that the local patterns initially start to grow at the landward side, and after some time develop into global patterns. Similar observations were made by Ter Brake [59], Ter Brake and Schuttelaars [82].

THE DEVELOPMENT OF CHANNEL AND SHOAL SYSTEMS

The development of channel-shoal bed forms was first simulated using 2DH process-based models. One of the first examples is reported in Wang *et al.* [83, 84] who simulated the long term evolution of the Frisian Inlet system and the effects of the closure of the Lauwers Sea on this evolution. They reproduced the overall morphological patterns in areas sheltered from waves. Their results also show the observed import of large amounts of sediment into the embayment. Other examples are the simulation of the Arcachon inlet in France (Cayocca [85]) and Morecambe Bay in England (Mason and Garg [86]). Marciano *et al.* [87] later used a highly schematised tidal environment and recovered the fractal like channel and shoal patterns as observed in many tidal inlets. Van der Wegen and Roelvink [74] used a similar model to analyse both the initial and long-term morphodynamic evolution of short and long basins. They found that small patterns initially start to grow at the landward end, slowly move to the seaward direction and become larger and deeper towards the seaward side. Boelens *et al.* [88] use an idealized model to investigate the morphodynamic equilibria, and found that the equilibrium bathymetry consists of a central ridge flanked by two channels when the width of the planform geometry increases towards the landward side.

D'Alpaos *et al.* [89] developed a depth-averaged process-based model to simulate the interaction between vegetation and morphodynamics in tidal embayments. The channel networks they found show features similar to those observed by D'Alpaos *et al.* [90] in the Venice Lagoon.

Schuttelaars [91] first extended the linear stability analysis to a non-linear one in idealized models. Later, using a bifurcation approach, it was found that morphodynamic equilibria composed by channel and shoal patterns can exist if the bottom friction is above a critical value (Dijkstra *et al.* [39], Ter Brake [59]). However, the results for realistic value of the bed friction were difficult to obtain. Ter Brake [59] studied a similar idealized

model and found periodic behaviour of channel and shoal patterns. She suggested that this phenomenon was caused by a phase shift between the concentration of sediment in the water column and bedforms.

1.4.2. DOUBLE-INLET SYSTEMS

Using a **semi-empirical model** (Sect. 1.4.1), Van de Kreeke [92, 93, 94] studied the stability of an inlet system with multiple inlets connecting the back-barrier basin to the open sea. To this end, he extended the single-inlet stability analysis of Escoffier [95]. The bathymetry in the back-barrier basin was fixed, while the inlets were morphodynamically active. The hydrodynamics for each inlet was treated linearly, and the water level in the back-barrier basin was approximated as spatially uniform (pumping mode). For double-inlet systems, he concluded that only one inlet will remain open. Even though he did not study a tidal basin system connected to the open sea by more than two inlets in detail, he stated that a stable equilibrium is highly unlikely to exist with more than one inlet open.

However, long-term observations suggest that double- and multiple-inlet systems exist, in contradiction with theoretical results. This motivated Van de Kreeke *et al.* [96] to extend the physics of his previous model by allowing for spatial variations of free surface elevation in the back-barrier basin. This resulted in stable multiple inlet systems, a finding confirmed by Brouwer *et al.* [97], de Swart and Volp [98] for double inlet systems and Roos *et al.* [7], Reef *et al.* [99] for multiple-inlet systems.

Meerman [100] developed an **idealized model** (Sect. 1.4.1) that extended the models of Schuttelaars and de Swart [57], Ter Brake and Schuttelaars [71] to double-inlet systems. She focused on the cross-sectionally averaged morphodynamic equilibria and found that multiple morphodynamic equilibria exist for certain parameter settings.

Dastgheib *et al.* [101] used a high-complexity **process-based model** (Sect. 1.4.1) to simulate the long term sediment transport and bottom evolution for a double-inlet system, resulting in the development of channel-shoal systems in the back-barrier basin. After simulating 2000 years, the system was assumed to be close to a morphodynamic equilibrium with both inlets still open.

1.5. RESEARCH QUESTIONS

Comparing the studies available in literature addressing single-inlet systems with those concerning double-inlet systems, it is found that no idealized two-dimensional model exists that:

- is morphodynamically active in both the back-barrier basins and the inlets;
- allows for a quick assessment of morphodynamic equilibria and their sensitivity to parameters;
- allows for a detailed process analysis.

Therefore, in this thesis I will develop an idealized model of double-inlet systems to answer the following research questions:

- Q1: How do variations in tidal forcings influence the morphodynamic equilibria in double-inlet systems? Specifically, how do these variations influence the existence and uniqueness of morphodynamic equilibria?
- Q2: How does the planform geometry of double-inlet systems influence the possible morphodynamic equilibria and how do these equilibria compare with observations in the Marsdiep–Vlie inlet system?
- Q3: What are the key mechanisms leading to the initiation and formation of channels and shoals in double-inlet systems?
- Q4: How does the number and stability of two-dimensional morphodynamic equilibria depend on friction and basin width?

1.6. METHODOLOGY

To answer the above research questions, an idealized model for double-inlet system is developed, extending the work of Schuttelaars and de Swart [64] and Meerman *et al.* [102]. The water motion is modeled by using the depth-averaged shallow water equations. Sediment is assumed to be mainly transported as suspended load, while the bed evolution is governed by the continuity equation for the sediment layer. The system of equations is made dimensionless using scaling analysis, leading to the identification of two time scales: the tidal time scale and the morphodynamic time scale. The scaled system is solved using a perturbation approach.

1.7. OUTLINE

In Chap. 2, the numerical methodology is presented and morphodynamic equilibria are obtained. Moreover, research questions Q1 and Q2 are addressed. In Chap. 3 the linear stability of morphodynamic equilibria is analysed using two-dimensional perturbations, answering research question Q3. In Chap. 4 the two-dimensional morphodynamic equilibria are studied and the research question Q4 is addressed. Finally, conclusions are provided in chapter 5.

REFERENCES

- [1] H. E. de Swart and J. T. F. Zimmerman, *Morphodynamics of tidal inlet systems*, Annual Review of Fluid Mechanics **41**, 203 (2009).
- [2] D. J. Glaeser, *Global distribution of barrier islands in terms of tectonic setting*, Journal of Geology **86**, 283 (1978).
- [3] G. Seminara, M. Bolla Pittaluga, N. Tambroni, and V. Garotta, *Open problems in modelling the long-term morphodynamic evolution of Venice lagoon*, Flooding and Environmental Challenges for Venice and its Lagoon, 345 (2005).
- [4] C. L. Amos, G. Umgiesser, G. Tosi, and I. H. Townend, *The coastal morphodynamics of Venice lagoon, Italy: An introduction*, Continental Shelf Research **30**, 837 (2010), the Coastal Morphodynamics of Venice Lagoon and its Inlets.

- [5] A. Oost and P. De Boer, *Sedimentology and development of barrier islands, ebb-tidal deltas, inlets and backbarrier areas of the Dutch Wadden Sea*, *Senckenbergiana Maritima*. Frankfurt/Main **24**, 65 (1994).
- [6] A. P. Oost, P. Hoekstra, A. Wiersma, B. Flemming, E. J. Lammerts, M. Pejrup, J. Hofstede, B. Van der Valk, P. Kiden, J. Bartholdy, M. Van der Berg, P. C. Vos, S. de Vries, and Z. B. Wang, *Barrier island management: Lessons from the past and directions for the future*, *Ocean & Coastal Management* **68**, 18 (2012).
- [7] P. C. Roos, H. M. Schuttelaars, and R. L. Brouwer, *Observations of barrier island length explained using an exploratory morphodynamic model*, *Geophysical Research Letters* **40**, 4338 (2013).
- [8] M. Hayes, *The Georgia Bight barrier system*, *Geology of Holocene Barrier Island Systems*, 233 (1994).
- [9] G. Gao, X. Wang, and X. Bao, *Land reclamation and its impact on tidal dynamics in Jiaozhou Bay Qingdao, China*, *Estuarine, Coastal and shelf Science* **151**, 285 (2014).
- [10] S. Yang, J. Zhang, and J. Zhu, *Response of suspended sediment concentration to tidal dynamics at a site inside the mouth of an inlet: Jiaozhou Bay (China)*, *Hydrology and Earth System Sciences* **8**, 170.
- [11] M. O. Hayes, *Morphology of sand accumulation in estuaries: An introduction to the symposium*, *Geology and Engineering*, 3 (1975).
- [12] K. J. H. Lenstra, S. Pluis, W. Ridderinkhof, G. Ruessink, and M. Van der Vegt, *Cyclic channel–shoal dynamics at the Ameland inlet: The impact on waves, tides, and sediment transport*, *Ocean Dynamics*, 409 (2019).
- [13] L. Sha, *Variation in ebb–delta morphologies along the West and East Frisian islands, the Netherlands and Germany*, *Marine Geology* **89**, 11 (1989).
- [14] D. M. FitzGerald, *Interactions between the ebb-tidal delta and landward shoreline: Price inlet, south carolina*, *Journal of Sedimentary Petrology* **54**, 1303 (1984).
- [15] D. FitzGerald, N. Kraus, and E. Hands, *Natural mechanisms of sediment bypassing at tidal inlets (ERDC/CHL CHETN-IV-30)*, U.S. Army Engineer Research and Development Center, Vicksburg, M.S. (2000).
- [16] W. Ridderinkhof, P. Hoekstra, M. Van der Vegt, and H. de Swart, *Cyclic behavior of sandy shoals on the ebb–tidal deltas of the wadden sea*, *Continental Shelf Research* **115**, 14 (2016).
- [17] D. M. FitzGerald, *Shoreline erosional depositional processes associated with tidal inlets*, in *Hydrodynamics and Sediment Dynamics of Tidal Inlets* (1988) pp. 186–225.
- [18] A. WestHuysen, *Spectral modeling of wave dissipation on negative current gradients*, *Coastal Engineering* **68**, 17 (2012).

- [19] E. L. P. Elias and J. E. Hansen, *Understanding processes controlling sediment transports at the mouth of a highly energetic inlet system (San Francisco Bay, CA)*, *Marine Geology* **345**, 207 (2013).
- [20] A. Nahon, X. Bertin, A. B. Fortunato, and A. Oliveira, *Process-based 2DH morphodynamic modeling of tidal inlets: A comparison with empirical classifications and theories*, *Marine Geology* **291**, 1 (2012).
- [21] M. Hayes, *General morphology and sediment patterns in tidal inlets*, *Sedimentary Geology* **26**, 139 (1980).
- [22] M. Duran-Matute, T. Gerkema, G. J. de Boer, J. J. Nauw, and U. Grawe, *Residual circulation and freshwater transport in the Dutch Wadden Sea: a numerical modelling study*, *Ocean Science* **10**, 611 (2014).
- [23] M. Sassi, M. Duran-Matute, T. van Kessel, and T. Gerkema, *Variability of residual fluxes of suspended sediment in a multiple tidal–inlet system: the Dutch Wadden Sea*, *Ocean Dynamics* **65**, 1321 (2015).
- [24] R. W. Dalrymple and R. N. Rhodes, *Chapter 13 estuarine dunes and bars*, in *Geomorphology and Sedimentology of Estuaries*, Developments in Sedimentology, Vol. 53, edited by G. Perillo (Elsevier, 1995) pp. 359–422.
- [25] J. Mulhern, C. Johnson, and J. Martin, *Is barrier island morphology a function of tidal and wave regime?* *Marine Geology* **387**, 74 (2017).
- [26] R. A. McBride, M. R. Byrnes, and M. W. Hiland, *Geomorphic response-type model for barrier coastlines: A regional perspective*, *Marine Geology* **126**, 143 (1995).
- [27] A. J. F. Van der Spek, *Tidal asymmetry and long-term evolution of holocene tidal basins in the Netherlands: Simulation of paleo-tides in the Scheldt estuaries*, *Marine Geology* **141**, 71 (1997).
- [28] M. C. Buijsman and H. Ridderinkhof, *Long-term feery-ADCP observations of tidal currents in the Marsdiep inlet*, *Journal of Sea Research* **57** (2007).
- [29] M. C. Buijsman and H. Ridderinkhof, *Long-term evolution of sand waves in the Marsdiep inlet. I: High-resolution observations*, *Continental Shelf Research* **28** (2008).
- [30] M. C. Buijsman and H. Ridderinkhof, *Long-term evolution of sand waves in the Marsdiep inlet. II: Relation to hydrodynamics*, *Continental Shelf Research* **28** (2008).
- [31] B. C. van Prooijen and Z. B. Wang, *A 1D model for tides waves and fine sediment in short tidal basins—application to the Wadden Sea*, *Ocean Dynamics* **63**, 1233 (2013).
- [32] L. D. Wright and B. G. Thom, *Coastal depositional landforms: A morphodynamic approach*, *Progress in Physical Geography* **1**, 412 (1977).

- [33] H. J. de Vriend, *Mathematical modelling and large-scale coastal behaviour (part I: Physical processes)*, *Journal of Hydraulic Research* **29**, 727 (1991).
- [34] H. J. de Vriend, *Mathematical modeling of meso-tidal barrier island coasts, part I: Empirical and semi-empirical models*, *Advances in Coastal and Ocean Engineering*, 115 (1996).
- [35] H. J. de Vriend and J. S. Ribberink, *Mathematical modeling of meso-tidal barrier island coasts, part II: Process-based simulation models*, *Advances in Coastal and Ocean Engineering*, 151 (1996).
- [36] I. Fairley, M. A. Davidson, K. Kingston, T. Dolphin, and R. Phillips, *Empirical orthogonal function analysis of shoreline changes behind two different designs of detached breakwaters*, *Coastal Engineering* **56**, 1097 (2009).
- [37] F. Alvarez and S. Pan, *Predicting coastal morphological changes with empirical orthogonal function method*, *Water Science and Engineering* **9**, 14 (2016).
- [38] M. P. O'Brien, *Estuary tidal prism related to entrance areas*, *Civ. Eng.* **1**, 738 (1931).
- [39] H. Dijkstra, F. Wubs, A. Cliffe, E. Doedel, I. Dragomirescu, B. Eckhardt, A. Gelfgat, A. Hazel, V. Lucarini, A. Salinger, E. Phipps, S. U. Juan, H. Schuttelaars, L. Tuckerman, and U. Thiele, *Numerical bifurcation methods and their application to fluid dynamics: Analysis beyond simulation*, *Communications in Computational Physics* **15**, 1 (2014).
- [40] G. T. Csanady, *Circulation in the Coastal Ocean* (Reidel, 1982).
- [41] C. B. Vreugdenhil, *Numerical methods for shallow-water flow* (Kluwer Academic Publisher, Boston, 1986).
- [42] J. Nihoul and F. Ronday, *The influence of the "tidal stress" on the residual circulation*, *Tellus* **22**, 484 (1975).
- [43] K. R. Dyer, *Coastal and estuarine sediment dynamics* (John Wiley and Sons, 1986).
- [44] K. R. Dyer and R. L. Soulsby, *Sand transport on the continental shelf*, *Annual Review of Fluid Mechanics* **20**, 295 (1988).
- [45] J. Fredsøe and D. G. Deigaard, *Mechanics of coastal sediment transport* (World Scientific, Singapore, 1992).
- [46] L. C. van Rijn, *Principles of sediment transport in rivers, estuaries and coastal seas* (Aqua Publications Amsterdam, 1993).
- [47] R. Soulsby, *Dynamics of marine sands* (Springer, 1997).
- [48] R. D. Pingree and D. K. Griffiths, *Sand transport paths around the British isles resulting from M2 and M4 tidal interactions*, *Journal of the Marine Biological Association of the United Kingdom* **59**, 497 (1979).

- [49] C. Friedrichs and D. Aubrey, *Nonlinear tidal distortion in shallow well mixed estuaries: A synthesis*, Estuarine, Coastal and shelf science **27**, 512 (1988).
- [50] J. Dronkers, *Dynamics of Coastal Systems* (World Scientific, Singapore, 2005).
- [51] H. Postma, *Hydrography of the Dutch Wadden Sea*, *Archives Neerlandaises de Zoologie* **10**, 405 (1954).
- [52] L. M. J. U. van Straaten and P. H. Kuenen, *Accumulation of fine grained sediments in the Dutch Wadden Sea*, Netherlands Journal Geoscience **18**, 1 (1994).
- [53] J. Dronkers, *Tidal asymmetry and estuarine morphology*, Netherlands Journal of Sea Research **20**, 117 (1986).
- [54] P. Groen, *On the residual transport of suspended matter by an alternating tidal current*, Netherlands Journal of Sea Research **3**, 564 (1967).
- [55] J. A. Sanders and F. Verhulst, *Averaging methods in nonlinear dynamical systems* (Spring Verlag, New York, 1985).
- [56] M. Krol, *On the averaging method in nearly time-periodic advection-diffusion problems*, SIAM Journal on Applied Mathematics **51**, 1622 (1991).
- [57] H. M. Schuttelaars and H. E. de Swart, *An idealized long-term morphodynamic model of a tidal embayment*, European Journal of Mechanics, B/Fluids **15**, 55 (1996).
- [58] H. M. Schuttelaars, *Evolution and stability analysis of bottom patterns in tidal embayment* (1997).
- [59] M. C. Ter Brake, *Tidal embayments: Modelling and understanding their morphodynamics* (2011).
- [60] S. M. van Leeuwen and H. E. de Swart, *The effect of advective processes on the morphodynamic stability of short tidal embayments*, Physics and Chemistry of the Earth (B) **26**, 735 (2001).
- [61] H. E. de Swart and M. Blaas, *Morphological evolutions in a 1D model for a dissipative tidal embayment*, Physics of Estuaries and Coastal Seas , 305 (1996).
- [62] K. De Jong and A. W. Heemink, *A model for long-term morphodynamic behaviour of tidal basins, long estuaries, and tidal rivers*, (1996).
- [63] K. De Jong, *Tidally averaged transport models* (1998).
- [64] H. M. Schuttelaars and H. E. de Swart, *Multiple morphodynamic equilibria in tidal embayments*, Journal of Geophysical Research **105**, 105 (2000).
- [65] S. Lanzoni and G. Seminara, *Long-term evolution and morphodynamic equilibrium of tidal channels*, Journal of Geophysical Research **107**, 1 (2002).

- [66] S. M. van Leeuwen, H. M. Schuttelaars, and H. E. de Swart, *Tidal and morphologic properties of embayments: Effect of sediment deposition processes and length variation*, *Physics and Chemistry of the Earth, Part B: Hydrology, Oceans and Atmosphere* **25**, 365 (2000).
- [67] S. M. van Leeuwen, *Tidal inlet systems: Bottom pattern formation and outer delta development* (2002).
- [68] C. Meerman, V. Rottschäfer, and H. Schuttelaars, *Influence of geometrical variations on morphodynamic equilibria in short tidal basins*, *Ocean Dynamics* **69**, 221 (2019).
- [69] A. Hibma, H. M. Schuttelaars, and Z. B. Wang, *Comparison of longitudinal equilibrium profiles of estuaries in idealised and process-based models*, *Ocean dynamics* **53**, 252 (2003).
- [70] A. Hibma, H. J. de Vriend, and M. J. F. Stive, *Numerical modelling of shoal pattern formation in well-mixed elongated estuaries*, *Estuarine, Coastal and Shelf Science* **57**, 981 (2003).
- [71] M. C. Ter Brake and H. M. Schuttelaars, *Modeling equilibrium bed profiles of short tidal embayment. On the effect of the vertical distribution of suspended sediment and the influence of the boundary conditions*, *Ocean Dynamics* **60**, 183 (2010).
- [72] N. Tambroni, M. Bolla Pittaluga, and G. Seminara, *Laboratory observations of the morphodynamic evolution of tidal channels and tidal inlets*, *Journal of Geophysical Research* **110**, F04009 (2005).
- [73] J. R. F. W. Leuven and M. G. Kleinhans, *Incipient tidal bar and sill formation*, *Journal of Geophysical Research* **124**, 1762 (2019).
- [74] M. Van der Wegen and J. A. Roelvink, *Long-term morphodynamic evolution of a tidal embayment using a two-dimensional process-based model*, *Journal of Geophysical Research* **7**, C03016 (2008).
- [75] G. Seminara and M. Tubino, *On the formation of estuaries free bars*, *J. Physics of Estuaries and Coastal Seas* **96**, 345 (1998).
- [76] G. P. Schramkowski, H. M. Schuttelaars, and H. E. de Swart, *The effect of geometry and bottom friction on local bed forms in a tidal embayment*, *Continental Shelf Research* **22**, 1821 (2002).
- [77] V. Garotta, M. Bolla Pittaluga, and G. Seminara, *On the migration of tidal free bars*, *Physics of Fluids* **18**, 096601 (2006).
- [78] T. Hepkema, *Nonlinear dynamics of tides and sandbars in tidal channels* (2021).
- [79] A. Hibma, H. M. Schuttelaars, and H. J. Vriend, *Initial formation and evolution of channel-shoal patterns in estuaries*, *Continental Shelf Research* **24**, 1637 (2004).

- [80] H. M. Schuttelaars and H. E. de Swart, *Initial formation of channels and shoals in a short tidal embayment*, *Journal of Fluid Mechanics* **386**, 15 (1999).
- [81] S. M. van Leeuwen and H. E. de Swart, *Effect of advective and diffusive sediment transport on the formation of local and global bottom patterns in tidal embayments*, *Ocean Dynamics* **54**, 441 (2004).
- [82] M. C. Ter Brake and H. M. Schuttelaars, *Channel and shoal development in a short tidal embayment: An idealized model study*, *Journal of Fluid Mechanics* **677**, 503 (2011).
- [83] Z. B. Wang, T. Louters, and H. J. de Vriend, *A morphodynamic model for tidal inlet*, *Computing Modelling in Ocean Engineering—Proceedings of the second international conference, Barcelona–Balkema Rotterdam* **91**, 235 (1992).
- [84] Z. B. Wang, T. Louters, and H. J. de Vriend, *Morphodynamic modelling for a tidal inlet in the Wadden Sea*, *Marine Geology* **126**, 289 (1995).
- [85] F. Cayocca, *Long-term morphological modeling of a tidal inlet: The Archachon basin, France*, *Coastal Engineering* **42**, 115 (2001).
- [86] D. C. Mason and P. K. Garg, *Morphodynamic modelling of intertidal sediment transport in Morecambe Bay*, *Estuarine, Coastal and Shelf Science* **53**, 79 (2001).
- [87] R. Marciano, Z. Wang, A. Hibma, H. De Vriend, and A. Defina, *Modeling of channel patterns in short tidal basins*, *Journal of Geophysical Research* **110** (2005), [10.1029/2003JF000092](https://doi.org/10.1029/2003JF000092).
- [88] T. Boelens, T. Qi, H. Schuttelaars, and T. De Mulder, *Morphodynamic equilibria in short tidal basins using a 2DH exploratory model*, *Journal of Geophysical Research: Earth Surface* **126** (2021).
- [89] A. D’Alpaos, S. Lanzoni, M. Marani, and A. Rinaldo, *Landscape evolution in tidal embayments: Modelling the interplay of erosion, sedimentation, and vegetation dynamics*, *Journal of Geophysical Research* **112**, F01008 (2007).
- [90] A. D’Alpaos, S. Lanzoni, M. Marani, A. Bonometto, G. Cecconi, and A. Rinaldo, *Spontaneous tidal network formation within a constructed salt marsh: Observations and morphodynamic modeling*, *Geomorphology* **91**, 186 (2007).
- [91] H. M. Schuttelaars, *Nonlinear, long term equilibrium bed profiles in a short tidal embayment*, *Physics of Estuaries and Coastal Seas*, 337 (1998).
- [92] J. Van de Kreeke, *Stability of tidal inlets—Pass Cavallo, Texas*, *Estuarine, Coastal and Shelf Science* **21**, 33 (1985).
- [93] J. Van de Kreeke, *Stability analysis of a two-inlet bay system*, *Coastal Engineering* **14**, 481 (1990).
- [94] J. Van de Kreeke, *Can multiple tidal inlets be stable?* *Estuarine, Coastal and Shelf Science* **30**, 261 (1990).

- [95] F. Escoffier, *The stability of tidal inlets*, Shore Beach **8**, 114 (1940).
- [96] J. Van de Kreeke, R. L. Brouwer, T. J. Zitman, and H. M. Schuttelaars, *The effect of a topographic high on the morphodynamical stability of a two inlet bay system*, Coastal Engineering **55**, 319 (2008).
- [97] R. L. Brouwer, J. Van de Kreeke, and H. M. Schuttelaars, *Entrance/exit losses and cross-sectional stability of double inlet systems*, Estuarine, Coastal and Shelf Science **107**, 69 (2012).
- [98] H. E. de Swart and N. D. Volp, *Effects of hypsometry on the morphodynamic stability of single and multiple tidal inlet systems*, Journal of Sea Research **74**, 35 (2012).
- [99] K. Reef, P. Roos, H. Schuttelaars, and S. Hulscher, *Influence of back-barrier basin geometry on multiple tidal inlet systems: The roles of resonance and bottom friction*, [Journal of Geophysical Research: Earth Surface](https://doi.org/10.1029/2019JF005261) **125** (2020), 10.1029/2019JF005261.
- [100] C. J. Meerman, *Morphodynamic equilibria in tidal inlet systems: Sensitivity to geometrical variations* (2021).
- [101] A. Dastgheib, J. A. Roelvink, and Z. B. Wang, *Long-term process-based morphological modeling of the Marsdiep tidal basin*, Marine Geology **256**, 90 (2008).
- [102] C. J. Meerman, H. M. Schuttelaars, and V. Rottschäfer, *Influence of geometrical variations on morphodynamic equilibria for single inlet systems*, [Ocean Dynamics](https://doi.org/10.1016/j.oceandyn.2019.02.001) **69**, 2 (2019).

2

MORPHODYNAMIC EQUILIBRIA IN DOUBLE INLET SYSTEMS: THEIR EXISTENCE AND STABILITY

The existence of morphodynamic equilibria in double-inlet systems is investigated using a cross-sectionally averaged morphodynamic model. The number of possible equilibria and their stability is found to strongly depend on the considered forcing conditions and geometry. This is illustrated by first studying a rectangular double-inlet system forced only by an M_2 tidal constituent. Depending on the M_2 amplitude and phase at both entrances, no equilibrium, one equilibrium or multiple morphodynamic equilibria may exist. In case no equilibrium is found, the minimum water depth becomes zero somewhere in the tidal basin, reducing the double-inlet system to two single-inlet systems. In the other cases, the location of the minimum water depth and the direction of the tidally-averaged sediment transport, as well as their actual values, depend strongly on characteristics of the M_2 forcing.

A parameter sensitivity is also observed when including the residual and M_4 forcing contributions to the water motion, and when allowing for width variations. This suggests that, when considering a specific system, the number and stability of morphodynamic equilibria, as well as the characteristics of these equilibria, can only be assessed by investigating in detail the specific system. As an example, the Marsdiep-Vlie inlet system in the Dutch Wadden Sea is considered. It is found that, by using parameter values and a geometry characteristic for this system, the water motion and bathymetry at morphodynamic equilibrium are qualitatively reproduced. Also the direction and order of magnitude of the tidally-averaged suspended sediment transport compare well with those obtained from a high-complexity numerical model.

This chapter is published as: **X. Deng**, C. Meerman, T. Boelens, T. De Mulder, P. Salles, and H. M. Schuttelaars. (2021) *Morphodynamic equilibria in double inlet systems: their existence and stability*. Journal of Geophysical Research, 126(12), e2021JF006266.

PLAIN LANGUAGE SUMMARY

An idealized model is developed to systematically investigate the cross-sectionally averaged morphodynamic equilibria in double-inlet systems with varying width. A bathymetric profile in equilibrium with the water motion and sediment transport is obtained if there is no accumulation of tidally averaged sediment transport. Considering a constant-width system, the number of morphodynamic equilibria strongly depends on the tidal forcings. For an M_2 tidal forcing only, it is found that no equilibrium, one equilibrium or more than one morphodynamic equilibria can exist. The location and the depth of the watershed, and the total sediment transport are used to characterize the morphodynamic equilibria. Typically, the watershed tends to get closer to the inlet with a larger tidal amplitude, and the total transport is directed from the inlet with the largest tidal amplitude to the one with the smallest tidal amplitude. Taking parameter values representative of the Marsdiep–Vlie system, one stable morphodynamic equilibrium is found. Inclusion of the large-scale width variations observed in the Marsdiep–Vlie system is essential to obtain an equilibrium profile that qualitatively reproduces the observed width-averaged bathymetry, water motion and tidally-averaged sediment transport.

2.1. INTRODUCTION

A large part of the world's coastline can be characterized as barrier coasts (Mulhern *et al.* [1]), consisting of barrier islands, back-barrier basins and tidal inlets connecting the back-barrier basins to the open sea (de Swart and Zimmerman [2]), with shape and size varying significantly from location to location (Glaeser [3], Stutz and Pilkey [4]). Barrier coasts are highly dynamic, in part due to the complex nonlinear interactions among water motion, sediment transport and morphological evolution, as well as to their sensitivity to changes in external conditions caused, for example, by increased storm frequency and intensity, sea level rise and human interference (McBride *et al.* [5], Van der Spek [6]). Barrier coasts are very important from an ecological and economical point of view. Their ecological value lies in their function as breeding and feeding grounds for aquatic and terrestrial species, their biodiversity and other ecosystem services they provide. Economical activities such as gas-mining, dredging and recreation are common in these regions. Furthermore, they are of importance for coastal safety (Glaeser [3]).

An example of a barrier coast, where the back-barrier basin is connected to the open sea by multiple inlets, is the Wadden Sea along the Dutch, German and Danish coast (Oost *et al.* [7]). In Fig. 2.1 a part of the Dutch Wadden Sea is shown as an example of such a system. Even though it is often assumed that the various inlets drain different sub-basins, separated from each other by a tidal watershed, recent studies have revealed a strong exchange of water (Duran-Matute *et al.* [8]) and sediment (Sassi *et al.* [9]) between adjacent sub-basins. Similar interactions are also found in the Ria Formosa in south Portugal (Salles *et al.* [10], Pacheco *et al.* [11]) and Venice Lagoon (Seminara *et al.* [12], Tambroni and Seminara [13]). This strongly suggests that to understand, model and predict the morphodynamic evolution of these systems, the interactions between sub-systems have to be taken into account, i.e., these systems should be considered as multiple inlet systems. This is also necessary for long-term analysis, as observations show that these



Figure 2.1: Satellite image showing the bathymetry of the part of the Dutch Wadden Sea that contains the Marsdiep, Eijerlandse Gat and Vlie inlet systems. (Copyright © USGS/ESA).

multiple inlet systems have been present for centuries.

To study the long-term morphodynamic stability of multiple inlet systems, Van de Kreeke [14, 15, 16] extended the single-inlet stability concept of Escoffier [17] to multiple inlets. In his approach only the inlets are assumed to be morphodynamically active, i.e., the bathymetry in the back-barrier basin is fixed. Furthermore, the water level in the back-barrier basin is approximated as spatially uniform (pumping mode). He showed for double-inlet systems, and speculated for multiple inlet systems, that ultimately only one inlet would remain open. Because this conclusion contradicted long-term observations, Van de Kreeke *et al.* [18] extended the physics of their previous models by allowing for spatial variations in the free surface elevation in the back-barrier basin. This resulted in stable double-inlet systems, a finding confirmed by the studies of Brouwer *et al.* [19], de Swart and Volp [20] for double-inlet systems and Roos *et al.* [21], Reef *et al.* [22] for multiple inlet systems.

One of the great advantages of these semi-empirical models is their computational efficiency, allowing for extensive sensitivity analysis of parameters such as tidal range, phase difference of the tidal forcing at the inlets and basin geometry, factors that strongly influence the morphodynamic stability of the inlet systems. However, these models do not allow the morphodynamic evolution of the back-barrier basin, even though field observations and model studies show that these regions are morphodynamically active. For example, Dastgheib *et al.* [23] used a high-complexity numerical model to simulate the long-term sediment transport and bottom evolution of a double-inlet system,

resulting in the development of channel–shoal systems in the back–barrier basin. After simulating 2000 years, the system was assumed to be close to a morphodynamic equilibrium with both inlets still open. A detailed analysis of the physical mechanisms resulting in the observed morphodynamic equilibrium is however challenging when using high–complexity numerical models. It is thus difficult to gain insight into the sensitivity of the morphodynamic equilibria to variations in parameters and geometric characteristics.

The aim of the present study is therefore to develop a process–based model of a double–inlet systems on mesotidal barrier coasts (Hayes [24]) in which both the tidal inlets and back–barrier basin are morphodynamically active. The model will be used to analyze the existence of morphodynamic equilibria, their stability, and sensitivity to parameters and geometry. It should allow for a systematic analysis of the physical mechanisms leading to these morphodynamic equilibria. Motivated by the insights gained from equilibrium models for single–inlet systems (Schuttelaars and de Swart [25, 26], Ter Brake and Schuttelaars [27], Meerman *et al.* [28]), this type of models will be extended to study the case of two tidal inlets connected to each other by a back–barrier basin of arbitrary length and width. Default parameters used in the model are characteristic of a double–inlet system in the Dutch Wadden Sea. The model results will be compared with field observations and numerical model results from the Marsdiep–Vlie system. The existence and sensitivity of morphodynamic equilibria to basin geometry and forcing conditions at the seaward sides of the two inlets, consisting of M_2 and M_4 tidal constituents and a subtidal signal, will be investigated in detail.

In Sect. 2.2 the equations governing water motion, transport of sediment and bed evolution are presented. The scaling of the system of equations and the solution method are presented in Sect. 2.3. In Sect. 2.4, morphodynamic equilibria in double–inlet systems and their linear stability are studied. In Sect. 2.5, the results are discussed and in Sect. 2.6 conclusions are presented.

2.2. MODEL DESCRIPTION

The geometry under consideration consists of a tidal inlet system connected to the open sea by two inlets (for a top view see Fig.2.2b, obtained using the observed field geometry of Fig.2.2a). The x axis in Fig. 2.2b represents the distance along the centerline indicated in Fig. 2.2a, whereas the y axis represents the distances normal to the centerline. The inlet system is aligned with the horizontal x axis, and has a prescribed length L . The basin is connected to the open sea at $x = 0$ and $x = L$, respectively. The width is allowed to vary with the longitudinal coordinate, and is denoted by $B(x) = B_2(x) - B_1(x)$, with B_2 and B_1 indicating the left and right coastal boundaries, looking from inlet I to inlet II . These coastal boundaries are assumed to be non-erodible. The width of inlet I is denoted by $B^I = B(0)$, and the width at inlet II by $B^{II} = B(L)$.

The undisturbed water depth at inlet I ($x = 0$) is denoted by H^I , and by H^{II} at $x = L$ (see Fig.2.2c for a side view). The free surface is represented by the equation $z = \zeta$, with the undisturbed free surface located at $z = 0$. The erodible bottom, that is assumed to consist of sandy material with a single grain size, is described by the equation $z = \hat{h} - H^I$, where H^I is used as the reference depth and \hat{h} is the local bed elevation measured from level identified by the reference depth. Hence, the instantaneous local water depth is given by $H^I - \hat{h} + \zeta$.

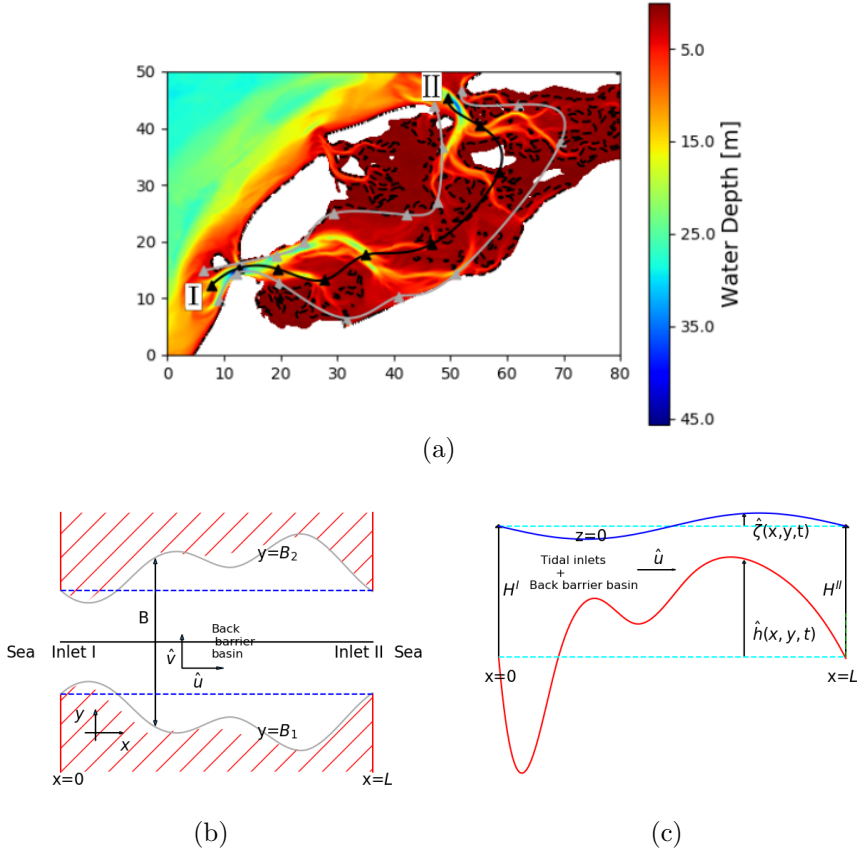


Figure 2.2: Sketch of a tidal embayment connected to the open sea at both ends. (a) The bathymetry surveyed in the Marsdiep–Vlie inlet system. The dark–grey solid lines indicate the coastal boundaries used in the model, whereas the centerline is indicated by a black solid line. For a more elaborate discussion, see Sect. 2.5.2. (b) A top view of the schematized double–inlet system with a varying width (dark–grey solid lines) and a uniform width (dashed blue lines). The longitudinal and lateral velocities are denoted by \hat{u} and \hat{v} . (c) A cross–sectional view of the double–inlet system, with the depth at inlet I denoted by H^I and the depth at inlet II denoted by H^{II} . The bed profile (red line) is denoted by $\hat{h}(x, y, t)$, and the free surface elevation (blue line) by $\hat{\zeta}(x, y, t)$.

Since both the length and width of the inlet system are much larger than the reference water depth, and the width is much smaller than the basin length and the Rossby deformation radius, the water motion can be described by the cross-sectionally averaged equations for a homogeneous fluid (Csanady [29]):

$$B\zeta_t + [B(H^I - h + \zeta)u]_x = 0, \quad (2.1a)$$

$$u_t + uu_x + g\zeta_x + \frac{r_* u}{H^I - h + \zeta} = 0. \quad (2.1b)$$

Here, ζ denotes the width-averaged sea surface elevation, defined as

$$\zeta(x, t) = \frac{1}{B_2 - B_1} \int_{B_1}^{B_2} \hat{\zeta}(x, y, t) dy. \quad (2.2)$$

Similarly, $u(x, t)$ denotes the width-averaged horizontal longitudinal velocity and h the width-averaged bed level. Time is denoted by t , and g denotes the gravitational acceleration. Subscripts denote a derivative with respect to that variable. Following Lorentz [30] and Zimmerman [31], a linearized formulation of the friction is used with the bottom friction coefficient defined as $r_* = 8Uc_d/3\pi$, with U a characteristic velocity scale and c_d a drag coefficient. The characteristic velocity U will be introduced in section 2.3.1.

The variables ζ and u can be decomposed in a residual and a time-varying contribution as $\zeta = \langle \zeta \rangle + \tilde{\zeta}$ and $u = \langle u \rangle + \tilde{u}$, where $\langle \cdot \rangle$ denotes tidal averaging, and $\tilde{\cdot}$ the deviation from the tidal average, such that $\langle \tilde{\cdot} \rangle = 0$. The time dependent sea surface elevations at the two inlets are prescribed as

$$\tilde{\zeta} = A_{M_2}^I \cos(\sigma t - \phi_{M_2}^I) + A_{M_4}^I \cos(2\sigma t - \phi_{M_4}^I) \quad \text{at } x = 0, \quad (2.3a)$$

$$\tilde{\zeta} = A_{M_2}^{II} \cos(\sigma t - \phi_{M_2}^{II}) + A_{M_4}^{II} \cos(2\sigma t - \phi_{M_4}^{II}) \quad \text{at } x = L. \quad (2.3b)$$

It should be noted that, when considering the morphodynamic *evolution* of a tidal basin, the effect of radiation damping on the tidal forcing at the seaward side can only be neglected in the so-called *deep sea limit* (Roos and Schuttelaars [32]). However, if one is only interested in morphodynamic equilibria, prescribing the tidal forcing is allowed. One should interpret the morphodynamic equilibria as obtained for that prescribed tidal forcing. For the tidally-averaged hydrodynamic components, we require

$$\langle \tilde{\zeta} \rangle = 0 \quad \text{at } x = 0, \quad (2.4a)$$

$$\langle B(H - h - \zeta)u \rangle = Q_* \quad \text{at } x = L. \quad (2.4b)$$

The constants $A_{M_2}^I$ ($A_{M_4}^I$) and $A_{M_2}^{II}$ ($A_{M_4}^{II}$) denote the amplitude of the M_2 (M_4) tide at the seaward sides of inlet I and II, respectively. Their corresponding phases are given by $\phi_{M_2}^I$ ($\phi_{M_4}^I$) and $\phi_{M_2}^{II}$ ($\phi_{M_4}^{II}$). The angular frequency of the M_2 tidal signal is given by $\sigma = 2\pi/T$, with T the M_2 tidal period. Condition (2.4a) implies that at the first inlet the tidally-averaged water depth is given by H^I , whereas the mean water depth at inlet II may deviate with respect to the undisturbed water level due to a mean difference in the mean sea surface elevation on the seaward side of the two inlets. The boundary condition (2.4b) at inlet II assumes the depth-averaged residual water transport equals

Q_* . When Q_* is positive it represents a residual transport from inlet I to II, a negative value implies a net transport from inlet II to inlet I.

The sediment of the tidal inlet system consists of noncohesive material with a uniform grain size of $2 \cdot 10^{-4}$ m. The sediment is assumed to be mainly transported as suspended load, and its dynamics is described by the width-averaged and depth-integrated concentration equation (Ter Brake and Schuttelaars [27, 33]):

$$BC_t + [BuC - k_{h*}B(C_x + \frac{w_s}{k_{v*}}\beta h_x C)]_x = B(\alpha u^2 - \frac{w_s^2}{k_{v*}}\beta C), \quad (2.5)$$

where C is the depth-integrated and width-averaged suspended sediment concentration, k_{h*} is the horizontal diffusivity, k_{v*} is the vertical diffusivity, w_s is the settling velocity, α is an erosion parameter (Dyer [34]) related to sediment properties, and β is a deposition parameter, defined by (see Ter Brake and Schuttelaars [27] for details)

$$\beta = \frac{1}{1 - \exp(-\frac{w_s}{k_{v*}}(H^I - h + \zeta))}. \quad (2.6)$$

The tidally-averaged erosion and deposition are assumed to balance each other at seaward entrances, and it is assumed that no diffusive boundary layers develop at these locations in the time-dependent parts of the sediment concentration (Schuttelaars and de Swart [26]). The resulting boundary conditions read

$$\langle \alpha u^2 - \frac{w_s^2}{k_{v*}}\beta C \rangle = 0 \quad \text{at } x = 0 \text{ and } L, \quad (2.7a)$$

$$\lim_{k_{h*} \rightarrow 0} \bar{C}(x, t, k_{h*}) = \bar{C}(x, t, k_{h*} = 0) \quad \text{at } x = 0 \text{ and } L. \quad (2.7b)$$

The width-averaged bed evolution equation is derived from the mass balance in the sediment layer and reads

$$B\rho_s(1-p)h_t = -B(\alpha u^2 - \frac{w_s^2}{k_{v*}}\beta C). \quad (2.8)$$

Here, ρ_s is the density of the sediment and p denotes the bed porosity. The first and second term on the right of Eq.(2.8) model the local erosion and deposition of sediment, respectively.

Substituting Eq.(2.5) into Eq.(2.8) results in the following bed evolution equation:

$$B[\rho_s(1-p)h_t + C_t] = -F_x, \quad (2.9)$$

with

$$F = \underbrace{-k_{h*}BC_x}_{F_{\text{diff}}} + \underbrace{-k_{h*}\frac{w_s}{k_{v*}}B\beta h_x C}_{F_{\text{topo}}} + \underbrace{BuC}_{F_{\text{adv}}}, \quad (2.10)$$

the total depth-integrated and width-averaged sediment transport. This transport consists of three terms: a diffusive contribution related to the diffusion of depth-integrated

concentration (F_{diff}), a diffusive contribution related to topographical variations (F_{topo}) and an advective contribution (F_{adv}).

At both boundaries, we prescribe the undisturbed bed level as

$$h = 0 \quad \text{at} \quad x = 0, \quad (2.11a)$$

$$h = H^I - H^{II} \quad \text{at} \quad x = L. \quad (2.11b)$$

Since erosion and deposition are assumed to balance each other at both entrances (see Eqs. 2.7), the undisturbed water depth at the entrances will not change during a morphodynamic experiment. The focus of this paper is on morphodynamic equilibria and not the evolution towards these equilibria. Hence these boundary conditions are appropriate to obtain morphodynamic equilibria characterised by the specific depths prescribed at the seaward sides of the inlet (see also Schuttelaars and de Swart [25, 26] for a discussion of boundary conditions in a single inlet system). When considering the morphodynamic evolution in time of tidal inlet systems, instead of focusing on morphodynamic equilibria, these boundary conditions are too restrictive and more dynamic ones have to be used (see for example Lanzoni and Seminara [35], Bolla Pittaluga *et al.* [36]).

2.3. SOLUTION METHOD

2.3.1. SCALING AND EXPANSION

To make the equations dimensionless, the physical variables are scaled as

$$x = L\check{x}, \quad t = \sigma^{-1}\check{t}, \quad u = U\check{u}, \quad (2.12a)$$

$$\zeta = A_{M_2}^I \check{\zeta}, \quad h = H^I \check{h}, \quad C = \frac{\alpha U^2 k_{v*}}{w_s^2} \check{C}, \quad B = B^I \check{B}, \quad (2.12b)$$

where the dimensionless variables are indicated by $\check{\cdot}$. For the horizontal coordinate x , the length L of the double-inlet system is the appropriate scale as the focus is on basin scale dynamics. The width is made dimensionless using the width at inlet I, B^I . Time is made dimensionless using the M_2 angular frequency σ , the surface elevation using the M_2 amplitude at the seaward side of inlet I, denoted by $A_{M_2}^I$, and the bed level is made dimensionless using the depth H^I at inlet I. The typical scale for the velocity is $U = A_{M_2}^I \sigma L / H^I$. It is obtained by assuming that the amplitude of the sea surface elevation at the first inlet is nonzero, otherwise the amplitude at the seaward side of the second inlet should be used (see details in Supplementary Information S1). The suspended sediment concentration is made dimensionless using $\alpha U^2 k_{v*} / w_s^2$, which follows from assuming an approximate balance between erosion and deposition. In Tab. 2.1, characteristic values of the relevant parameters are given for the Marsdiep–Vlie system.

Substituting these dimensionless variables in the equations and suppressing the checks $\check{\cdot}$, the system of dimensionless equations reads:

$$B\zeta_t + [B(1 - h + \epsilon\zeta)u]_x = 0, \quad (2.13a)$$

$$u_t + \epsilon uu_x + \lambda_L^{-2} \zeta_x + \frac{ru}{1 - h + \epsilon\zeta} = 0, \quad (2.13b)$$

$$a[BC_t + (BeuC - k_h BC_x - k_h \lambda_d B \beta h_x C)_x] = B(u^2 - \beta C), \quad (2.13c)$$

$$B(h_t + a\delta_s C_t) = \delta_s B [ak_h C_x + ak_h \lambda_d \beta h_x C - \epsilon u C]_x, \quad (2.13d)$$

| Tidal System | Sediment | Bed |
|---|--|-----------------------------------|
| $L = 59 \text{ km}$ | $k_{h*} = 10^2 \text{ m}^2 \text{ s}^{-1}$ | $\rho_s = 2650 \text{ kg m}^{-3}$ |
| $g = 9.81 \text{ m s}^{-2}$ | $\alpha = 0.5 \cdot 10^{-2} \text{ kg s m}^{-4}$ | $p = 0.4$ |
| $c_d = 0.0025$ | $w_s = 0.015 \text{ m s}^{-1}$ | |
| $\sigma = 1.4 \cdot 10^{-4} \text{ s}^{-1}$ | $k_{v*} = 0.1 \text{ m}^2 \text{ s}^{-1}$ | |
| $T = 44.9 \cdot 10^3 \text{ s}$ | $d_{50} = 2 \cdot 10^{-4} \text{ m}$ | |
| $Q_* = -900 \text{ m}^3 \text{ s}^{-1}$ | | |
| Marsdiep Inlet | Vlie Inlet | |
| $H^I = 11.7 \text{ m}$ | $H^{II} = 11.9 \text{ m}$ | |
| $A_{M_2}^I = 0.62 \text{ m}$ | $A_{M_2}^{II} = 0.77 \text{ m}$ | |
| $\phi_{M_2}^I = 148^\circ$ | $\phi_{M_2}^{II} = -158^\circ$ | |
| $B^I = 5954 \text{ m}$ | $B^{II} = 5619 \text{ m}$ | |
| $A_{M_4}^I = 0.11 \text{ m}$ | $A_{M_4}^{II} = 0.06 \text{ m}$ | |
| $\phi_{M_4}^I = 155^\circ$ | $\phi_{M_4}^{II} = -121^\circ$ | |

Table 2.1: Relevant variables adopted in the model. Characteristic values are those estimated for the Marsdiep-Vlie inlet system by Duran-Matute *et al.* [8], Ridderinkhof [37].

with the dimensionless deposition parameter β given by

$$\beta = \frac{1}{1 - \exp(-\lambda_d(1 - h + \epsilon\zeta))}. \quad (2.14)$$

The parameter $\epsilon = A_{M_2}^I / H^I$ is the ratio of the M_2 tidal amplitude to the water depth at inlet I. In many tidal inlet systems $\epsilon \sim 0.1$, indicating that ϵ is a small parameter. Hereafter, it is assumed that $\epsilon\zeta$ is always much smaller than the local undisturbed water depth $1 - h$, thus neglecting the effects of drying and flooding. Note that ϵ is also equal to the ratio of the tidal excursion length and the length of the tidal inlet system $U/(\sigma L)$. The parameter $\lambda_L = k_g L$ is the product of the frictionless tidal wavenumber $k_g = \sigma / \sqrt{H^I g}$ and the length of the inlet system. The dimensionless friction parameter is denoted by r and is defined as $r = r_* / H^I \sigma$. The ratio of the deposition timescale to the tidal period is denoted by $a = k_{v*} \sigma / w_s^2$, and the sediment Péclet number $\lambda_d = H^I w_s / k_{v*}$ is the ratio of the typical time it takes for a particle to be mixed through the water column to the typical time it takes to settle in the water column. The dimensionless diffusion parameter is denoted by $k_h = k_{h*} / L^2 \sigma$. The parameter $\delta_s = \alpha U^2 / (\rho(1 - p) H^I \sigma)$ denotes the ratio of tidal period T to the time scale related to suspended load and is typically small. All dimensionless parameters and the assigned values are summarized in Tab.2.2.

The bed evolution equation (2.13d) shows that at the tidal timescale the bed changes are very small, namely of $O(\delta_s)$. This implies that the bed changes significantly at a much larger time scale, the so-called morphodynamic time scale, defined as $\tau = \delta_s t$. To distinguish between these time scales, a multiple timescale method is used, with t the short tidal time variable and τ the long morphodynamic time variable. Using this multiple timescale approximation, it can be demonstrated that at the leading order of approximation the bed changes are due to tidally-averaged convergences and divergences of sediment (see Sanders and Verhulst [38], Krol [39]). The resulting tidally-averaged bed

| Parameter | Definition | Value | Parameter | Definition | Value |
|----------------|--|-----------------------|-------------------|--|----------------------|
| ϵ | $\frac{A_{M_2}^I}{H^I} = \frac{U}{\sigma L}$ | $5.30 \cdot 10^{-2}$ | λ_L | $\frac{\sigma L}{\sqrt{H^I g}}$ | 0.77 |
| r | $\frac{r_*}{H^I \sigma}$ | $5.67 \cdot 10^{-1}$ | a | $\frac{k_{\nu*} \sigma}{w_s^2}$ | $6.22 \cdot 10^{-2}$ |
| k_h | $\frac{k_{h*}}{L^2 \sigma}$ | $2.05 \cdot 10^{-4}$ | δ_s | $\frac{\alpha U^2}{\rho_s(1-p)H^I \sigma}$ | $3.68 \cdot 10^{-4}$ |
| Q | $\frac{Q_*}{B^I H^I U}$ | $-2.95 \cdot 10^{-2}$ | λ_d | $\frac{H^I w_s}{k_{\nu*}}$ | 1.75 |
| γ | $\frac{A_{M_4}^I}{A_{M_2}^I}$ | $1.83 \cdot 10^{-1}$ | $A_{r_2}^{II}$ | $\frac{A_{M_2}^{II}}{A_{M_2}^I}$ | 1.25 |
| $A_{r_4}^{II}$ | $\frac{A_{M_4}^{II}}{A_{M_4}^I}$ | 0.535 | $\phi_{r_2}^{II}$ | $\phi_{M_2}^{II} - \phi_{r_2}^I$ | 54° |
| $\phi_{r_4}^I$ | $\phi_{M_4}^I - 2\phi_{M_2}^I$ | -141° | $\phi_{r_4}^{II}$ | $\phi_{M_4}^{II} - 2\phi_{M_2}^I$ | -57° |

Table 2.2: The definition of dimensionless parameters and their values for the Marsdiep-Vlie system.

evolution equation reads

$$Bh_\tau = \langle -F \rangle_x, \quad (2.15)$$

with

$$F = \underbrace{-ak_h BC}_F \underbrace{-ak_h \lambda_d B \beta h_x C}_F + \underbrace{aeBuC}_F.$$

$F_{\text{diff}} \qquad F_{\text{topo}} \qquad F_{\text{adv}}$

The dimensionless boundary conditions associated to Eqns.(2.13) and (2.15) read

$$\zeta = \cos t + \gamma \cos(2t - \phi_{r_4}^I) \quad \text{at } x = 0, \quad (2.16a)$$

$$\zeta = A_{r_2}^{II} \cos(t - \phi_{r_2}^{II}) + \gamma A_{r_4}^{II} \cos(2t - \phi_{r_4}^{II}) \quad \text{at } x = 1, \quad (2.16b)$$

$$\langle \zeta \rangle = 0 \quad \text{at } x = 0, \quad (2.16c)$$

$$\langle B(1 - h + \epsilon \zeta) u \rangle = Q \quad \text{at } x = 1, \quad (2.16d)$$

$$\langle u^2 - \beta C \rangle = 0 \quad \text{at } x = 0, 1, \quad (2.16e)$$

$$\lim_{k_h \rightarrow 0} \bar{C}(x, t, k_h) = \bar{C}(x, t, k_h = 0) \quad \text{at } x = 0, 1. \quad (2.16f)$$

The parameter γ is the ratio of the amplitude of the M_4 tide and M_2 tide at inlet I, and $A_{r_2}^{II} = A_{M_2}^{II} / A_{M_2}^I$ ($A_{r_4}^{II} = A_{M_4}^{II} / A_{M_4}^I$) is the ratio of the amplitude of the M_2 (M_4) tide at inlet II and at inlet I. Parameter $\phi_{r_2}^{II} = \phi_{M_2}^{II} - \phi_{r_2}^I$ ($\phi_{r_4}^I = \phi_{M_4}^I - 2\phi_{M_2}^I$, $\phi_{r_4}^{II} = \phi_{M_4}^{II} - 2\phi_{M_2}^I$) is the phase difference between the M_2 tide at inlet II (the M_4 tide at inlet I, the M_4 tide at inlet II) and M_2 tide at inlet I. $Q = Q_* / (B^I H^I U)$ is the dimensionless residual water transport.

In most tidal inlet systems, the parameters ϵ and γ are much smaller than 1 (see Tab.2.2), allowing for the introduction of an asymptotic expansion in ϵ and γ of the physical variables $\Phi \in \{\zeta, u, C\}$,

$$\Phi = \Phi^{00} + \epsilon \Phi^{10} + \gamma \Phi^{01} + \text{h.o.t.}, \quad (2.17)$$

where the first superscript denotes the order in ϵ while the second denotes the order in γ . Because the water motion is forced with a time-periodical signal, each physical variable can be decomposed as a (infinite) sum of tidal constituents and a residual component,

$$\Phi = \Phi_{\text{res}}(x) + \sum_{k=1}^{\infty} [\Phi_{ck}(x) \cos kt + \Phi_{sk}(x) \sin kt], \quad (2.18)$$

where the subscript 'res' denotes the tidally-averaged contribution to the variable Φ , and the contributions of tidal constituents that temporally vary as cosines (sines) with frequency k are denoted with the subscript ck (sk).

The system of equations (2.13a), (2.13b), (2.13c), (2.15) and the boundary conditions (2.16) can first be ordered in terms of ϵ and γ , and then in terms of the tidal constituents.

To obtain the tidally-averaged contributions that include both the dominant advective and diffusive transport mechanisms, the system of equations (2.13a), (2.13b), (2.13c) and (2.15) has to be solved up to the orders $\mathcal{O}(\epsilon)$ and $\mathcal{O}(\gamma)$. Both the water motion and the suspended sediment concentration consist of an M_2 and a M_4 tidal constituent, and a residual component. This results in tidally-averaged sediment transport contributions due to diffusive and advective processes. The diffusive transport consists of the two contributions F_{diff}^{00} and F_{topo}^{00} . The advective transport can be decomposed in two contributions, denoted as F_{adv}^{20} and F_{adv}^{11} of order $\mathcal{O}(\epsilon^2)$ and $\mathcal{O}(\epsilon\gamma)$, respectively. The internally-generated advective transport F_{adv}^{20} is due to the temporal correlation of internally-generated overtides and residual velocities at $\mathcal{O}(\epsilon)$ with the leading order concentration fields, and the correlation of the leading order velocities with the $\mathcal{O}(\epsilon)$ concentration. The externally-generated advective transport F_{adv}^{11} results from the temporal correlation of externally-generated overtides with the leading order concentration fields, and the correlation of the leading order velocities with the $\mathcal{O}(\gamma)$ concentration. The resulting tidally-averaged sediment transport contributions are then given by

$$\langle F_{\text{diff}}^{00} \rangle = -ak_h BC_{\text{res},x}^{00}, \quad (2.19)$$

$$\langle F_{\text{topo}}^{00} \rangle = -ak_h \beta \lambda_a B h_x C_{\text{res}}^{00}, \quad (2.20)$$

$$\langle F_{\text{adv}}^{20} \rangle = \frac{1}{2} a \epsilon^2 B (u_{c1}^{00} C_{c1}^{10} + u_{s1}^{00} C_{s1}^{10} + 2u_{\text{res}}^{10} C_{\text{res}}^{00} + u_{c2}^{10} C_{c2}^{00} + u_{s2}^{10} C_{s2}^{00}), \quad (2.21)$$

$$\langle F_{\text{adv}}^{11} \rangle = \frac{1}{2} a \epsilon \gamma B (u_{c1}^{00} C_{c1}^{01} + u_{s1}^{00} C_{s1}^{01} + u_{c2}^{01} C_{c2}^{00} + u_{s2}^{01} C_{s2}^{00}). \quad (2.22)$$

2.3.2. MORPHODYNAMIC EQUILIBRIA AND LINEAR STABILITY

The resulting system of morphodynamic equations, ordered in terms of the small parameters and expanded in tidal constituents, can be written as

$$K\Psi_\tau = G(\Psi, \mathbf{p}), \quad (2.23)$$

where Ψ is a vector of amplitudes of all physical variables and \mathbf{p} the vector of model parameters. Namely, $\Psi = (\zeta_{c1}^{00}, \zeta_{s1}^{00}, \zeta_{\text{res}}^{10}, \zeta_{c2}^{10}, \zeta_{s2}^{10}, \zeta_{c2}^{01}, \zeta_{s2}^{01}, \dots, h)$. The matrix K is a diagonal matrix, with a non-zero element only in the row associated with the bed evolution equation. The nonlinear operator G depends on the parameters \mathbf{p} and works on the physical variables Ψ .

To obtain solutions of this system of equations, Eq. (2.23) is discretized using a finite element method with continuous Lagrange elements (Alnæs *et al.* [40], see also Appendix A.2.1). Adopting a weak formulation and using a Galerkin method (Brenner and Scott [41]), the discretized system of equations reads

$$\mathcal{K}\tilde{\Psi}_\tau = \mathcal{G}(\tilde{\Psi}, \mathbf{p}), \quad (2.24)$$

in which $\tilde{\Psi}$ is the discretisation of Ψ , \mathcal{K} is the discretized matrix corresponding to K and \mathcal{G} is the discretized nonlinear operator working on $\tilde{\Psi}$ and the parameters \mathbf{p} .

This discretized system of equations can be analyzed using two different approaches, the *initial value* and the *bifurcation* approach. The latter approach aims at the direct identification of morphodynamic equilibria, whereas with the former approach an initially prescribed bathymetry is integrated in time.

In this paper, the focus is on the bifurcation approach with which we directly solve for equilibrium states $\tilde{\Psi}_e$ that satisfy

$$\mathcal{G}(\tilde{\Psi}_e, \mathbf{p}_0) = 0, \quad (2.25)$$

in which \mathbf{p}_0 is a vector of prescribed parameter values. To obtain the equilibrium solutions $\tilde{\Psi}_e$, a Newton–Raphson iterative method is used. An initial guess $\tilde{\Psi}_i$ of a morphodynamic equilibrium is updated iteratively until the corrections are small enough (in this study the iteration is stopped when the maximum correction is smaller than 10^{-8}).

For this iterative procedure to converge, the initial guess $\tilde{\Psi}_i$ has to be close enough to the morphodynamic equilibrium associated with the parameter vector \mathbf{p}_0 . If no information about an approximate morphodynamic equilibrium is available, a good initial guess can be obtained by integrating the discretized system (2.24) starting from an arbitrary initial bed profile in time (in this study a backward Euler method is used as time–integration method, see Appendix A.2.3 for details), until an approximate equilibrium is reached. This approximate equilibrium can then be used as the initial guess $\tilde{\Psi}_i$ in the Newton–Raphson iterative procedure. If for a given parameter vector \mathbf{p}_0 a morphodynamic equilibrium is found, a so–called continuation method (Seydel [42]) can be employed to find equilibria for different parameter values \mathbf{p}_1 by slowly changing the parameters from \mathbf{p}_0 to \mathbf{p}_1 . During this continuation process, the previously obtained equilibrium is used as a first guess in the iteration process, resulting in the morphodynamic equilibrium for the new parameter vector \mathbf{p}_1 . The continuation method employed in this paper is the arclength method (see Dijkstra *et al.* [43], Crisfield [44] and the discussion in Appendix A.2.2).

The linear stability of the morphodynamic equilibria $\tilde{\Psi}_e$ (corresponding to parameter \mathbf{p}_e) can be investigated by substituting $\tilde{\Psi} = \tilde{\Psi}_e + \Delta\tilde{\Psi} \exp(\omega\tau)$ into Eq.(2.24) and linearizing the resulting equation. The resulting eigenvalue problem reads

$$\omega \mathcal{K} \Delta\tilde{\Psi} = \mathcal{J}_{\mathcal{G}}(\tilde{\Psi}_e, \mathbf{p}_e) \Delta\tilde{\Psi}, \quad (2.26)$$

in which $\mathcal{J}_{\mathcal{G}}(\tilde{\Psi}_e, \mathbf{p}_e)$ is the Jacobian, ω the eigenvalue and $\Delta\tilde{\Psi}$ the associated eigenvector. An equilibrium is called linearly stable if all its eigenvalues have a negative real part, and unstable if at least one eigenvalue has a positive real part.

2.4. RESULTS

In the numerical experiments presented in this section, the influence of the forcing conditions and geometry on morphodynamic equilibria is presented. Assuming a constant width, i.e., a system with a rectangular planform, the morphodynamic equilibria are first obtained for a water motion forced by an M_2 tidal constituent using the continuation approach. (A first initial guess is obtained for a limited number of parameter values

through time integration after which the equilibria for other parameter values are obtained by continuation) The results are presented in Sect. 2.4.1. Next (Sect. 2.4.2) all hydrodynamic forcing contributions are included. Finally (Sect. 2.4.3) the influence of width variations is investigated. All results are obtained using parameter values that are representative of the Marsdiep–Vlie inlet system (see Tab.2.1), unless mentioned otherwise.

2.4.1. CONSTANT–WIDTH SYSTEM SUBJECTED TO AN M_2 TIDAL FORCING

The influence of variations in the prescribed M_2 tidal constituent on the resulting morphodynamic equilibria has been studied by setting the amplitude and phase of the M_2 tide at inlet I equal to 0.62 m and 0° and varying the M_2 amplitude and phase at inlet II. To focus only on the influence of the M_2 forcing, the amplitudes of the externally prescribed overtides ($A_{M_4}^I$ and $A_{M_4}^{II}$) are assumed to be zero. Furthermore, the undisturbed water depths at both inlets are taken to be 11.7 m and the tidally–averaged water transport Q at the second inlet is set to zero. Sensitivity to inlet depth and tidally–averaged water transport at inlet II, assuming no M_4 tidal forcing, is discussed in Appendix A.3. All other parameter values are taken from Tab. 2.1.

The resulting morphodynamic equilibrium condition reads (see Eq. (2.15))

$$\frac{d}{dx} \left(\langle F_{\text{diff}}^{00} \rangle + \langle F_{\text{topo}}^{00} \rangle + \langle F_{\text{adv}}^{20} \rangle \right) = 0, \quad (2.27)$$

where for the numerical experiment under consideration, the width within the inlet system is constant, i.e. $B(x) = B^I$.

To obtain these morphodynamic equilibria, an initial value approach is employed by studying the evolution of a spatially uniform bed (i.e. the system of equations (2.24) is integrated in time using a Backward-Euler method). If the divergence of the tidally–averaged sediment transport vanishes, an equilibrium is reached. Two numerical experiments have been carried out with different M_2 tidal forcings applied at the second inlet.

In the first numerical experiment, we take $A_{M_2}^{II} = 0.77$ m, $\phi_{M_2}^{II} = 54^\circ$ (default value). The resulting bed evolution is shown in Fig. 2.3a. After approximately 2500 years, the bed profile reaches its equilibrium with a maximum water depth (WD_{max}) of 17.8 m, located at approximately 20 km from inlet I.

In the second numerical experiment, we take $A_{M_2}^{II} = 0.77$ m and $\phi_{M_2}^{II} = 0^\circ$. The development of the bed profile for the first 23200 years is shown in Fig. 2.3b. This figure clearly shows that the water depth decreases over time, and after approximately 23300 years, it vanishes near km 32. The two inlets are not connected anymore, and a system formed by two single inlets is eventually obtained.

From the previous two numerical experiments, it is evident that a morphodynamic equilibrium in which both inlets are connected does not necessarily exist for all combinations of $A_{M_2}^{II}$ and $\phi_{M_2}^{II}$. The minimum water depth, denoted by WD_{min} , can vanish at some location, disconnecting the two inlets. To assess the existence of morphodynamic equilibria with both inlets connected for a wider range of forcing conditions, we take $A_{M_2}^{II} = 0.77$ m, and vary $\phi_{M_2}^{II}$ from -180° to 180° . Here the continuation approach is employed, thus the equilibria are obtained directly without resorting to time integration. Fig. 2.3c shows the equilibrium water depth as a function of position along the

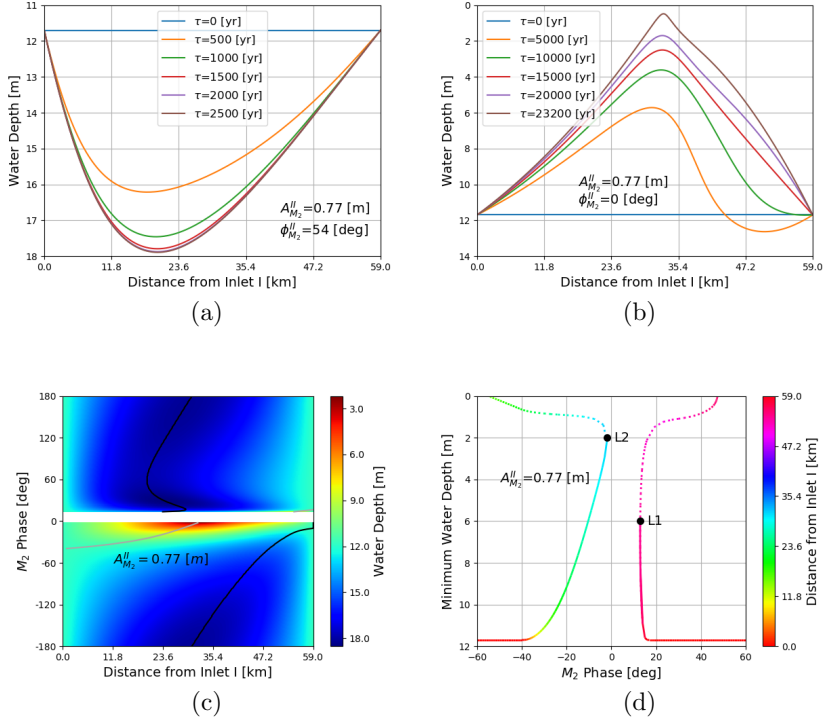


Figure 2.3: Bed evolution computed for a constant-width double-inlet system forced with an M_2 tide. In panel (a) the bed profile starts to evolve from an initial flat bottom. The temporal evolution is computed using the Backward-Euler time-integration method with $A_{M_2}^{II} = 0.77$ m and $\phi_{M_2}^{II} = 54^\circ$, the unit of τ is year. Panel (b) shows the results of the numerical experiment as in panel (a) but with $A_{M_2}^{II} = 0.77$ m and $\phi_{M_2}^{II} = 0^\circ$. Panel (c) shows equilibrium water depth for $A_{M_2}^{II} = 0.77$ m and $\phi_{M_2}^{II}$ varying from -180° to 180° , with colder colors denoting larger water depths and warmer colors smaller water depths. If no equilibrium is found, a white color code is used. The location of WD_{\min} is indicated by gray contours and the location of the WD_{\max} is indicated by black contours. Panel (d) shows WD_{\min} of equilibrium bed profiles with $A_{M_2}^{II} = 0.77$ m and $\phi_{M_2}^{II}$ varying from -60° to 60° . The color indicates the distance of the WD_{\min} from inlet I, with warmer colors closer to (one of) the entrance(s), and colder colors more towards the middle of the inlet system. Morphodynamic equilibria that are linearly stable are indicated by a solid line, while those indicated by a dashed line are linearly unstable.

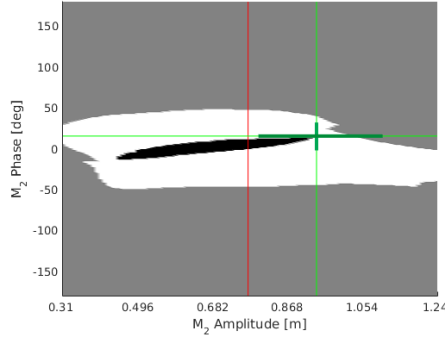


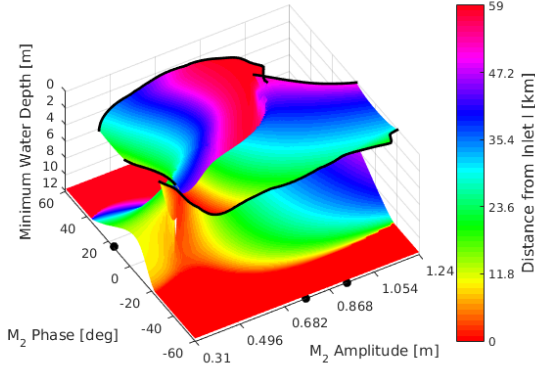
Figure 2.4: Number of morphodynamic equilibria as a function of amplitude (horizontal axis) and phase (vertical axis) of the forcing tidal constituent. Regions with no morphodynamic equilibria are shown in black, regions with one equilibrium in gray, and regions with two or more morphodynamic equilibria in white. The red and (dark) green lines correspond to the amplitudes and phases used in Figs. 2.3d, 2.5b and 2.5c

embayment (horizontal axis) and the M_2 phase at inlet II (vertical axis). The equilibrium water depth is found to strongly depend on the tidal phase at inlet II. By increasing $\phi_{M_2}^{\text{II}}$ from -180° to -2° , WD_{\min} decreases from 11.7 m to 2.5 m, and by decreasing $\phi_{M_2}^{\text{II}}$ from 180° to 13° , WD_{\min} varies from 11.7 m to 6.0 m. For a phase between -2° and 13° , no double-inlet morphodynamic equilibrium exists.

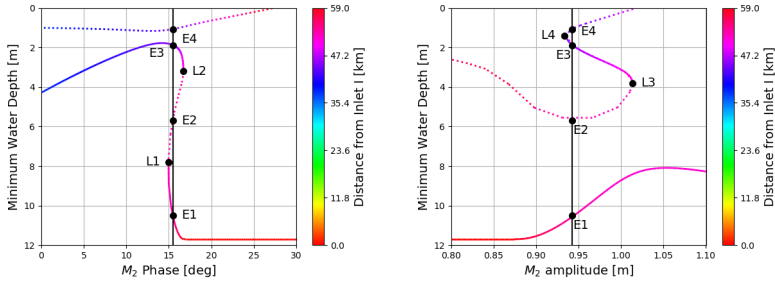
To quickly characterize these morphodynamic equilibria, the quantities WD_{\min} and its location are used. As an example, using a constant amplitude $A_{M_2}^{\text{II}} = 0.77$ m, WD_{\min} is shown as a function of $\phi_{M_2}^{\text{II}}$ in Fig. 2.3d. Two distinct branches of morphodynamic equilibrium solutions are found, each consisting of a stable (solid) and unstable (dashed) part. The stable and unstable solutions on each branch are connected by a so-called limit point, denoted by $L1$ and $L2$. For phases with values between the two limit points, no equilibria were found with both inlets connected. Note that the stable solutions correspond to the equilibria shown in Fig. 2.3c.

To be more precise, Fig. 2.3d indicates that the number of morphodynamic equilibria and their stability strongly depends on the value of the phase at inlet II. For $-1.9^\circ \leq \phi_{M_2}^{\text{II}} \leq 12.8^\circ$ no morphodynamic equilibrium exists, for $-53^\circ \leq \phi_{M_2}^{\text{II}} \leq -1.9^\circ$ and $12.8^\circ \leq \phi_{M_2}^{\text{II}} \leq 47^\circ$ two morphodynamic equilibria (one stable and one unstable) exist, whereas for all other phase values one stable equilibrium exists. Furthermore, the number of morphodynamic equilibria and their stability not only depends on the phase of the M_2 tide at inlet II, but also on its amplitude. Fig. 2.4 shows the number of morphodynamic equilibria as a function of the amplitude $A_{M_2}^{\text{II}}$ and the phase $\phi_{M_2}^{\text{II}}$.

To further study these equilibria, the dependency of WD_{\min} on the amplitude and phase at inlet II is investigated (Fig. 2.5). For $0.31 \text{ m} \leq A_{M_2}^{\text{II}} \leq 1.24 \text{ m}$ and phases $|\phi_{M_2}^{\text{II}}| \geq 60^\circ$ it is found that WD_{\min} for stable equilibria occur at the entrances reaching the minimum water depth of 11.7 m. Therefore, in the following we focus on $|\phi_{M_2}^{\text{II}}| < 60^\circ$, while $A_{M_2}^{\text{II}}$ is varied between 0.31 m and 1.24 m. In Fig. 2.5a, the depth of the watersheds is shown as a function of the amplitude and phase of the M_2 tide at inlet II. From this figure it follows that by increasing $A_{M_2}^{\text{II}}$ from 0.31 m to 1.24 m and/or $\phi_{M_2}^{\text{II}}$ from -60° to 60°



(a)



(b)

(c)

Figure 2.5: Morphodynamic equilibria for a constant-width inlet system forced with an M_2 tide. Panel (a) shows WD_{\min} for the equilibrium configurations computed with $\phi_{M_2}^{II}$ in the range $(-60^\circ, 60^\circ)$ and $A_{M_2}^{II}$ varying from 0.31 m to 1.24 m. The black dots denote the parameter values used in Figs. 2.3d, 2.5b and 2.5c. Panel (b) shows WD_{\min} of equilibria for $A_{M_2}^{II} = 0.94$ m and $\phi_{M_2}^{II}$ varying in the range $(0^\circ, 30^\circ)$. Panel (c) shows the same information as in panel (b) but with $\phi_{M_2}^{II} = 15.5^\circ$ and $A_{M_2}^{II}$ in the range (0.80 m, 1.10 m). The color indicates the location of the WD_{\min} , with warmer colors closer to (one of) the entrance(s), and colder colors more towards the middle of the tidal basin. Solid lines in plots (b) and (c) denote linearly stable equilibrium configurations, while dotted lines correspond to linearly unstable equilibrium configurations.

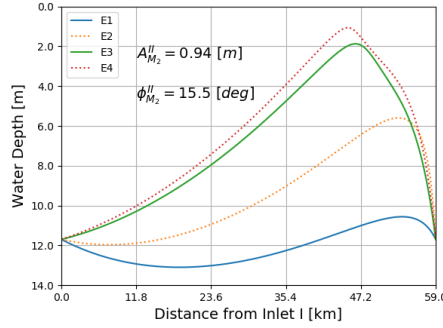


Figure 2.6: The bed profiles corresponding to the equilibrium configurations $E1$, $E2$, $E3$ and $E4$ indicated by black dots in Figs. 2.5b and 2.5c.

results in a shift of WD_{\min} from a location closer to inlet I to a location closer to inlet II. The black line in the figure denotes the location where WD_{\min} vanishes and, consequently, the double-inlet system reduces to two single-inlet systems.

In two regions in the $(A_{M_2}^{II}, \phi_{M_2}^{II})$ -space, complex bifurcation structures occur, indicating that possibly multiple stable morphodynamic equilibria exist. To assess the number of equilibria, the bifurcation structure is carefully analysed over two paths in the parameter space, with one path characterized by a fixed amplitude and varying phase, and the second path by a fixed phase and varying amplitude.

The values of WD_{\min} for the first path in parameter space, i.e. $A_{M_2}^{II} = 0.94$ m and $\phi_{M_2}^{II}$ in the range of 0° to 30° is shown in Fig. 2.5b. This figure shows that the number of morphodynamic equilibria depends sensitively on the phase angle. Similarly in Fig. 2.5c, WD_{\min} is shown for M_2 amplitudes varied between 0.80 m and 1.10 m, with the phase fixed at 15.5° . This figure illustrates that the number of morphodynamic equilibria also depends sensitively on the tidal amplitude.

The vertical black lines in Figs. 2.5b and 2.5c correspond to the same parameter values ($A_{M_2}^{II} = 0.94$ m, $\phi_{M_2}^{II} = 15.5^\circ$). Hence, the equilibrium bed configurations denoted by $E1$, $E2$, $E3$ and $E4$, are the same in both figures. The corresponding bed profiles are shown in Fig. 2.6. Equilibria $E1$ and $E3$ are linearly stable, whereas $E2$ and $E4$ are linearly unstable. Each equilibrium is characterized by a different balance between the various tidally-averaged transport terms in Eq.(2.15), contributing to a different, spatially uniform, total sediment transport. These contributions, divided in two diffusive contributions and one total advective contribution (see Eq.(2.10) and (2.15)), and the total transport are shown in Figs. 2.7a, c, e, g, while Figs. 2.7b, d, f, h show the different contributions to the advective contribution. In all cases, the total transport is positive, indicating a net transport from inlet I to inlet II. These plots show that all transport mechanisms result in significant contributions to the total transport.

Moreover, Fig. 2.8 indicates that the direction and magnitude of the total tidally-averaged transport strongly depends on the forcing conditions at inlet II. Note the presence in the parameter space of a region in which the net sediment transport is negative, indicating a tidally-averaged total transport from inlet II to inlet I. Increasing $\phi_{M_2}^{II}$ results

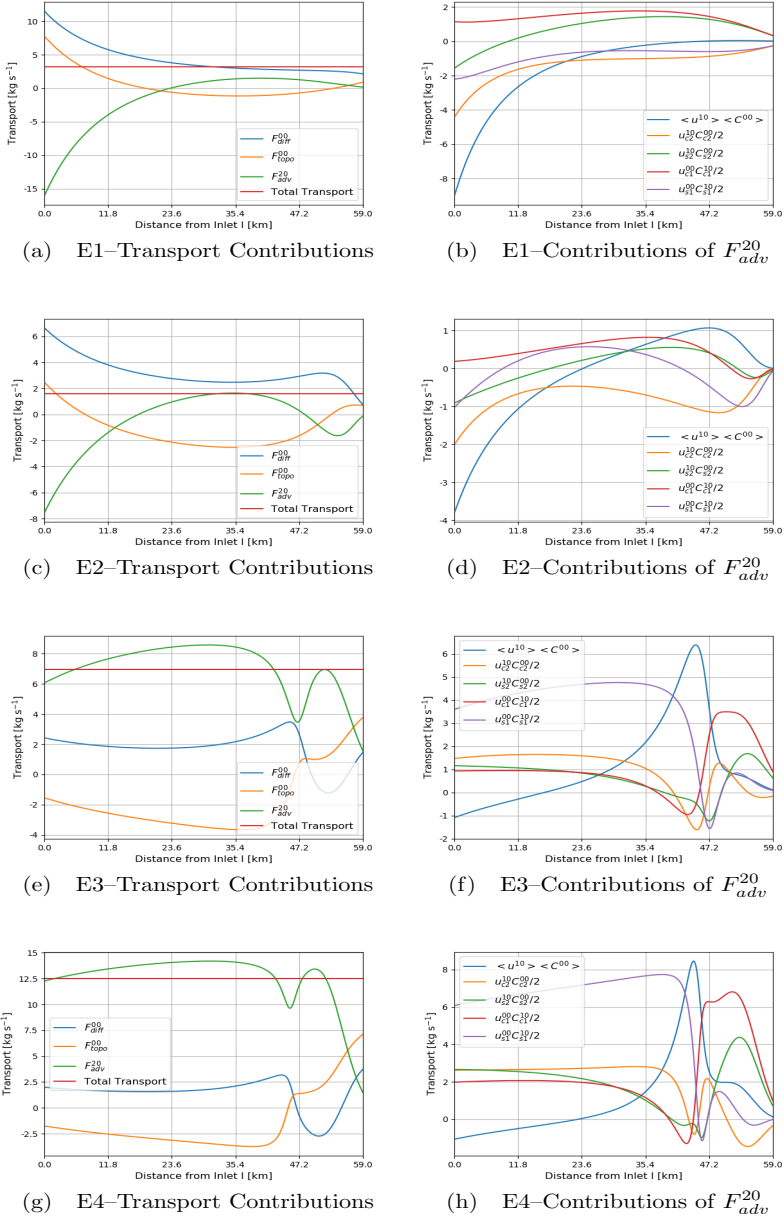


Figure 2.7: Panels (a), (c), (e) and (g) show the various transport contributions characterizing the equilibrium configurations $E1$, $E2$, $E3$ and $E4$ as a function of the location within the inlet system. Panels (b), (d), (f) and (h) depict the contributions to the tidally-averaged advective transport for $E1$, $E2$, $E3$ and $E4$.

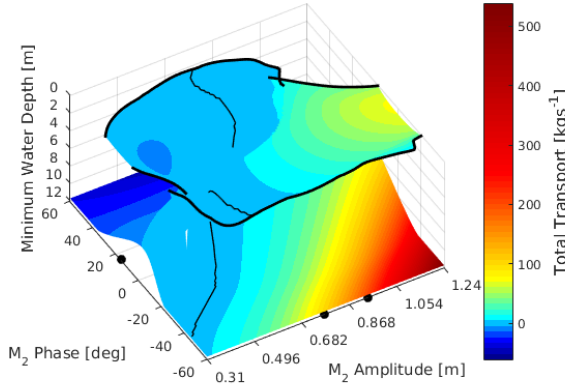


Figure 2.8: Total tidally-averaged transport characterizing the equilibrium bed profiles as a function of tidal amplitude and tidal phase of the forcing applied at the inlet II. The thin black lines indicate equilibria with a vanishing tidally-averaged total transport. The black dots denote the parameter values used in Figs. 2.3d, 2.5b and 2.5c.

in a decrease of net transport from inlet II to inlet I on the left of the thin black lines, that indicate a zero transport, or an increase of net transport from inlet I to inlet II on the right of these lines.

2.4.2. CONSTANT-WIDTH SYSTEM SUBJECTED TO ALL FORCINGS

In this section, all hydrodynamic forcings are taken into account. They consist of M_2 and M_4 constituents prescribed at both inlets and a tidally-averaged water transport, prescribed at inlet II. The complete morphodynamic equilibrium condition up to orders $O(\epsilon^2, \epsilon\gamma)$ has to be solved. It reads:

$$\frac{d}{dx} \left(\langle F_{\text{diff}}^{00} \rangle + \langle F_{\text{topo}}^{00} \rangle + \langle F_{\text{adv}}^{20} \rangle + \langle F_{\text{adv}}^{11} \rangle \right) = 0, \quad (2.28)$$

with the transport terms on the left-hand side given in Eqs. (2.20)–(2.22). All parameter values are taken from Tab. 2.1, except for the M_4 phase at inlet II, $\phi_{M_4}^{\text{II}}$, which is varied between -180° and 180° . Only linearly stable morphodynamic equilibria are discussed below.

The sensitivity of morphodynamic equilibria to $\phi_{M_4}^{\text{II}}$ is illustrated in Fig. 2.9a, where the water depth is shown as a function of distance from inlet I (horizontal axis) and $\phi_{M_4}^{\text{II}}$ (vertical axis). The total sediment transport of the stable morphodynamic equilibria is shown in Fig. 2.9b as a function of $\phi_{M_4}^{\text{II}}$, illustrating the sensitivity of both direction and magnitude of the total transport to $\phi_{M_4}^{\text{II}}$.

In Fig. 2.9c, the equilibrium water depths are shown for some selected values of $\phi_{M_4}^{\text{II}}$. Focusing on -121° (for the other phases, see Appendix A.4), while the total sediment transport, split into its four main contributions is shown in Fig. 2.9d. The two diffusive contributions, $\langle F_{\text{diff}}^{00} \rangle$ and $\langle F_{\text{topo}}^{00} \rangle$, are only significant near inlet I. The sediment transport related to the internally-generated overides, $\langle F_{\text{adv}}^{20} \rangle$, is mostly directed from inlet

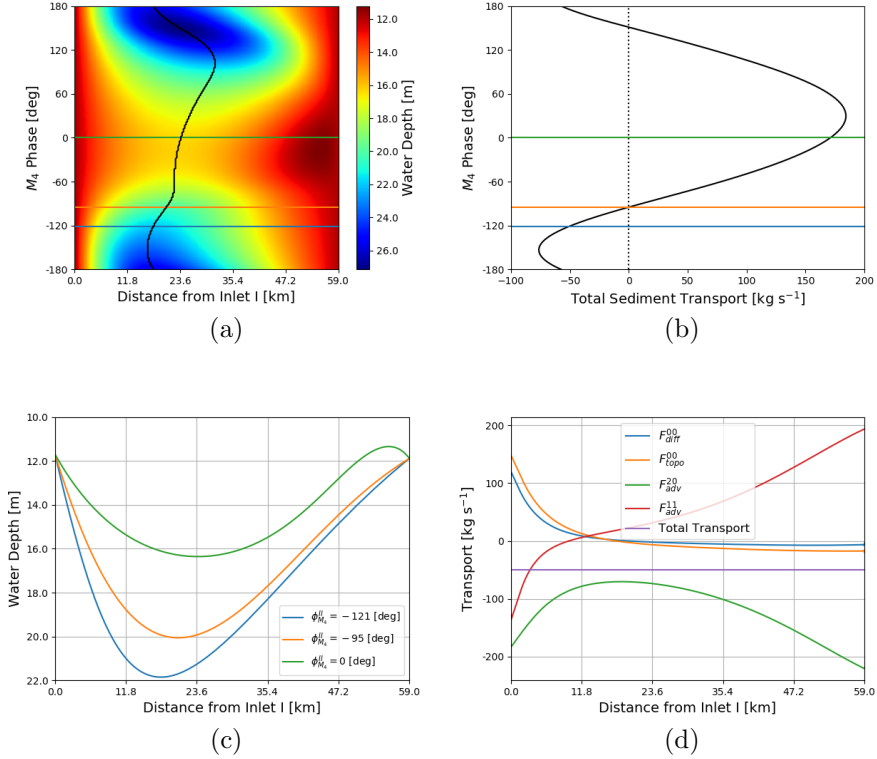


Figure 2.9: Stable morphodynamic equilibria obtained by varying $\phi_{M_4}^{II}$ and including all forcing terms. Panel (a) shows the bed profiles of stable morphodynamic equilibria, with warmer (colder) colors indicating smaller (larger) water depths. The black line indicates the location of WD_{max} . Panel (b) shows the total sediment transport of the morphodynamic equilibria. Panel (c) reports equilibrium bed profiles for some selected values of $\phi_{M_4}^{II}$, namely $\phi_{M_4}^{II} = 0^\circ, -95^\circ$ and -121° , respectively. The water depths and total transports for these phases are indicated by the blue, orange and green line in Fig. 2.9a–b. The associated tidally-averaged transports obtained with $\phi_{M_4}^{II} = -121^\circ$ (the default value for $\phi_{M_4}^{II}$, see Tab. 2.1) are shown in panel (d). Total transport, and contributions due to $\langle F_{diff}^{00} \rangle$, $\langle F_{topo}^{00} \rangle$, $\langle F_{adv}^{20} \rangle$ and $\langle F_{adv}^{11} \rangle$ are indicated by the purple, blue, orange, green and red lines, respectively.

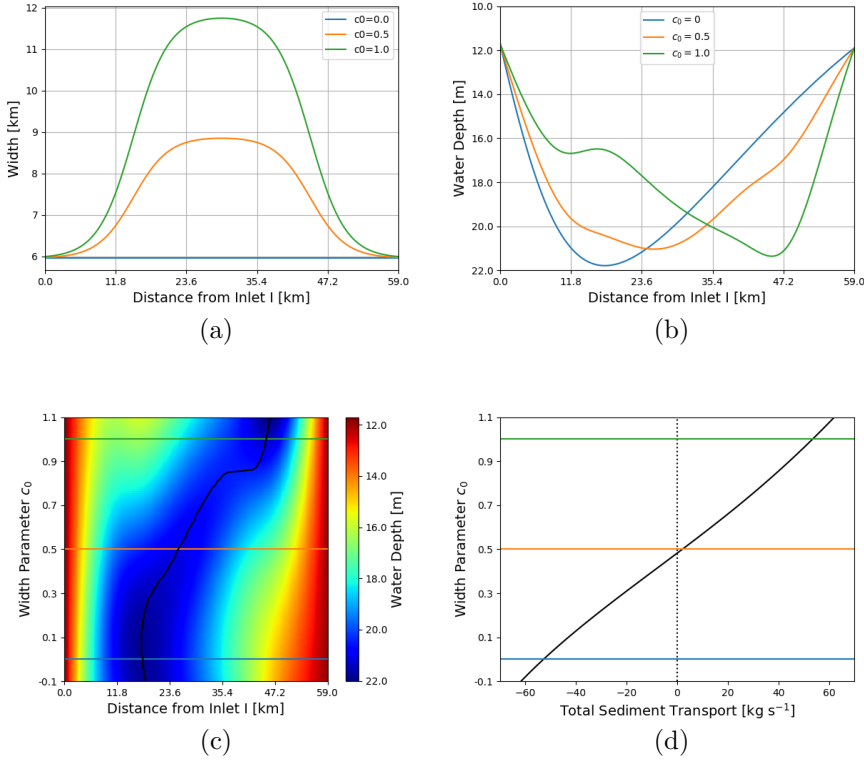


Figure 2.10: Stable morphodynamic equilibria obtained for different width distributions of the double-inlet system, including all forcings. Panel (a) shows the width distributions for some selected values of the width parameter c_0 (0, 0.5, 1). Panel (b) reports the corresponding bed profile. Panel (c) shows the stable equilibrium bed profiles obtained for c_0 varying from -0.1 to 1.1 . Panel (d) shows the total tidally-averaged sediment transport of stable equilibria for the same variations of c_0 .

II to inlet I, whereas the transport due to external overtides, $\langle F_{adv}^{11} \rangle$, occurs in most of the double-inlet system and is directed from inlet I to inlet II. The advective contributions can be further divided in different components (see Appendix A.4). It turns out that only two contributions dominate $\langle F_{adv}^{20} \rangle$, namely the transport of tidally-averaged concentration by the tidally-averaged flow $\langle u^{10} \rangle \langle C^{00} \rangle$ and the correlation of $u_{c1}^{00} C_{c1}^{10}$. Similarly, there are two main contributions to $\langle F_{adv}^{11} \rangle$, i.e. $u_{c1}^{00} C_{c1}^{01}$ and $u_{c2}^{01} C_{c2}^{00}$.

2.4.3. VARYING-WIDTH SYSTEM SUBJECTED TO ALL FORCINGS

To illustrate the influence of width variations on the morphodynamic equilibria, the width is varied as

$$B/B^I = 1 + \frac{c_0}{2 \tanh(2.5)} \left[\tanh\left(\frac{0.75 - x/L}{0.1}\right) + \tanh\left(\frac{x/L - 0.25}{0.1}\right) \right], \quad (2.29)$$

where c_0 is a parameter that controls the width variation. This width distribution is chosen to systematically vary the width when moving away from the entrances, a geometric trend often observed in tidal inlet systems. When $c_0 = 0$ the geometry reduces to the constant width–geometry analyzed in the previous sections. Increasing (decreasing) c_0 results in a double–inlet system characterised by a width that increases (decreases) towards the middle of the inlet system as shown in Fig. 2.10a. The associated equilibrium water depths are shown in Fig. 2.10b, while Fig. 2.10c reports the equilibrium water depth as a function of c_0 (color scale) and of location in the double–inlet system (horizontal axis). Fig. 2.10d shows the total sediment transport as a function of c_0 . This transport is directed from inlet II to inlet I for a rectangular inlet system ($c_0 = 0$), and decreases for increasing width variation. If the width in the middle of the inlet system is approximately 50% larger than at the inlets, the total transport vanishes. For even larger width variations, the transport is directed from inlet I to inlet II.

The various contributions to the transport can again be split into its different contributions (see Appendix A.4). For small enough c_0 (i.e. $c_0 < 0.5$), the magnitude of $\langle F_{adv}^{20} \rangle$ is larger than that of $\langle F_{adv}^{11} \rangle$. Since $\langle F_{adv}^{20} \rangle$ is directed from inlet II to inlet I, the total transport is negative. When c_0 is increased, the relative importance of $\langle F_{adv}^{11} \rangle$ increases, resulting in a total transport from inlet I to inlet II for large enough c_0 .

2.5. DISCUSSION

2.5.1. MORPHODYNAMIC EQUILIBRIA

The results presented in Sect. 2.4 suggest that the number and (linear) stability of morphodynamic equilibria in double–inlet systems depends sensitively on the forcing conditions and model geometry. For a rectangular geometry, with the water motion forced by one tidal constituent, the full bifurcation diagram indicates that for most parameter values, either one unique stable equilibrium or no morphodynamic equilibrium may exist in a system with the two inlets connected together. However, in a small part of the parameter space, more than one stable equilibrium was found.

Qualitatively, these observations are consistent with results obtained using the modelling approach employed by Van de Kreeke *et al.* [18] and Brouwer *et al.* [19]. In these models, only the tidal inlets are morphodynamically active, while the prescribed bathymetry in the back–barrier basin is assumed uniform and constant in time. In particular, Van de Kreeke *et al.* [18] investigated the influence of a topographic high on the existence and stability of morphodynamic equilibria. They found that, depending on the height of this topographic high, no equilibrium, one unique stable equilibrium or two stable equilibria could exist. On the other hand, Brouwer *et al.* [19] showed that the existence of these equilibria depends sensitively on the amplitude and phase of the M_2 tide at the seaward side of the tidal inlets. Even though these results seem to confirm the findings of Sect. 2.4 (i.e. sensitivity of the number and the stability of morphodynamic equilibria to geometry and forcing), it should be pointed out that the model formulations are quite different and hence that results obtained with the different approaches are difficult to compare.

2.5.2. COMPARISON WITH RESULTS OF A COMPLEX NUMERICAL MODEL

In this section, we compare the cross-sectionally averaged water motion provided by the present model, with the results of a state-of-the-art process-based numerical model, while the modeled equilibrium bathymetry is compared with that observed in the field. The numerical model used to calculate the water motion is the General Estuarine Transport Model (GETM), a three-dimensional model that solves the hydrodynamic equations using a finite difference approach. Effects of drying and flooding are included. For an extensive discussion of the features of the model and of the application site we refer the reader to Duran-Matute *et al.* [8]. The planform geometry and the bathymetry of the double-inlet tidal system were obtained from field observations and are shown in Fig. 2.2a. In this figure, the Marsdiep inlet is denoted as inlet I and the Vlie inlet as inlet II. The Wadden islands and mainland are colored in white, whereas the water depth is shown in color scale.

The width distribution as a function of distance from inlet I to be used in the present model were obtained by smoothly connecting points with a water depth of 1 m, indicated with triangles in Fig. 2.2a. Using these lines, the basin centerline was constructed. This line was parameterized by the spatial coordinate x , which starts at inlet I ($x = 0$) and ends at inlet II ($x = 59$ km). The width as a function of x is defined as the length of the lines perpendicular to the basin centerline. Furthermore, the mean depth is obtained by averaging the observed depths over the width.

The resulting width profile is shown in Fig. 2.11a. The double-inlet system is characterized by a small width near the seaward sides, but also around kilometer 31. At this location, the width is restricted by the presence of the tidal divide between the Eierlandse gat and the Marsdiep–Vlie system on the northern side, and the mainland in the south. This width profile has then been used to compute the values of the width-averaged depth at both entrances, as well as the amplitudes and phases of the tidal constituents (see Tab.2.1).

Fig. 2.11b shows the width-averaged amplitudes of the M_2 and M_4 tidal constituents obtained with the present equilibrium model and computed through the GETM model. The overall trend appears to be well captured. Furthermore, there is a good correspondence with the tidal amplitudes computed with the present model and those presented in Ridderinkhof [37], Hepkema *et al.* [45], in which the hydrodynamics of the Marsdiep–Vlie system was investigated through cross-sectionally averaged models.

The width-averaged equilibrium water depth is shown in Fig. 2.11c. There is a good qualitative comparison between the depths observed in the field and those computed by the model. In particular the dramatic depth increase when moving from inlet I a few kilometers into the basin is well captured. When further moving towards inlet II, the distribution of the depth variations is captured qualitatively, but the water depth in the model is typically overestimated with respect to observed data. In Fig. 2.11d the various transport contributions in morphodynamic equilibrium are shown. It is observed that the total sediment transport is from inlet I to inlet II. In the first few kilometers, the dominant transport contribution is given by topographic diffusion and is directed from inlet I to II, whereas all other contributions are in the opposite direction. The topographic diffusive sediment transport contribution is directly related to the relatively fast increase of the water depth when moving into the basin. When moving further into the basin, the

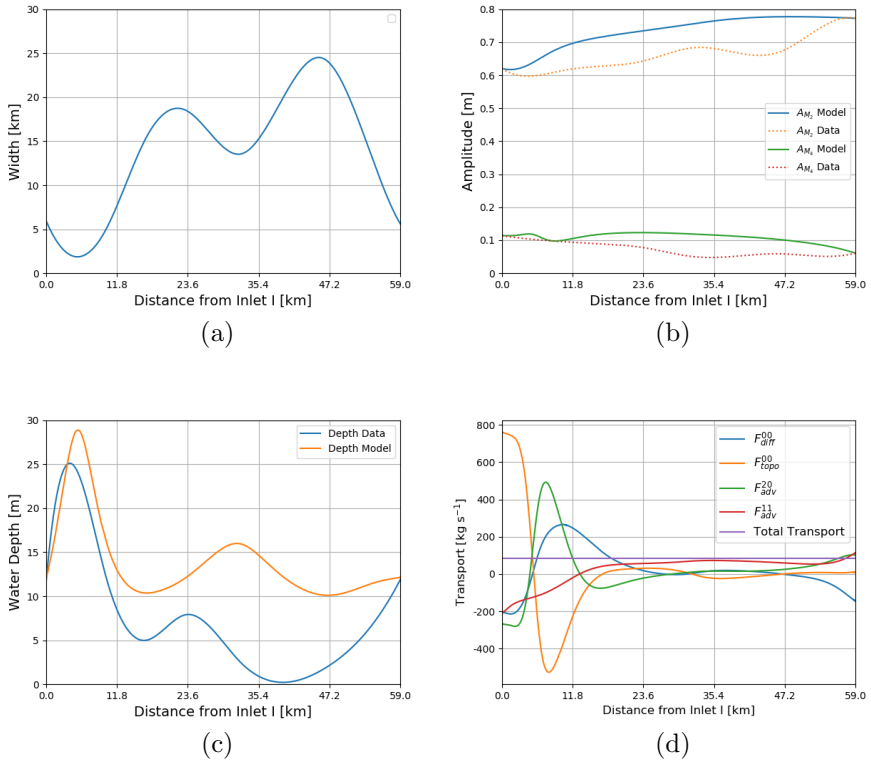


Figure 2.11: Comparison between the stable morphodynamic equilibria predicted by the present model (marked by model in the figure), the real bathymetric data and the water motion obtained with the General Estuarine Transport Model (GETM)(marked by data in the figure). The width of the double-inlet system is shown in panel (a). The amplitude of the M_2 and M_4 tides obtained from the GETM and the present model are compared in panel (b), while the bed profiles computed by the present model and observed in the field are compared in panel (c). Panel (d) displays the various sediment transport contributions, together with the total sediment transport (indicated with the purple line) which is directed from inlet I to inlet II.

water depth decreases and topographic diffusion changes sign. However, still the net transport is directed towards inlet II due to internally-generated advection and diffusion that changes sign as well. Moving even further towards inlet II ($x > 24$ km), the transport due to the externally-prescribed overtide dominates, resulting in a net transport in the direction of inlet II. The direction of transport at inlet I, the Marsdiep Inlet, is in agreement with the transport direction found in Sassi *et al.* [9]. In our model setup, this finding directly implies that at the second inlet, the Vlie, sediment should be exported. In Sassi *et al.* [9] the median value of the sediment transport at the Vlie is close to zero, with prevailing import or export, depending on the specific forcing conditions. However, in the model setup of Sassi *et al.* [9], the Wadden Sea is modeled as a multiple-inlet system, allowing for sediment transport over watersheds to adjacent basins that are not taken into account in the model schematization used in this thesis.

Even though the main characteristics of the water motion (from a refined numerical model), and the main bathymetric features (from observations), are reproduced qualitatively, still some qualitative differences are evident. They concern the hydrodynamic quantities in regions with extensive tidal flats and multiple channels. In this study, how variations over the cross-sectional area are not explicitly taken into account. It is possible to include these effects by modelling parametrically the effects of mass storage and momentum sinks (Hepkema *et al.* [45], Friedrichs and Aubrey [46]). However, to capture these effects dynamically, the existence and stability of morphodynamic equilibria in a two-dimensional (depth-averaged) model have to be studied. The results obtained with the cross-sectionally averaged model are essential input for models in which the above effects are incorporated explicitly (Dijkstra *et al.* [43], Boelens *et al.* [47]). Furthermore, in reality water and sediment are transported over the watersheds to adjacent tidal inlet systems (Duran-Matute *et al.* [8], Sassi *et al.* [9]). These transport processes can only be captured by extending the present model to a morphodynamic model for multiple inlet systems (Roos *et al.* [21], Reef *et al.* [22]).

Also the width-averaged equilibrium bathymetry obtained with the present model exhibits the largest deviations with respect to the observed data in regions with extensive tidal flats. There, the effects of wind and waves can play an important role (de Swart and Zimmerman [2], Marciano *et al.* [48]). Furthermore, the possible import of sediment due to littoral drift along the coast of the sea is neglected in the present study. This transport mechanism was shown to be important by Van de Kreeke *et al.* [18], Roos *et al.* [21].

2.6. CONCLUSIONS

An idealized model has been developed to systematically investigate the existence of cross-sectionally averaged morphodynamic equilibria in double-inlet systems. A morphodynamic equilibrium is defined by the condition for which the bottom does not evolve anymore, requiring the tidally-averaged sediment transport to be spatially uniform. The present model is based on the cross-sectionally averaged shallow water equations, a width-averaged and depth-integrated advection-diffusion equation for the suspended sediment dynamics and a width-averaged bed evolution equation.

The morphodynamic equilibria have been computed by using a so-called *bifurcation method*. This approach allows to obtain the equilibrium bed profile (and associated water surface elevation, velocity and concentration fields) directly for given values of the

relevant parameters, of the tidal forcing constituents, of the water depth at the seaward boundaries and the system geometry, without resorting to time–integration techniques.

Considering a double–inlet system with a constant width and forced by an M_2 tidal constituent at the seaward boundaries, it was shown that, depending on the prescribed M_2 amplitudes and phases, no equilibrium, one equilibrium or more than one morphodynamic equilibrium configurations can exist. In the absence of a morphodynamic equilibrium, the water depth vanishes somewhere within the tidal basin and the double–inlet system reduces to two uncoupled single–inlet systems. In case of multiple morphodynamic equilibria, most often two equilibrium solutions are found, one linearly stable and the other one linearly unstable. However, for very specific regions of the parameter space, more than one stable equilibrium can be found, with typically one equilibrium having a much smaller minimum water depth than the other. When only one morphodynamic equilibrium was found, the equilibrium was always linearly stable.

The location of the watershed, its local depth, and the total tidally–averaged sediment transport are used to characterize the morphodynamic equilibria, since these properties are sensitive to changes in tidal forcing. Typically, the watershed tends to get closer to the inlet with a larger tidal amplitude. The total transport is usually directed from the inlet with the largest tidal amplitude to the one with the smallest tidal amplitude, with a weak dependency on the phase difference between the tidal forcing at the two inlets.

The model results have been compared with field observations by forcing the system with the first two tidal constituents and considering a tidally–averaged water velocity at one of the inlets. Furthermore, the observed width distribution along the basin was prescribed in the model. Taking parameter values representative of the Marsdiep–Vlie system one stable morphodynamic equilibrium was found. To assess the robustness of this equilibrium, the phase of the M_4 tide at one of the inlets and the width distribution throughout the double–inlet system were systematically varied. The resulting bathymetry and direction of sediment transport were found to strongly depend on these parameters. This finding suggests that information concerning morphodynamic equilibria for double–inlet systems with characteristics different from those of the Marsdiep–Vlie system can only be obtained by dedicated numerical experiments to explore the parameter space.

Taking the large–scale width variations observed in the Marsdiep–Vlie system into account, the main characteristics of the observed width–averaged bathymetry in this double–inlet system were qualitatively reproduced. The large water depth near the Texel island was reproduced by the model results, as well as the presence of two shallower regions, divided by a deeper part, when moving towards the Vlie inlet. Even though the residual water transport observed in the field is directed from the Vlie inlet to the Marsdiep inlet, the model predicts a sediment transport in the opposite direction, as also resulting from much more refined numerical models. The order of magnitude of this transport, predicted by these numerical models, is well–reproduced by the present idealized model.

REFERENCES

- [1] J. Mulhern, C. Johnson, and J. Martin, *Is barrier island morphology a function of tidal and wave regime?* *Marine Geology* **387**, 74 (2017).
- [2] H. E. de Swart and J. T. F. Zimmerman, *Morphodynamics of tidal inlet systems*, *Annual Review of Fluid Mechanics* **41**, 203 (2009).
- [3] D. J. Glaeser, *Global distribution of barrier islands in terms of tectonic setting*, *Journal of Geology* **86**, 283 (1978).
- [4] M. L. Stutz and O. H. Pilkey, *Open-ocean barrier islands: Global influence of climatic, oceanographic, and depositional settings*, *Journal of Coastal Research* **27**, 207 (2011).
- [5] R. A. McBride, M. R. Byrnes, and M. W. Hiland, *Geomorphic response-type model for barrier coastlines: A regional perspective*, *Marine Geology* **126**, 143 (1995).
- [6] A. J. F. Van der Spek, *Tidal asymmetry and long-term evolution of holocene tidal basins in the Netherlands: Simulation of paleo-tides in the Scheldt estuaries*, *Marine Geology* **141**, 71 (1997).
- [7] A. P. Oost, P. Hoekstra, A. Wiersma, B. Flemming, E. J. Lammerts, M. Pejrup, J. Hofstede, B. Van der Valk, P. Kiden, J. Bartholdy, M. Van der Berg, P. C. Vos, S. de Vries, and Z. B. Wang, *Barrier island management: Lessons from the past and directions for the future*, *Ocean & Coastal Management* **68**, 18 (2012).
- [8] M. Duran-Matute, T. Gerkema, G. J. de Boer, J. J. Nauw, and U. Grawe, *Residual circulation and freshwater transport in the Dutch Wadden Sea: a numerical modelling study*, *Ocean Science* **10**, 611 (2014).
- [9] M. Sassi, M. Duran-Matute, T. van Kessel, and T. Gerkema, *Variability of residual fluxes of suspended sediment in a multiple tidal-inlet system: the Dutch Wadden Sea*, *Ocean Dynamics* **65**, 1321 (2015).
- [10] P. Salles, G. Voulgaris, and D. G. Aubrey, *Contribution of nonlinear mechanisms in the persistence of multiple tidal inlet systems*, *Estuarine, Coastal and Shelf Science* **65**, 475 (2005).
- [11] A. Pacheco, A. Vila-Concejo, O. Ferreira, and J. A. Dias, *Assessment of tidal inlet evolution and stability using sediment budget computations and hydraulic parameter analysis*, *Marine Geology* **247**, 104 (2008).
- [12] G. Seminara, M. Bolla Pittaluga, N. Tambroni, and V. Garotta, *Open problems in modelling the long-term morphodynamic evolution of Venice lagoon*, *Flooding and Environmental Challenges for Venice and its Lagoon*, 345 (2005).
- [13] N. Tambroni and G. Seminara, *Are inlets responsible for the morphological degradation of venice lagoon?* *Journal of Geophysical Research: Earth Surface* **111** (2006), [10.1029/2005JF000334](https://doi.org/10.1029/2005JF000334).

- [14] J. Van de Kreeke, *Stability of tidal inlets—Pass Cavallo, Texas*, Estuarine, Coastal and Shelf Science **21**, 33 (1985).
- [15] J. Van de Kreeke, *Can multiple tidal inlets be stable?* Estuarine, Coastal and Shelf Science **30**, 261 (1990).
- [16] J. Van de Kreeke, *Stability analysis of a two-inlet bay system*, Coastal Engineering **14**, 481 (1990).
- [17] F. Escoffier, *The stability of tidal inlets*, Shore Beach **8**, 114 (1940).
- [18] J. Van de Kreeke, R. L. Brouwer, T. J. Zitman, and H. M. Schuttelaars, *The effect of a topographic high on the morphodynamical stability of a two inlet bay system*, Coastal Engineering **55**, 319 (2008).
- [19] R. L. Brouwer, J. Van de Kreeke, and H. M. Schuttelaars, *Entrance/exit losses and cross-sectional stability of double inlet systems*, Estuarine, Coastal and Shelf Science **107**, 69 (2012).
- [20] H. E. de Swart and N. D. Volp, *Effects of hypsometry on the morphodynamic stability of single and multiple tidal inlet systems*, Journal of Sea Research **74**, 35 (2012).
- [21] P. C. Roos, H. M. Schuttelaars, and R. L. Brouwer, *Observations of barrier island length explained using an exploratory morphodynamic model*, Geophysical Research Letters **40**, 4338 (2013).
- [22] K. Reef, P. Roos, H. Schuttelaars, and S. Hulscher, *Influence of back-barrier basin geometry on multiple tidal inlet systems: The roles of resonance and bottom friction*, [Journal of Geophysical Research: Earth Surface](https://doi.org/10.1029/2019JF005261) **125** (2020), 10.1029/2019JF005261.
- [23] A. Dastgheib, J. A. Roelvink, and Z. B. Wang, *Long-term process-based morphological modeling of the Marsdiep tidal basin*, Marine Geology **256**, 90 (2008).
- [24] M. O. Hayes, *Barrier island morphology as a function of tidal and wave regime*, edited by S. P. Leatherman (Academic Press, New York, 1979) pp. 1–27.
- [25] H. M. Schuttelaars and H. E. de Swart, *An idealized long-term morphodynamic model of a tidal embayment*, European Journal of Mechanics, B/Fluids **15**, 55 (1996).
- [26] H. M. Schuttelaars and H. E. de Swart, *Multiple morphodynamic equilibria in tidal embayments*, Journal of Geophysical Research **105**, 105 (2000).
- [27] M. C. Ter Brake and H. M. Schuttelaars, *Modeling equilibrium bed profiles of short tidal embayment. On the effect of the vertical distribution of suspended sediment and the influence of the boundary conditions*, Ocean Dynamics **60**, 183 (2010).
- [28] C. J. Meerman, H. M. Schuttelaars, and V. Rottschäfer, *Influence of geometrical variations on morphodynamic equilibria for single inlet systems*, [Ocean Dynamics](https://doi.org/10.1007/s12237-019-0921-1) **69**, 2 (2019).
- [29] G. T. Csanady, *Circulation in the Coastal Ocean* (Reidel, 1982).

- [30] H. Lorentz, *Het in rekening brengen van den weerstand bij schommelende vloeistofbewegingen*, De Ingenieur, 695 (1922).
- [31] J. T. F. Zimmerman, *On the Lorentz linearization of a nonlinearly damped tidal Helmholtz oscillator*, Proceedings KNAW **95**, 127 (1992).
- [32] P. Roos and H. Schuttelaars, *Resonance properties of tidal channels with multiple retention basins: Role of adjacent sea*, *Ocean Dynamics* **65**, 311 (2015).
- [33] M. C. Ter Brake and H. M. Schuttelaars, *Channel and shoal development in a short tidal embayment: An idealized model study*, *Journal of Fluid Mechanics* **677**, 503 (2011).
- [34] K. R. Dyer, *Coastal and estuarine sediment dynamics* (John Wiley and Sons, 1986).
- [35] S. Lanzoni and G. Seminara, *Long-term evolution and morphodynamic equilibrium of tidal channels*, *Journal of Geophysical Research* **107**, 1 (2002).
- [36] M. Bolla Pittaluga, N. Tambroni, A. Canestrelli, R. Slingerland, S. Lanzoni, and G. Seminara, *Where river and tide meet: The morphodynamic equilibrium of alluvial estuaries*, *Journal of Geophysical Research: Earth Surface* **120**, 75 (2014).
- [37] H. Ridderinkhof, *Tidal and residual flows in the western dutch wadden sea i1: An analytical model to study the constant flow between connected tidal basins*, *Netherlands Journal of Sea Research* **22**, 185 (1988).
- [38] J. A. Sanders and F. Verhulst, *Averaging methods in nonlinear dynamical systems* (Springer Verlag, New York, 1985).
- [39] M. Krol, *On the averaging method in nearly time-periodic advection-diffusion problems*, *SIAM Journal on Applied Mathematics* **51**, 1622 (1991).
- [40] M. Alnæs, J. Blechta, J. Hake, A. Johansson, B. Kehlet, A. Logg, C. Richardson, J. Ring, M. E. Rognes, and G. N. Wells, *The FEniCS project version 1.5*, *Archive of Numerical Software* **3** (2015), [10.11588/ans.2015.100.20553](https://doi.org/10.11588/ans.2015.100.20553).
- [41] S. C. Brenner and L. R. Scott, *The mathematical theory of finite element methods*, 2nd ed. (Springer, New York (N.Y.), 2002).
- [42] R. Seydel, *Practical Bifurcation and Stability Analysis* (Springer, New York, 1994).
- [43] H. Dijkstra, F. Wubs, A. Cliffe, E. Doedel, I. Dragomirescu, B. Eckhardt, A. Gelfgat, A. Hazel, V. Lucarini, A. Salinger, E. Phipps, S. U. Juan, H. Schuttelaars, L. Tuckerman, and U. Thiele, *Numerical bifurcation methods and their application to fluid dynamics: Analysis beyond simulation*, *Communications in Computational Physics* **15**, 1 (2014).
- [44] M. A. Crisfield, *A fast incremental/iterative solution procedure that handles snap through*, *Computers and Structures* **13**, 55 (1981).

- [45] T. Hepkema, H. de Swart, A. Zagaris, and M. Duran–Matute, *Sensitivity of tidal characteristics in double inlet systems to momentum dissipation on tidal flats: a perturbation analysis*, *Ocean Dynamics* **68**, 439 (2018).
- [46] C. Friedrichs and D. Aubrey, *Tidal propagation in strongly convergent channels*, *Journal of Geophysical Research* **99**, 3321 (1994).
- [47] T. Boelens, T. Qi, H. Schuttelaars, and T. De Mulder, *Morphodynamic equilibria in short tidal basins using a 2DH exploratory model*, *Journal of Geophysical Research: Earth Surface* **126** (2021).
- [48] R. Marciano, Z. Wang, A. Hibma, H. De Vriend, and A. Defina, *Modeling of channel patterns in short tidal basins*, *Journal of Geophysical Research* **110** (2005), [10.1029/2003JF000092](https://doi.org/10.1029/2003JF000092).

3

INITIAL FORMATION OF CHANNEL–SHOAL PATTERNS IN DOUBLE–INLET SYSTEMS

Channel–shoal patterns are often observed in the back–barrier basins of inlet systems and are important from both an economical and ecological point of view. Focussing on double–inlet systems, the initial formation of these patterns is investigated using an idealized model. The model is governed by the depth–averaged shallow water equations, a depth–integrated concentration equation and a tidally–averaged bottom evolution equation. Focussing on rectangular basins and neglecting the effects of earth rotation, it is found that laterally uniform morphodynamic equilibria can become linearly unstable, resulting in initial patterns that resemble channels and shoals.

When the water motion is only forced by an M_2 tidal constituent, the existence of (laterally uniform) morphodynamic equilibria for which both inlets are connected strongly depends on the relative phase and amplitudes of the tidal forcing. If such equilibria exist, they can be either stable against small perturbations or linearly unstable. If these equilibria are linearly unstable, two instability mechanisms can be identified, the first related to the convergences and divergences of diffusive transports, the second mechanism related to a combination of advective and diffusive transports. In the former case, all eigenvalues are real and the bedforms grow exponentially in time. In the latter case, the eigenvalues are complex, resulting in bedforms that both migrate and grow in time. In case external over-tides and a time–independent discharge are included, no diffusive instabilities are found anymore for the parameters considered in this thesis. This implies that all instabilities are migrating in time.

In all cases considered, the bed perturbations have only an appreciable amplitude at locations where the underlying laterally uniform equilibrium has a local minimum in water

This chapter is published as: **X. Deng**, T. De Mulder, and H. M. Schuttelaars. (2023) *Initial formation of channel–shoal patterns in double–inlet systems*. *Ocean Dynamics* 73, 1–21.

depth. This is consistent with observations from numerical models and laboratory experiments.

3.1. INTRODUCTION

Around 12% of the world's coastline (Mulhern *et al.* [1]) can be characterised as barrier coasts. They consist of barrier islands, back-barrier basins and tidal inlets connecting the back-barrier basins to the open sea (de Swart and Zimmerman [2]), and have shapes and sizes changing from place to place (Glaeser [3], Stutz and Pilkey [4]). Barrier coasts are very important in terms of ecology and economy. They provide a habitat for many aquatic and terrestrial species and other ecosystem services, and are themselves important elements of biodiversity. They are attractive areas for economical activities such as gas-mining, dredging and recreation. Furthermore, these systems are of importance for coastal safety (Glaeser [3]). An example of a barrier coast is the Wadden Sea along the Dutch, German and Danish coast (Oost *et al.* [5]).

Barrier coasts are highly dynamic because of the complex interactions among water motion, sediment transport and bottom evolution and because of external changes like sea level rise and human interference (McBride *et al.* [6], Van der Spek [7]). In these morphologically active areas, bottom patterns with multiple shoals separated by meandering deep channels are often observed (Dalrymple and Rhodes [8]). These channel–shoal patterns have length scales ranging from several meters to kilometers (de Swart and Zimmerman [2]). Moreover, these patterns can exhibit a cyclic morphodynamic evolution of several years to decades (Israel and Dunsbergen [9]).

To simulate the morphodynamic development of these channels and shoals in barrier coasts, complex process-based models were developed (Marciano *et al.* [10], D'Alpaos *et al.* [11], Hibma *et al.* [12, 13]). For example, Van der Wegen and Roelvink [14] simulated bottom evolution of a laterally-uniform constantly-sloping bed profile in a tidal basin. They found that channels and shoals are initiated in the shallow regions near the landward end of the tidal basin, after which these patterns branch out toward the seaward side of the tidal basin. However, the essential mechanisms that cause these bottom patterns to develop are difficult to assess from these complex state-of-the-art models.

To gain insight into the physical mechanisms initializing channel and shoal development in a single-inlet system, Schuttelaars and de Swart [15] analyzed the linear stability of laterally uniform morphodynamic equilibria (Schuttelaars and de Swart [16]) in short basins using an idealized width-averaged model. By assuming that, tidally averaged, sediment was mainly transported by diffusive processes, they found that the basic states were unstable if the bottom friction parameter exceeded a critical value. van Leeuwen and de Swart [17, 18] extended the model with internally generated advective transport. They found that channels and shoals were on the seaward boundary if the sediment transport is dominated by advective processes. Ter Brake and Schuttelaars [19] further discussed the effect of bottom friction including topographic variations in the diffusive transport, and showed that channel–shoal patterns started to grow in the landward shallow regions.

However, these studies of channels and shoals focused on single-inlet systems, namely tidal basins with one inlet connecting to the open sea. Recent studies show that there is a strong water and sediment exchange between adjacent sub-basins in the Wadden

Sea (Duran-Matute *et al.* [20], Sassi *et al.* [21]). Such interactions are also found in the Ria Formosa in south Portugal (Salles *et al.* [22], Pacheco *et al.* [23]) and Venice Lagoon (Seminara *et al.* [24], Tambroni and Seminara [25]). This strongly suggests that to understand, model and predict the morphodynamic evolution of barrier coasts, back barrier basins should be considered as multiple-inlet systems.

The present study aims at analyzing the initial formation of channels and shoals in a double-inlet system, consisting of a basin with two inlets connecting to the open sea. Only rectangular planform geometries will be considered and the effects of earth rotation on the water motion is neglected. By studying the linear stability (Schuttelaars and de Swart [15], van Leeuwen and de Swart [17], Ter Brake and Schuttelaars [19]) of laterally uniform morphodynamic equilibria in double-inlet systems (Deng *et al.* [26]), insight in the 2DH stability of these systems is obtained, thus extending the 1D stability analysis performed in Deng *et al.* [26]. Furthermore, the mechanisms resulting in these instabilities can be identified. Default parameters used are characteristic for the Marsdiep-Vlie inlet system in the Dutch Wadden Sea, even though a direct comparison with the patterns observed in this system cannot be made because of the assumption of a rectangular basin. The sensitivity of the linear stability of the basic state to tidal forcings will be investigated in detail. The linear stability analysis is a first step in systematically obtaining morphodynamic equilibria with a more complex (finite amplitude) channel-shoal structure.

In Sect. 3.2, the equations governing water motion, transport of sediment and bed evolution are presented. The scaling of the system of equations and the solution method are presented in Sect. 3.3. In Sect. 3.4, morphodynamic equilibria in double-inlet systems and their linear stability are studied. In Sect. 3.5, the results are discussed and conclusions presented.

3.2. MODEL DESCRIPTION

We consider a rectangular tidal basin with a prescribed length L and width B (see Fig. 3.1a for a top view). This basin is connected to the open sea by two inlets, located at $x = 0$ and $x = L$, with x the coordinate in the along-basin (or longitudinal) direction. The landward boundaries of the rectangular tidal basin are located at $y = 0$ and $y = B$, where y is the coordinate in the cross-basin (or lateral) direction. The landward boundaries are assumed to be both impermeable for water and sediments, and non-erodible.

The free surface is located at $z = \hat{\zeta}$, measured from the undisturbed free surface found at $z = 0$ (see Fig. 3.1b for a side view). The undisturbed water depth of the tidal basin at $x = 0$ is denoted by H^I and at $x = L$ by H^{II} , both are assumed to be laterally uniform. The erodible bottom consisting of uniform sandy material is found at $z = \hat{h} - H^I$, where \hat{h} denotes the bed level measured from the reference depth H^I . Hence, the instantaneous local water depth is given by $H^I - \hat{h} + \hat{\zeta}$.

The tidal basins we consider have a water depth much smaller than both the length and width. Hence, the water motion can be described by the depth-averaged shallow water equations for a homogeneous fluid (Csanady [27]). Assuming the basin width to be much smaller than the Rossby deformation radius allows for neglecting earth rotation

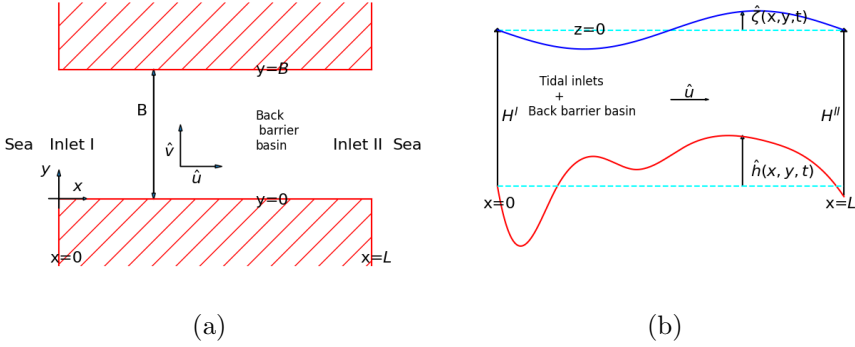


Figure 3.1: A sketch of an idealized tidal basin connected to the open sea at both ends. (a) A top view of the schematized double–inlet system with a uniform width B . The longitudinal and lateral velocities are denoted by \hat{u} and \hat{v} . (b) A longitudinal cross–section view of the double–inlet system, with the depth at inlet I denoted by H^I and the depth at inlet II denoted by H^{II} . The bed profile (red line) is denoted by $\hat{h}(x, y, t)$, and the free surface elevation (blue line) by $\hat{\zeta}(x, y, t)$.

effects. The resulting equations read:

$$\nabla \cdot [(H^I - \hat{h} + \hat{\zeta})\hat{\mathbf{u}}] + \hat{\zeta}_t = 0, \quad (3.1a)$$

$$\hat{\mathbf{u}}_t + \hat{\mathbf{u}} \cdot \nabla \hat{\mathbf{u}} + g \nabla \hat{\zeta} + \frac{r_* \hat{\mathbf{u}}}{H^I - \hat{h} + \hat{\zeta}} = 0, \quad (3.1b)$$

with Eq.(3.1a) the depth–averaged continuity equation and Eq.(3.1b) the depth–averaged momentum equation. In these equations, the horizontal velocity is denoted by $\hat{\mathbf{u}} = (\hat{u}, \hat{v})$, with \hat{u} the velocity in the longitudinal and \hat{v} the velocity in lateral direction. Time is denoted by t and g denotes the gravitational acceleration. Subscripts indicate a derivative with respect to that variable, and the horizontal derivative operator is denoted as $\nabla = (\partial_x, \partial_y)$. The inner product is denoted by a dot. Following Lorentz [28] and Zimmerman [29], bottom friction is linearized using the bottom friction coefficient defined as $r_* = 8Uc_d/3\pi$, with U a characteristic velocity scale (which will be defined in Sect. 3.3.1) and c_d a drag coefficient.

The variables $\hat{\zeta}$ and $\hat{\mathbf{u}}$ are decomposed into a tidally–averaged and a time–varying contribution as $\hat{\zeta} = \langle \hat{\zeta} \rangle + \tilde{\hat{\zeta}}$ and $\hat{\mathbf{u}} = \langle \hat{\mathbf{u}} \rangle + \tilde{\hat{\mathbf{u}}}$, where the angular brackets $\langle \cdot \rangle = \int_0^T \cdot dt / T$ denote the tidally averaged contribution, with T the M_2 tidal period, and an overbar $\tilde{\cdot}$ the instantaneous deviation from this tidal average such that $\langle \tilde{\cdot} \rangle = 0$.

The time–varying parts of the sea surface elevations at the two seaward sides of the inlets are assumed to be forced by prescribed M_2 and M_4 tidal constituents,

$$\tilde{\hat{\zeta}} = A_{M_2}^I \cos(\sigma t - \phi_{M_2}^I) + A_{M_4}^I \cos(2\sigma t - \phi_{M_4}^I) \quad \text{at } x=0, \quad (3.2a)$$

$$\tilde{\hat{\zeta}} = A_{M_2}^{II} \cos(\sigma t - \phi_{M_2}^{II}) + A_{M_4}^{II} \cos(2\sigma t - \phi_{M_4}^{II}) \quad \text{at } x=L. \quad (3.2b)$$

The constants $A_{M_2}^I$ ($A_{M_4}^I$) and $A_{M_2}^{II}$ ($A_{M_4}^{II}$) denote the amplitudes of the M_2 (M_4) tidal constituents at inlet I and II , while the corresponding phases are denoted by $\phi_{M_2}^I$ ($\phi_{M_4}^I$) and $\phi_{M_2}^{II}$ ($\phi_{M_4}^{II}$). Even though these amplitudes and phases may in principle depend on the lateral coordinate y , we assume them to be uniform in the lateral direction. The angular frequency of the M_2 tidal signal is given by $\sigma = 2\pi/T$.

Furthermore, the tidally averaged mean sea surface elevation at inlet I is required to be zero and a tidally averaged discharge is prescribed at inlet II :

$$\langle \hat{\zeta} \rangle = 0 \quad \text{at} \quad x = 0, y \in [0, B], \quad (3.3a)$$

$$\langle (H - \hat{h} - \hat{\zeta}) \hat{u} \rangle = Q_* / B \quad \text{at} \quad x = L, y \in [0, B], \quad (3.3b)$$

with Q_* the residual water transport at inlet II . A positive (negative) Q_* represents a residual water transport out of (into) the system at inlet II . For an extensive discussion of these boundary conditions, see Deng *et al.* [26].

The condition of impermeability at the landward boundaries of the back-barrier islands reads

$$(H - \hat{h} + \hat{\zeta}) \hat{\mathbf{u}} \cdot \mathbf{n} = 0 \quad \text{at} \quad y = 0 \text{ and } B, \quad (3.4)$$

in which \mathbf{n} denotes the outward pointing unit vector normal to the boundary.

The sediment in the tidal basin consists of fine sand with a uniform grain size that is mainly transported as suspended load (see the scaling analysis in Sect. 3.3, the bedload transport contribution is given in Eq. (3.10)). The associated depth-integrated concentration equation (Ter Brake and Schuttelaars [19, 30]) reads

$$\hat{C}_t + \nabla \cdot [\hat{\mathbf{u}} \hat{C} - k_{h*} (\nabla \hat{C} + \frac{w_s}{k_{v*}} \beta \hat{C} \nabla \hat{h})] = \alpha \hat{\mathbf{u}} \cdot \hat{\mathbf{u}} - \frac{w_s^2}{k_{v*}} \beta \hat{C}, \quad (3.5)$$

where \hat{C} is the *depth-integrated* suspended sediment concentration. The horizontal diffusivity k_{h*} , the vertical diffusivity k_{v*} , the settling velocity w_s and the erosion parameter α (with units kgsm^{-4}) related to sediment properties (Dyer [31]) are assumed to be constant in space and time. The deposition parameter β is defined by (see Ter Brake and Schuttelaars [30] for details, also for the explicit expression of the settling term)

$$\beta = \frac{1}{1 - \exp(-\frac{w_s}{k_{v*}} (H^I - \hat{h} + \hat{\zeta}))}. \quad (3.6)$$

The boundary conditions at the two inlets read (Ter Brake and Schuttelaars [30], Schuttelaars and de Swart [32])

$$\lim_{k_{h*} \rightarrow 0} \hat{C}(x, t, k_{h*}) = \hat{C}(x, t, k_{h*} = 0) \quad \text{at} \quad x = 0 \text{ and } L, \quad (3.7)$$

which, based on Eqn. (3.5), can be rewritten as

$$\hat{C}_t + \nabla \cdot (\hat{\mathbf{u}} \hat{C}) = \alpha \hat{\mathbf{u}} \cdot \hat{\mathbf{u}} - \frac{w_s^2}{k_{v*}} \beta \hat{C} \quad \text{at} \quad x = 0 \text{ and } L. \quad (3.8)$$

At the lateral boundaries we require that no suspended load transport occurs through these boundaries,

$$[\hat{\mathbf{u}}\hat{C} - k_{h*}(\nabla\hat{C} + \frac{w_s}{k_{v*}}\beta\hat{C}\nabla\hat{h})] \cdot \mathbf{n} = 0 \quad \text{at } y = 0 \text{ and } B, \quad (3.9)$$

with \mathbf{n} defined above.

The bed evolution equation (Meerman *et al.* [33]) is derived from the mass balance in the sediment layer and reads

$$\rho_s(1-p)(\hat{h}_t - \lambda\nabla^2\hat{h}) = -(\alpha\hat{\mathbf{u}} \cdot \hat{\mathbf{u}} - \frac{w_s^2}{k_{v*}}\beta\hat{C}). \quad (3.10)$$

Here, ρ_s is the sediment density and p denotes the bed porosity. The first and second term on the right-hand side of Eq. (3.10) model the local erosion and deposition of sediment, respectively. The first term on the left-hand side models the temporal bed changes, whereas the second term models the effects of the gravitational transport present in the bedload transport, using a highly simplified parameterisation with constant $\lambda \sim \mathcal{O}(10^{-6} - 10^{-4}) \text{ m}^2 \text{ s}^{-1}$, see Schuttelaars and de Swart [16] for a detailed discussion. Following Schuttelaars and de Swart [15], Falqués *et al.* [34] this latter term is retained because, even though bedload transport is typically small in the systems we consider, the stabilizing effects of the slope terms may play an important role when considering the stability properties of morphodynamic equilibria.

Substituting Eq.(3.5) into Eq.(3.10) allows for rewriting the bed evolution equation as

$$\rho_s(1-p)\hat{h}_t + \hat{C}_t = -\nabla \cdot \mathbf{F}, \quad (3.11)$$

with

$$\mathbf{F} = \underbrace{-k_{h*}\nabla\hat{C}}_{\mathbf{F}_{\text{diff}}} - \underbrace{k_{h*}\frac{w_s}{k_{v*}}\beta\hat{C}\nabla\hat{h}}_{\mathbf{F}_{\text{topo}}} + \underbrace{\hat{\mathbf{u}}\hat{C}}_{\mathbf{F}_{\text{adv}}} - \underbrace{\rho_s(1-p)\lambda\nabla\hat{h}}_{\mathbf{F}_{\text{bed}}} \quad (3.12)$$

being the total depth-integrated sediment transport. This transport consists of four terms, that is a classical diffusive contribution (\mathbf{F}_{diff}), a topographically induced diffusive contribution (\mathbf{F}_{topo}), an advective contribution (\mathbf{F}_{adv}), and a bedload contribution (\mathbf{F}_{bed}).

At the seaward boundaries the depths are assumed to be fixed:

$$\hat{h} = 0 \quad \text{at } x = 0, \quad (3.13a)$$

$$\hat{h} = H^I - H^{II} \quad \text{at } x = L. \quad (3.13b)$$

Using Eq. (3.9), the requirement of no sediment transport through the lateral boundaries reduces to

$$\nabla\hat{h} \cdot \mathbf{n} = 0 \quad \text{at } y = 0 \text{ and } B, \quad (3.14)$$

implying no bedload transport due to slope effects is allowed through these side walls.

3.3. SOLUTION METHOD

3.3.1. SCALING AND EXPANSION

To assess the dominant balances in the system of equations (3.1), (3.5) and (3.10), the relevant variables are made dimensionless by using the following scaling:

$$(x, y) = L(\check{x}, \check{y}), \quad t = \sigma^{-1} \check{t}, \quad \hat{\mathbf{u}} = U\check{\mathbf{u}}, \quad (3.15a)$$

$$\hat{\zeta} = A_{M_2}^I \check{\zeta}, \quad \hat{h} = H^I \check{h}, \quad \hat{C} = \frac{\alpha U^2 k_{v*}}{w_s^2} \check{C}, \quad (3.15b)$$

where dimensionless quantities are indicated by a check $\check{\cdot}$. The longitudinal x and lateral coordinate y are made dimensionless by the length L of the double-inlet system (implying that $0 \leq \check{y} \leq B/L$), time is made dimensionless using the M_2 angular frequency σ , the surface elevation is normalized with the M_2 amplitude at the seaward side of inlet I, denoted by $A_{M_2}^I$, and the bed level is made dimensionless using the depth H^I at inlet I. The typical scale for the velocity is given by $U = A_{M_2}^I \sigma L / H^I$ (see Deng *et al.* [26] for a motivation of this velocity scale). Assuming an approximate balance between erosion and deposition, the suspended sediment concentration is made dimensionless using $\alpha U^2 k_{v*} / w_s^2$.

Substituting these dimensionless variables in the governing equations and suppressing the checks, the system of equations reads (see Tab. 3.1 for a definition of the various dimensionless constants)

$$\zeta_t + \nabla \cdot [(1 - h + \epsilon \zeta) \mathbf{u}] = 0, \quad (3.16a)$$

$$\mathbf{u}_t + \epsilon \mathbf{u} \cdot \nabla \mathbf{u} + \lambda_L^{-2} \nabla \zeta + \frac{r \mathbf{u}}{1 - h + \epsilon \zeta} = 0, \quad (3.16b)$$

$$a[C_t + \nabla \cdot (\epsilon \mathbf{u} C - k_h \nabla C - k_h \lambda_d \beta \nabla h C)] = \mathbf{u} \cdot \mathbf{u} - \beta C, \quad (3.16c)$$

$$h_t + a \delta_s C_t = -\delta_s a \nabla \cdot [\epsilon \mathbf{u} C - k_h \nabla C - k_h \lambda_d \beta \nabla h C] - \delta_b \nabla h, \quad (3.16d)$$

with the dimensionless deposition parameter β now defined as

$$\beta = \frac{1}{1 - \exp(-\lambda_d(1 - h + \epsilon \zeta))}. \quad (3.17)$$

The parameter $\epsilon = A_{M_2}^I / H^I$ is the ratio of the M_2 tidal amplitude to the water depth at inlet I. The parameter $\lambda_L = k_g L$ is the product of the frictionless tidal wavenumber $k_g = \sigma / \sqrt{H^I g}$ and the length of the inlet system. The dimensionless friction parameter is denoted by r and is defined as $r = r_* / H^I \sigma$. The ratio of the deposition timescale to the tidal period is denoted by $a = k_{v*} \sigma / w_s^2$, and the sediment Peclet number $\lambda_d = H^I w_s / k_{v*}$ is the ratio of the typical time it takes for a particle to settle in the water column to the typical time needed to mix particles through the water column. The dimensionless diffusion parameter is denoted by $k_h = k_{h*} / L^2 \sigma$. The parameter $\delta_s = \alpha U^2 / (\rho_s (1 - p) H^I \sigma)$ denotes the ratio of tidal period T over the time scale related to suspended load, while $\delta_b = \lambda / \sigma H^I L$ is the ratio between the tidal period T and the time scale related to the gravitational term in the bedload transport. For a definition of all parameters, see Tab. 3.1.

Parameters & Definition

$$\begin{aligned}
\epsilon &= \frac{A_{M_2}^I}{H^I} = \frac{U}{\sigma L} & \lambda_L &= \frac{\sigma L}{\sqrt{H^I g}} \\
r &= \frac{r_*}{H^I \sigma} & a &= \frac{k_{v*} \sigma}{w_s^2} \\
k_h &= \frac{k_{h*}}{L^2 \sigma} & Q &= \frac{Q_*}{BH^I U} \\
\delta_s &= \frac{\alpha U^2}{\rho_s (1-p) H^I \sigma} & \delta_b &= \frac{\lambda}{\sigma H^I L} \\
\lambda_d &= \frac{H^I w_s}{k_{v*}} & \gamma &= \frac{A_{M_4}^I}{A_{M_2}^I} \\
A_{r2}^{II} &= \frac{A_{M_2}^{II}}{A_{M_2}^I} & A_{r4}^{II} &= \frac{A_{M_4}^{II}}{A_{M_4}^I} \\
\Delta \phi_{M_2} &= \phi_{M_2}^{II} - \phi_{M_2}^I & \phi_{r4}^I &= \phi_{M_4}^I - 2\phi_{M_2}^I \\
\phi_{r4}^{II} &= \phi_{M_4}^{II} - 2\phi_{M_2}^I
\end{aligned}$$

Table 3.1: Definition of the dimensionless parameters.

Both parameters associated to sediment transport (i.e., morphodynamic) timescale are small: $\delta_s \ll 1$ and $\delta_b \ll 1$. Therefore, using equation (3.16d) it follows that the bed changes on the tidal timescale are very small. Using a multiple timescale approach (Sanders and Verhulst [35], Krol [36]), the evolution can be approximated by considering the tidally averaged bed evolution equation:

$$\begin{aligned}
h_\tau &= -\nabla \cdot \langle \mathbf{F} \rangle, & (3.18) \\
\text{with } \mathbf{F} &= \underbrace{-ak_h \nabla C}_{\mathbf{F}_{\text{diff}}} - \underbrace{ak_h \lambda_d \beta C \nabla h}_{\mathbf{F}_{\text{topo}}} + \underbrace{a \epsilon \mathbf{u} C}_{\mathbf{F}_{\text{adv}}} - \underbrace{\frac{\delta_b}{\delta_s} \nabla h}_{\mathbf{F}_{\text{bed}}},
\end{aligned}$$

with $\tau = \delta_s t$ the long (morphodynamic) timescale, i.e., the timescale at which bed changes are significant.

The associated dimensionless boundary conditions read

$$\zeta = \cos t + \gamma \cos(2t - \phi_{r4}^I) \quad \text{at } x = 0, \quad (3.19a)$$

$$\bar{\zeta} = A_{r2}^{II} \cos(t - \Delta \phi_{M_2}) + \gamma A_{r4}^{II} \cos(2t - \phi_{r4}^I) \quad \text{at } x = 1, \quad (3.19b)$$

$$\langle (1 - h + \epsilon \zeta) u \rangle = Q \quad \text{at } x = 1, \quad (3.19c)$$

$$(1 - h + \epsilon \zeta) \mathbf{u} \cdot \mathbf{n} = 0 \quad \text{at } y = 0, B/L, \quad (3.19d)$$

$$\langle \mathbf{u} \cdot \mathbf{u} - \beta C \rangle = 0 \quad \text{at } x = 0, 1, \quad (3.19e)$$

$$\lim_{k_h \rightarrow 0} \bar{C}(x, t, k_h) = \bar{C}(x, t, k_h = 0) \quad \text{at } x = 0, 1 \quad (3.19f)$$

$$(\epsilon \mathbf{u} C - k_h \nabla C - k_h \lambda_d C \nabla h) \cdot \mathbf{n} = 0 \quad \text{at } y = 0, B/L, \quad (3.19g)$$

$$h = 0 \quad \text{at } x = 0, \quad (3.19h)$$

$$h = 1 - \frac{H^{II}}{H^I} \quad \text{at } x = 1, \quad (3.19i)$$

$$\nabla h \cdot \mathbf{n} = 0 \quad \text{at } y = 0, B/L. \quad (3.19j)$$

Here, the parameter γ is the ratio of the amplitudes of the M_4 and M_2 tidal constituents at inlet I , and $A_{r2}^{II} = A_{M_2}^{II} / A_{M_2}^I$ ($A_{r4}^{II} = A_{M_4}^{II} / A_{M_4}^I$) the ratio of the amplitudes of the M_2 (M_4)

tide at inlet II and at inlet I . The parameter $\Delta\phi_{M_2} = \phi_{M_2}^{II} - \phi_{M_2}^I$ is the phase difference between the M_2 tide at inlet II and at inlet I . The relative phases at inlets I and II are defined as $\phi_{r4}^I = \phi_{M_4}^I - 2\phi_{M_2}^I$ and $\phi_{r4}^{II} = \phi_{M_4}^{II} - 2\phi_{M_2}^I$. The dimensionless residual water transport at inlet II is denoted by $Q = Q_*/(BH^I U)$ and is assumed to be of order ϵ .

For the systems we consider, the parameters ϵ and γ are much smaller than 1 (see Tab. 3.2 for a typical example), allowing for the introduction of an asymptotic expansion in ϵ and γ of the physical variables $\Phi \in \{\zeta, u, v, C\}$,

$$\Phi = \Phi^{00} + \epsilon\Phi^{10} + \gamma\Phi^{01} + \text{h.o.t.}, \quad (3.20)$$

where the first superscript denotes the order in ϵ while the second one denotes the order in γ . Substituting this asymptotic expansion in Eqns. (3.16a)–(3.16c), (3.18) and in the boundary conditions (3.19), we obtain a series of equations ordered with respect to the small parameters ϵ and γ . At the leading order, the morphodynamic balance depends only on the leading order and first order contributions of the water motion and concentration equation in ϵ and γ . The time dependency of the various physical variables can be written as an (infinite) sum of tidal constituents and a residual component,

$$\Phi^{ij}(x, y, t) = \Phi_{\text{res}}^{ij}(x, y) + \sum_{k=1}^{\infty} \left[\Phi_{ck}^{ij}(x, y) \cos kt + \Phi_{sk}^{ij}(x, y) \sin kt \right], \quad (3.21)$$

where the subscript 'res' denotes the tidally-averaged (i.e., residual) contribution to the variable $\Phi(x, y, t)$, while the contributions that temporally vary as cosines (sines) with frequency k are denoted with the subscript ck (sk). The superscript i denotes the order in ϵ and the second superscript j the order in γ .

By using the specific forcing of the water motion prescribed at the inlets (see Eqns. (3.2) and (3.3)), it follows that the temporal variation of the physical variables is restricted to only a few tidal constituents. This can be seen by substituting the Fourier expansion Eqn. (3.21) in the system of equations (3.16). Next, collecting terms of the same order in ϵ and γ and of same tidal constituent and using the prescribed boundary conditions, the water motion at leading order is found to be controlled by the M_2 tidal constituent only; at order ϵ a residual and M_4 contributions are generated, while M_4 contributions are found at order γ :

$$\begin{aligned} \mathbf{u}(x, y, t) = & \mathbf{u}_{c1}^{00}(x, y) \cos(t) + \mathbf{u}_{s1}^{00}(x, y) \sin(t) \\ & + \epsilon \left[\mathbf{u}_{\text{res}}^{10}(x, y) + \mathbf{u}_{c2}^{10}(x, y) \cos(2t) + \mathbf{u}_{s2}^{10}(x, y) \sin(2t) \right] \\ & + \gamma \left[\mathbf{u}_{c2}^{01}(x, y) \cos(2t) + \mathbf{u}_{s2}^{01}(x, y) \sin(2t) \right]. \end{aligned} \quad (3.22)$$

A similar expansion holds for the sea surface elevation $\zeta(x, y, t)$. These water motion components act as forcing terms in the concentration equation. At the leading order, a residual and M_4 concentrations are generated. At order ϵ and γ only the M_2 concentrations are calculated, as the concentration that varies with the M_6 tidal frequency does not produce a residual sediment transport at the leading order. The expansion of $C(x, y, t)$

then reads

$$\begin{aligned} C(x, y, t) = & C_{\text{res}}^{00}(x, y) + C_{c2}^{00}(x, y) \cos(2t) + C_{s2}^{00}(x, y) \sin(2t) \\ & + \epsilon [C_c^{10}(x, y) \cos(t) + C_s^{10}(x, y) \sin(t)] \\ & + \gamma [C_c^{01}(x, y) \cos(t) + C_s^{01}(x, y) \sin(t)]. \end{aligned} \quad (3.23)$$

Using expressions (3.22) and (3.23), the leading order tidally-averaged sediment transport contributions are given by

$$\langle \mathbf{F}_{\text{diff}}^{00} \rangle = -ak_h \nabla C_{\text{res}}^{00}, \quad (3.24)$$

$$\langle \mathbf{F}_{\text{topo}}^{00} \rangle = -ak_h \beta \lambda_d C_{\text{res}}^{00} \nabla h, \quad (3.25)$$

$$\langle \mathbf{F}_{\text{adv}}^{20} \rangle = \frac{1}{2} a \epsilon^2 (\mathbf{u}_{c1}^{00} C_{c1}^{10} + \mathbf{u}_{s1}^{00} C_{s1}^{10} + 2\mathbf{u}_{\text{res}}^{10} C_{\text{res}}^{00} + \mathbf{u}_{c2}^{10} C_{c2}^{00} + \mathbf{u}_{s2}^{10} C_{s2}^{00}), \quad (3.26)$$

$$\langle \mathbf{F}_{\text{adv}}^{11} \rangle = \frac{1}{2} a \epsilon \gamma (\mathbf{u}_{c1}^{00} C_{c1}^{01} + \mathbf{u}_{s1}^{00} C_{s1}^{01} + \mathbf{u}_{c2}^{01} C_{c2}^{00} + \mathbf{u}_{s2}^{01} C_{s2}^{00}), \quad (3.27)$$

$$\langle \mathbf{F}_{\text{bed}} \rangle = -\frac{\delta_b}{\delta_s} \nabla h, \quad (3.28)$$

in which $\mathbf{F}_{\text{diff}}^{00}$ is the classical diffusive contribution and $\mathbf{F}_{\text{topo}}^{00}$ is the topographically induced diffusive contribution. The advective transport is decomposed in two contributions, the internally generated advection denoted as $\mathbf{F}_{\text{adv}}^{20}$ and the externally generated advection denoted as $\mathbf{F}_{\text{adv}}^{11}$. The transport due to the gravitational effect on bedload is denoted by \mathbf{F}_{bed} . This term is always much smaller than the topographically induced diffusive contribution (Hepkema *et al.* [37]) and will be added to the topographically induced diffusive transport when plotting the various contributions.

3.3.2. BASIC STATE AND LINEAR STABILITY

The resulting system of morphodynamic equations, ordered according to the small parameters ϵ , γ and expanded in terms of the tidal constituents, can be written as

$$K\Psi_\tau = G(\Psi), \quad (3.29)$$

where Ψ is a 29-dimensional vector of the amplitudes of all physical variables considered. Namely, $\Psi = (\zeta_{c1}^{00}, \zeta_{s1}^{00}, \zeta_{\text{res}}^{10}, \zeta_{c2}^{10}, \zeta_{s2}^{10}, \zeta_{c2}^{01}, \zeta_{s2}^{01}, \dots, h)$, where the dots indicate the amplitudes of the longitudinal velocity u , lateral velocity v and concentration C . The matrix K is a diagonal matrix, with a non-zero element (equal to one) only at the row associated with the bed evolution equation and G (see Appendix E for a simple discussion of operator G) is a nonlinear operator applied to the vector Ψ .

For a double inlet system with a *rectangular* geometry and in which the forcing due to the earth rotation is neglected, the system of equations (3.29) allows for morphodynamic equilibria $\Psi_e = \Psi_e(x)$ that are laterally uniform and satisfy

$$G(\Psi_e) = 0. \quad (3.30)$$

These morphodynamic equilibria do not depend on the lateral coordinate y and the amplitudes of the lateral velocities considered are zero. To obtain these basic states Ψ_e , the

system of equations is first discretized using a finite element method with continuous Langrange elements. The number of elements used in the longitudinal direction is 800 (increasing the number of elements resulting in small relative changes, typically smaller than 0.01 in the amplitudes, not shown) with the degree of each element 2, resulting in a total number of degrees of freedom of 46429. Next, a Newton–Raphson iterative method is employed to numerically find the solution of Eq. (3.30), see Deng *et al.* [26] for a detailed discussion.

These laterally uniform morphodynamic equilibria can be unstable against both one dimensional (laterally uniform) and two–dimensional perturbations (perturbations with lateral structure). To assess this stability for infinitesimal perturbations, a small two–dimensional perturbation is added to the basic state Ψ_e ,

$$\Psi(x, y, \tau) = \Psi_e(x) + \Psi'(x, y, \tau), \quad (3.31)$$

which is then substituted into Eq. (3.29). Since the perturbations are small, only linear terms are retained. The resulting linearized equations allow for a solution using the ansatz

$$\Psi' = \Re[\hat{\Psi}'(x, y) \exp(\omega\tau)].$$

The quantity $\Re(\omega)$ is the real part of ω , indicating the exponential growth rate of perturbations. The imaginary part of ω , $\Im(\omega)$, gives the frequency. Substituting eq. (3.31) into eq. (3.29) results in the following eigenvalue problem

$$\omega K \hat{\Psi}' = L(\Psi_e) \hat{\Psi}', \quad (3.32)$$

with L the Jacobian matrix associated with the operator G , evaluated at Ψ_e . This eigenvalue problem is discretized using the same method adopted to solve the equilibrium problem. Note that the linear stability analysis only gives information of the patterns that might start to develop on the laterally uniform equilibrium configuration, no information concerning the final bathymetry can be directly inferred from this analysis. In system (3.32), the lateral structure of the various components of the eigenvector $\hat{\Psi}'$ can be inferred from the boundary conditions, resulting in:

$$\begin{aligned} \hat{u}'(x, y) &= u'_n(x) \cos(l_n y), & \hat{v}'(x, y) &= v'_n(x) \sin(l_n y), \\ \hat{\zeta}'(x, y) &= \zeta'_n(x) \cos(l_n y), & \hat{C}'(x, y) &= C'_n(x) \cos(l_n y), \\ \hat{h}'(x, y) &= h'_n(x) \cos(l_n y). \end{aligned}$$

The longitudinal structure of the eigenfunctions is indicated by \cdot' while the dimensionless wave number l_n is defined by

$$l_n = n\pi L/B, \quad n = 0, 1, 2, \dots, \quad (3.34)$$

with n the lateral mode number. When $n = 0$, the eigenpatterns are laterally uniform and the associated eigenvalues determine stability against perturbations without any lateral structure. For $n \neq 0$, the eigenpatterns are laterally varying and the eigenvalues determine the stability of the laterally uniform morphodynamic equilibria against laterally varying perturbations.

| Quantities in the dimensional model | |
|---|---|
| System | Sediment & Bed |
| $L = 59 \text{ km}$ | $k_{h*} = 10^2 \text{ m}^2 \text{ s}^{-1}$ |
| $g = 9.81 \text{ ms}^{-2}$ | $\alpha = 0.5 \cdot 10^{-2} \text{ kg s m}^{-4}$ |
| $c_d = 0.0025$ | $\lambda \sim 10^{-6} - 10^{-4} \text{ m}^2 \text{ s}^{-1}$ |
| $\sigma = 1.4 \cdot 10^{-4} \text{ s}^{-1}$ | $k_{v*} = 0.1 \text{ m}^2 \text{ s}^{-1}$ |
| $T = 44.9 \cdot 10^3 \text{ s}$ | $d_{50} = 2 \cdot 10^{-4} \text{ m}$ |
| $Q_* = -900 \text{ m}^3 \text{ s}^{-1}$ | $\rho_s = 2650 \text{ kg m}^{-3}$ |
| | $p = 0.4$ |
| | $w_s = 0.015 \text{ m s}^{-1}$ |
| Inlet specific parameters | |
| Marsdiep Inlet | Vlie Inlet |
| $H^I = 11.7 \text{ m}$ | $H^{II} = 11.9 \text{ m}$ |
| $A_{M_2}^I = 0.62 \text{ m}$ | $A_{M_2}^{II} = 0.77 \text{ m}$ |
| $\phi_{M_2}^I = 148^\circ$ | $\phi_{M_2}^{II} = -158^\circ$ |
| $B^I = 5.954 \text{ km}$ | $B^{II} = 5.619 \text{ km}$ |
| $A_{M_4}^I = 0.11 \text{ m}$ | $A_{M_4}^{II} = 0.06 \text{ m}$ |
| $\phi_{M_4}^I = 155^\circ$ | $\phi_{M_4}^{II} = -121^\circ$ |
| Quantities in the non-dimensional model | |
| $\epsilon = 5.30 \cdot 10^{-2}$ | $\lambda_L = 0.77$ |
| $r = 5.67 \cdot 10^{-1}$ | $a = 6.22 \cdot 10^{-2}$ |
| $k_h = 2.05 \cdot 10^{-4}$ | $Q = -2.95 \cdot 10^{-2}$ |
| $\delta_s = 3.68 \cdot 10^{-4}$ | $\delta_b \sim 10^{-8} - 10^{-6}$ |
| $\lambda_d = 1.75$ | $\gamma = 1.83 \cdot 10^{-1}$ |
| $A_{r2}^{II} = 1.25$ | $A_{r4}^{II} = 0.535$ |
| $\Delta\phi_{M_2} = 54^\circ$ | $\phi_{r4}^I = -141^\circ$ |
| $\phi_{r4}^{II} = -57^\circ$ | |

Table 3.2: Characteristic values representative for the Marsdiep–Vlie inlet system (Duran-Matute *et al.* [20], Ridderinkhof [38]). In the experiments in this paper, the depth at inlet *II* is taken to be 11.7 m, a rectangular inlet system is used with a uniform width of 6 km. This results in $l_n = 30.9n$

3.4. RESULTS

The linear stability of laterally uniform morphodynamic equilibria is investigated and the associated instability mechanisms are discussed. In Sect. 3.4.1, the water motion in the double inlet system is forced by a prescribed M_2 tidal forcing at both inlets. The influence of prescribed external overtides and discharge are treated in Sect. 3.4.2. All results are obtained using parameter values representative of the Marsdiep–Vlie inlet system (see Tab. 3.2), unless mentioned otherwise. A uniform width B of 6 km is considered in all numerical experiments. Furthermore, since the undisturbed water depths observed at both inlets, H^I and H^{II} , are very close together, they are for simplicity both taken to be equal to 11.7 m. Hence, the dimensionless boundary condition (3.19i) reduces to $h = 0$ at $x = 1$.

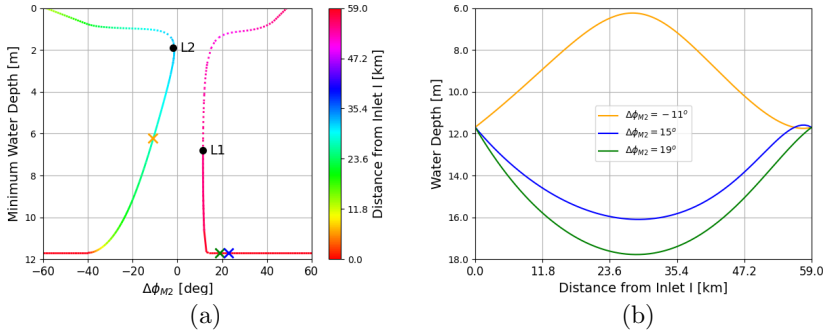


Figure 3.2: Laterally uniform morphodynamic equilibria when taking diffusive and internally generated advective transport, as well as bedload transport into account. The water motion is only forced with M_2 tidal constituents. Panel (a) shows WD_{\min} , the minimum water depth of equilibrium bed profiles, with its location coded with color. Panel (b) shows the equilibrium bed profiles for three different values of $\Delta\phi_{M_2}$.

3.4.1. M_2 TIDAL FORCING

In this section, the water motion is forced by prescribed M_2 tidal amplitudes and phases at inlets I and II , while the amplitudes of the externally prescribed overtides ($A_{M_4}^I$ and $A_{M_4}^{II}$) and the discharge Q at inlet II are assumed to be zero. With this forcing, the sediment transport is controlled by diffusive processes (both the standard diffusive process and the one related to the topographic variations), advective transport driven by internally generated overtides and bedload transport. Hence, the bottom evolution equation (3.18) reduces to

$$h_\tau = -\nabla \cdot \left(\langle \mathbf{F}_{\text{diff}}^{00} \rangle + \langle \mathbf{F}_{\text{topo}}^{00} \rangle + \langle \mathbf{F}_{\text{adv}}^{20} \rangle + \langle \mathbf{F}_{\text{bed}} \rangle \right),$$

with the various transport terms defined in Eqns. (3.24)–(3.26) and Eq.(3.28).

To systematically investigate the influence of the M_2 tidal forcing on the linear stability of associated laterally uniform equilibria, we first determined these equilibria using the bifurcation approach discussed in Deng *et al.* [26]. The system of morphodynamic equations is thus averaged over the width and morphodynamic equilibrium solutions (i.e., not varying on the long timescale) are directly searched for using a continuation procedure (for details, see Deng *et al.* [26]). In Fig. 3.2a the minimum water depth WD_{\min} of the resulting equilibrium is shown as a function of the relative phase between inlet I and II , $\Delta\phi_{M_2}$ (varied between -60° and 60°). The distance of WD_{\min} from inlet I is color coded.

From these results it follows that the number of morphodynamic equilibria and their linear stability to one-dimensional perturbations (denoted as 1D-stability) strongly depend on the relative phase. For $\Delta\phi_{M_2}$ between -2° and -14° (indicated by the labels $L2$ and $L1$, respectively) no morphodynamic equilibrium is found for which both inlets are connected. For the other phases considered, there is always one 1D-stable equilibrium (indicated by the solid line), while for most phases also a 1D-unstable equilibrium exists

(dotted line).

The 1D–stable morphodynamic equilibria are not necessarily 2D–stable, i.e. linearly stable against perturbations with a lateral structure. To illustrate this, we consider three morphodynamic solutions that are stable against one–dimensional perturbations, obtained with $\Delta\phi_{M_2} = -11^\circ$, $\Delta\phi_{M_2} = 15^\circ$ and $\Delta\phi_{M_2} = 19^\circ$ (see the orange, blue and green crosses in Fig. 3.2a, with the laterally uniform equilibrium beds shown in Fig. 3.2b).

In Fig. 3.3a (Fig. 3.3b) the real (imaginary) part of the eigenvalue of the most unstable eigenfunction is shown as a function of the lateral wavenumber $l_n = n\pi L/B$ for three relative phases. The results can be summarized as follows:

- $\Delta\phi_{M_2} = -11^\circ$ (orange lines in Fig. 3.3): all eigenvalues are real. Eigenpatterns associated with $l_n \lesssim 100$ and $l_n \gtrsim 1010$ are linearly stable, while for $100 \lesssim l_n \lesssim 1010$ the eigenmodes are linearly unstable. The maximum growth rate is found for $l_n \approx 550$. The longitudinal structure of the most unstable eigenmode is shown in Fig. 3.3c, indicating that the bed perturbations are nonzero within a region of ~ 10 km around the location where the water depth of the equilibrium is minimal. The spatial structure of the fastest growing bed perturbation superposed on the laterally uniform underlying morphodynamic equilibrium is illustrated in Fig. 3.3e. Here, a width of $B = 6$ km is used, resulting in $n = 18$ (see Eqn. (3.34)). This finding suggests the formation of channels and shoals close to the middle of the inlet system. Note that, because of the linear nature of the considered stability analysis, the amplitude used for the bed perturbation is arbitrary.
- $\Delta\phi_{M_2} = 15^\circ$ (blue lines in Fig. 3.3): all eigenvalues of the most unstable mode are again real. However, in contrast to the previous case, all eigenpatterns have a negative growth rate, indicating that the considered laterally uniform equilibrium bed profile is linearly stable. The solid blue line in Fig. 3.3c shows the longitudinal structure of the bed perturbation associated with the $l_n = 0$ eigenmode.
- $\Delta\phi_{M_2} = 19^\circ$ (green lines in Fig. 3.3): the eigenvalues of the most unstable eigenmode are real for $0 \leq l_n \lesssim 500$. When $l_n \sim 500$, two complex–conjugated eigenmodes, characterised by complex conjugate eigenvalues, become the fastest growing ones. The real part of these complex eigenvalues is positive for $850 \lesssim l_n \lesssim 1750$, whereas the absolute values of the imaginary parts increase for increasing l_n . In Fig. 3.3d the real (solid green) and imaginary (dashed green) parts of the most unstable bed pattern are shown. The bottom perturbations tend to concentrate near inlet I : their spatial extent is ~ 2 km, and the associated bed variations have multiple crests and troughs.

From the above, it follows that the linear stability of 1D–stable laterally uniform equilibria strongly depends on the relative phase difference $\Delta\phi_{M_2}$. In Fig. 3.4 this dependency is further illustrated by analysing the linear stability as a function of $A_{M_2}^H$ and $\Delta\phi_{M_2}$. In this figure, the region in parameter space where no laterally uniform morphodynamic equilibrium exists is indicated by the white color. Linearly stable equilibria correspond to the black colored area. In both the dark and light gray colored areas, the laterally uniform morphodynamic equilibria are linearly unstable. The mechanisms controlling this instability (i.e., for which the growth rate is largest) in the light gray area

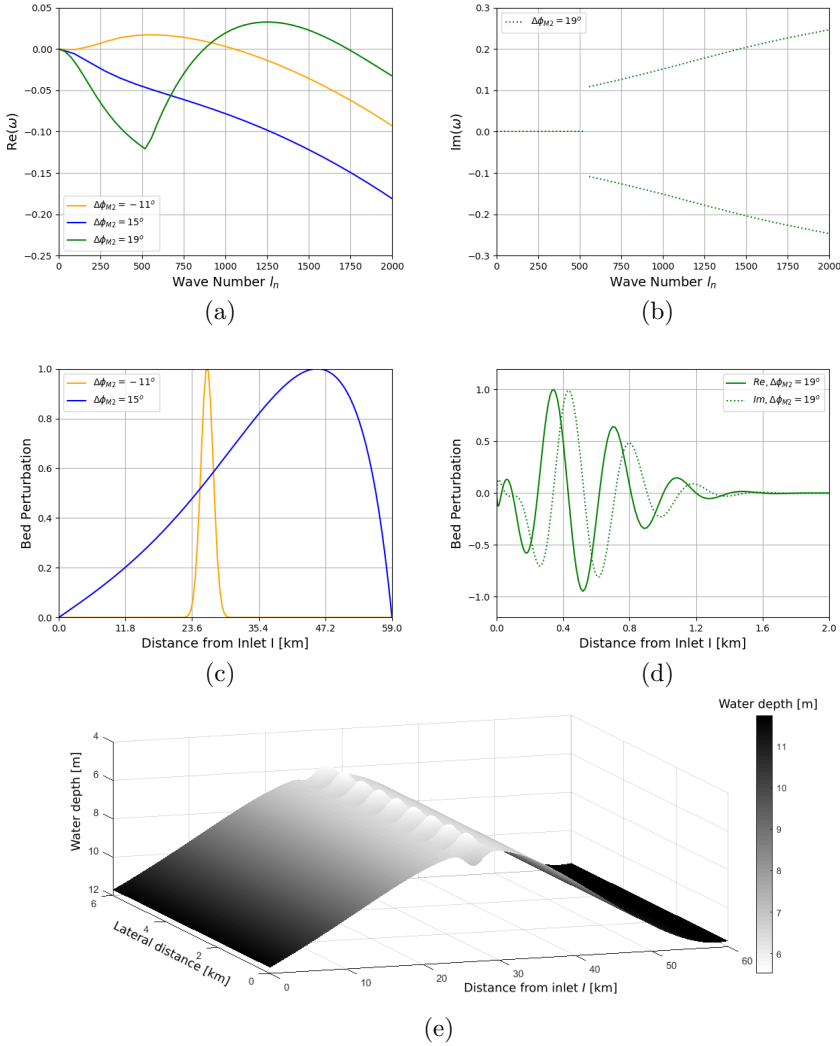


Figure 3.3: The dimensionless growth rate $\Re(\omega)$ and, the associated imaginary part $\Im(\omega)$ (if non-zero) of the most unstable eigenmode (panels (a) and (b), respectively) for $\Delta\phi_{M_2} = -11^\circ$ (orange), $\Delta\phi_{M_2} = 15^\circ$ (blue) and $\Delta\phi_{M_2} = 19^\circ$ (green) are plotted as a function of wave number l_n . The corresponding bed patterns (scaled to have a dimensionless amplitude of one for the real part) of the most unstable eigenmodes for the first two phases are shown in panel (c). The orange solid line denotes the bed pattern associated with $l_n \approx 550$ and $\Delta\phi_{M_2} = -11^\circ$, the blue solid line corresponds to the pattern for $l_n = 0$ and $\Delta\phi_{M_2} = 15^\circ$. In panel (d), corresponding to $\Delta\phi_{M_2} = 19^\circ$, the green solid (dotted) line indicates the real (imaginary) part of the complex bed eigenfunction with mode number $l_n \approx 1200$. Panel (e) shows the spatial structure of the bed perturbation for $\Delta\phi = -11^\circ$.

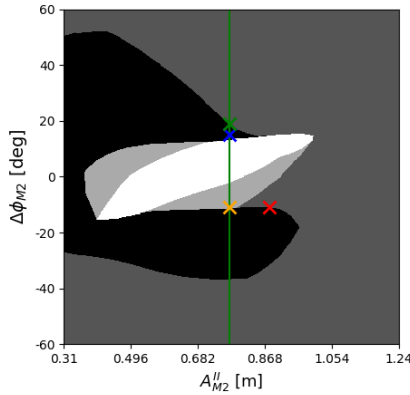


Figure 3.4: Linear stability of stable laterally uniform morphodynamic equilibria as a function of the M_2 tidal amplitude at inlet II (horizontal axis) and the relative phase (vertical axis). The white area corresponds to the absence of any laterally uniform equilibrium configuration. Black, dark-gray and light-gray regions indicate where linearly stable, diffusively unstable and advectively unstable morphodynamic equilibria are found, respectively. If the considered equilibrium configuration is unstable, the mechanism resulting in the largest positive growth rate is assumed to control the instability mechanism. The crosses indicate the experiments discussed in detail in the main text.

are due to diffusive transport, whereas advective transport dominates in the dark gray region.

To illustrate the two instability mechanisms, we again consider the results obtained for $\Delta\phi_{M_2} = -11^\circ$ and $\Delta\phi_{M_2} = 19^\circ$ with the default A_{M_2} amplitudes. In the first case instability is due to a diffusive mechanism, while in the latter case instability is due to an advective mechanism.

DIFFUSIVELY DOMINATED INSTABILITY MECHANISM

To determine the prevailing instability mechanisms, we consider the divergence of the various transport contributions for the relative phase $\Delta\phi_{M_2} = -11^\circ$ and $l_n \sim 550$. The longitudinal bed profile associated with the most unstable eigenfunction is shown in Fig. 3.3c, orange line. The associated divergences of the classical diffusive flux $\langle \mathbf{F}_{\text{diff}}^{00} \rangle$, the topographically induced diffusive flux $\langle \mathbf{F}_{\text{topo}}^{00} \rangle$, the internally generated advective flux $\langle \mathbf{F}_{\text{adv}}^{20} \rangle$ and the total flux $\langle \mathbf{F} \rangle$, evaluated at $y = 0$, are shown in Fig. 3.5a. The classical diffusive transport is destabilizing, i.e., it leads to a convergence of sediment near the tops of the bed perturbation, while the topographically induced diffusive transport is stabilizing causing a divergence of the transport at the maxima of bed perturbation. These two transport terms are much bigger than the other two contributions, and they almost balance. To evaluate the net diffusive effect, the divergence of the total diffusive transport defined as $\nabla \cdot (\langle \mathbf{F}_{\text{diff}}^{00} \rangle + \langle \mathbf{F}_{\text{topo}}^{00} \rangle)$ is compared with the divergence of the internally generated advective and total transport in Fig. 3.5b. It appears that the combined contribution of the different diffusive transport terms is still dominant; the advective contribution only modifies the divergence of the total transport. Hence the instability mechanism is a *diffusive* one. This observation is corroborated by experiments in which

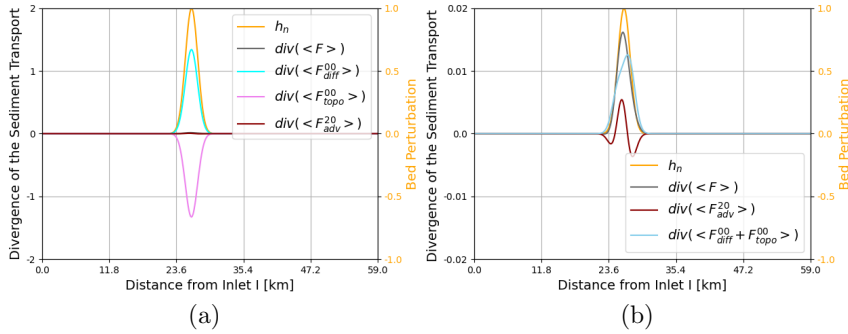


Figure 3.5: Dimensionless divergences of the various transport contributions for $\Delta\phi_{M_2} = -11^\circ$ and $l_n \sim 550$, together with the associated bed perturbation (orange line) at $y = 0$. Panel (a) shows all divergences separately, while in Panel (b) the two diffusive contributions are combined.

only the diffusive transport is considered: similar eigenpatterns, resulting from the same instability mechanism, are found (see Appendix C, Fig. C.3). The driving physical mechanism is described in detail in Schuttelaars and de Swart [15] with the stability effect of the topographically induced diffusive transport dominating over that of bedload transport (see also Hepkema *et al.* [37] and Appendix C).

Whether a bed perturbation is linearly stable or unstable strongly depends on the lateral wave number l_n considered, see the linear stability curve in Fig. 3.3a: for stable (unstable) eigenfunctions, the stabilizing effects of the divergences of the topographically induced transports dominate over (are dominated by) those of the destabilizing classical diffusive ones.

ADVECTIVELY DOMINATED INSTABILITY MECHANISM

The eigenvalue for the case with $\Delta\phi_{M_2} = 19^\circ$ and $l_n \sim 1200$ is complex (Figs. 3.3a and 3.3b). This implies that also the eigenfunction consists of a real and an imaginary part. The real and imaginary part of the fastest growing bed perturbation are plotted in Fig. 3.6a and Fig. 3.6c as the green solid and green dotted lines. In Figs. 3.6a and 3.6c the associated divergences of the various transport terms are shown. As in the previous case, the convergences of diffusive transports are dominant and approximately balance each other. The relative importance of the divergences of the advective and total transports is larger in this case than in the case discussed in Sect. 3.4.1. Again, by considering the diffusive transports together, we can focus on the relative importance of the diffusive and advective contributions to the total divergence. From Figs. 3.6b and 3.6d, it follows that the divergences of the advective transport are larger than those of the total diffusive transport, and is very similar to the divergence of the total transport. This suggests that the instabilities are mainly driven by advective processes, hence the instability mechanism is *advective*. This is confirmed by the experiments discussed in Appendix C, in which the advective transport was neglected and consequently the instabilities observed in the present section were not found.

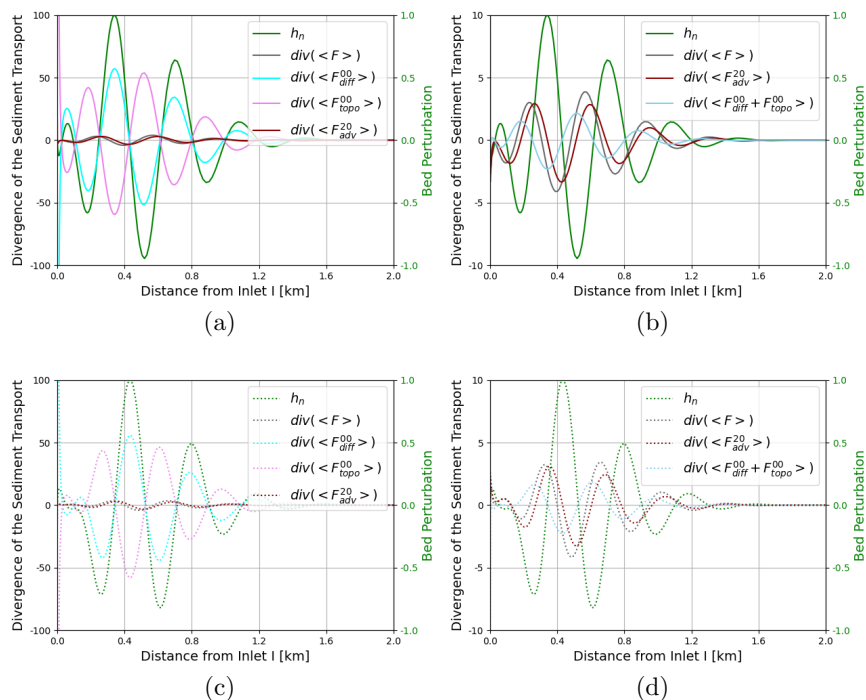


Figure 3.6: Dimensionless divergences of the various transport contributions for $\Delta\phi_{M_2} = 19^\circ$ and $I_n \sim 1200$, together with the associated bed perturbation (green line) at $y = 0$. Panels (a) and (c) show the real and imaginary part of the divergences separately, while in Panels (b) and (d) the two diffusive contributions are combined.

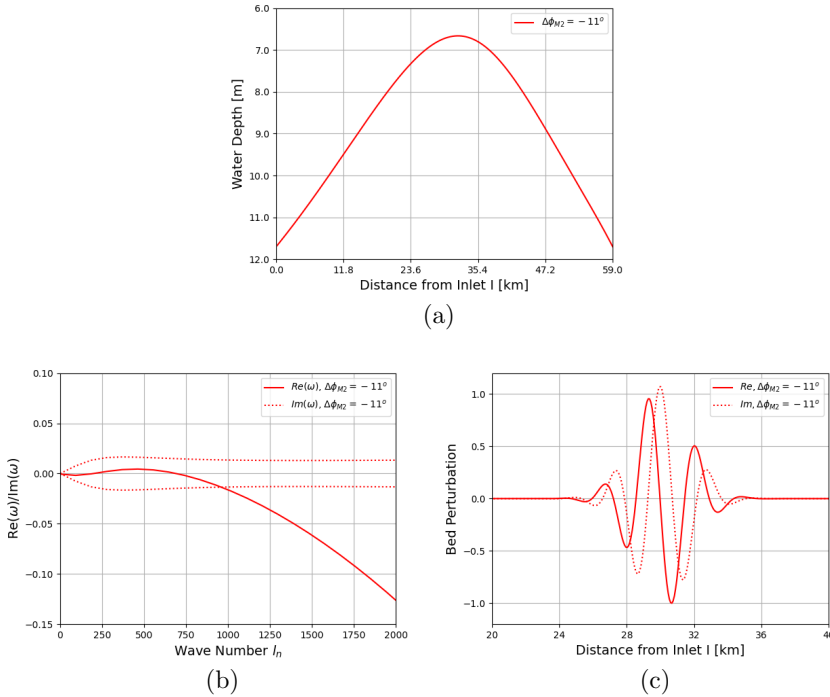


Figure 3.7: (a) Laterally uniform morphodynamic equilibrium obtained with $A_{M_2}^H = 0.87$ m and $\Delta\phi_{M_2} = -11^\circ$. (b) The real and imaginary parts of the eigenvalue associated with the most unstable eigenfunction are plotted as a function of the lateral wave number. (c) Bed pattern of the most unstable eigenfunction.

It should also be noted that the divergences associated with the real and imaginary parts of the eigenfunction are out of phase with the bed pattern associated with this eigenfunction. This is consistent with the fact that these bed patterns do not only grow in time, but are also periodic in time, with the angular frequency given by $\Im(\omega)$.

The location where the fastest growing eigenpatterns have appreciable amplitudes coincides with a local minimum in water depth of the underlying width-averaged equilibrium. In the previous example, the minimum water depth was found at inlet I , and the linearly fastest growing mode was also observed close to that inlet. When changing the parameters to $A_{M_2}^H = 0.87$ m and $\Delta\phi_{M_2} = -11^\circ$ (red cross in Fig. 3.4) the corresponding morphodynamic equilibrium configuration has a local minimum in water depth at 30 km from inlet I (Fig. 3.7a). This laterally uniform equilibrium is linearly unstable (Fig. 3.7b). The spatial structure of the bed pattern associated with the fastest growing eigenmode ($l_n \sim 470$) is shown in Fig. 3.7c. The instability mechanism is still dominated by convergences of internally generated advective transports (not shown). The largest amplitudes of the eigenfunctions are also found at 30 km from inlet I , coinciding with a local minimum in water depth of the underlying morphodynamic equilibrium.

3.4.2. ALL FORCINGS INCLUDED

In this section, the water motion is forced by both the M_2 and M_4 tidal constituents, prescribed at each inlet, and a discharge Q at inlet II . Since all forcings are included, all contributions in the bottom evolution equation (3.18) have to be taken into account when calculating the morphodynamic equilibria and their linear stability.

In this section the influence of the relative M_2 phase $\Delta\phi_{M_2}$ on the stability of the possible width–averaged equilibria is investigated by changing the M_2 phase at inlet II . All other parameters maintain their default values, reported in Tab. 3.2. To assess this influence, first the associated laterally uniform morphodynamic equilibria have to be obtained. Similar to the numerical experiments described in Sect. 3.4.1, these equilibria are computed using a continuation technique, which results in the bifurcation diagram shown in Fig. 3.8a. In this figure, the minimum water depth of the morphodynamic equilibria is shown as a function of $\Delta\phi_{M_2}$. In the interval $5^\circ \lesssim \Delta\phi_{M_2} \lesssim 25^\circ$ no morphodynamic equilibria exist for which the two inlets are connected. For $-60^\circ \leq \Delta\phi_{M_2} \lesssim 5^\circ$ and $25^\circ \leq \Delta\phi_{M_2} \leq 60^\circ$ two morphodynamic equilibria are found, one 1D–stable (solid line) and the other one 1D–unstable (dashed line).

The two–dimensional stability of the 1D–stable equilibria depends on $\Delta\phi_{M_2}$. For values of $\Delta\phi_{M_2}$ between -17° and 3° , the 1D–stable equilibria are also linearly stable against two–dimensional perturbations (not shown). For all other $\Delta\phi_{M_2}$, the laterally uniform equilibria that were 1D–stable turn out to be linearly unstable against two–dimensional perturbations (not shown). All instabilities are dominated by advective transport, due to both internally generated and externally prescribed advection. To illustrate this, we consider $\Delta\phi_{M_2} = 31^\circ$. The associated equilibrium bed profile is shown in Fig. 3.8b. The real and imaginary part of the eigenvalues are shown in Fig. 3.8c. From this figure it follows that eigenfunctions with lateral wave number l_n between 400 and 2750 have a positive growth rate, with a maximum growth rate found for $l_n \sim 1100$. This maximum growth rate increases very quickly for increasing $\Delta\phi_{M_2}$ and is associated with ever increasing lateral mode number (not shown). The real and imaginary part of the associated eigenfunction are shown in Fig. 3.8d, indicating that the bed perturbations are located close to inlet I .

In Fig. 3.9 the various contributions to the real (panels a and b) and imaginary (panels c and d) part of the divergence of suspended sediment transports are shown. As observed in Sect. 3.4.1, the diffusive contributions dominate when considered separately, but when adding them together all contributions are of the same order of magnitude. From Figs. 3.9b and 3.9d it appears that the total diffusive transports $\langle \mathbf{F}_{\text{diff}}^{00} \rangle + \langle \mathbf{F}_{\text{topo}}^{00} \rangle$ and the advective transport due to external overtides $\langle \mathbf{F}_{\text{adv}}^{11} \rangle$ are in phase, except near the entrance where the term $\langle \mathbf{F}_{\text{adv}}^{11} \rangle$ dominates the transport. All contributions are of the same order of magnitude, indicating that the advective transport mechanism, due to both internally generated and externally prescribed overtides, is important for these instabilities.

3.5. DISCUSSION AND CONCLUSIONS

In this paper, we show that stable laterally uniform morphodynamic equilibria of rectangular double–inlet systems can become linearly unstable when two dimensional per-

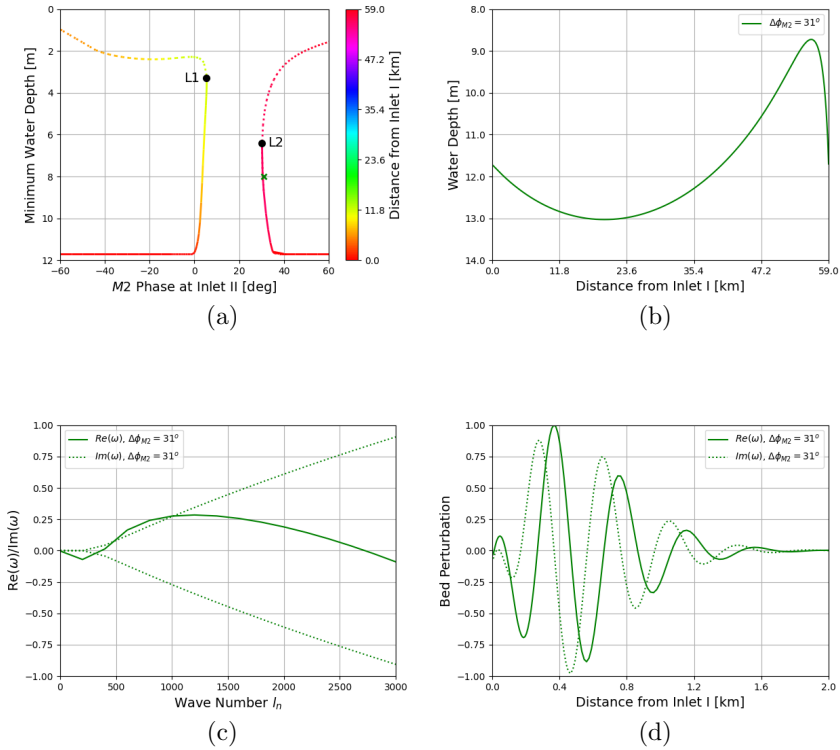


Figure 3.8: Panel (a) shows WD_{\min} , the minimum water depth of laterally uniform equilibrium bed profiles, with the location of WD_{\min} color-coded. Panel (b) shows the laterally uniform equilibrium bed profile for $\Delta\phi_{M_2} = 31^\circ$, (c) the real and imaginary parts of the eigenvalue associated with the most unstable eigenfunction as a function of the lateral wave number and (d) the bed perturbations of the most unstable eigenfunction.

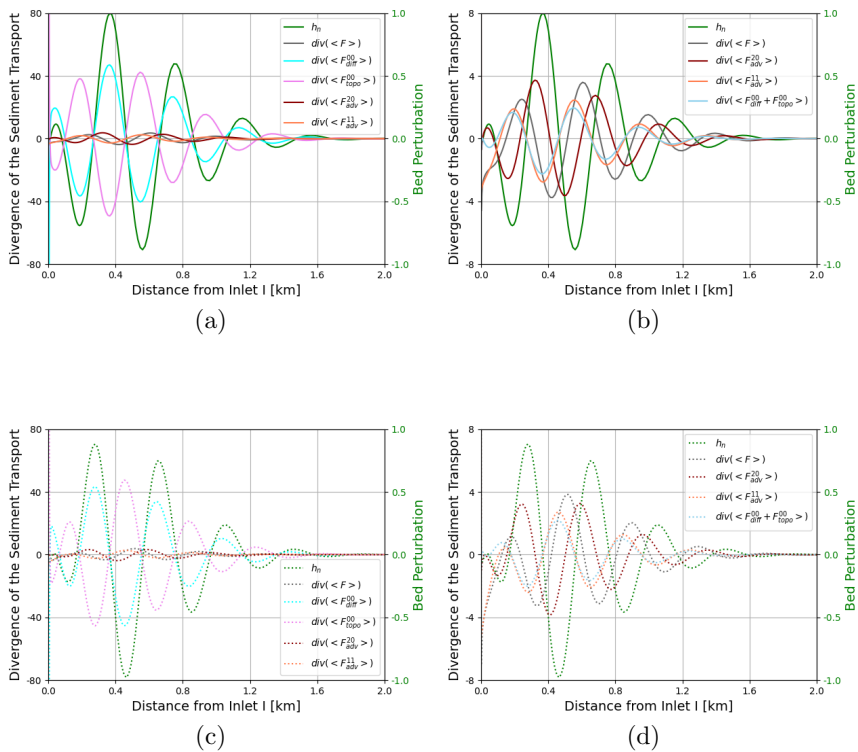


Figure 3.9: Dimensionless divergences of the various sediment transport contributions for $\Delta\phi_{M_2} = 31^\circ$ and $l_n \sim 1100$, together with the associated bed perturbation (green line) at $y = 0$. Panels (a) and (c) show the real and imaginary part of the divergences separately, while in panels (b) and (d) the two diffusive contributions are summed together.

turbations are considered. The instability leads to the formation of channels and shoals as a result of a positive feedback mechanism between the tidal flow and the bottom dynamics. The water motion is described by the shallow water equations and is driven by the M_2 and M_4 tidal constituents, prescribed at both inlets, and by a constant discharge, prescribed at one of the inlets. Sediment is transported both as suspension load due to advective and diffusive processes and as bedload due to bedslope effects. Coriolis circulations are neglected owing to the relatively small size of the total system. Since the tidal time scale is much shorter than the morphodynamic time scale, the method of averaging is applied to describe separately the dynamics of the water motion and the bottom. Owing to the assumption of a rectangular inlet system, no direct comparison can be made with observations of real world systems. However, the result study provides valuable insights for better understanding the various mechanisms causing the instability of double-inlet systems.

When the water motion is forced only by an M_2 tidal constituent, both advective and diffusive processes contribute to tidally averaged suspended sediment transport. The advective transport arises from nonlinear interactions between the directly forced signals. Two different sediment transport mechanisms are identified: for diffusive sediment transport the classical one related to spatial gradients in the depth-integrated tidally-averaged suspended sediment concentrations and a topographically induced suspended sediment transport associated with gradients in the bed level. Keeping the amplitude and phase of the M_2 tidal forcing at one inlet fixed, and varying these parameters for the other inlet, it is found that there exists an area in the amplitude-phase plane where no laterally uniform morphodynamic equilibria exist for which both inlets are still connected. In regions of the parameter space where such equilibria exist, the equilibrium can be stable against two-dimensional perturbations, linearly unstable due to convergences of diffusive transport terms, or linearly unstable due to convergences related to advective terms.

When the morphodynamic equilibrium becomes unstable due to diffusive sediment transport, the classical diffusive mechanism destabilizes laterally uniform morphodynamic equilibria, while the sediment diffusion related to topographic gradients has a stabilizing effect. The relative importance of these mechanisms determines whether a laterally uniform equilibrium is linearly stable or unstable. This instability mechanism is similar to the one described by Schuttelaars and de Swart [15], Ter Brake and Schuttelaars [19] for single-inlet systems. The eigenvalues are all real, implying an exponential growth in time. When advective sediment transport contributes dominantly to linear instability, the eigenvalues are found to be complex-valued. This implies that bedforms do not only grow in time, but also migrate. In this case divergences of both advective and diffusive transports contribute significantly to the linear growth of the bed perturbations.

When including external overtides and a residual discharge, the dependency on the relative M_2 phase between the M_2 forcing at the two inlets is studied, using default values for all other parameters. In particular, it was found that either no morphodynamic equilibria that connect both inlets exists or equilibria are unstable due to the divergences of both advective and diffusive transport terms which are of equal importance. The advective transport is a result of internally generated overtides as well as of the prescribed

external overtide and sediment discharge.

In all cases the bed perturbations are found to have their largest amplitudes in the regions where the water depth of the considered morphodynamic equilibrium has a local minimum. This observation is in line with the remark of Schuttelaars and de Swart [15] that a necessary condition for instability is the presence of bottom frictional torques. In the present model, a similar conclusion can be drawn: when reducing the friction parameter below a critical value, the laterally uniform morphodynamic equilibrium is always stable. Conversely, when introducing the effects of bottom friction, the underlying equilibria become unstable, both when the sediment transport is dominated by diffusive and advective mechanisms.

The linear instabilities found in this paper lead to the initial formation of channels and shoals in the shallower regions of the tidal basin system. The location of these patterns coincides with results obtained in numerical models and laboratory experiments (Hibma *et al.* [12], Van der Wegen and Roelvink [14], Leuven and Kleinhans [39]). To compare results beyond the initial stage of channel–shoal formation, a nonlinear analysis has to be performed. This will be the topic of a subsequent study.

REFERENCES

- [1] J. Mulhern, C. Johnson, and J. Martin, *Is barrier island morphology a function of tidal and wave regime?* *Marine Geology* **387**, 74 (2017).
- [2] H. E. de Swart and J. T. F. Zimmerman, *Morphodynamics of tidal inlet systems*, Annual Review of Fluid Mechanics **41**, 203 (2009).
- [3] D. J. Glaeser, *Global distribution of barrier islands in terms of tectonic setting*, Journal of Geology **86**, 283 (1978).
- [4] M. L. Stutz and O. H. Pilkey, *Open-ocean barrier islands: Global influence of climatic, oceanographic, and depositional settings*, Journal of Coastal Research **27**, 207 (2011).
- [5] A. P. Oost, P. Hoekstra, A. Wiersma, B. Flemming, E. J. Lammerts, M. Pejrup, J. Hofstede, B. Van der Valk, P. Kiden, J. Bartholdy, M. Van der Berg, P. C. Vos, S. de Vries, and Z. B. Wang, *Barrier island management: Lessons from the past and directions for the future*, Ocean & Coastal Management **68**, 18 (2012).
- [6] R. A. McBride, M. R. Byrnes, and M. W. Hiland, *Geomorphic response-type model for barrier coastlines: A regional perspective*, Marine Geology **126**, 143 (1995).
- [7] A. J. F. Van der Spek, *Tidal asymmetry and long-term evolution of holocene tidal basins in the Netherlands: Simulation of paleo-tides in the Scheldt estuaries*, Marine Geology **141**, 71 (1997).
- [8] R. W. Dalrymple and R. N. Rhodes, *Chapter 13 estuarine dunes and bars*, in *Geomorphology and Sedimentology of Estuaries*, Developments in Sedimentology, Vol. 53, edited by G. Perillo (Elsevier, 1995) pp. 359–422.

- [9] C. G. Israel and D. W. Dunsbergen, *Cyclic morphological development of the ameland inlet, the netherlands*, River, Coastal and Estuarine Morphodynamics **1**, 701 (2000).
- [10] R. Marciano, Z. Wang, A. Hibma, H. De Vriend, and A. Defina, *Modeling of channel patterns in short tidal basins*, *Journal of Geophysical Research* **110** (2005), 10.1029/2003JF000092.
- [11] A. D'Alpaos, S. Lanzoni, M. Marani, and A. Rinaldo, *Landscape evolution in tidal embayments: Modelling the interplay of erosion, sedimentation, and vegetation dynamics*, *Journal of Geophysical Research* **112**, F01008 (2007).
- [12] A. Hibma, H. J. de Vriend, and M. J. F. Stive, *Numerical modelling of shoal pattern formation in well-mixed elongated estuaries*, *Estuarine, Coastal and Shelf Science* **57**, 981 (2003).
- [13] A. Hibma, H. M. Schuttelaars, and H. J. Vriend, *Initial formation and evolution of channel–shoal patterns in estuaries*, *Continental Shelf Research* **24**, 1637 (2004).
- [14] M. Van der Wegen and J. A. Roelvink, *Long-term morphodynamic evolution of a tidal embayment using a two-dimensional process-based model*, *Journal of Geophysical Research* **7**, C03016 (2008).
- [15] H. M. Schuttelaars and H. E. de Swart, *Initial formation of channels and shoals in a short tidal embayment*, *Journal of Fluid Mechanics* **386**, 15 (1999).
- [16] H. M. Schuttelaars and H. E. de Swart, *An idealized long-term morphodynamic model of a tidal embayment*, *European Journal of Mechanics, B/Fluids* **15**, 55 (1996).
- [17] S. M. van Leeuwen and H. E. de Swart, *The effect of advective processes on the morphodynamic stability of short tidal embayments*, *Physics and Chemistry of the Earth (B)* **26**, 735 (2001).
- [18] S. M. van Leeuwen and H. E. de Swart, *Effect of advective and diffusive sediment transport on the formation of local and global bottom patterns in tidal embayments*, *Ocean Dynamics* **54**, 441 (2004).
- [19] M. C. Ter Brake and H. M. Schuttelaars, *Channel and shoal development in a short tidal embayment: An idealized model study*, *Journal of Fluid Mechanics* **677**, 503 (2011).
- [20] M. Duran-Matute, T. Gerkema, G. J. de Boer, J. J. Nauw, and U. Grawe, *Residual circulation and freshwater transport in the Dutch Wadden Sea: a numerical modelling study*, *Ocean Science* **10**, 611 (2014).
- [21] M. Sassi, M. Duran-Matute, T. van Kessel, and T. Gerkema, *Variability of residual fluxes of suspended sediment in a multiple tidal–inlet system: the Dutch Wadden Sea*, *Ocean Dynamics* **65**, 1321 (2015).

- [22] P. Salles, G. Voulgaris, and D. G. Aubrey, *Contribution of nonlinear mechanisms in the persistence of multiple tidal inlet systems*, *Estuarine, Coastal and Shelf Science* **65**, 475 (2005).
- [23] A. Pacheco, A. Vila-Concejo, O. Ferreira, and J. A. Dias, *Assessment of tidal inlet evolution and stability using sediment budget computations and hydraulic parameter analysis*, *Marine Geology* **247**, 104 (2008).
- [24] G. Seminara, M. Bolla Pittaluga, N. Tambroni, and V. Garotta, *Open problems in modelling the long-term morphodynamic evolution of Venice lagoon*, *Flooding and Environmental Challenges for Venice and its Lagoon*, 345 (2005).
- [25] N. Tambroni and G. Seminara, *Are inlets responsible for the morphological degradation of venice lagoon?* *Journal of Geophysical Research: Earth Surface* **111** (2006), [10.1029/2005JF000334](https://doi.org/10.1029/2005JF000334).
- [26] X. Deng, C. Meerman, T. Boelens, T. De Mulder, P. Salles, and H. M. Schuttelaars, *Morphodynamic equilibria in double-inlet systems: existence and stability*, *Journal of Geophysical research* **126**, 2021JF006266 (2021).
- [27] G. T. Csanady, *Circulation in the Coastal Ocean* (Reidel, 1982).
- [28] H. Lorentz, *Het in rekening brengen van den weerstand bij schommelende vloeistofbewegingen*, *De Ingenieur*, 695 (1922).
- [29] J. T. F. Zimmerman, *On the Lorentz linearization of a nonlinearly damped tidal Helmholtz oscillator*, *Proceedings KNAW* **95**, 127 (1992).
- [30] M. C. Ter Brake and H. M. Schuttelaars, *Modeling equilibrium bed profiles of short tidal embayment. On the effect of the vertical distribution of suspended sediment and the influence of the boundary conditions*, *Ocean Dynamics* **60**, 183 (2010).
- [31] K. R. Dyer, *Coastal and estuarine sediment dynamics* (John Wiley and Sons, 1986).
- [32] H. M. Schuttelaars and H. E. de Swart, *Multiple morphodynamic equilibria in tidal embayments*, *Journal of Geophysical Research* **105**, 105 (2000).
- [33] C. Meerman, V. Rottschäfer, and H. Schuttelaars, *Influence of geometrical variations on morphodynamic equilibria in short tidal basins*, *Ocean Dynamics* **69**, 221 (2019).
- [34] A. Falqués, A. Montoto, and V. Iranzo, *Bed-flow instability of the longshore current*, *Cont. Shelf Res.* **15**, 1927 (1996).
- [35] J. A. Sanders and F. Verhulst, *Averaging methods in nonlinear dynamical systems* (Spring Verlag, New York, 1985).
- [36] M. Krol, *On the averaging method in nearly time-periodic advection-diffusion problems*, *SIAM Journal on Applied Mathematics* **51**, 1622 (1991).
- [37] T. Hepkema, H. De Swart, and H. Schuttelaars, *The sensitivity of tidal bar wavelength to channel width*, *J. Geophys. Res. Earth Surf.* **124**, 2417 (2019).

- [38] H. Ridderinkhof, *Tidal and residual flows in the western dutch wadden sea i1: An analytical model to study the constant flow between connected tidal basins*, Netherlands Journal of Sea Research **22**, 185 (1988).
- [39] J. R. F. W. Leuven and M. G. Kleinans, *Incipient tidal bar and sill formation*, Journal of Geophysical Research **124**, 1762 (2019).

4

THE CHANNEL AND SHOAL PATTERNS IN SHORT DOUBLE-INLET SYSTEMS

Channel–shoal patterns are common features in back–barrier basins of many barrier coasts. These bedforms are very sensitive to internal and external forcing conditions and their changes. In particular, for short double–inlet systems of uniform width it is here shown that small patterns develop due to a positive feedback between water motion, sediment transport and bedforms. The water motion is governed by the depth–averaged (2DH) shallow water equations forced by a prescribed laterally uniform sea surface elevation at the seaward sides. The suspended sediment is transported only by diffusion (including effects of topographic variations), with source and sink terms, while the bed evolution is controlled by the divergence of the suspended sediment transport. The resulting morphodynamic equilibria, i.e., bed profiles that do not evolve on the morphodynamic time scale anymore, are systematically obtained using a dynamical system's approach in which the equilibria are sought for without employing time integration.

For all systems considered in this chapter, laterally uniform equilibria were found characterised by a shallow region in between the two inlets connected to the sea. These laterally uniform morphodynamic equilibria become unstable when the friction is sufficiently large. For larger widths, the critical value of the friction for which the laterally uniform morphodynamic equilibria become linearly unstable decreases. For friction values larger than the critical value, new linearly stable morphodynamic equilibria exist that are characterised by channel–shoal patterns located in shallow regions. The number of channels and shoals depends sensitively on the width of the double–inlet system and the frictional strength. It is found that the patterns forming when considering values of the parameters close to the critical ones do not necessarily predict the number of channels and shoals for values of the parameters far from the critical ones.

4.1. INTRODUCTION

Barrier coasts consist of one or more back-barrier basins separated from the near sea by barrier islands and connected to the open sea by tidal inlets (de Swart and Zimmerman [1]). This type of coasts is common along the world's coastlines (Stutz and Pilkey [2], Mulhern *et al.* [3]). Examples are the Wadden Sea along the Dutch, German and Danish coast (Oost *et al.* [4]), the Ria Formosa in south Portugal (Salles *et al.* [5], Pacheco *et al.* [6]) and Venice Lagoon in Italy (Tambroni and Seminara [7]).

In the back-barrier basins, fractal-like patterns are often observed: large channels starting at the seaward side branch into smaller channels. In the Wadden Sea it has been shown by Cleveringa and Oost [8] that these networks can be characterised as three to four times branching networks. These complex channel and shoal systems are a result of strong interactions between water motion, sediment transport and the bed topography.

To study the formation of these channel-shoal systems in back-barrier basins, morphodynamic models are typically employed. In single inlet systems (in which one inlet channel connects the back-barrier basin to the open sea) these channel-shoal patterns have been found to form in both process-based idealized and high complexity morphodynamic models. One of the first results obtained with a high complexity model was presented by Wang *et al.* [9] who used a 2DH complex process-based model to reproduce the channel-shoal patterns in the Frisian inlet system, one of the back-barrier basins in the Dutch part of the Wadden Sea. Since then, this work has been extended using numerical models with a varying level of complexity (Marciano *et al.* [10], D'Alpaos *et al.* [11], Van der Wegen and Roelvink [12], Zhou *et al.* [13], Styles *et al.* [14]), see also the review of Dissanayke *et al.* [15]. Most of the numerical experiments performed in these papers start from an idealized bathymetry. For example, Van der Wegen and Roelvink [12] simulated the bed evolution in a rectangular basin, starting from a constantly sloping bed profile. They found that channels and shoals first develop in the relatively shallow part near the landward end of the basin. Only after approximately 50 years bedforms appear at the seaward end of the rectangular basin.

Concerning idealized models, they were initially used to assess the physical mechanisms that result in the initial formation of channels and shoals (Schuttelaars and de Swart [16], van Leeuwen and de Swart [17, 18], Ter Brake and Schuttelaars [19]). Ter Brake and Schuttelaars [19] found that the initial formation of channels and shoals took place near the landward boundary, in agreement with the simulation model results of Van der Wegen and Roelvink [12]. Recently, some advances have been made in obtaining finite amplitude channel-shoal patterns using exploratory models (Ter Brake [20], Dijkstra *et al.* [21], Boelens [22]).

The results discussed above are all obtained for single inlet systems. However, recent studies have clearly shown that there is a strong exchange of water (Duran-Matute *et al.* [23]) and sediment (Sassi *et al.* [24]) between the various subbasins of multiple-inlet systems. This strongly suggests that to understand, model and predict the morphodynamic evolution of these systems, including the observed channel-shoal systems, the interactions between sub-basins have to be taken into account by considering these sub-systems as part of a multiple inlet system. However, the morphodynamic evolution of multiple inlet systems has not received much attention in the literature. Using a simulation model, Dastgheib *et al.* [25] analysed the long-term sediment transport and bot-

tom evolution for a double-inlet system, resulting in the development of channel-shoal systems in the back-barrier basin. After simulating 2,000 years, the system was assumed to be close to a morphodynamic equilibrium with both inlets still open. A detailed analysis of the physical mechanisms responsible for the observed morphodynamic equilibrium as well as an assessment of the sensitivity to parameters variations are however very challenging when using this type of models. To obtain such information, typically exploratory models are used. However, at this point no idealized models exist that allow for such an analysis.

In view of this, the aim of the present study is to develop an exploratory model for a double-inlet system in which both the tidal inlets and back-barrier basin are morphodynamically active. The model will be an extension of the model presented in Dijkstra *et al.* [21] to double-inlet systems. Using this newly developed model, the existence and stability of morphodynamic equilibria possibly with an appreciable lateral variation will be systematically investigated, thus complementing the results of chapter 2 and 3. As a first step, a rectangular geometry will be considered. The influence of the strength of the bed friction and the width on the resulting channel-shoal patterns will be systematically investigated using tools from dynamical system theory.

In section 2 the equations governing the water motion, sediment transport and bed evolution are presented. This system of equations is scaled and analyzed using an asymptotic method in section 3. Furthermore, numerical methods to obtain morphodynamic equilibria, to analyze linear stability and bifurcation are introduced in this section. In section 4 resulting morphodynamic equilibria and their linear stability are studied. In section 5 the results are discussed, and in the final section conclusions are presented.

4.2. MODEL DESCRIPTION

The morphodynamic model, derived in this section, is specifically geared toward the investigation of the formation of channels and shoals in double-inlet systems in which the dominant instability mechanism is a diffusive one. Following Deng *et al.* [26], this implies that only the leading order tidal forcing (Sect. 4.2.2) and only diffusive sediment transport (Sect. 4.2.3) is considered. Before discussing these model equations, first the geometry of the system is introduced in Sect. 4.2.1; in Sect. 4.2.4 the associated bed evolution equation is discussed.

4.2.1. GEOMETRY

The geometry under consideration is that of a rectangular tidal inlet system with prescribed length L and width B (see Fig. 4.1a for a top view). The coordinate in the along basin direction is denoted by x and in the cross basin direction by y . The tidal inlet system is connected to the open sea at $x = 0$ and $x = L$ respectively. The coastal boundaries of the rectangular tidal basin, located at $y = 0$ and $y = B$, are assumed to be both impermeable to the transport of water and sediment. Furthermore, they are assumed to be non-erodible.

The free surface is described by the equation $z = \hat{\zeta}$, with the undisturbed free surface located at $z = 0$. The undisturbed width-averaged water depth at $x = 0$ is denoted by H^I , and at $x = L$ by H^{II} (see Fig. 4.1b for a side view). In the following both undisturbed water

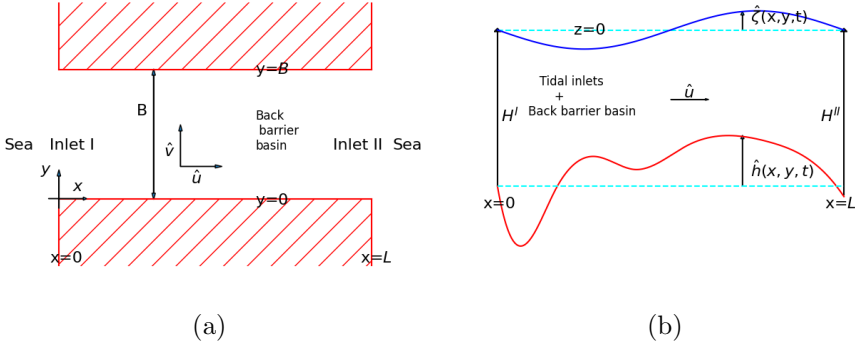


Figure 4.1: A sketch of a tidal embayment connected to the open sea at both ends. Panel (a) shows a top view of the schematized double-inlet system with a uniform width. The longitudinal and lateral velocities are denoted by \hat{u} and \hat{v} , respectively. Panel (b) shows a cross-sectional view of the double-inlet system, with the undisturbed width-averaged depth at inlet *I* denoted by H^I and the undisturbed width-averaged depth at inlet *II* denoted by H^{II} . The bed profile is denoted by $\hat{h}(x, y, t)$, and the surface elevation by $\hat{\zeta}(x, y, t)$.

depths are assumed to be laterally uniform. The erodible bottom, which is assumed to consist of sandy material with a single grain size $d_{50} = 2 \times 10^{-4}$ m, is located at $z = \hat{h} - H^I$. Here H^I is used as reference depth and \hat{h} is the local bed elevation measured from the reference depth. Hence the instantaneous local water depth is given by $H^I - \hat{h} + \hat{\zeta}$.

4.2.2. HYDRODYNAMIC EQUATIONS

Both the length and width of the tidal basins under consideration are much larger than the reference water depth, allowing the water motion to be described by the depth-averaged shallow water equations for a homogenous fluid. Since the width is typically much smaller than the Rossby deformation radius, Coriolis effects can be neglected. Moreover, the ratio of the amplitude of the M_2 tidal constituent and the water depth is much smaller than one, which allows the use of a perturbation approach to solve the equations (Schuttelaars and de Swart [27], Meerman *et al.* [28]). From this analysis, it follows that at leading order the nonlinear terms can be neglected such that the water motion at leading order is described by the linearized shallow water equations:

$$\hat{\zeta}_t + \nabla \cdot [(H^I - \hat{h})\hat{\mathbf{u}}] = 0, \quad (4.1a)$$

$$\hat{\mathbf{u}}_t + g\nabla\hat{\zeta} + \frac{r_*\hat{\mathbf{u}}}{H^I - \hat{h}} = 0. \quad (4.1b)$$

Here, the horizontal velocity vector is denoted by $\hat{\mathbf{u}} = (\hat{u}, \hat{v})$ with \hat{u} the velocity in longitudinal direction and \hat{v} in lateral direction. Time is denoted by t , and g denotes the gravitational acceleration. Subscripts denote a derivative with respect to that variable, and the horizontal derivative operator is denoted by $\nabla = (\partial_x, \partial_y)$. The inner product is

denoted by a dot. A linearized formulation of the bottom friction is used with the bottom friction coefficient defined as $r_* = 8Uc_d/3\pi$ (see Lorentz [29] and Zimmerman [30]). In this expression, U is a characteristic velocity scale (which will be introduced in section 4.3.1) and c_d a drag coefficient.

Assuming that the *deep sea limit* (Roos and Schuttelaars [31]) is a good approximation at the seaward boundaries, the sea surface elevations $\hat{\zeta}$ at the entrances can be prescribed as

$$\hat{\zeta} = A_{M_2}^I \cos(\sigma t - \phi_{M_2}^I) \quad \text{at } x = 0, \quad (4.2a)$$

$$\hat{\zeta} = A_{M_2}^{II} \cos(\sigma t - \phi_{M_2}^{II}) \quad \text{at } x = L. \quad (4.2b)$$

Here, the constants $A_{M_2}^I$ and $A_{M_2}^{II}$ denote the amplitudes of the M_2 tide at the seaward sides of inlet I and II , respectively. Their corresponding phases are given by $\phi_{M_2}^I$ and $\phi_{M_2}^{II}$. The angular frequency of the M_2 tidal signal is given by $\sigma = 2\pi/T$, with T the M_2 tidal period.

Since the coastal boundaries are assumed to be impermeable, the boundary condition at the lateral boundaries of the tidal basin read

$$(H - \hat{h})\hat{\mathbf{u}} \cdot \mathbf{n} = 0 \quad \text{at } y = 0 \text{ and } y = B, \quad (4.3)$$

with \mathbf{n} denoting the outward pointing unit vector normal to the boundaries.

4.2.3. CONCENTRATION EQUATION

The sediment, consisting of non-cohesive sandy material with a uniform grain size, is mainly transported as suspended load. Following Ter Brake and Schuttelaars [32], the evolution of the suspended sediment is modeled as a depth-integrated advection-diffusion equation, with sink and source terms. The source term is assumed to not only depend on the tide induced velocity, but also on wind induced velocity (Roos *et al.* [33]). It is assumed that the wind induced velocity is independent of the tide induced velocity. Similar to the hydrodynamics, a perturbation approach is employed. From this approach, it follows that at leading order sediment advection can be neglected, resulting in the following concentration equation (Ter Brake and Schuttelaars [19, 32], Roos *et al.* [33]):

$$\hat{C}_t - \nabla \cdot [k_{h*} \nabla \hat{C} + k_{h*} \frac{w_s}{k_{v*}} \beta \hat{C} \nabla \hat{h}] = \alpha (\hat{\mathbf{u}} \cdot \hat{\mathbf{u}} + \frac{1}{2} \hat{u}_w^2) - \frac{w_s^2}{k_{v*}} \beta \hat{C}, \quad (4.4)$$

where \hat{C} is the depth-integrated suspended sediment concentration. The horizontal diffusivity k_{h*} , the vertical diffusivity k_{v*} , the settling velocity w_s and the erosion parameter (Dyer [34]) related to sediment properties α are all assumed to be constant in space and time. It is assumed that the deposition parameter β is defined by

$$\beta = \frac{1}{1 - \exp(-\frac{w_s}{k_{v*}}(H^I - \hat{h}))}. \quad (4.5)$$

The erosion of sediment due to wind waves is modeled as $\frac{\alpha}{2} \hat{u}_w^2$ (Roos *et al.* [33]), with \hat{u}_w the wave-induced near-bed orbital velocity amplitude. Following Roos *et al.* [33], it

is assumed that \hat{u}_w is inversely proportional to the local water depth, i.e.,

$$\hat{u}_w = U_w \left(\frac{H^I - \hat{h}}{H^I} \right)^{-m}, \quad (4.6)$$

where m is taken as $m = 1$. The coefficient U_w is smaller than the characteristic velocity scale U in magnitude, and is taken to be $1.0 \times 10^{-2} \text{ ms}^{-1}$. It should be remarked that the effect of wave breaking is not taken into account.

At the seaward boundary, it is assumed that no diffusive boundary layer develops (Schuttelaars and de Swart [27]). Hence, the boundary conditions at the entrances read

$$\hat{C}_t = \alpha(\hat{\mathbf{u}} \cdot \hat{\mathbf{u}} + \frac{1}{2}\hat{u}_w^2) - \frac{w_s^2}{k_{v*}}\beta\hat{C}, \quad \text{at } x = 0 \text{ and } L. \quad (4.7)$$

At the lateral boundaries of the back-barrier basin, a vanishing suspended load transport is required:

$$[k_{h*}\nabla\hat{C} + k_{h*}\frac{w_s}{k_{v*}}\beta\hat{C}\nabla\hat{h}] \cdot \mathbf{n} = 0 \quad \text{at } y = 0 \text{ and } y = B. \quad (4.8)$$

4.2.4. BED EVOLUTION EQUATION

The bed evolution equation is derived from the mass balance in the sediment layer and reads

$$\rho_s(1-p)(\hat{h}_t - \lambda\nabla^2\hat{h}) = - \left[\alpha(\hat{\mathbf{u}} \cdot \hat{\mathbf{u}} + \frac{1}{2}\hat{u}_w^2) - \frac{w_s^2}{k_{v*}}\beta\hat{C} \right]. \quad (4.9)$$

Here, ρ_s is the density of the sediment, and p denotes the bed porosity. The first term on the left hand side accounts for the temporal bed changes, whereas the second term models the divergence of the bed load transport due to gravitational effects, using a highly simplified parameterisation with constant $\lambda \sim \mathcal{O}(10^{-6} - 10^{-4})$ (Schuttelaars and de Swart [35]). The terms on the right of Eq. (4.9) are associated with the local erosion caused by the tide, the local erosion caused by wind and the deposition of sediment, respectively.

Substituting Eq.(4.4) into Eq.(4.9) results in the following bed evolution equation:

$$\rho_s(1-p)\hat{h}_t + \hat{C}_t = -\nabla \cdot \mathbf{F}, \quad (4.10)$$

with

$$\mathbf{F} = \underbrace{-k_{h*}\nabla\hat{C}}_{\mathbf{F}_{\text{diff}}} - \underbrace{k_{h*}\frac{w_s}{k_{v*}}\beta\hat{C}\nabla\hat{h}}_{\mathbf{F}_{\text{topo}}} - \underbrace{\rho_s(1-p)\lambda\nabla\hat{h}}_{\mathbf{F}_{\text{bed}}} \quad (4.11)$$

the total depth-integrated sediment transport. This transport consists of a classical diffusive contribution (\mathbf{F}_{diff}), a topographically induced diffusive contribution (\mathbf{F}_{topo}) and a bed load contribution (\mathbf{F}_{bed}).

At seaward boundaries, we prescribe the undisturbed bed level as

$$\hat{h} = 0 \quad \text{at } x = 0, \quad (4.12a)$$

$$\hat{h} = H^I - H^{II} \quad \text{at } x = L. \quad (4.12b)$$

| Parameter & Definition | |
|---|--|
| $U = \frac{A_{M_2}^I \sigma L}{H^I}$ | $\lambda_L = \frac{\sigma L}{\sqrt{H^I g}}$ |
| $r = \frac{r_*}{H^I \sigma}$ | $a = \frac{k_{v*} \sigma}{w_s^2}$ |
| $k_h = \frac{k_{h*}}{L^2 \sigma}$ | $\lambda_d = \frac{H^I w_s}{k_{v*}}$ |
| $\delta_w = \frac{U_w}{U}$ | |
| $\delta_s = \frac{\alpha U^2}{\rho_s (1-p) H^I \sigma}$ | $\delta_b = \frac{\lambda}{\sigma H^I L}$ |
| $A_{r2}^II = \frac{A_{M_2}^II}{A_{M_2}^I}$ | $\Delta \phi_{M_2} = \phi_{M_2}^II - \phi_{M_2}^I$ |

Table 4.1: The definition of dimensionless parameters.

Using Eq.(4.8), the requirement of no sediment transport through the lateral boundaries reduces to

$$\nabla \hat{h} \cdot \mathbf{n} = 0 \quad \text{at } y = 0 \text{ and } y = B, \quad (4.13)$$

which implies no bed load transport is allowed through the lateral boundaries.

4.3. SOLUTION METHOD

4.3.1. DIMENSIONLESS EQUATIONS

To make the equations dimensionless, the physical variables are scaled as

$$(x, y) = L(\check{x}, \check{y}), \quad t = \frac{1}{\sigma} \check{t}, \quad \hat{\mathbf{u}} = U \check{\mathbf{u}}, \quad (4.14a)$$

$$\hat{\zeta} = A_{M_2}^I \check{\zeta}, \quad \hat{h} = H^I \check{h}, \quad \hat{C} = \frac{\alpha U^2 k_{v*}}{w_s^2} \check{C}, \quad (4.14b)$$

where the dimensionless variables are indicated by a check $\check{\ast}$. The horizontal coordinate x and lateral coordinate y are made dimensionless by L , the tidal system length. Time is made dimensionless using σ , the M_2 angular frequency, the surface elevation is scaled using $A_{M_2}^I$, the M_2 amplitude at the seaward side of inlet I, and the bed level is made dimensionless using H^I , the depth at inlet I. The typical scale for the velocity is $U = A_{M_2}^I \sigma L / H^I$ (Deng *et al.* [36]). The suspended sediment concentration is made dimensionless using $\alpha U^2 k_{v*} / w_s^2$, a scaling which is determined by assuming an approximate balance between erosion by tides and deposition.

Substituting these dimensionless variables in the equations and suppressing the checks $\check{\ast}$, the system of dimensionless equations becomes:

$$\zeta_t + \nabla \cdot [(1-h)\mathbf{u}] = 0, \quad (4.15a)$$

$$\mathbf{u}_t + \lambda_L^{-2} \nabla \zeta + \frac{r\mathbf{u}}{1-h} = 0, \quad (4.15b)$$

$$a[C_t - \nabla \cdot (k_h \nabla C - k_h \lambda_d \beta \nabla h C)] = \mathbf{u} \cdot \mathbf{u} + \frac{1}{2} \delta_w^2 (1-h)^{-2} - \beta C, \quad (4.15c)$$

$$h_t + a \delta_s C_t = \nabla \cdot [\delta_s a k_h \nabla C + \delta_s a k_h \lambda_d \beta \nabla h C + \delta_b \nabla h], \quad (4.15d)$$

with the dimensionless deposition parameter β given by

$$\beta = \frac{1}{1 - \exp(-\lambda_d(1-h))}. \quad (4.16)$$

The parameter $\lambda_L = k_g L$ is the product of the frictionless tidal wavenumber $k_g = \sigma/\sqrt{H^I g}$ and the length of the inlet system L . The dimensionless friction parameter is denoted by r and defined as $r = r_*/H^I \sigma$. The ratio of the deposition timescale to the tidal period is denoted by $a = k_{v*} \sigma/w_s^2$, and the sediment Peclet number $\lambda_d = H^I w_s/k_{v*}$ is the ratio of the typical time a particle takes to settle in the water column to the typical time needed to mix particles through the water column. The dimensionless diffusion parameter is denoted by $k_h = k_{h*}/L^2 \sigma$. The ratio of the typical scale of orbital velocity due to the wind stress and the typical tidal velocity scale is denoted by $\delta_w = U_w/U$. The parameter $\delta_s = \alpha U^2/(\rho(1-p)H^I \sigma)$ denotes the ratio of tidal period T over the time scale related to suspended load, and $\delta_b = \lambda/\sigma H^I L$ is the ratio of tidal period T to the time scale related to slope term in the bed load transport. All parameters are summarized in Tab. 4.1.

From the bed evolution equation (4.15d) it follows that the bed changes on the tidal timescale are very small, because both morphodynamic timescales δ_s and δ_b are much smaller than one. Hence, a multiple timescale approach (see Sanders and Verhulst [37], Krol [38]) is employed to approximate the bed evolution by considering the tidally averaged bed evolution equation

$$h_\tau = -\nabla \cdot \langle \mathbf{F} \rangle, \quad (4.17)$$

with $\mathbf{F} = \underbrace{-ak_h \nabla C}_{\mathbf{F}_{\text{diff}}} - \underbrace{ak_h \lambda_d \beta \nabla h C}_{\mathbf{F}_{\text{topo}}} - \underbrace{\frac{\delta_b}{\delta_s} \nabla h}_{\mathbf{F}_{\text{bed}}}$

where the angular brackets $\langle \cdot \rangle$ denote tidally averaging. In these equations, $\tau = \delta_s t$ is the long timescale at which the bed changes significantly.

The associated dimensionless boundary conditions read

$$\zeta = \cos t \quad \text{at } x = 0, \quad (4.18a)$$

$$\zeta = A_{r2}^{\text{II}} \cos(t - \Delta\phi_{M_2}) \quad \text{at } x = 1, \quad (4.18b)$$

$$(1-h)\mathbf{u} \cdot \mathbf{n} = 0 \quad \text{at } y = 0 \text{ and } y = B/L, \quad (4.18c)$$

$$\lim_{k_h \rightarrow 0} C(x, t, k_h) = C(x, t, k_h = 0) \quad \text{at } x = 0, 1 \quad (4.18d)$$

$$(k_h \nabla C + k_h \lambda_d \beta C \nabla h) \cdot \mathbf{n} = 0 \quad \text{at } y = 0 \text{ and } y = B/L, \quad (4.18e)$$

$$h = 0 \quad \text{at } x = 0, \quad (4.18f)$$

$$h = 1 - \frac{H^{\text{II}}}{H^{\text{I}}} \quad \text{at } x = 1, \quad (4.18g)$$

$$\nabla h \cdot \mathbf{n} = 0 \quad \text{at } y = 0 \text{ and } y = B/L. \quad (4.18h)$$

The parameter $A_{r2}^{\text{II}} = A_{M_2}^{\text{II}}/A_{M_2}^{\text{I}}$ is the ratio of the amplitude of the M_2 tide at inlet II to that at inlet I, and parameter $\Delta\phi_{M_2} = \phi_{M_2}^{\text{II}} - \phi_{M_2}^{\text{I}}$ is the phase difference between the M_2 tide at inlet II and that at inlet I.

From the boundary condition (4.18a) and (4.18b), the sea surface elevation ζ can be decomposed as the sum of a cosine and a sine component:

$$\zeta = \zeta_{c1} \cos(t) + \zeta_{s1} \sin(t), \quad (4.19)$$

with the subscript $c1(s1)$ denoting the amplitude of the sea surface elevation that varies as a cosine (sine) with unit radial frequency. Similarly, the longitudinal velocity u and the lateral velocity v can be written as

$$u = u_{c1} \cos(t) + u_{s1} \sin(t), \quad v = v_{c1} \cos(t) + v_{s1} \sin(t). \quad (4.20)$$

From eq. (4.15c) it follows that the sediment concentration C has a residual and a M_4 component. Since we are focusing on the morphodynamic evolution of tidal inlets in which diffusive transport is dominant, only the residual component is calculated, resulting in

$$C = C_{res}. \quad (4.21)$$

With these expressions and boundary conditions, the leading order tidally averaged sediment transport contributions are given by

$$\langle \mathbf{F}_{diff} \rangle = -ak_h \nabla C_{res}, \quad (4.22a)$$

$$\langle \mathbf{F}_{topo} \rangle = -ak_h \beta \lambda_d C_{res} \nabla h, \quad (4.22b)$$

$$\langle \mathbf{F}_{bed} \rangle = -\frac{\delta_b}{\delta_s} \nabla h. \quad (4.22c)$$

It should be remarked that the bed load contribution is much smaller than the topographically induced diffusive contribution (Hepkema *et al.* [39]).

4.3.2. MORPHODYNAMIC EQUILIBRIA AND LINEAR STABILITY

After substituting eqns. (4.19)-(4.21) in equations (4.15) and boundary conditions (4.18), the system of morphodynamic equations can be written as

$$K\Psi_\tau = G(\Psi, \mathbf{p}), \quad (4.23)$$

where $\Psi = (\zeta_{c1}, \zeta_{s1}, u_{c1}, u_{s1}, v_{c1}, v_{s1}, C_{res}, h)$ is the vector of the amplitudes of the physical variables, and \mathbf{p} the vector of model parameters. The matrix K is an 8×8 diagonal matrix, with a non-zero element only at the row associated with the bed evolution equation. The nonlinear operator G , which contains derivatives w.r.t. both x and y , depends on the parameters \mathbf{p} and works on the vector Ψ .

For a specific parameter setting \mathbf{p}_e , a stationary morphodynamic equilibrium $\Psi_e = \Psi_e(x, y)$ of eqn. (4.23) is found when

$$G(\Psi_e, \mathbf{p}_e) = 0. \quad (4.24)$$

To get a morphodynamic equilibrium, an initial guess Ψ_0 of the unknown Ψ_e has to be provided. If the initial guess is close to the actual morphodynamic equilibrium Ψ_e , a Newton-Raphson iterative method can be employed to obtain Ψ_e iteratively. To this end,

the i th approximation Ψ_i of Ψ_e (with Ψ_0 the initial guess) is used to obtain a correction $\Delta\Psi_{i+1}$ to Ψ_i by solving the systems of equations

$$G(\Psi_i, \mathbf{p}_e) + J_G(\Psi_i, \mathbf{p}_e)\Delta\Psi_{i+1} = 0, \quad (4.25)$$

in which $J_G(\Psi_i, \mathbf{p}_e)$ is the Jacobian matrix of the nonlinear operator G evaluated in (Ψ_i, \mathbf{p}_e) . In the next iteration, $\Psi_{i+1} = \Psi_i + \Delta\Psi_{i+1}$ (see Deng *et al.* [36] for a detailed discussion). If the correction $\Delta\Psi_{i+1}$ is small enough (i.e., smaller than 10^{-6}), Ψ_i is considered to be close enough to the actual morphodynamic equilibrium and the iterative process is stopped.

The linear stability of the morphodynamic equilibria Ψ_e can be investigated by substituting

$$\Psi(x, y, \tau) = \Psi_e(x, y) + \tilde{\Psi}(x, y, \tau) \quad (4.26)$$

into Eq.(4.23) and linearizing the resulting equation. Here, $\tilde{\Psi}(x, y, \tau)$ is an infinitesimally small perturbation. The resulting linearized equation allows for the ansatz

$$\tilde{\Psi} = \Re[\Psi'(x, y) \exp(\omega\tau)], \quad (4.27)$$

where ω denotes the (generally complex) eigenvalue and Ψ' the associated eigenvector. The real part of ω , $\Re(\omega)$, denotes the exponential growth rate, while the imaginary part $\Im(\omega)$ is the perturbation frequency. Substituting (4.26) into (4.23), the resulting eigenvalue problem reads

$$\omega K\Psi' = J_G(\Psi_e, \mathbf{p}_e)\Psi', \quad (4.28)$$

in which $J_G(\Psi_e, \mathbf{p}_e)$ is the Jacobian associated with the operator G , evaluated at (Ψ_e, \mathbf{p}_e) . An equilibrium is called linearly stable if all exponential growth rates are negative, and unstable if at least one exponential growth rate $\Re(\omega)$ is positive.

When varying one or more parameters of the vector \mathbf{p} , one or more of the exponential growth rates $\Re(\omega)$ can change sign. Such a change in stability is called a bifurcation. This allows for a systematic way of identifying the various equilibrium solutions (Seydel [40]): By using the eigenvector $\Psi'(x, y)$ that changed stability as a load vector, the arclength method allows for switching from one branch to another (see also Deng *et al.* [36]).

In this chapter, a rectangular geometry is considered. Within this setting, morphodynamic equilibria can be expressed as a combination of laterally uniform components and an infinite sum of laterally varying ones. The lateral variations consist of cosines and/or sines characterized by a lateral mode number n . Specifically, taking the associated boundary conditions into account, the bed profile can be decomposed as

$$h_e = h_{1D}(x) + \sum_{n=1}^{\infty} h_n(x) \cos(l_n y), \quad (4.29)$$

where h_{1D} is the laterally uniform component of the bed profile and h_n is the amplitude of the laterally varying cosine component with lateral mode number n . The associated dimensionless lateral wave number is defined by $l_n = n\pi L/B$.

By changing parameter values, the number and stability of morphodynamic equilibria as function of this parameter can change. This is visualized in a so-called bifurcation diagram, with on the horizontal axis the parameter that is varied and on the vertical axis the maximum of the absolute value of the real part of the bed profile component with mode n ,

$$|\Re(h_n(x_0))| \geq |\Re(h_n(x))| \text{ for all } x, \quad (4.30)$$

as characteristic value (vertical axis) for this mode.

To explicitly obtain morphodynamic equilibria Ψ_e from system (4.24), and to obtain the eigenvector Ψ' from system (4.28), these systems of equations are spatially discretized using the finite element method. Here, a structured mesh is used with 100 elements in longitudinal direction and 20 elements in lateral direction. The degree of each element considered is 2. The total number of degrees of freedom is 129928.

4.4. RESULTS

In this section, the sensitivity of the existence and number of morphodynamic equilibria to the friction parameter and width will be investigated for a rectangular double-inlet system with characteristic parameter values given in Tab. 4.2. Most of the parameter values are those observed for the Marsdiep–Vlie inlet system (Duran-Matute *et al.* [23], Ridderinkhof [41]) except for the length (30 km instead of the 59 km characterising the Marsdiep–Vlie inlet system). The choice of a shorter length is motivated by our focus on morphodynamic instabilities resulting from diffusive processes. Indeed in Deng *et al.* [26] it was shown that both advective and diffusive sediment transport are of equal importance for the observed system length. By reducing the length, diffusive instabilities become dominant, thus allowing us to focus on the morphodynamic equilibria resulting from diffusive processes only.

In Sect. 4.4.1, the laterally uniform morphodynamic equilibrium associated with the default parameter values for a rectangular inlet system with a length of 30 km is discussed. Next, in Sect. 4.4.2, a bifurcation analysis is performed, in which the friction parameter is used as bifurcation parameter. The resulting morphodynamic equilibria are characterized by the mode amplitudes defined in Eqn. (4.30). Bifurcation diagrams obtained considering different uniform basin widths are studied in Sect. 4.4.2.

4.4.1. LATERALLY UNIFORM MORPHODYNAMIC EQUILIBRIA AND THEIR LINEAR STABILITY

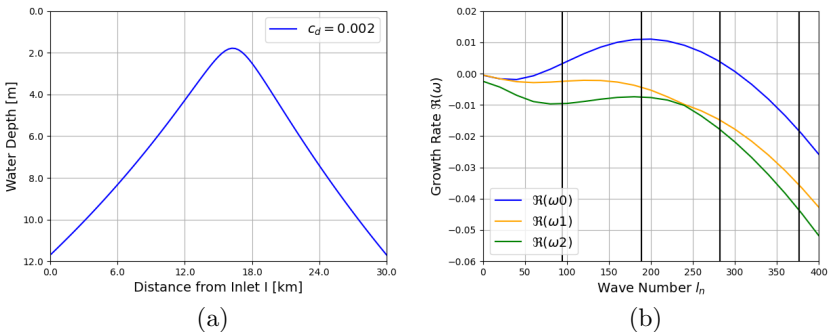
DEFAULT PARAMETER VALUES

The bed profile of the laterally uniform morphodynamic equilibrium obtained using the default values of Tab. 4.2 is shown in Fig. 4.2a. This figure shows that at the seaward entrances, the water depth is approximately 11.7 m, while a minimum water depth of 1.8 m is found at a distance of about 16 km from inlet I.

The linear stability of this morphodynamic equilibrium with respect to two dimensional perturbation is shown in Fig. 4.2b. In this figure, the three largest growth rates, denoted by $\Re(\omega_0)$, $\Re(\omega_1)$ and $\Re(\omega_2)$, are plotted as a function of the dimensionless lateral wave number l_n . The largest growth rate $\Re(\omega_0)$ is negative when $l_n = 0$, and hence the

| Quantities in the dimensional model | |
|--|---|
| System | Sediment & Bed |
| $L = 30 \text{ km}$ | $k_{h*} = 100 \text{ m}^2 \text{ s}^{-1}$ |
| $g = 9.81 \text{ m s}^{-2}$ | $\alpha = 0.5 \times 10^{-2} \text{ kg s m}^{-4}$ |
| $c_d = 0.0020$ | $\lambda \sim 10^{-6} - 10^{-4} \text{ m}^2 \text{ s}^{-1}$ |
| $\sigma = 1.4 \times 10^{-4} \text{ s}^{-1}$ | $k_{v*} = 0.2 \text{ m}^2 \text{ s}^{-1}$ |
| $T = 44.9 \times 10^3 \text{ s}$ | $d_{50} = 2 \times 10^{-4} \text{ m}$ |
| | $\rho_s = 2650 \text{ kg m}^{-3}$ |
| | $p = 0.4$ |
| | $w_s = 0.015 \text{ m s}^{-1}$ |
| | $U_w = 1.0 \times 10^{-2} \text{ m s}^{-1}$ |
| Inlet specific parameters | |
| Inlet I | Inlet II |
| $H^I = 11.7 \text{ m}$ | $H^{II} = 11.7 \text{ m}$ |
| $A_{M_2}^I = 0.62 \text{ m}$ | $A_{M_2}^{II} = 0.62 \text{ m}$ |
| $\phi_{M_2}^I = 0^\circ$ | $\phi_{M_2}^{II} = 1^\circ$ |
| $B^I = 1000 \text{ m}$ | $B^{II} = 1000 \text{ m}$ |
| Quantities in the non-dimensional model | |
| $\epsilon = 5.30 \cdot 10^{-2}$ | $\lambda_L = 0.39$ |
| $r = 0.23$ | $a = 0.28$ |
| $k_h = 7.9 \cdot 10^{-4}$ | $\delta_s = 9.5 \cdot 10^{-5}$ |
| $\lambda_d = 0.59$ | $A_{r_2}^{II} = 1.0$ |
| $\delta_w = 4.5 \cdot 10^{-2}$ | $\phi_{r_2}^{II} = 1^\circ$ |

Table 4.2: Parameter values adopted in the model.

Figure 4.2: The laterally uniform equilibrium bed profile obtained for the default parameter setting is plotted as a function of the distance from inlet I in panel (a). Panel (b) shows the three largest growth rates of this morphodynamic equilibrium as function of dimensionless (lateral) wave number l_n .

morphodynamic equilibrium is stable against laterally uniform perturbations. Increasing l_n from 0 to 200, $\Re(\omega_0)$ quickly becomes positive and increases to approximately 0.011, which corresponds to a dimensional growth rate of $4.6 \times 10^{-3} \text{ yr}^{-1}$. When increasing l_n further, $\Re(\omega_0)$ starts to decrease and becomes again zero at $l_n = 300$. Next, increasing l_n results in $\Re(\omega_0)$ becoming negative. The figure also shows that the second and third eigenmodes are linearly stable, because both $\Re(\omega_1)$ and $\Re(\omega_2)$ are negative for all the considered l_n .

Using the parameter values in Tab. 4.2, the dimensionless lateral wave number of the mode $n = 1$ is $l_1 = \pi L/B = 94.2$. In a similar way, l_2, l_3 etc can be obtained. In Fig. 4.2b, these lateral wave numbers are indicated by the solid vertical lines. It appears that modes $n = 1, 2, 3$ have a positive growth rate $\Re(\omega)$, indicating that these perturbations will grow in time. All perturbations with a higher mode number ($n \geq 4$) are linearly stable.

SENSITIVITY TO THE FRICTION PARAMETER

In Fig. 4.3a the equilibrium bed profiles of the laterally uniform morphodynamic equilibria are shown as a function of the distance from inlet I (horizontal axis) and the friction parameter c_d (vertical axis). From this figure it follows that when increasing the friction parameter c_d from 0.0015 to 0.0025 the morphodynamic equilibria do not change too much: for example the location of WD_{\min} , indicated by the gray line, is always found at $x \sim 16$ km. This is also evident from Fig. 4.3b where the equilibrium bed profiles for three selected friction parameter values, namely $c_d = 0.0018$, $c_d = 0.0019$ and $c_d = 0.0020$, are shown.

However the linear stability properties of the laterally uniform morphodynamic equilibria sensitively depend on the friction parameter c_d . In Fig. 4.3c the largest growth rate $\Re(\omega_0)$ is shown for the c_d values used in Fig. 4.3b. By increasing the friction parameter c_d , the growth rate $\Re(\omega_0)$ of the fastest growing eigenpattern becomes larger for all wave numbers l_n . This is also demonstrated in Fig. 4.3d, in which the neutral stability curve of $\Re(\omega_0)$, i.e., the location in the $l_n - c_d$ space where $\Re(\omega_0) = 0$ is plotted as a blue solid line. The neutral stability curves of the eigenpattern with the second and third largest growth rate, $\Re(\omega_1)$ and $\Re(\omega_2)$, are shown as red and orange solid lines, respectively. The three black vertical lines in this figure indicate the value of the wave number of mode 1 ($l_1 = 94.2$), mode 2 ($l_2 = 188.4$) and mode 3 ($l_3 = 282.6$). When the friction parameter c_d increases from 0.0015 to 0.0025, first mode 2 becomes linearly unstable (indicated by $P0$ for $c_d = 0.00184$). Next modes 1 and 3 become unstable, as indicated by $P1$ ($c_d = 0.00188$) and $P2$ ($c_d = 0.00196$), respectively.

SENSITIVITY TO THE WIDTH

In the above discussion, the width is taken to be $B = 1$ km. When this width is varied, the laterally uniform morphodynamic equilibrium does not change. Its linear stability, on the other hand, may change because the values of the admissible wave number l_n change: indeed the dimensionless wave number l_n is inversely proportional to the width B . In Fig. 4.4, the three largest growth rates are shown as a function of dimensionless wave number l_n , using the default value for c_d ($=0.002$). The black lines indicate the admissible wave numbers of the first mode, indicated by l_1 , for different basin width. For $B = 0.25$ km, the first admissible wave number becomes $l_1 = 376.8$. The associated growth rate is negative. The growth rates associated with admissible wave number l_n

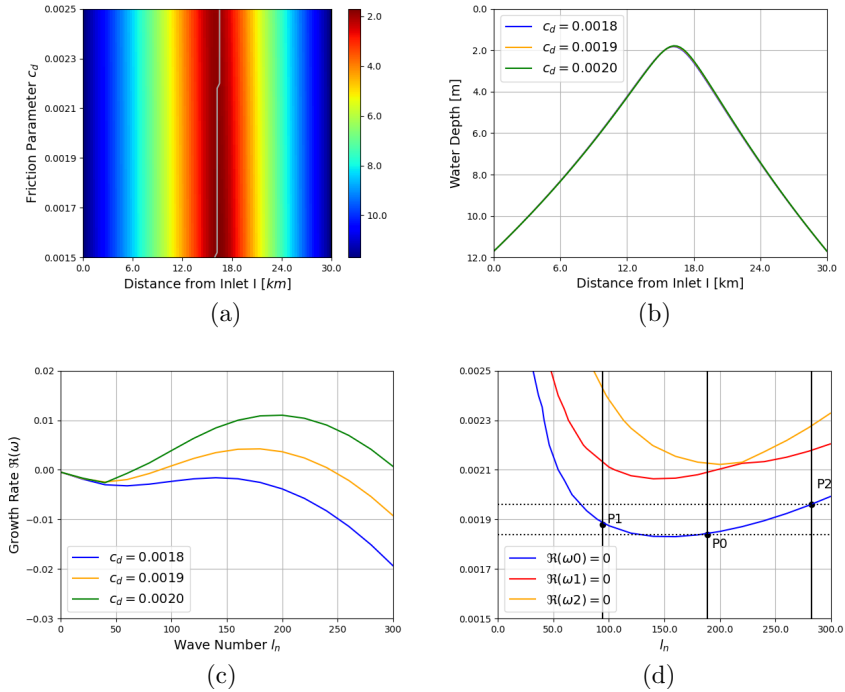


Figure 4.3: Morphodynamic equilibria for different values of the friction parameter c_d . Panel (a) shows the water depth of the morphodynamic equilibria as a function of distance from inlet I and friction parameter c_d , with cold color denoting large water depth and warm color small water depth. Panel (b) shows the water depth for three selected values of the friction parameter c_d . Panel (c) shows the growth rate of the most unstable/least stable eigenfunctions $R(\omega_0)$, is shown as a function of dimensionless lateral wave number l_n . In panel (d) the neutral stability curves of $R(\omega_0)$, $R(\omega_1)$ and $R(\omega_2)$ are shown.

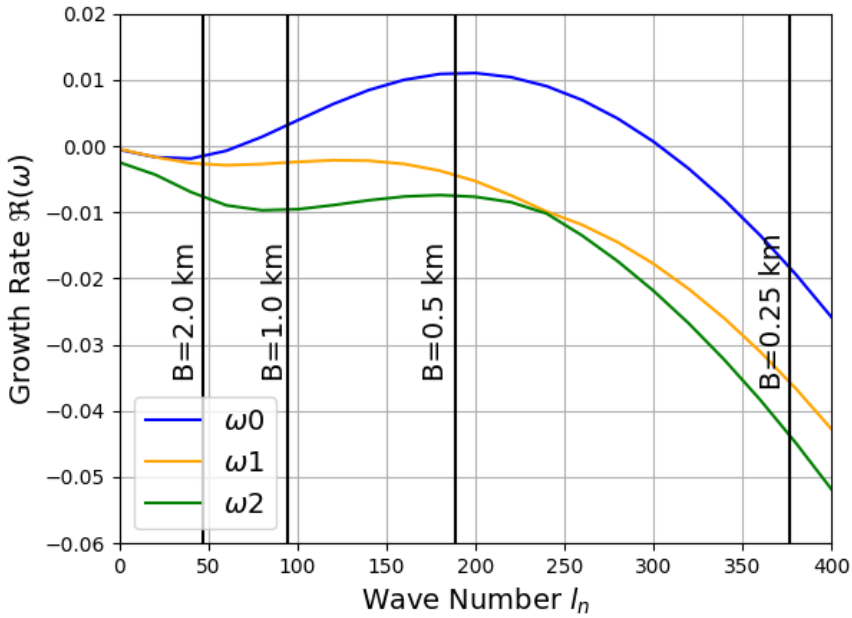


Figure 4.4: The three largest growth rates of the morphodynamic equilibria using default parameter values (see table 4.2) are shown as functions of the dimensionless (lateral) wave number l_n . The black lines indicate the first associated wavenumber l_1 for different basin widths.

with $n \geq 2$ are all negative (not shown), and the corresponding laterally uniform morphodynamic equilibrium is linearly stable. When the width becomes larger, the first admissible wave number becomes smaller. For example, when $B = 0.5\text{ km}$ ($B = 1.0\text{ km}$), $l_1 = 188.4$ ($l_1 = 94.2$). The associated growth rate is positive, and the associated laterally uniform morphodynamic equilibrium is linearly unstable. For $B = 2.0\text{ km}$, the first admissible wave number becomes $l_1 = 47.1$ and the corresponding largest growth rate associated with $l_1 = 47.1$ is negative. However, since there are other modes with a positive growth rate (for example, l_2), the associated laterally uniform morphodynamic equilibrium is linearly unstable.

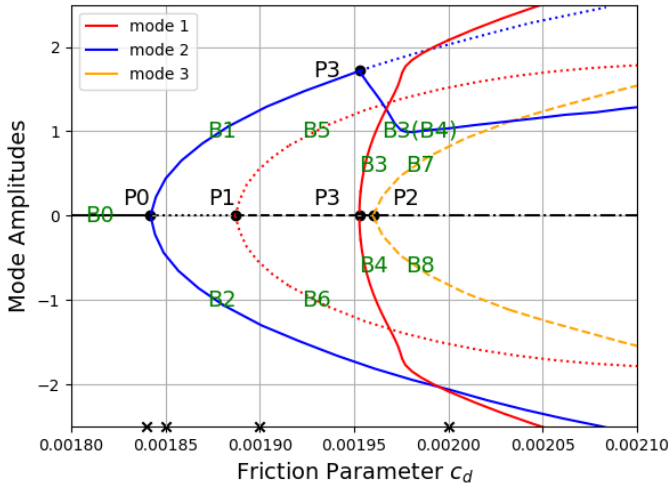
4.4.2. LATERALLY VARYING MORPHODYNAMIC EQUILIBRIA

When the laterally uniform morphodynamic equilibria change their linear stability properties, dynamical system theory (see for example Dijkstra *et al.* [21]) stipulates that a so-called bifurcation has occurred. In Sect. 4.4.2, we focus on the bifurcation structure of a double-inlet system with a uniform width of $B = 1\text{ km}$, varying the friction parameter c_d . The influence of width variations is studied in Sect. 4.4.2.

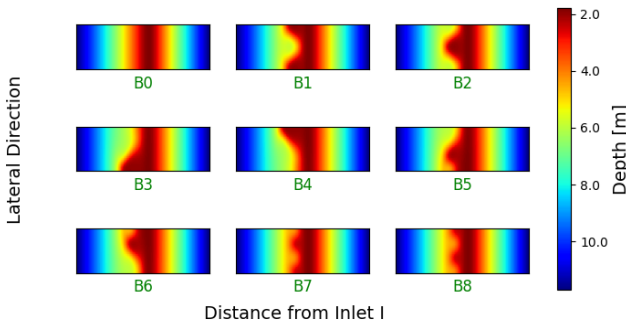
VARIATIONS OF THE FRICTION PARAMETER

For the friction values indicated by the points $P0$, $P1$ and $P2$ in Fig. 4.3b bifurcations occur. To further study these bifurcations, Fig. 4.5a shows the bifurcation diagram using the default parameter values for the double-inlet system, except for the friction parameter c_d which is used as bifurcation parameter. In this diagram all morphodynamic equilibria that exist for a specific value of c_d are characterized by the amplitudes of the first three lateral modes of the bed profile. In Fig. 4.5a it is shown that when increasing the friction parameter c_d from 0.0018 to 0.0021, three supercritical pitchfork bifurcations, denoted by $P0$ ($c_d = 0.00184$), $P1$ ($c_d = 0.00188$) and $P2$ ($c_d = 0.00196$) are found on the branch of laterally uniform morphodynamic equilibria, denoted as branch $B0$ (black line, with solid, dotted and dashed indicating none, 1 and 2 eigenpatterns with positive growth rates; the dash-dotted line indicates that at least three linearly unstable eigenpatterns exist). This branch is characterized by all mode amplitudes equal to zero (see $B0$ in Fig. 4.5e for the bed profile obtained for $c_d = 0.002$).

The first pitchfork bifurcation $P0$ results in two new branches, denoted by $B1$ and $B2$, of linearly stable morphodynamic equilibria (indicated by the solid blue lines in Fig. 4.5a). The branch $B1$ is characterized by a positive amplitude for mode 2, branch $B2$ by a negative amplitude. Following branch $B1$ by increasing the friction parameter c_d , a supercritical pitchfork bifurcation $P3$ is found at $c_d = 0.00195$. At this bifurcation, branch $B1$ becomes unstable (indicated by the dotted blue line), while two new branches, denoted by $B3$ and $B4$, of linearly stable morphodynamic equilibria are found that are characterized by a positive amplitude of mode 2 (blue solid lines), and non-zero amplitudes for all other modes as well. Here, only the amplitudes of mode 1 for these two new branches are shown as the solid red lines (see also Appendix D for a further explanation). The amplitude of mode 1 on branch $B3$ is positive, while on branch $B4$ a negative amplitude is found for mode 1. The bed profiles of branches $B1$ to $B4$ for $c_d = 0.002$ are shown in Fig. 4.5b. In the lateral direction, the bed profile of branch $B1$ ($B2$) is shallow (deep) near the lateral boundaries and deep (shallow) in the middle of the



(a)



(b)

Figure 4.5: Bifurcation diagram for morphodynamic equilibria obtained by varying the friction parameter c_d . In panel (a) the bifurcation configuration is shown. Lines colored with red, blue and orange indicate the amplitudes of mode 1, 2 and 3 of morphodynamic equilibria, respectively. The black line indicates laterally uniform morphodynamic equilibria. Solid, dotted and dashed lines indicate the number of positive growth rates: none, 1 and 2. The crosses on the horizontal axis denote the friction values used in Figs. 6–8. Panel (b) shows representative morphodynamic equilibria for each branch, with warm colors denoting smaller water depths and cold colors larger water depths. These equilibria are all obtained by using a friction parameter $c_d = 0.002$.

basin, which is typical for a positive (negative) amplitude of mode 2. In both cases, the morphodynamic equilibria are symmetric around $y = 500 \text{ m}$ ($= B/2$). The bed profiles associated with branch $B3$ ($B4$) are shallow (deep) near the right lateral boundary and deep (shallow) near the left lateral boundary, looking from inlet I to inlet II .

Just right of the second pitchfork bifurcation $P1$ on branch $B0$ two new unstable branches (red dotted lines) are found, characterized by one unstable eigenmode. The laterally uniform morphodynamic equilibrium is now unstable with two eigenpatterns. The newly found branches are denoted by $B5$ (characterized by a positive amplitude of mode 1) and $B6$ (characterized by a negative amplitude). The representative bed profiles of branches $B5$ and $B6$ are shown in Fig. 4.5b again for $c_d = 0.002$. Note that these equilibria are linearly unstable. Looking from inlet I to inlet II , the bed profile of $B5$ ($B6$) is shallow (deep) in the left coastal boundary and deep (shallow) in the right coastal boundary, while the shallowest region is observed in the middle left. This indicates that the characteristic bed profile of $B5$ ($B6$) not only consists of mode 1, but is also strongly influenced by the amplitude of mode 2 (not shown in Fig. 4.5, see Appendix D).

The third pitchfork bifurcation at $B0$ is denoted by $P2$ and new unstable branches are found, one with positive amplitude of mode 3, denoted by $B7$ (upper dashed orange line), and another with negative amplitude, denoted by $B8$ (lower dashed orange line). These two branches are characterized by two positive growth rates $\Re(\omega)$, while the number of positive growth rate $\Re(\omega)$ of the branch (black dash-dotted line) of laterally uniform morphodynamic equilibria becomes 3. Associated (linearly unstable) morphodynamic equilibria of branches $B7$ and $B8$ for $c_d = 0.002$ are shown in Fig. 4.5b as well. Looking from inlet I to inlet II , the bed profile of $B7$ ($B8$) is shallow (deep) in the left coastal boundary and has another shallow (deep) region near the middle right.

VARIATIONS OF UNIFORM WIDTH B

Similar to variations of friction parameter c_d , a rich bifurcation structure forms when the uniform width B of the system is varied. Fig. 4.6a shows the bifurcation diagram for friction parameter $c_d = 0.00184$, with width B varying from 200 m to 1800 m. The figure shows that five pitchfork bifurcations are found on the branch of laterally uniform morphodynamic equilibria (denoted by $B0$ and indicated by the black line), denoted by $P0$ - $P4$. The first bifurcation $P0$, which is a supercritical pitchfork bifurcation, is found at $B = 510 \text{ m}$. Two new branches (solid red lines) with non-zero amplitudes of mode 1 are found, one with a positive amplitude (denoted by $B1$) and the other one with a negative amplitude (denoted by $B2$). It should be noted that these two branches also have non-zero amplitudes for the other modes. As an example, the amplitude of mode 2 (solid blue line connecting $P0$ and $P1$) is shown in figure 4.6a. These two branches come again together with the $B0$ branch at $B = 755 \text{ m}$, forming the (subcritical) pitchfork bifurcation $P1$. Like the pitchfork bifurcation $P0$, the bifurcation $P2$, found at $B = 1020 \text{ m}$, is a supercritical pitchfork bifurcation. The bifurcation $P2$ results in two new branches of morphodynamic equilibria with a non-zero amplitude of mode 2 (solid blue lines), the branch with a positive amplitude is denoted by $B3$ and a negative amplitude by $B4$. These two branches join the branch $B0$ at $B = 1510 \text{ m}$, forming the (subcritical) pitchfork bifurcation $P3$. Similar to $P0$ and $P2$, the last bifurcation $P4$ found at $B = 1530 \text{ m}$ is a supercritical pitchfork bifurcation. This bifurcation results in two new branches of morphodynamic equilibria with a non-zero amplitude of mode 3 (solid orange lines),

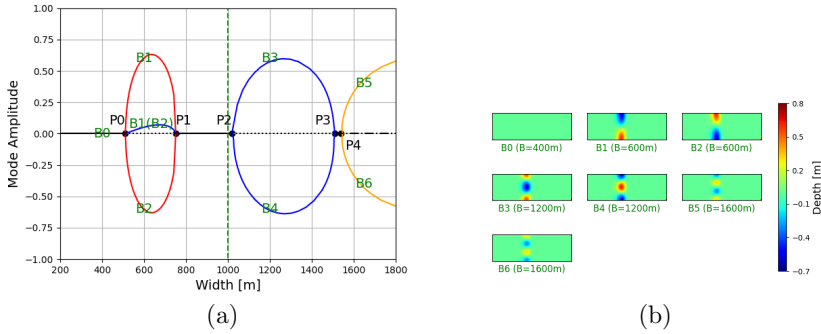


Figure 4.6: Bifurcation diagram for morphodynamic equilibria obtained for varying width. Panel (a) shows the bifurcation diagram with a friction parameter $c_d=0.00184$. The black lines indicate laterally uniform morphodynamic equilibria, while the red, blue and orange colored lines indicate branches of morphodynamic equilibria with a lateral structure. The amplitude of the mode 1 pattern is indicated in red, for the amplitude of the mode 2 pattern, blue is used, and orange is used for the amplitude of mode 3. Solid lines indicate that the morphodynamic equilibria are linearly stable. The dotted lines indicate morphodynamic equilibria with 1 positive growth rate $Re(\omega)$, while dash-dotted lines indicate equilibria with one or more positive growth rates. These equilibria are not discussed in detail in the text. The vertical green dashed line indicates the morphodynamic solutions found for a width of 1 km. The characteristic lateral variations of bed profile are shown in panels (b).

one with a positive amplitude (denoted by B5) and the other with a negative amplitude (denoted by B6). Between bifurcations P_0 (P_2) and P_1 (P_3), the branch B0 is unstable (black dotted lines). The lateral deviations from the underlying laterally uniform morphodynamic equilibrium of characteristic bed profiles for branches B0-B4 are shown in Fig. 4.6b. It appears that the lateral variations of branches B1 and B2 (B3 and B4, B5 and B6) are typical of bed patterns associated with mode 1 (2, 3).

In Fig. 4.7a, the bifurcation diagram for uniform widths varying between 200 m and 1800 m and friction parameter $c_d = 0.00185$ is shown. In Fig. 4.7b the bifurcation structure for widths between 1400 m and 1700 m is shown in detail. The lateral deviations from the underlying laterally uniform component of the morphodynamic equilibrium bed profiles for different branches are shown in Fig. 4.7c and 4.7d. Similar to the case with $c_d = 0.00184$ (Fig. 4.6a), pitchfork bifurcations P_0 - P_4 and the branches B0-B6 are found, even though these bifurcations occur for different width values (P_0 at $B = 470$ m, P_1 at $B = 810$ m, P_2 at $B = 940$ m, P_3 at $B = 1620$ m and P_4 at $B = 1440$ m). Compared to the bifurcation structure shown in Fig. 4.6a for a lower c_d value, the morphodynamic equilibria on branches B5 and B6 resulting from bifurcation P_4 are linearly unstable.

On branches B5 and B6, new supercritical pitchfork bifurcations, denoted by P_7 and P_8 , are found (at $B = 1510$ m, see Fig 4.7b). Bifurcation P_7 (P_8) results in two new unstable branches (dotted orange lines and dotted blue lines) with a non-zero amplitude of mode 2. The branches with a positive amplitude of mode 2 are denoted by B7 and B8, while the branches with a negative amplitude by B9 and B10. Starting at P_7 (P_8)

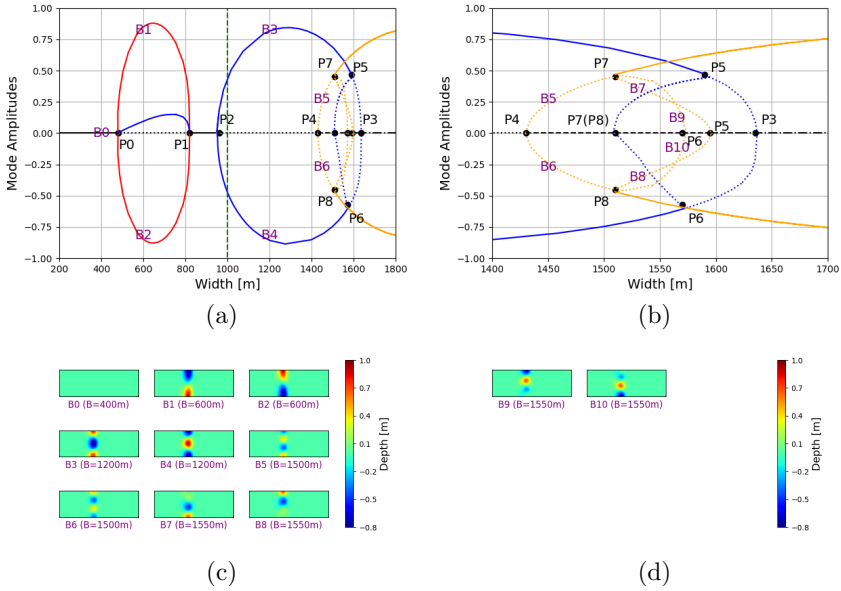


Figure 4.7: Bifurcation diagram for morphodynamic equilibria with the width as bifurcation parameter. Panel (a) shows the bifurcation diagram with friction parameter c_d fixed as 0.00185, with a closer look at the complex bifurcation structure around $B = 1550$ m in panel (b). In all panels, the black line indicates laterally uniform morphodynamic equilibria, while the lines with red, blue and orange colors indicate amplitudes of mode 1, mode 2 and mode 3 of the laterally varying components of the morphodynamic equilibria. Solid, dotted and dashed lines indicate the number of possible eigenmodes: 0, 1 and 2 positive growth rates. The vertical green dashed line indicates the morphodynamic equilibria found for a width of 1 km. The characteristic lateral variations of bed profile are shown in panels (c), (d).

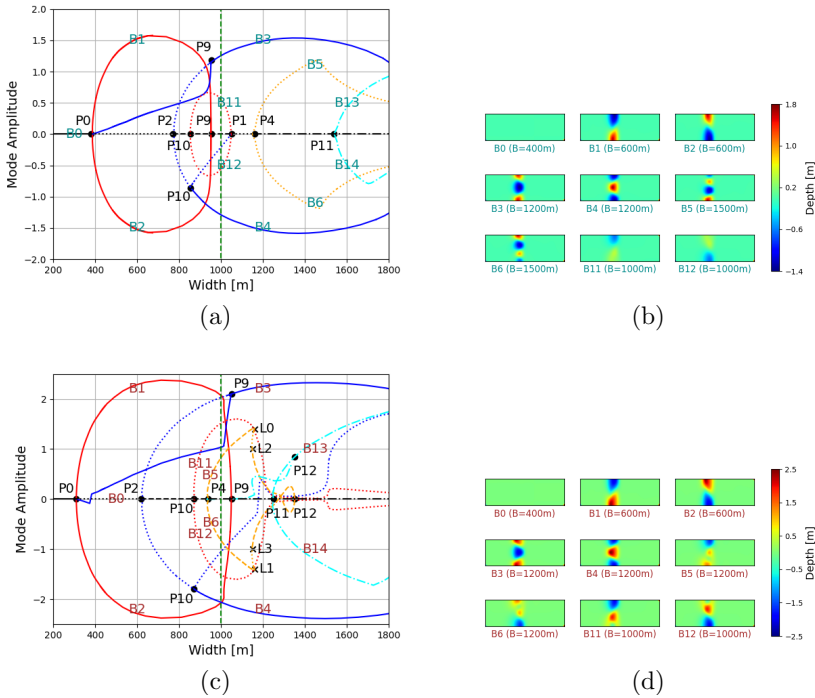


Figure 4.8: Bifurcation diagram for morphodynamic equilibria with the width as bifurcation parameter. Panels (a) and (c) show the bifurcation diagrams with friction parameter c_d equal to 0.0019 and 0.0020, respectively. In all panels, the black lines indicate laterally uniform morphodynamic equilibria, while the lines colored with red, blue, orange and cyan indicate amplitudes of mode 1, mode 2, mode 3 and mode 4. Solid, dotted and dashed lines indicate the number of positive eigenmodes: 0, 1 and 2 positive growth rates. The dash-dotted line indicate equilibria with one or more positive growth rates. These equilibria are not discussed in detail in the text. The vertical green dashed line indicates the morphodynamic solutions found for a width of 1 km. The characteristic lateral variations of bed profile are shown in panels (b) and (d).

and increasing the width B , branch $B5$ ($B6$) becomes linearly stable. Branches $B7$ ($B9$) and $B8$ ($B10$) join the branch $B3$ ($B4$) at $B = 1590$ m ($B = 1570$ m), forming a subcritical pitchfork bifurcation $P5$ ($P6$). Between $P5$ ($P6$) and $P3$, branch $B3$ ($B4$) becomes linearly unstable.

Similar to the plots in Fig. 4.6b, the largest lateral variations of morphodynamic equilibria on branches $B1$ - $B10$, shown in Fig. 4.7c and 4.7d, are found in the middle between the two inlets. The lateral variations of the morphodynamic equilibria on branches $B1$ ($B2$), $B3$ ($B4$) and $B5$ ($B6$) are typical for bed patterns associated with a positive (negative) amplitude of mode 1, 2 and 3, respectively. The variations of branches $B7 \sim B10$ consist of an amplitude of mode 2 and 3.

The bifurcation configuration for the friction parameter $c_d = 0.0019$ is shown in Fig. 4.8a, with the lateral deviations from the underlying laterally uniform component of the morphodynamic equilibrium bed profiles for various branches shown in Fig. 4.8b. Compared to the bifurcation structure obtained with $c_d = 0.00185$, the supercritical bifurcation $P2$ is found for a smaller width value than the bifurcation $P1$ on the branch $B0$. At the supercritical pitchfork bifurcation $P0$ two stable branches are found, denoted by $B1$ and $B2$. At the supercritical bifurcation $P2$ two linear unstable branches, denoted by $B3$ and $B4$ are found. The branches $B1$ and $B2$ join branch $B3$ at a subcritical pitchfork bifurcation, denoted by $P9$, resulting in $B3$ becoming linearly stable. On the branch $B4$, a supercritical pitchfork bifurcation denoted by $P10$ is found. At this bifurcation the branch $B4$ becomes linearly stable and two new unstable branches are generated (dotted blue line and dotted red lines), one with a positive amplitude of mode 1 ($B11$) and one with a negative amplitude ($B12$). These two new branches connect to the branch $B0$ at the subcritical bifurcation $P1$. On branch $B0$, supercritical pitchfork bifurcation $P4$ is also found, resulting in two unstable branches $B5$ and $B6$.

When using the default friction parameter $c_d = 0.002$, the bifurcation structure becomes more complicated. The resulting bifurcation diagram is shown Fig. 4.8c, with the lateral deviations from the underlying laterally uniform component of the morphodynamic equilibrium bed profiles for various branches shown in Fig. 4.8d. Even though the bifurcation diagram for this default value shows many differences, compared to the one obtained with $c_d = 0.0019$, the bifurcation structure of the stable branches is quite similar. The pitchfork bifurcation $B0$ results in two stable branches ($B1$ and $B2$) of morphodynamic equilibria. These two branches join the unstable branch $B3$ at $P9$, resulting in branch $B3$ becoming stable. The supercritical pitchfork bifurcation $P10$ results in $B4$ becoming stable. $B3$ and $B4$ are branched from supercritical pitchfork bifurcation $P2$. On branch $B0$, the supercritical pitchfork bifurcation $P4$ is found for a smaller width value than bifurcation $P1$ on the branch $B0$. At this pitchfork bifurcation, two linearly unstable branches are found, denoting the one with a positive amplitude of mode 3 by $B5$ and the one with a negative amplitude of mode 3 by $B6$. The branches $B5$ and $B6$ join to a new branch ($B13$ cyan dash-dotted line, see also Fig. 4.8a) with positive amplitude of mode 4 at a new bifurcation $P12$.

4.5. DISCUSSIONS

The results presented in the previous section indicate that the existence and number of morphodynamic equilibria, depends on the friction parameter and width.

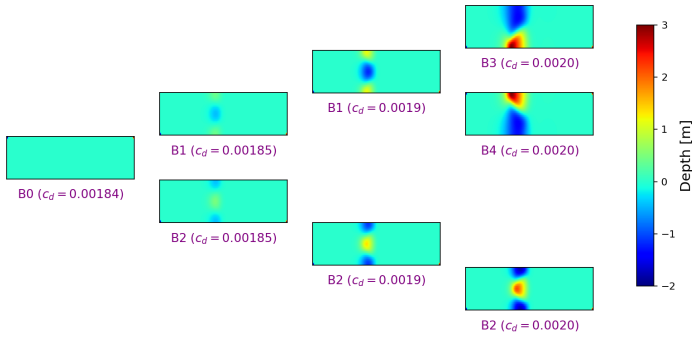


Figure 4.9: The stable morphodynamic equilibria obtained for a width of 1 km and $c_d = 0.00184$, $c_d = 0.00185$, $c_d = 0.0019$ and $c_d = 0.0020$.

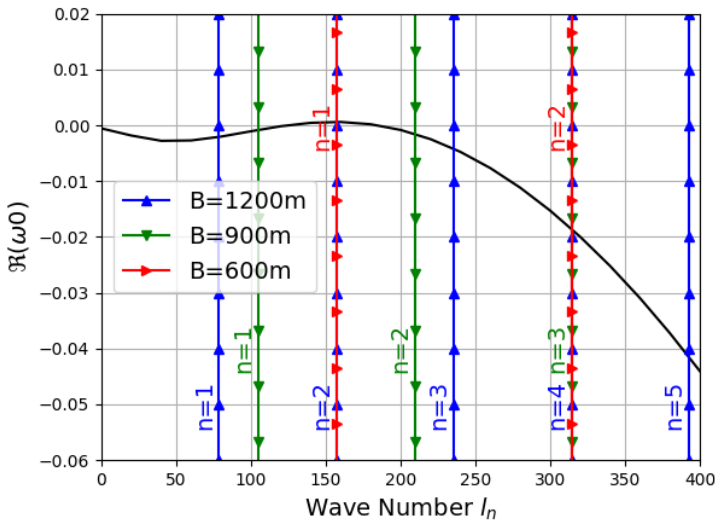


Figure 4.10: The largest growth rate $\Re(\omega_0)$ obtained by using friction parameter $c_d = 0.00184$ as function of dimensionless wave number l_n . The blue, green and red vertical lines indicate mode numbers for width $B = 1200\text{m}$, $B = 900\text{m}$ and $B = 600\text{m}$, respectively.

Focusing on the stable morphodynamic equilibria for a double-inlet system with a width of 1 km (Fig. 4.5), we see that for $c_d \lesssim 0.00184$ the only morphodynamic equilibrium found is laterally uniform. This is consistent with the results shown in Fig. 4.6, where for a fixed value of $c_d = 0.00184$ the solutions for a width of 1 km are indicated by the vertical green dashed-green line: only the laterally uniform equilibrium is found for this set of parameters. The deviation from the laterally uniform equilibrium (in this case zero everywhere) is depicted in Fig. 4.9, is linearly stable. Keeping the width equal to 1 km and increasing the friction parameter first results in two morphodynamically stable equilibria, one characterised by a channel flanked by two shallow regions, see $B1(c_d = 0.00185)$ and $B1(c_d = 0.0019)$ in Fig. 4.9. The other equilibrium is characterized by a shallow region in the middle flanked by two deeper channels near the landward boundaries, see $B2(c_d = 0.00185)$ and $B2(c_d = 0.0019)$ in Fig. 4.9. Note that for the larger friction value, the channels get deeper and the shallow regions get shallower. These solutions are also found in Fig. 4.7, 4.8a and 4.8b, indicated by the vertical green-dashed line. For even larger friction parameters, three stable morphodynamic equilibria are found. The first one, shown as $B2(c_d = 0.0020)$ in Fig. 4.9, still consists of two channels at the landward boundaries, separated by a channel, but with a larger amplitude than for the smaller friction values. The other two stable equilibria consist of a channel to one side, flanked by a shoal attached to the other landward boundary, see $B3(c_d = 0.0020)$ and $B3(c_d = 0.0020)$ in Fig. 4.9. These solutions do *not* resemble the characteristic bottom pattern associated with those found at the onset of instability (i.e. around $c_d \sim 0.00184$), indicating that the patterns at onset are not necessarily a good predictor of the patterns observed far from equilibrium. Again, the three stable solutions are also found in Fig. 4.8c and 4.8d.

In Figs. 4.6–4.8 the influence of the width on the number and stability of morphodynamic equilibria is systematically investigated for different values of the friction parameter. Even though the resulting bifurcation structure becomes more complicated for increasing c_d , some overarching conclusions can be drawn regarding the stable morphodynamic solutions. For relatively small friction values, the bifurcation structure is quite simple: for wider double-inlet systems, the resulting morphodynamic equilibria are characterised by higher mode numbers. However, there are widths for which the underlying laterally uniform morphodynamic equilibrium is linearly stable. This can be understood by plotting the growth rate of the linearly most unstable mode, see Fig. 4.9b. From this figure it follows that for a relatively small width, only mode $n = 1$ is linearly unstable, resulting in a pattern consisting of a channel to one lateral side of the double-inlet system and a shoal to the other side. It should be noted that all other modes also have a non-zero amplitude. Then, if the width is increased all eigenmodes are linearly stable, indicating that the laterally uniform morphodynamic equilibrium is expected to be observed for these parameter values. Increasing the width further, mode $n = 1$ stays linearly stable but mode $n = 2$ becomes unstable resulting in the channel-shoal structure depicted in Fig. 4.6b.

The relatively simple bifurcation structure, observed for $c_d = 0.00184$, becomes more complicated when the friction parameter is increased. For a slightly larger friction value and for a relatively small width, the first non-trivial morphodynamic equilibria are again dominated by the $n = 1$ mode (all other modes have a non-zero amplitude as well). In-

creasing the width further results in laterally uniform stable morphodynamic equilibria. Similar as for $c_d = 0.00184$, for widths ~ 1000 m mode 2 dominates the resulting stable morphodynamic equilibria. Contrary to the results for $c_d = 0.00185$ there are no large widths anymore for which the laterally uniform morphodynamic equilibria become linearly stable again. Now, for larger widths a linearly stable morphodynamic equilibrium appears that is dominated by the $n = 3$ mode. For intermediate width values (here $1510 \text{ m} \leq B \leq 1570 \text{ m}$) there are *four* linearly stable morphodynamic equilibria, two dominated by the $n = 2$ mode and two by the $n = 3$ mode.

When increasing the friction parameter even further, the dependency of the stable morphodynamic equilibria on width seems to simplify a bit. For small enough widths, the laterally uniform morphodynamic equilibrium is linearly stable. The largest width for which this is the case decreases with increasing value of the friction value c_d . When the width exceeds a critical value, there are two linearly stable morphodynamic equilibria, both dominated by the $n = 1$ mode. When the width is further increased, a third linearly stable equilibrium is formed; this equilibrium is dominated by the $n = 2$ mode. Increasing the width even further, the stable equilibria dominated by the $n = 1$ mode disappear and, apart from the already existing $n = 2$ equilibrium, another equilibrium dominated by $n = 2$ is found. Hence two stable equilibria, both dominated by $n = 2$ are found for widths that are large enough. For widths considered in our experiments (up to 1800 m) no other equilibria were found.

Even though morphodynamic equilibria are obtained that have a channel-shoal structure in shallow locations, these results are difficult to compare with both field observations and lab experiments. There are two main reasons for that: first, in the model developed in this paper the focus was on diffusive sediment transport processes, neglecting advective transport mechanisms. This leads to large-scale morphodynamic structures, while in both observations and lab experiments smaller scale structures also are typically observed. This suggests that advective processes are important as well, since these processes result, at least initially, in smaller scale bottom patterns (Deng *et al.* [26]). A second reason why a comparison with observations is limited is the fact that most inlet systems in the real world have a complicated planform geometry. This strongly influences the underlying lateral uniform equilibrium (Deng *et al.* [36]) which may in turn influence the channel-shoal patterns (Boelens [22], Boelens *et al.* [42]).

4.6. CONCLUSION

In this paper an exploratory model was developed to investigate the morphodynamic equilibria of tidal inlet systems that are connected to the outer sea by two inlets. To systematically gain first insights in the spatial structure of the bed patterns associated with these equilibria a highly schematized domain is considered, i.e., a rectangular one with only the bed erodible. The water motion is described by the linearized depth-averaged shallow water equations, neglecting the Coriolis force, and forced by prescribed M_2 sea surface elevations at both connections to the open sea. Sediment is eroded from the bed and transported in suspension by diffusive processes, while the sediment can settle again on the bed because of gravitation. Convergences and divergences of the diffusive transports result in changes of the bathymetry.

Instead of studying the morphodynamic evolution of the double-inlet system, we

aim at identifying the existence of morphodynamic equilibria directly. A tidal inlet system is considered to be in morphodynamic equilibrium if the divergence of the tidally-averaged sediment transport vanishes. To compute these equilibria directly, a good initial guess or an actual equilibrium has to be known for a specific set of parameters. Here we use the laterally uniform morphodynamic equilibria obtained by Deng *et al.* [36]. Next, a continuation method (Newton–Raphson method together with arclength method (Crisfield [43])) is employed to get possible morphodynamic equilibria. This also allows one to assess the number of morphodynamic equilibria and their linear stability. The linear stability is obtained by calculating the growth rates of infinitesimally small perturbations. Characteristic amplitudes of the morphodynamic equilibria and their stability are plotted as a function of the parameter that is varied, resulting in so-called bifurcation diagrams.

4

The sensitivity of morphodynamic equilibria to the friction coefficient and the system width is investigated. It is found that laterally uniform morphodynamic equilibria are quite insensitive to both the width and the magnitude of the friction coefficient, but that their linear stability strongly depends on these parameters. If the width is small enough, laterally uniform morphodynamic equilibria are linearly stable. The larger the friction parameter, the narrower the inlet system has to be for having a stable equilibrium. For relatively small values of the friction coefficient intervals of larger widths exist for which laterally uniform equilibria are still linearly stable. These intervals become smaller and eventually disappear when the strength of the bottom friction is large enough.

If the laterally uniform morphodynamic equilibrium is linearly unstable, either two or four linearly stable morphodynamic equilibria are found that are characterised by a channel–shoal pattern. These patterns are found close to the middle of the double–inlet system where the depth of the laterally uniform equilibrium configuration is relatively small. For narrow tidal inlet systems, there are two stable morphodynamic equilibria with bathymetries consisting of one channel and one shoal (mode 1 patterns). Increasing the width, but considering small enough values of the drag coefficient, non-trivial morphodynamic equilibria are found that are characterised by a pattern of two channels to the lateral sides to the system separated by a shoal in the middle, or by two shoals to the lateral sides separated by a deep channel (mode 2 patterns). Such equilibria are also found for larger values of the friction coefficient when considering larger widths. In this case, however, also slightly smaller widths exist for which four stable morphodynamic equilibria exist. The resulting channel–shoal patterns are a combination of mode 1 and mode 2 patterns.

Even though the results are promising, it is not possible to directly compare them to field observations or results obtained with lab experiments. To be able to make such a comparison, the physical formulation has to be extended to allow for advective processes. Furthermore, a more realistic geometry has to be considered as it is shown that the planform geometry of the double–inlet system can strongly influence the morphodynamic equilibrium (Deng *et al.* [36]), and hence the resulting channel–shoal patterns.

REFERENCES

- [1] H. E. de Swart and J. T. F. Zimmerman, *Morphodynamics of tidal inlet systems*, Annual Review of Fluid Mechanics **41**, 203 (2009).
- [2] M. L. Stutz and O. H. Pilkey, *Open-ocean barrier islands: Global influence of climatic, oceanographic, and depositional settings*, Journal of Coastal Research **27**, 207 (2011).
- [3] J. Mulhern, C. Johnson, and J. Martin, *Is barrier island morphology a function of tidal and wave regime?* Marine Geology **387**, 74 (2017).
- [4] A. P. Oost, P. Hoekstra, A. Wiersma, B. Flemming, E. J. Lammerts, M. Pejrup, J. Hofstede, B. Van der Valk, P. Kiden, J. Bartholdy, M. Van der Berg, P. C. Vos, S. de Vries, and Z. B. Wang, *Barrier island management: Lessons from the past and directions for the future*, Ocean & Coastal Management **68**, 18 (2012).
- [5] P. Salles, G. Voulgaris, and D. G. Aubrey, *Contribution of nonlinear mechanisms in the persistence of multiple tidal inlet systems*, Estuarine, Coastal and Shelf Science **65**, 475 (2005).
- [6] A. Pacheco, A. Vila-Concejo, O. Ferreira, and J. A. Dias, *Assessment of tidal inlet evolution and stability using sediment budget computations and hydraulic parameter analysis*, Marine Geology **247**, 104 (2008).
- [7] N. Tambroni and G. Seminara, *Are inlets responsible for the morphological degradation of venice lagoon?* Journal of Geophysical Research: Earth Surface **111** (2006), [10.1029/2005JF000334](https://doi.org/10.1029/2005JF000334).
- [8] J. Cleveringa and A. Oost, *The fractal geometry of tidal-channel systems in the Dutch Wadden Sea*, Geologie en Mijnbouw **78**, 21 (1999).
- [9] Z. B. Wang, T. Louters, and H. J. de Vriend, *A morphodynamic model for tidal inlet*, Computing Modelling in Ocean Engineering—Proceedings of the second international conference, Barcelona–Balkema Rotterdam **91**, 235 (1992).
- [10] R. Marciano, Z. Wang, A. Hibma, H. De Vriend, and A. Defina, *Modeling of channel patterns in short tidal basins*, Journal of Geophysical Research **110** (2005), [10.1029/2003JF000092](https://doi.org/10.1029/2003JF000092).
- [11] A. D’Alpaos, S. Lanzoni, M. Marani, A. Bonometto, G. Cecconi, and A. Rinaldo, *Spontaneous tidal network formation within a constructed salt marsh: Observations and morphodynamic modeling*, Geomorphology **91**, 186 (2007).
- [12] M. Van der Wegen and J. A. Roelvink, *Long-term morphodynamic evolution of a tidal embayment using a two-dimensional process-based model*, Journal of Geophysical Research **7**, C03016 (2008).
- [13] Z. Zhou, G. Coco, M. Jimenez, M. Olabarrieta, M. van der Wegen, and I. Townend, *Morphodynamics of river-influenced back-barrier tidal basins: The role of landscape and hydrodynamic settings*, Water Resources Research **50**, 1 (2014).

- [14] R. Styles, M. Brown, K. Brutsche, H. Li, T. M. Beck, and A. Sanchez, *Long-Term Morphological Modeling of Barrier Island Tidal Inlets* (ERDC/CHL TR-18-12, 2018).
- [15] P. Dissanayke, D. Roelvink, and M. van der Wegen, *Modelled channel pattern in schematised tidal inlet*, *Coastal Engineering* **56**, 1069 (2009).
- [16] H. M. Schuttelaars and H. E. de Swart, *Initial formation of channels and shoals in a short tidal embayment*, *Journal of Fluid Mechanics* **386**, 15 (1999).
- [17] S. M. van Leeuwen and H. E. de Swart, *The effect of advective processes on the morphodynamic stability of short tidal embayments*, *Physics and Chemistry of the Earth (B)* **26**, 735 (2001).
- [18] S. M. van Leeuwen and H. E. de Swart, *Effect of advective and diffusive sediment transport on the formation of local and global bottom patterns in tidal embayments*, *Ocean Dynamics* **54**, 441 (2004).
- [19] M. C. Ter Brake and H. M. Schuttelaars, *Channel and shoal development in a short tidal embayment: An idealized model study*, *Journal of Fluid Mechanics* **677**, 503 (2011).
- [20] M. C. Ter Brake, *Tidal embayments: Modelling and understanding their morphodynamics* (2011).
- [21] H. Dijkstra, F. Wubs, A. Cliffe, E. Doedel, I. Dragomirescu, B. Eckhardt, A. Gelfgat, A. Hazel, V. Lucarini, A. Salinger, E. Phipps, S. U. Juan, H. Schuttelaars, L. Tuckerman, and U. Thiele, *Numerical bifurcation methods and their application to fluid dynamics: Analysis beyond simulation*, *Communications in Computational Physics* **15**, 1 (2014).
- [22] T. Boelens, *Depth-averaged idealised modelling of the hydro- and morphodynamics of tidal inlet systems and estuaries* (2020).
- [23] M. Duran-Matute, T. Gerkema, G. J. de Boer, J. J. Nauw, and U. Grawe, *Residual circulation and freshwater transport in the Dutch Wadden Sea: a numerical modelling study*, *Ocean Science* **10**, 611 (2014).
- [24] M. Sassi, M. Duran-Matute, T. van Kessel, and T. Gerkema, *Variability of residual fluxes of suspended sediment in a multiple tidal-inlet system: the Dutch Wadden Sea*, *Ocean Dynamics* **65**, 1321 (2015).
- [25] A. Dastgheib, J. A. Roelvink, and Z. B. Wang, *Long-term process-based morphological modeling of the Marsdiep tidal basin*, *Marine Geology* **256**, 90 (2008).
- [26] X. Deng, T. De Mulder, and H. M. Schuttelaars, *Initial formation of channel-shoal patterns in double-inlet systems*, *Ocean Dynamics* **73**, 1 (2023).
- [27] H. M. Schuttelaars and H. E. de Swart, *Multiple morphodynamic equilibria in tidal embayments*, *Journal of Geophysical Research* **105**, 105 (2000).

- [28] C. Meerman, V. Rottschäfer, and H. Schuttelaars, *Influence of geometrical variations on morphodynamic equilibria in short tidal basins*, *Ocean Dynamics* **69**, 221 (2019).
- [29] H. Lorentz, *Het in rekening brengen van den weerstand bij schommelende vloeistofbewegingen*, *De Ingenieur*, 695 (1922).
- [30] J. T. F. Zimmerman, *On the Lorentz linearization of a nonlinearly damped tidal Helmholtz oscillator*, *Proceedings KNAW* **95**, 127 (1992).
- [31] P. Roos and H. Schuttelaars, *Resonance properties of tidal channels with multiple retention basins: Role of adjacent sea*, *Ocean Dynamics* **65**, 311 (2015).
- [32] M. C. Ter Brake and H. M. Schuttelaars, *Modeling equilibrium bed profiles of short tidal embayment. On the effect of the vertical distribution of suspended sediment and the influence of the boundary conditions*, *Ocean Dynamics* **60**, 183 (2010).
- [33] P. C. Roos, S. J. M. H. Hulscher, M. A. F. Knaapen, and R. M. J. Van Damme, *The cross-sectional shape of tidal sandbanks: Modeling and observations*, *Journal of Geophysical Research* **109**, F02003 (2004).
- [34] K. R. Dyer, *Coastal and estuarine sediment dynamics* (John Wiley and Sons, 1986).
- [35] H. M. Schuttelaars and H. E. de Swart, *An idealized long-term morphodynamic model of a tidal embayment*, *European Journal of Mechanics, B/Fluids* **15**, 55 (1996).
- [36] X. Deng, C. Meerman, T. Boelens, T. De Mulder, P. Salles, and H. M. Schuttelaars, *Morphodynamic equilibria in double-inlet systems: existence and stability*, *Journal of Geophysical research* **126**, 2021JF006266 (2021).
- [37] J. A. Sanders and F. Verhulst, *Averaging methods in nonlinear dynamical systems* (Springer Verlag, New York, 1985).
- [38] M. Krol, *On the averaging method in nearly time-periodic advection-diffusion problems*, *SIAM Journal on Applied Mathematics* **51**, 1622 (1991).
- [39] T. Hepkema, H. de Swart, A. Zagaris, and M. Duran-Matute, *Sensitivity of tidal characteristics in double inlet systems to momentum dissipation on tidal flats: a perturbation analysis*, *Ocean Dynamics* **68**, 439 (2018).
- [40] R. Seydel, *Practical Bifurcation and Stability Analysis* (Springer, New York, 1994).
- [41] H. Ridderinkhof, *Tidal and residual flows in the western dutch wadden sea i1: An analytical model to study the constant flow between connected tidal basins*, *Netherlands Journal of Sea Research* **22**, 185 (1988).
- [42] T. Boelens, T. Qi, H. Schuttelaars, and T. De Mulder, *Morphodynamic equilibria in short tidal basins using a 2DH exploratory model*, *Journal of Geophysical Research: Earth Surface* **126** (2021).
- [43] M. A. Crisfield, *A fast incremental/iterative solution procedure that handles snap through*, *Computers and Structures* **13**, 55 (1981).

5

CONCLUSIONS

5.1. GENERAL CONCLUSIONS

Motivated by Schuttelaars and de Swart [1] and Meerman *et al.* [2], an idealized model is developed to study the morphodynamic equilibria in a double-inlet system. The model consists of depth-averaged water motion equations forced by tidal constituents, a depth-integrated advection-diffusion equation for sediment transport with sink and source terms and a depth-averaged bed evolution equation. Using scaling analysis to make the system of equations dimensionless, a tidal time scale and a morphodynamic time scale are identified. The system is taken to be in a morphodynamic equilibrium state if the bed profile does not evolve on the long morphodynamic timescale. This condition essentially occurs when the divergence of the tidally averaged sediment transports vanishes.

First, morphodynamic equilibria are obtained and analysed by using direct root-finding approaches to numerically solve the dimensionless system of equations. In the parameter space spanned by the relative phase and amplitudes of M_2 tidal forcing, it was found that there are regions where no equilibrium, one equilibrium or multiple equilibria can exist. In the absence of morphodynamic equilibria, the double-inlet system is reduced to two uncoupled single-inlet systems. For specific contributions of M_2 and M_4 tidal forcing, four morphodynamic equilibria, two unstable and two stable, were found. The width-averaged characteristics of the Marsdiep-Vlie inlet system are reproduced by the idealized model.

Next, using a 2DH (depth-averaged) model with a rectangular geometry, the initial formation of channels and shoals is investigated for the morphodynamic equilibria which are linearly stable against one-dimensional perturbations, using perturbations that have a lateral structure. When morphodynamic equilibria are unstable due to diffusive mechanisms, the associated eigenvalues are real, and, hence the channel-shoal patterns can only grow/decay in time. When morphodynamic equilibria are unstable due to advective mechanisms, the associated eigenvalues become complex, such that the eigen patterns not only can grow/decay in time, but also migrate.

An idealized 2DH model is finally used to study the morphodynamic equilibria with a lateral structure in a short rectangular double-inlet system. In this case, only diffusive mechanisms are important and considered. If the friction parameter and the width are larger than a critical value, multiple morphodynamic equilibria can exist. The corresponding bifurcation diagrams are constructed by varying separately the friction parameter and the tidal system width.

5.2. DISCUSSION OF THE RESEARCH QUESTIONS

In this thesis, the morphodynamic equilibria of a double-inlet system, as well as their linear stability have been studied using an idealized model. These investigations enable us to answer the research questions posed in Chap. 1. In what follows, the questions addressed in Chap. 1 are repeated and answered.

- **Q1: How do variations in tidal forcings influence the morphodynamic equilibria in double-inlet systems? Specifically, how do these variations influence the existence and uniqueness of morphodynamic equilibria?**

Using direct root-finding approaches in a cross-sectionally averaged model, the sensitivity of the morphodynamic equilibria on tidal forcings was studied. It has been shown that no morphodynamic equilibrium, one morphodynamic equilibrium or more than one equilibrium configurations can exist, depending on the M_2 tidal constituent prescribed at the seaward boundaries. In case of no morphodynamic equilibrium, the water depth vanishes somewhere within the tidal basin and the double inlet system reduces to two uncoupled single-inlet systems. For a specific tidal forcing condition, even four morphodynamic equilibria, two stable and two unstable, were found. (Chap. 2)

- **Q2: How does the planform geometry of the double-inlet systems influence the resulting morphodynamic equilibria and how do resulting morphodynamic equilibria compare with observations in the Marsdiep-Vlie inlet system?**

The equilibrium bed profiles, as well as the directions of the sediment transport, were found to strongly depend on the prescribed width profile. In order to qualitatively compare the model results with the observations in the Marsdiep-Vlie inlet system, the width variations observed in this inlet system were taken into account. The resulting equilibrium bed profile showed a good qualitative agreement with the observed width-averaged basin bathymetry. Moreover, the model predicts a sediment transport from the Marsdiep inlet to the Vlie inlet, which has the same order of magnitude as the transport computed with more advanced numerical models. (Chap. 2)

- **Q3: What are key mechanisms resulting in the initiation and formation of channels and shoals in double-inlet systems?**

Both diffusive and advective mechanisms are responsible for the formation of channel-shoal patterns. These patterns are usually localized near local maxima of water depth. When the morphodynamic equilibria are linearly unstable due to a diffusive mechanism, the associated eigenvalues are real. When the instabilities

are governed by both diffusive and advective mechanisms, the associated eigenvalues become complex, resulting in a cyclic growth of equilibrium bed profiles. (Chap. 3)

- **Q4: How does the number and stability of the resulting two-dimensional morphodynamic equilibria depend on the friction and width?**

The number of the resulting two-dimensional morphodynamic equilibria sensitively depends on the friction parameter and tidal system width. When both the friction and width are larger than a critical value, multiple morphodynamic equilibria exist leading to intricate bifurcation configurations (Chap. 4)

5.3. OUTLOOKS

In this thesis, the morphodynamic equilibria in a double-inlet system were studied, answering to the research questions reported above. However, improvements of the analysis and further investigations are recommended.

Further attention must be paid to study the influence of different parameterizations. In the present idealized model many assumptions were made, which might have an influence on the resulting morphodynamic equilibria. For example, the width distributions can seriously change equilibrium bed profiles, as well as the direction of the net sediment transport. In this thesis, a rectangular geometry has been used as a first approximation when discussing the 2DH results. The type of sediment, which is assumed to be fine sand in this thesis, might also have an influence on the morphodynamic equilibria.

It is also recommended to investigate the linear stability of the morphodynamic equilibria. In this thesis, the channel-shoal patterns are very localized, while the observed channels and shoals are usually longer in extent and further studies are necessary. Moreover, the formulation of sediment transport might also influence linear stability.

It is also recommended to further study channels and shoals in a long double-inlet system, including in the model also the advective transports. The 2DH idealized model in this thesis studied a short basin, which is a half of the length of the Marsdiep-Vlie inlet system. Long basins might be characterised by different morphodynamic equilibria, and bifurcation configurations.

REFERENCES

- [1] H. M. Schuttelaars and H. E. de Swart, *Multiple morphodynamic equilibria in tidal embayments*, *Journal of Geophysical Research* **105**, 105 (2000).
- [2] C. J. Meerman, H. M. Schuttelaars, and V. Rottschäfer, *Influence of geometrical variations on morphodynamic equilibria for single inlet systems*, *Ocean Dynamics* **69**, 2 (2019).

A

SUPPORTING INFORMATION FOR "MORPHODYNAMIC EQUILIBRIA IN DOUBLE-INLET SYSTEMS: THEIR EXISTENCE AND STABILITY"

A.1. VELOCITY SCALE

To obtain the typical velocity scale, a double-inlet system of constant width B , length L and uniform depth H is considered. The linearized continuity and momentum equation, ignoring bottom friction and Coriolis, are combined, resulting in (Ippen [1]):

$$\frac{\partial^2 \zeta}{\partial t^2} + gH \frac{\partial^2 \zeta}{\partial x^2} = 0, \quad (\text{A.1})$$

with boundary conditions $\zeta(0, t) = A_{M_2}^I \cos(\sigma t - \phi_{M_2}^I)$ and $\zeta(L, t) = A_{M_2}^{II} \cos(\sigma t - \phi_{M_2}^{II})$. By substituting $\zeta(x, t) = \hat{\zeta} \exp(i\sigma t)$, an explicit expression for $\hat{\zeta}$ is found, reading

$$\hat{\zeta} = \frac{1}{e^{ikL} - e^{-ikL}} \left[(\tilde{B} - \tilde{A}e^{-ikL}) e^{ikx} + (\tilde{A}e^{ikL} - \tilde{B}) e^{-ikx} \right], \quad (\text{A.2})$$

with $\tilde{A} = A_{M_2}^I \exp(-i\phi_{M_2}^I)$, $\tilde{B} = A_{M_2}^{II} \exp(-i\phi_{M_2}^{II})$, and $k = \sigma / \sqrt{gH}$. Using the linearized momentum equation, the velocity $u = \hat{u} \exp(i\sigma t)$ is found to have as amplitude

$$\hat{u} = -\frac{gk}{\sigma} \frac{1}{e^{ikL} - e^{-ikL}} \left[(\tilde{B} - \tilde{A}e^{-ikL}) e^{ikx} + (\tilde{A}e^{ikL} - \tilde{B}) e^{-ikx} \right]. \quad (\text{A.3})$$

To get an estimate for the typical velocity scale in the double-inlet systems, assume that $kL \ll 1$. Using a Taylor expansion for \hat{u} , we find that

$$\hat{u} \sim -\frac{g}{\sigma} \left\{ \frac{\tilde{B} - \tilde{A}}{L} - \frac{[3(x/L)^2 - 1] \tilde{B} - [3(x/L)^2 - 6x/L + 2] \tilde{A}}{6L} (kL)^2 \right\}. \quad (\text{A.4})$$

| Scheme | Degree of Lagrange element corresponding to $[h, \zeta^{00}, u^{00}, C^{00}, \zeta^{10}, u^{10}, C^{10}, \zeta^{01}, u^{01}, C^{01}]$ | Number of elements | Degrees of freedom |
|---------------------|---|--------------------|--------------------|
| <i>Advective</i> | [1, 1, 1, 1, 1, 1, 1, 1, 1, 1] | 1000 | 22022 |
| <i>HR Advective</i> | [2, 2, 2, 2, 2, 2, 2, 2, 2, 2] | 1000 | 44044 |

Table A.1: The possible choices of degree of Lagrange elements for each variable and the number of elements. The variables, for example ζ_{c1}^{00} and ζ_{s1}^{00} , are abbreviated as ζ^{00} . In total there are 22 unknowns per element when using $p = 1$ elements and 44 unknowns when using $p = 2$ elements.

Assuming $\tilde{A} \neq 0$, substitute $\tilde{B} = \tilde{A} + \Delta\tilde{A}$ in the above expression (if $\tilde{A} = 0$, interchange the role of \tilde{A} and \tilde{B}). This results in

$$\hat{u} \sim -\frac{g}{\sigma} \left\{ \frac{\Delta\tilde{A}}{L} + \frac{(2x/L - 1)}{2L} \tilde{A} (kL)^2 \right\}, \tag{A.5}$$

where it has been assumed that $|\Delta\tilde{A}| \ll |\tilde{A}|$. If the first term on the right hand side is much larger than the second term (i.e., if $|\Delta\tilde{A}|/|\tilde{A}| \gg (kL)^2$), the typical velocity scale is given by $U_1 = g|\Delta\tilde{A}|/\sigma L$. If the second term dominates, the characteristic velocity scale reads $U_2 = g|\tilde{A}|Lk^2/\sigma = |\tilde{A}|\sigma L/H$. The first velocity scale U_1 can be rewritten as

$$U_1 = \frac{1}{(kL)^2} \frac{|\Delta\tilde{A}|}{|\tilde{A}|} U_2. \tag{A.6}$$

For the double-inlet systems considered in this paper, we assume that $U_1 \sim U_2$. Hence the typical velocity scale used to make the equations dimensionless is defined as $U = U_2 = A_{M_2}^I \sigma L/H$. We would like to stress that this derivation is only strictly valid for *short* basins. However, we will use this scaling for long basins as well. We checked a posteriori that the scaling of the resulting velocities was valid for all cases considered.

A.2. DETAILS CONCERNING THE NUMERICAL IMPLEMENTATION

A.2.1. ELEMENT ORDER

When discretizing the system of equations using a finite element method, the order of the continuous Lagrange elements (Alnæs *et al.* [2]) used for the various physical quantities has to be chosen. In Tab.A.1, two choices of the degree of the Lagrange elements for each variable, the number of elements used and the resulting number of degrees of freedom to discretize the equations are given. The first choice, denoted as *Advective* is generally used to obtain the results in the main text. However, there are small regions in the parameter space where either a better spatial resolution or a higher degree of the Lagrange elements is necessary to get well converged results. The numerical setup for these experiment is denoted by *HR* (high resolution) *Advective*.

A.2.2. NUMERICAL BIFURCATION APPROACH

By employing a root-finding method, we directly solve for equilibrium states $\tilde{\Psi}_e$ of the discretized system of equations,

$$\mathcal{G}(\tilde{\Psi}_e, \mathbf{p}_0) = 0, \tag{A.7}$$

in which \mathbf{p}_0 is a vector of prescribed parameter values. To obtain equilibrium solutions $\tilde{\Psi}_e$ of Eq. (A.7), a Newton-Raphson iterative method is used. The iterations in the Newton-Raphson method are given by

$$\mathcal{G}(\tilde{\Psi}_i, \mathbf{p}_0) + \mathcal{J}_{\mathcal{G}}(\tilde{\Psi}_i, \mathbf{p}_0) \Delta \tilde{\Psi}_{i+1} = 0, \quad (\text{A.8})$$

in which $\tilde{\Psi}_i$ is the i_{th} approximation of $\tilde{\Psi}_e$, $\Delta \tilde{\Psi}_{i+1}$ is a correction to $\tilde{\Psi}_i$, and $\mathcal{J}_{\mathcal{G}}(\tilde{\Psi}_i)$ is the Jacobian matrix of operator \mathcal{G} evaluated in $\tilde{\Psi}_i$. In the next iteration, $\tilde{\Psi}_{i+1} = \tilde{\Psi}_i + \Delta \tilde{\Psi}_{i+1}$. During the iterations, it may occur that $\max(\tilde{h}_{i+1}) > 1$, which is not allowed from a physical point of view, as this indicates that the bed level is above the undisturbed water level somewhere in the domain of interest. This can be avoided by introducing a control parameter θ , which satisfies $0 < \theta \leq 1$, such that $\tilde{h}_i + \theta \Delta \tilde{h}_{i+1} < 1$. Numerically, this is reflected by using underrelaxation to obtain the next update: $\tilde{\Psi}_{i+1} = \tilde{\Psi}_i + \theta \Delta \tilde{\Psi}_{i+1}$. If the correction $\Delta \tilde{\Psi}_{i+1}$ is sufficiently small (in our experiments when the maximum of the absolute value of $\Delta \tilde{\Psi}_{i+1}$ is smaller than 10^{-8}), we stop the iteration and identify $\tilde{\Psi}_i$ as a morphodynamic equilibrium $\tilde{\Psi}_e$.

In this paper, we aim at finding morphodynamic equilibria using the *numerical bifurcation* approach. In this approach parameters are slowly varied, and the previously obtained equilibrium solutions are used as first guess in the iteration process. The continuation method employed in this paper is the arclength method [3], resulting in a fast convergence, even when the water depth is very small. For the arclength method, the known morphodynamic equilibrium, denoted by $\tilde{\Psi}_e$, is associated with the value p_e corresponding to parameter p , which is the only parameter varied out of all parameters in the parameter vector \mathbf{p}_0 . The new equilibrium $\tilde{\Psi}'_e$, and value p'_e are expected to be approximated by $\tilde{\Psi}_e + \tilde{\Psi}_f$ and $p_e + p_f$, where $\tilde{\Psi}_f$ is a small correction to $\tilde{\Psi}_e$ and p_f is a small correction to parameter p_e .

To obtain $\tilde{\Psi}_f$ and p_f , the Newton-Raphson method is again applied, but now the operator \mathcal{G} is derived with respect to both $\tilde{\Psi}$ and p :

$$\begin{aligned} & \mathcal{J}_{\mathcal{G}}(\tilde{\Psi}_e + \tilde{\Psi}_{f,i}, p_e + p_{f,i}) \Delta \tilde{\Psi}_{i+1} + \mathcal{G}_p(\tilde{\Psi}_e + \tilde{\Psi}_{f,i}, p_e + p_{f,i}) \Delta p_{i+1} \\ + & \mathcal{G}(\tilde{\Psi}_e + \tilde{\Psi}_{f,i}, p_e + p_{f,i}) = 0, \end{aligned} \quad (\text{A.9})$$

where \mathcal{G}_p , which is usually referred to as the load vector, is the derivative of operator \mathcal{G} with respect to parameter p . The update of $\tilde{\Psi}_f$ is $\tilde{\Psi}_{f,i+1} = \tilde{\Psi}_{f,i} + \Delta \tilde{\Psi}_{i+1}$, and the update of p_f is $p_{f,i+1} = p_{f,i} + \Delta p_{i+1}$.

Because an extra variable is introduced, the unknown parameter Δp_{i+1} , one more equation, the so-called constraint equation is required. Following Crisfield [4], the constraint equation reads

$$\|\tilde{\Psi}_{f,i} + \Delta \tilde{\Psi}_{i+1}\|^2 + (p_{f,i} + \Delta p_{i+1})^2 \|\mathcal{G}_p(\tilde{\Psi}_e + \tilde{\Psi}_{f,i}, p_e + p_{f,i})\|^2 = \Delta l^2, \quad (\text{A.10})$$

in which Δl is a fixed parameter, called the arc length. $\|\tilde{\Psi}_f\| = \sqrt{\tilde{\Psi}_f^T \cdot \tilde{\Psi}_f}$ is the length of $\tilde{\Psi}_f$. If both $\Delta \tilde{\Psi}_{i+1}$ and Δp_{i+1} are sufficiently small, we stop iteration, and identify $\tilde{\Psi}_e + \tilde{\Psi}_{f,i}$ as the morphodynamic equilibrium corresponding to $p_e + p_{f,i}$.

A.2.3. TIME-INTEGRATION METHOD

To assess the morphodynamic evolution to a morphodynamic equilibrium from an arbitrary initial condition, a time-integration method has to be applied. Here we use the backward Euler method to integrate the discretized morphodynamic system of equations,

$$\mathcal{K} \frac{\tilde{\Psi}_n - \tilde{\Psi}_{n-1}}{\Delta\tau} = \mathcal{G}(\tilde{\Psi}_n, \mathbf{p}_0), \quad (\text{A.11})$$

where $\Delta\tau$ is the morphodynamic time step size, $\tilde{\Psi}_n = \tilde{\Psi}(t = n\Delta\tau)$ is the evolution of $\tilde{\Psi}$ at time $\tau = n\Delta\tau$. The prescribed initial condition is denoted by $\tilde{\Psi}_0$. In all experiments, we take $\Delta\tau$ such that its dimensional value corresponding to a time step of 100 years.

Eq.(A.11) can be numerically solved using the Newton-Raphson method, resulting in

$$\mathcal{K} \frac{\tilde{\Psi}_{n,i} + \Delta\tilde{\Psi}_{n,i+1} - \tilde{\Psi}_{n-1}}{\Delta\tau} = \mathcal{G}(\tilde{\Psi}_{n,i}, \mathbf{p}_0) + \mathcal{J}\mathcal{G}(\tilde{\Psi}_{n,i}, \mathbf{p}_0)\Delta\tilde{\Psi}_{n,i+1}. \quad (\text{A.12})$$

The new approximation, denoted by $\tilde{\Psi}_{n,i+1}$, is $\tilde{\Psi}_{n,i+1} = \tilde{\Psi}_{n,i} + \theta\Delta\tilde{\Psi}_{n,i+1}$, where θ is again a control parameter. If the correction $\Delta\tilde{\Psi}_{n,i+1}$ is sufficiently small, we stop the Newton-Raphson iteration and $\tilde{\Psi}_{n,i}$ is the morphodynamic solution at time $n\Delta\tau$. If the difference between $\tilde{\Psi}_n$ and $\tilde{\Psi}_{n-1}$ is sufficiently small (here 10^{-8} is taken), an equilibrium state is reached.

A.3. SENSITIVITY OF MORPHODYNAMIC EQUILIBRIA TO INLET DEPTH AND PRESCRIBED TIDALLY-AVERAGED WATER TRANSPORT

A.3.1. VARYING INLET DEPTHS

To assess the influence of a depth difference between the two inlets, the depth of inlet II is varied from 9 m to 14 m. Again, the amplitude of the externally prescribed overtides and the tidally-averaged water transport at inlet II are put to zero, using the default values for all other parameters. For clarity, we only focus on linearly stable equilibria.

In Fig. A.1a the water depth (with colder colors denoting larger water depths and warmer colors smaller water depths) of the stable equilibria is shown as a function of position in the embayment (horizontal axis) and the water depth at inlet II, H^{II} on the vertical axis. From this figure, it follows that the location of WD_{\max} is found closer to inlet I. When H^{II} becomes larger, WD_{\max} is moving towards the middle of the tidal inlet system. In Fig. A.1c the water depth of the stable equilibria with $H^{II} = 10, 11.9, 14$ m is explicitly shown.

Fig.A.1b shows the total sediment transport of the stable morphodynamic equilibria as a function of H^{II} . When H^{II} increasing from 9 m to 14 m, the total sediment transport decreases from 64 kgs^{-1} to 20 kgs^{-1} .

A.3.2. VARYING RESIDUAL WATER TRANSPORT AT INLET II

To assess the influence of the prescribed tidally-averaged water transport Q_* at inlet II on the morphodynamic equilibria, Q_* is varied from $-2000 \text{ m}^3 \text{ s}^{-1}$ to $2000 \text{ m}^3 \text{ s}^{-1}$, with

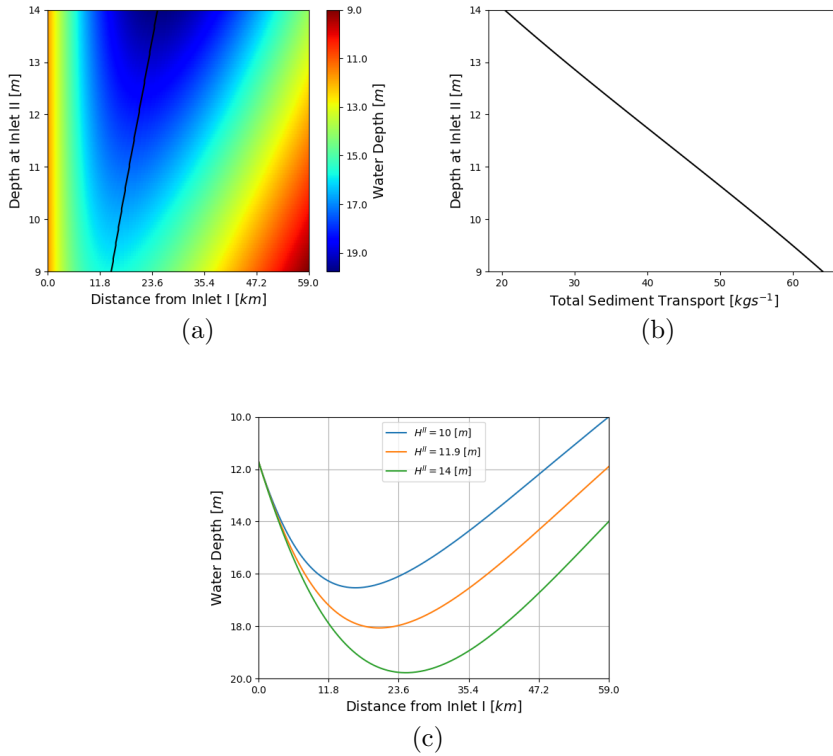


Figure A.1: Stable morphodynamic equilibria for varying H^{II} , including diffusive and internally generated advective processes with $A_{M_2}^{\text{II}} = 0.77 \text{ m}$ and $\phi_{M_2}^{\text{II}} = 54^\circ$. In panel (a), the bed profiles of stable morphodynamic equilibria with H^{II} varying from 9 m to 14 m are shown as a color image. Panel (b) shows the total sediment transport (horizontal axis) of stable equilibria as a function of H^{II} (vertical axis). In panel (c), some selected bed profiles of stable morphodynamic equilibria are shown.

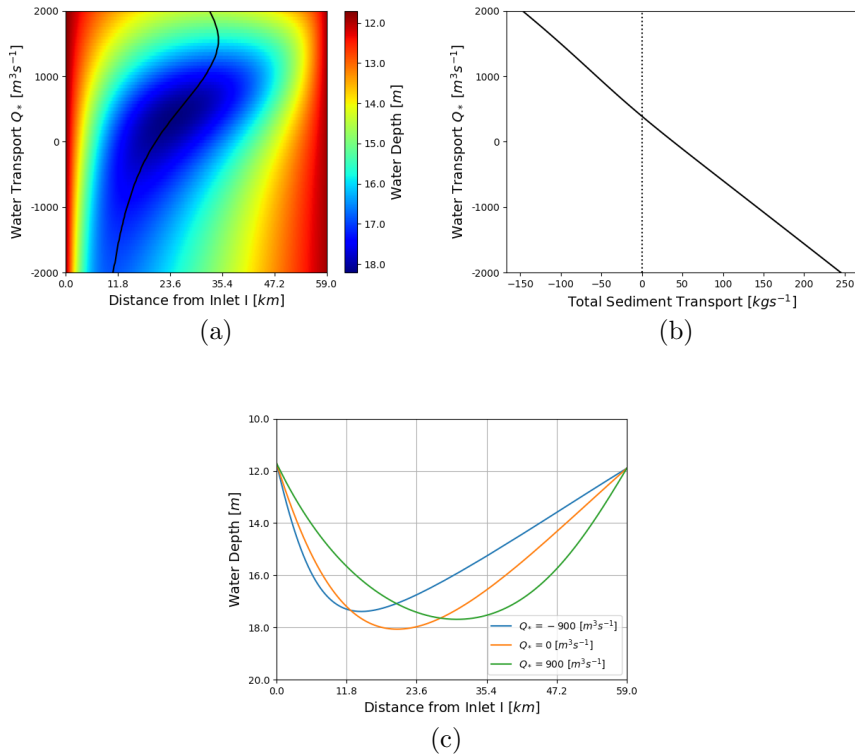


Figure A.2: Stable morphodynamic equilibria for varying Q_* , including diffusive and internally generated advective processes, with $A_{M_2}^H = 0.77$ m, $\phi_{M_2}^H = 54^\circ$ and $H^H = 11.9$ m. In panel (a), the bed profiles of stable morphodynamic equilibria with Q_* varying from $-2000 m^3 s^{-1}$ to $2000 m^3 s^{-1}$ are shown as a color image. Panel (b) shows the total sediment transport of stable equilibria on the horizontal axis as a function of Q_* on the vertical axis. In panel (c), some selected bed profiles of stable morphodynamic equilibria are shown.

positive values indicating tidally-averaged water transport from inlet I to inlet II. The amplitude of the externally prescribed overtides and the tidally-averaged water transport at inlet II are put to zero, using the default values for all other parameters. For clarity, we only focus on linearly stable equilibria, and all other parameters have their default values.

Fig.A.2a shows that WD_{\max} of the stable equilibria is approximately 16.5m when $-2000\text{m}^3\text{s}^{-1}$ and located 10km from inlet I. Varying Q_* from $-2000\text{m}^3\text{s}^{-1}$ to $500\text{m}^3\text{s}^{-1}$, WD_{\max} of the stable equilibria becomes larger, with WD_{\max} found closer to the middle of the double-inlet system. Increasing Q_* further from $500\text{m}^3\text{s}^{-1}$ to $1500\text{m}^3\text{s}^{-1}$ results in a smaller WD_{\max} found closer to the middle of the double-inlet system. When increasing Q_* even further, WD_{\max} still decreases but the location of maximum depth now moves away from the center of the double-inlet system, closer to inlet I. In Fig.A.2c the equilibrium water depth of the stable equilibria with $Q_* = -900, 0, 900\text{m}^3\text{s}^{-1}$ is shown.

Fig.A.2b shows the total sediment transport (horizontal axis) as a function of Q_* (vertical axis). When Q_* increasing from $-2000\text{m}^3\text{s}^{-1}$ to $2000\text{m}^3\text{s}^{-1}$, the total sediment transport decreases from $245\text{kg}\text{s}^{-1}$ to $-150\text{kg}\text{s}^{-1}$.

A.4. ADVECTIVE TRANSPORT CONTRIBUTIONS

The transport contributions in morphodynamic equilibria for a double-inlet system with rectangular planform geometry, including all forcing contributions, are shown in Fig. A.3 for $\phi_{M_4}^{\text{II}} \in \{0^\circ, -95^\circ, -121^\circ\}$, thus complementing Fig. 8 in the main text. The upper row concerns the transport terms for $\phi_{M_4}^{\text{II}} = -121^\circ$, for the middle row $\phi_{M_4}^{\text{II}} = -95^\circ$, and $\phi_{M_4}^{\text{II}} = 0^\circ$ for the bottom row. The left column shows the aggregated transport contributions, whereas the middle and right column show the various contributions to the internally generated and externally forced advective contributions, respectively.

The transport contributions in morphodynamic equilibria for a double-inlet system with varying width are shown in Fig. A.4, thus complementing Fig. 9 in the main text. The upper row concerns the transport terms for $c_0 = 0$ (a rectangular planform geometry), for the middle row $c_0 = 0.5$, and for the bottom row $c_0 = 1$. The left column shows the aggregated transport contributions, whereas the middle and right column show the various contributions to the internally generated and externally forced advective contributions, respectively.

REFERENCES

- [1] A. T. Ippen, *Tidal dynamics in estuaries, I: Estuaries of rectangular section*, in *Estuary and Coastline Hydrodynamics*, edited by A. T. Ippen (McGraw-Hill, New York, 1966) pp. 493–522.
- [2] M. Alnæs, J. Blechta, J. Hake, A. Johansson, B. Kehlet, A. Logg, C. Richardson, J. Ring, M. E. Rognes, and G. N. Wells, *The FEniCS project version 1.5*, [Archive of Numerical Software](https://arxiv.org/abs/1011.5462) **3** (2015), [10.11588/ans.2015.100.20553](https://doi.org/10.11588/ans.2015.100.20553).
- [3] R. Seydel, *Practical Bifurcation and Stability Analysis* (Springer, New York, 1994).

A

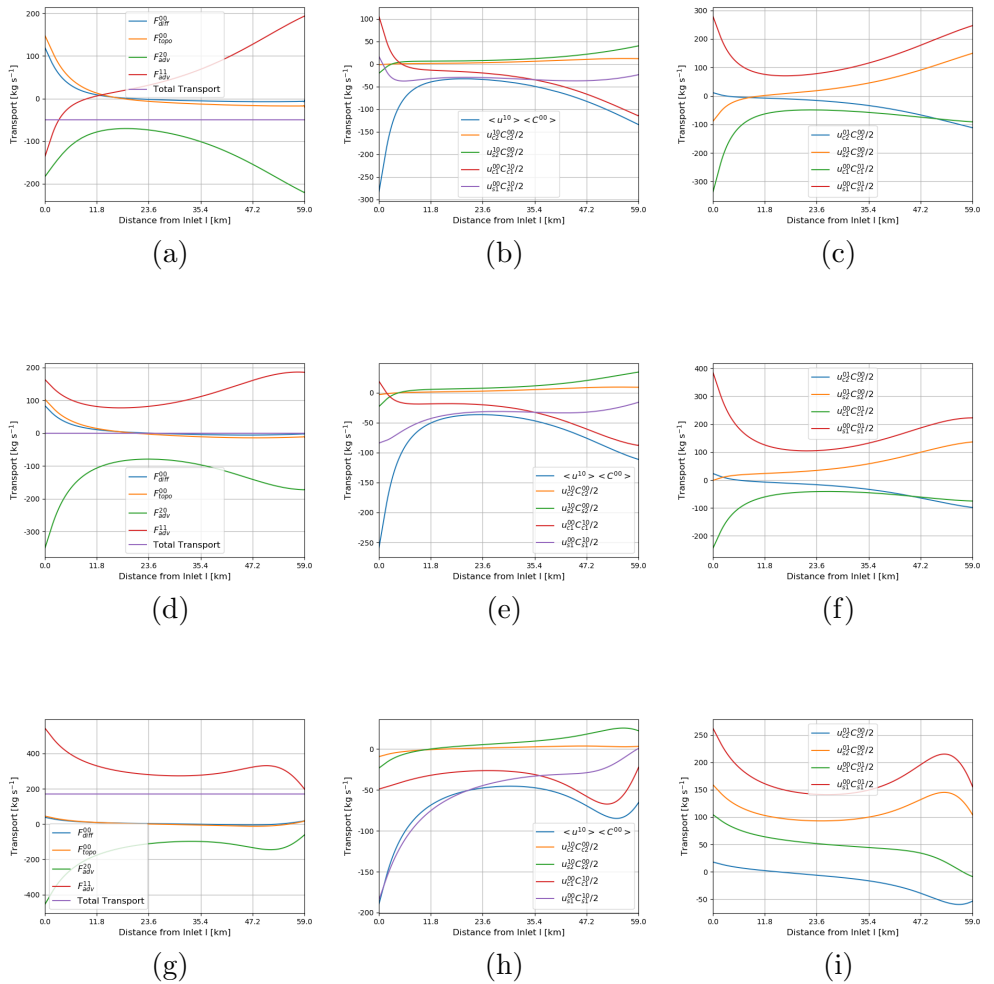


Figure A.3: Full decomposition of the various transport contributions, complementing Fig. 8 of the main paper.

- [4] M. A. Crisfield, *A fast incremental/iterative solution procedure that handles snap through*, *Computers and Structures* **13**, 55 (1981).

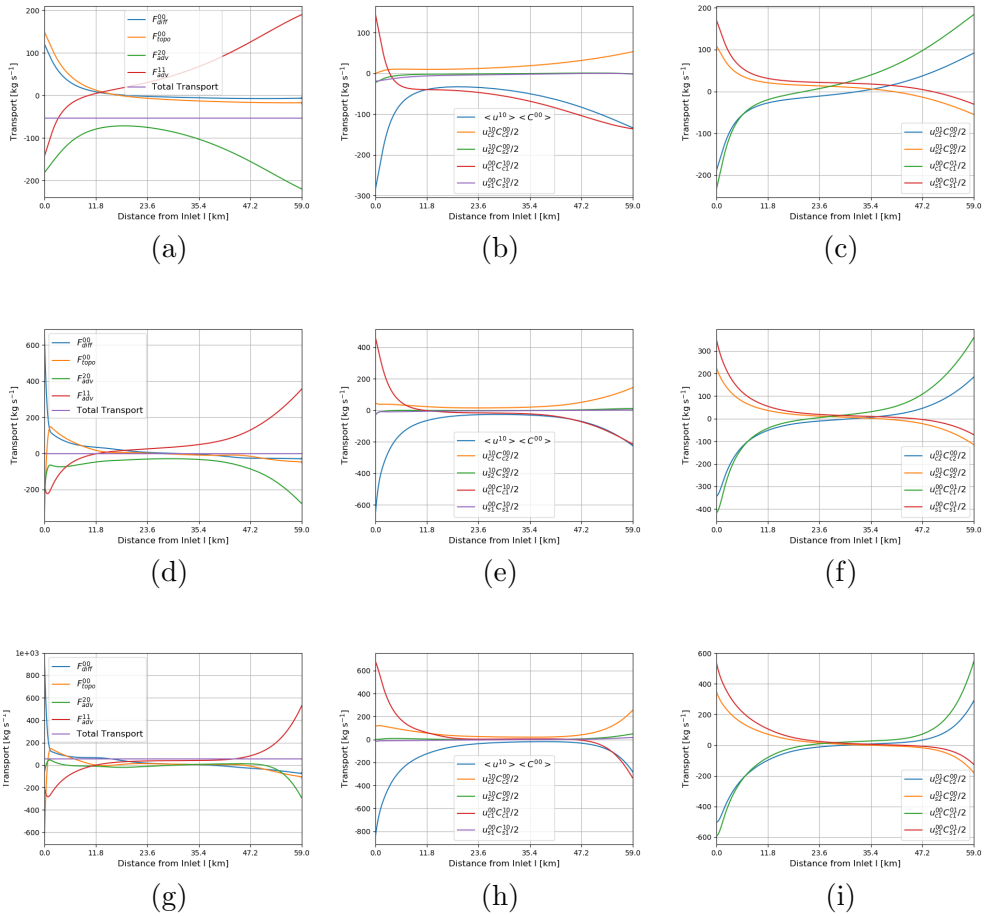


Figure A.4: Full decomposition of the various transport contributions, complementing Fig. 9 of the main paper.

B

MORPHODYNAMIC EQUILIBRIA IN SYSTEMS WITH DIFFUSIVELY DOMINATED TRANSPORT

When only taking diffusive transport into account, the influence of the forcing conditions on morphodynamic equilibria is presented in this appendix. The system of equations, forced only by prescribed M_2 tides at both inlets, is modeled in a rectangular geometry. In B.1, the morphodynamic equilibria when the system is dominated by diffusive transport without topographical variations is presented, while morphodynamic equilibria when taking diffusive transport with topographical variations into account is presented in B.2. All results are obtained using the parameter values in Tab.B.1, which are representative for the Marsdiep–Vlie inlet system, unless mentioned otherwise.

B.1. MORPHODYNAMIC EQUILIBRIA OF DIFFUSION WITHOUT TOPOGRAPHICAL VARIATIONS

When only diffusion without topographical variations is taken into account, neglecting the other processes, the bed evolution equation for morphodynamic equilibria reduces to

$$\frac{d}{dx} \langle F_{\text{diff}}^{00} \rangle = 0. \quad (\text{B.1})$$

In Fig.B.1a, the depth of the watersheds, i.e. WD_{min} (vertical axis), and their location (color code, with warmer colors closer to (one of) the entrance(s), and colder colors more towards the middle of the channel) for the morphodynamic equilibria are shown. Increasing $A_{M_2}^H$ from 0.37 [m] to 1.48 [m] results in a shift of the watershed from a location closer to inlet I to a location closer to inlet II. The black line in the figure denotes

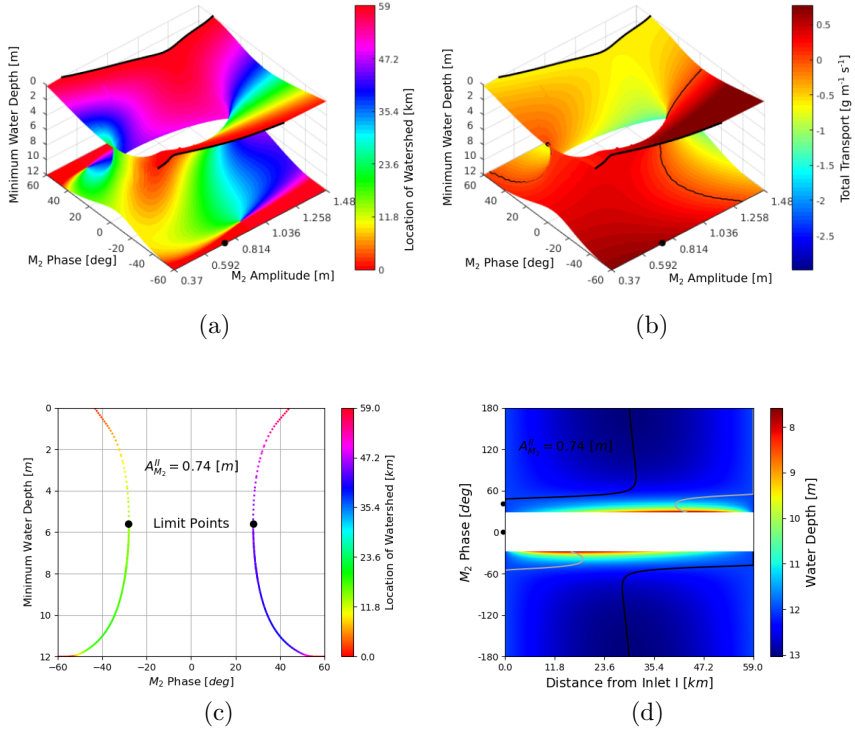


Figure B.1: Morphodynamic equilibria when only diffusion without topographical variations is taken into account. Panel (a) shows the WD_{\min} of the morphodynamic equilibria, its location is indicated by color code, as a function of $A_{M_2}^{II}$ varying from 0.37 m to 1.24 m and $\phi_{M_2}^{II}$ varying from -180° to 180° . Panel (b) shows the same WD_{\min} again, but its color code indicates the total (width-averaged) diffusive transport. In panel (c), the WD_{\min} of morphodynamic equilibria for $A_{M_2}^{II} = 0.74\text{ m}$ is shown as a function of $\phi_{M_2}^{II}$ varying from -60° to 60° . In panel (d) morphodynamic equilibrium bed profiles for $A_{M_2}^{II} = 0.74\text{ m}$ is shown as a function of $\phi_{M_2}^{II}$ varying from -180° to 180° and the distance from inlet I, where the location of WD_{\min} is indicated by gray contours and the location of the WD_{\max} is indicated by black contours.

| System | Sediment | Bed |
|---|--|-----------------------------------|
| $L = 59 \text{ km}$ | $k_{h*} = 10^2 \text{ m}^2 \text{ s}^{-1}$ | $\rho_s = 2650 \text{ kg m}^{-3}$ |
| $g = 9.81 \text{ m s}^{-2}$ | $\alpha = 0.5 \cdot 10^{-2} \text{ kg s m}^{-4}$ | $p = 0.4$ |
| $c_d = 0.0025$ | $w_s = 0.015 \text{ m s}^{-1}$ | |
| $\sigma = 1.4 \cdot 10^{-4} \text{ s}^{-1}$ | $k_{v*} = 0.1 \text{ m}^2 \text{ s}^{-1}$ | |
| $T = 44.9 \cdot 10^3 \text{ s}$ | $d_{50} = 2 \cdot 10^{-4} \text{ m}$ | |
| Marsdiep Inlet | Vlie Inlet | |
| $H^I = 12 \text{ m}$ | $H^{II} = 12 \text{ m}$ | |
| $A_{M_2}^I = 0.74 \text{ m}$ | $A_{M_2}^{II} = 0.84 \text{ m}$ | |
| $\phi_{M_2}^I = 148^\circ$ | $\phi_{M_2}^{II} = -158^\circ$ | |
| $B^I = 6000 \text{ m}$ | $B^{II} = 6000 \text{ m}$ | |

Table B.1: The variables in this table are defined in the following paragraphs. Characteristic values for the Marsdiep-Vlie inlet system are taken from Ridderinkhof [1], Duran-Matute *et al.* [2].

the location where the WD_{\min} vanishes, namely where two single-inlet systems begin to form. The diffusive transport without topographical variations defined in Eq.(2.20) is location-independent in morphodynamic equilibrium, and hence indicates the direction of the residual sediment transport. This is shown in Fig.B.1b by color code. The two thin black contour lines indicate where a zero diffusive transport is found. Positive total diffusive transport implies that there is a net (i.e., tidally averaged) sediment transport from inlet I to inlet II, while negative diffusive transport indicates a net transport from inlet II to inlet I. Increasing $A_{M_2}^{II}$ and/or $\phi_{M_2}^{II}$ results in a decrease of net transport from inlet II to inlet I on the left of the two contour lines, and an increase of net transport on the right of those contours.

To demonstrate the bifurcation structure, the WD_{\min} of morphodynamic equilibria for $A_{M_2}^{II} = 0.74 \text{ [m]}$ and varying $\phi_{M_2}^{II}$ between -60° and 60° is shown in Fig.B.1c, while the location of the watershed is indicated by color code. This figure corresponds to the results in Fig.B.1a for $A_{M_2}^{II} = 0.74 \text{ [m]}$, which is indicated by a black dot. Using arclength method, increasing (decreasing) $\phi_{M_2}^{II}$ from -60° (60°) to -28.1° (28.1°), morphodynamic equilibria can be with WD_{\min} decreasing from 12 [m] to 5.5 [m] and a limit point indicated by a black dot can be found at $\pm 28.1^\circ$. After the limit point, decreasing (increasing) $\phi_{M_2}^{II}$ from -28.1° (28.1°) to -45° (45°), new morphodynamic equilibria with WD_{\min} decreasing from 5.5 [m] to zero can be found. The analysis of the linear stability of the morphodynamic equilibria by calculation of the associated eigenvalues shows that the morphodynamic equilibria indicated by the solid line, are linearly stable, while those indicated by the dashed line are linearly unstable.

In Fig.B.1d, the water depth (with colder colors denoting larger water depths and warmer colors smaller water depths) of morphodynamic equilibria for $A_{M_2}^{II} = 0.74 \text{ [m]}$ are shown as a function of $\phi_{M_2}^{II}$ varying from -180° to 180° and the distance from inlet I. If no equilibrium for which the two inlets are connected is found, a white color code is used. The equilibrium water depth strongly depends on the tidal phase at inlet II. Increasing $\phi_{M_2}^{II}$ from -180° to -29° or decreasing $\phi_{M_2}^{II}$ from 180° to 29° results in reducing the WD_{\min} , its location is indicated by gray lines, from 12 [m] to 7.7 [m] . The WD_{\max} is

indicated by black lines.

B.2. MORPHODYNAMIC EQUILIBRIA OF DIFFUSION WITH TOPOGRAPHICAL VARIATIONS

When diffusion with topographical variations is taken into account, the resulting equilibria satisfy the following morphodynamic equilibrium condition:

$$\frac{d}{dx} (\langle F_{\text{diff}}^{00} \rangle + \langle F_{\text{topo}}^{00} \rangle) = 0. \quad (\text{B.2})$$

In Fig.B.2a, the WD_{min} and its location (color coded as in B.1a) of morphodynamic equilibria are shown for $A_{M_2}^H$ varying from 0.37 [m] to 1.48 [m] and $\phi_{M_2}^H$ varying from -60° to 60° . Similar to Fig.B.1a, increasing $A_{M_2}^H$ from 0.37 [m] to 1.48 [m] results in a shift of the watershed from a location closer to inlet I to a location closer to inlet II. The black line in this figure also denotes the location where the WD_{min} vanishes. Like Fig.B.1b, the total sediment transport, which is a constant every where in the model rectangular embayment and consists of contributions of diffusive transport and topographical variations, is depicted in Fig.B.2b, with positive values indicating a net sediment transport from inlet I to inlet II, while negative values indicate a net sediment transport from inlet II to inlet I.

Unlike the case when taking diffusion without topographical variations into account, there exists three the morphodynamic equilibria in certain combination of M_2 amplitude and phase at inlet II when diffusive transport with topographical variations being taken into account, which is demonstrates in Fig.B.2c. In this figure, the WD_{min} is shown for fixed $A_{M_2}^H = 1.080$ [m] corresponding to the black dot in B.1a and $\phi_{M_2}^H$ varying from -60° to 60° , with its position color coded. Increasing $\phi_{M_2}^H$ from -60° to approximately 27° results in a decrease of the WD_{min} . For approximately $\phi_{M_2}^H = 27^\circ$ the WD_{min} becomes zero. Decreasing $\phi_{M_2}^H$ from 60° to 22.2° results in a decrease of the MinWD to approximately 6[m]. For $\phi_{M_2}^H = 22.2^\circ$ a limit point is found, indicated by a black dot in Fig.B.2a. Increasing $\phi_{M_2}^H$ again, starting from the equilibria at the limit point, results in a decreases of the WD_{min} to zero. Linear stability analyses of the various morphodynamic equilibria show that the morphodynamic equilibria indicated by the solid lines are stable, while those indicated by the dashed lines are unstable. From Fig.B.2a it follows that for phases $22.2^\circ \leq \phi_{M_2}^H \leq 27^\circ$, there exist multiple equilibria, of which two are stable.

REFERENCES

- [1] H. Ridderinkhof, *Tidal and residual flows in the western dutch wadden sea i1: An analytical model to study the constant flow between connected tidal basins*, Netherlands Journal of Sea Research **22**, 185 (1988).
- [2] M. Duran-Matute, T. Gerkema, G. J. de Boer, J. J. Nauw, and U. Grawe, *Residual circulation and freshwater transport in the Dutch Wadden Sea: a numerical modelling study*, Ocean Science **10**, 611 (2014).

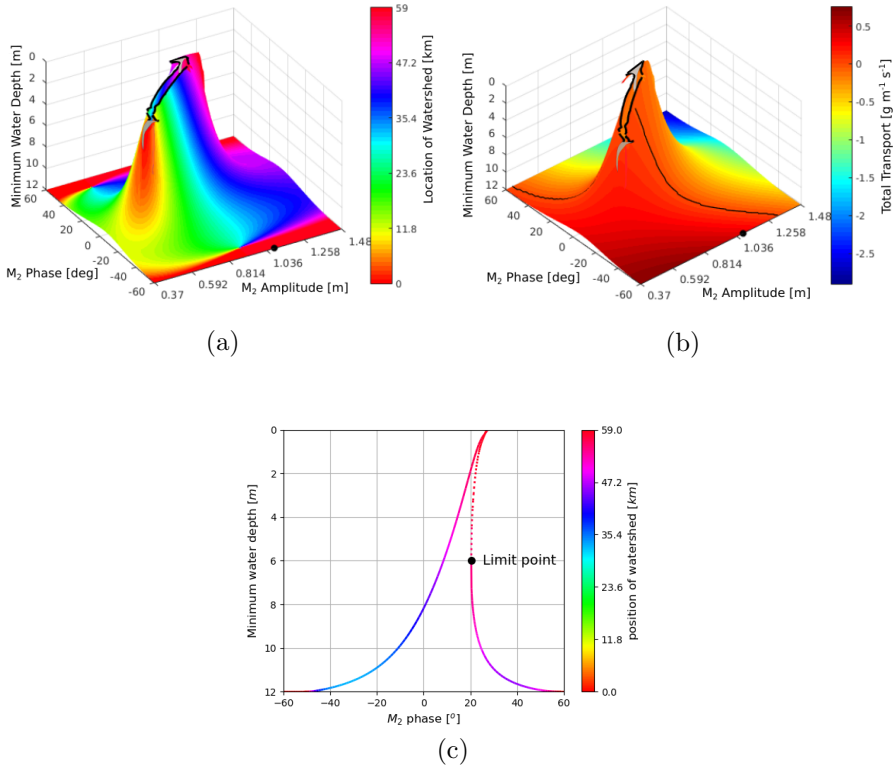


Figure B.2: Morphodynamic equilibria when taking diffusive transport with topographical variations into account. Both panel (a) and (b) show the WD_{\min} of morphodynamic equilibria as a functions of $A_{M_2}^H$ varying from 0.37 [m] to 1.48 [m] and $\phi_{M_2}^H$ varying from -60° to 60° . In panel (a) the position of WD_{\min} is color coded, and in panel (b) the total transport. In panel (a) the WD_{\min} of the morphodynamic equilibria is shown for a fixed $A_{M_2}^H = 1.080$ [m] and $\phi_{M_2}^H$ varied from -60° to 60° , the positions of WD_{\min} are color coded.

C

INITIAL FORMATION OF CHANNEL–SHOAL PATTERNS IN DOUBLE–INLET SYSTEMS: DIFFUSIVELY DOMINATED TRANSPORT

The influence of the relative M_2 phase, $\Delta\phi_{M_2}$, on the diffusively dominated morphodynamic equilibria is investigated. For simplicity, the undisturbed water depth at inlet II is taken to be equal to 11.7 m, the same water depth as inlet I . All other parameter values are taken from Tab. 3.2. When the sediment transport is dominated by diffusion, the morphodynamic equilibrium condition reduces to

$$\nabla \cdot \left(\langle \mathbf{F}_{\text{diff}}^{00} \rangle + \langle \mathbf{F}_{\text{topo}}^{00} \rangle + \langle \mathbf{F}_{\text{bed}} \rangle \right) = 0. \quad (\text{C.1})$$

In a rectangular geometry, morphodynamic equilibria which are laterally uniform can be found using the bifurcation approach discussed in Deng *et al.* [1]. As an example, Fig. C.1a shows the minimum water depths WD_{min} of these morphodynamic equilibria as a function of $\Delta\phi_{M_2}$ varying from -60° to 60° . It demonstrates that the existence of morphodynamic equilibria depends on the relative M_2 phase: for $\Delta\phi_{M_2}$ between 10° to 16° , no morphodynamic equilibrium is found for which both inlets are connected. For other relative M_2 phases considered, there is always a 1D–stable equilibrium.

To investigate the linear stability of these 1D–stable morphodynamic equilibria to the perturbations with lateral structure, morphodynamic equilibria obtained with $\Delta\phi_{M_2} = 19^\circ$ (orange), $\Delta\phi_{M_2} = 20^\circ$ (green) and $\Delta\phi_{M_2} = 25^\circ$ (red) are examined. Their bed profiles are shown in Fig. C.1b. These three equilibrium bed profiles correspond to WD_{min} indicated by crosses (with colors associated to their bed profiles) in Fig. C.1a. The largest

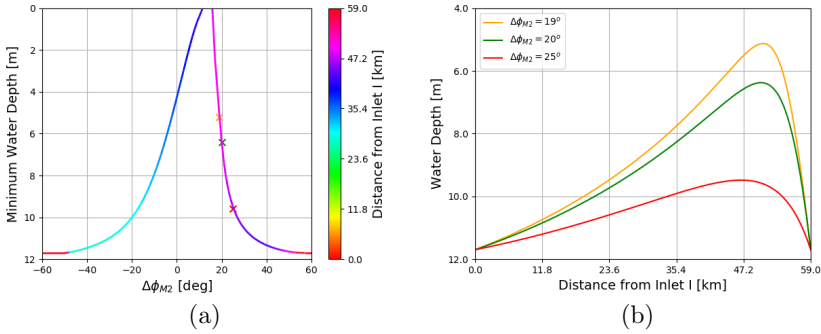


Figure C.1: Laterally uniform morphodynamic equilibria for diffusively dominated transport. Panel (a) shows WD_{\min} the minimum water depth of equilibrium bed profiles, with its location coded with color. Panel (b) shows the equilibrium bed profiles for three different values of $\Delta\phi_{M_2}$. The minimum water depths in the cases shown in panel(b) are indicated by cross-shaped markers in panel (a).

dimensionless growth rate $\Re(\omega)$ of these three morphodynamic equilibria as a function of dimensionless wave number l_n is shown in Fig.C.2a. It shows that at $l_n = 0$ the largest dimensionless growth rate $\Re(\omega)$ is negative for all three selected $\Delta\phi_{M_2}$, which shows these three morphodynamic equilibria are 1D–stable. Increasing the dimensionless wave number l_n from 0 to 1200, the largest dimensionless growth rate $\Re(\omega)$ for $\Delta\phi_{M_2} = 19^\circ$ first increases, till a maximum is obtained at approximately $l_n = 560$, and then decreases to become negative for $l_n \sim 1200$. Positive $\Re(\omega)$ indicates that the laterally uniform morphodynamic equilibrium for $\Delta\phi_{M_2} = 19^\circ$ is unstable against perturbations with a lateral structure. Unlike $\Delta\phi_{M_2} = 19^\circ$, the largest dimensionless growth rate $\Re(\omega)$ for $\Delta\phi_{M_2} = 25^\circ$ is negative for all l_n considered, which indicates the corresponding equilibrium is stable against perturbations with lateral structure. The critical value of the relative M_2 phase, $\Delta\phi_{M_2}$, that separates stable and unstable morphodynamic equilibrium against perturbations with lateral structure, is $\Delta\phi_{M_2} = 20^\circ$.

When using width $B = 6 \text{ km}$, the dimensionless wave number $l_n = 555.9$, at which $\Re(\omega)$ for $\Delta\phi_{M_2} = 19^\circ$ reaching a maximum, corresponds to a mode number $n = 18$. The bed patterns h_n for $n = 18$ ($l_n = 555.9$) are shown in Fig. C.2c. Compared with the bed patterns for $n = 0$ shown in Fig. C.2b, the bed patterns for $n = 18$ are more localized, i.e., the bed patterns for $n = 18$ are nonzero within a region of approximately 15 km , while the bed patterns for $n = 0$ are nonzero everywhere between the two inlets. Fig. C.2c also shows that the bed patterns for $n = 18$ are close to where WD_{\min} is found. The morphodynamic equilibrium for $\Delta\phi_{M_2} = 19^\circ$ is called diffusively unstable, since only diffusive transport plays a role.

To study the instability mechanism in detail, the classical diffusive transport $\langle \mathbf{F}_{\text{diff}}^{00} \rangle$, the topographically induced diffusive transport $\langle \mathbf{F}_{\text{topo}}^{00} \rangle$ and the total transport $\langle \mathbf{F} \rangle$ of the first 1 km in lateral direction for $\Delta\phi_{M_2} = 19^\circ$ and mode number $n = 0$ are shown in Fig. C.3a, C.3c and C.3e, while those for $\Delta\phi_{M_2} = 19^\circ$ and mode number $n = 18$ are

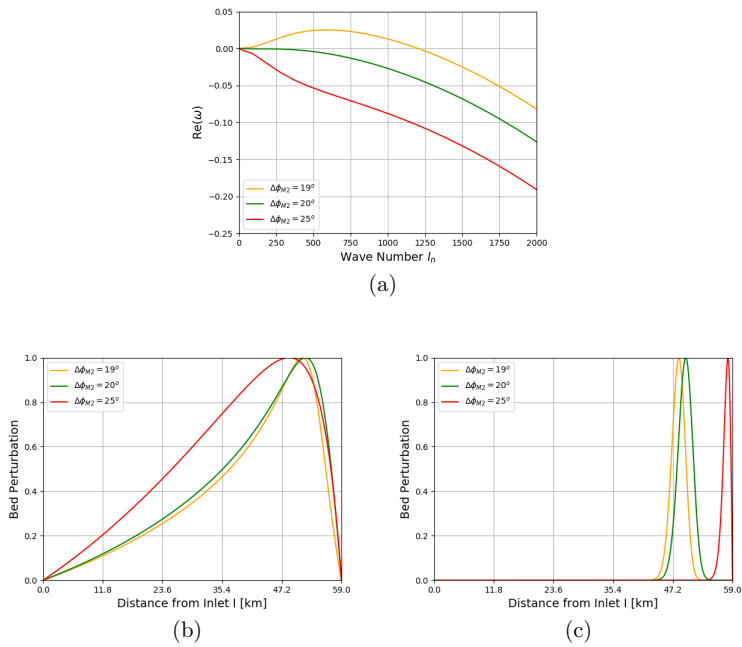


Figure C.2: The dimensionless growth rate $\Re(\omega)$ for three different $\Delta\phi_{M_2}$ (Panel (a)). The corresponding bottom patterns h_n for mode number $n = 0$ ($l_n = 0$) are shown in panel (b), while those for mode number $n = 18$ ($l_n = 555.9$) are shown in panel (c).

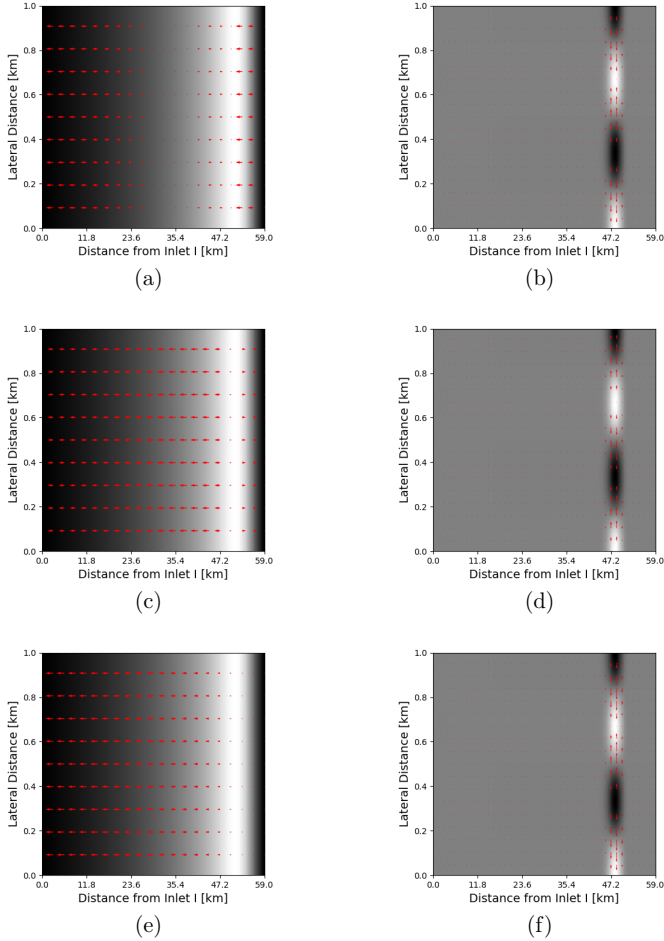


Figure C.3: Bottom patterns of laterally uniform morphodynamic equilibria for diffusively dominated transport. Panels (a), (c) and (e) show the bottom patterns for $\Delta\phi_{M_2} = 19^\circ$ and $n = 0$, with white areas representing crests and dark areas representing troughs. The arrows indicate the direction and relative magnitude of classical diffusive flux $\langle \mathbf{F}_{\text{diff}}^{00} \rangle$, the topographically induced diffusive flux $\langle \mathbf{F}_{\text{topo}}^{00} \rangle$ and the total flux $\langle \mathbf{F} \rangle$. Panels (b), (d) and (f) show the same but for $\Delta\phi_{M_2} = 19^\circ$ and $n = 18$.

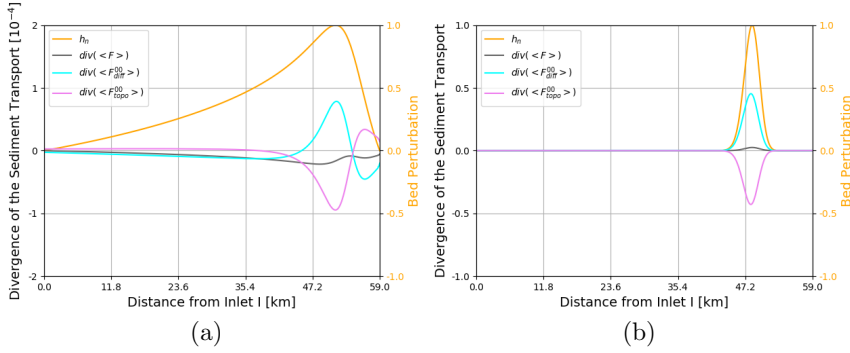


Figure C.4: Divergences of sediment fluxes. Panel (a) shows the divergences of the sediment fluxes for $\Delta\phi_{M_2} = 19^\circ$ and mode number $n = 0$ at $y = 0$, together with the corresponding bottom pattern. Panel (b) shows the same but for $\Delta\phi_{M_2} = 19^\circ$ and mode number $n = 18$.

shown in Fig. C.3b, C.3d and C.3f, respectively. These figures show that the topographically induced diffusive transport $\langle F_{topo}^{00} \rangle$ is directed from crests to troughs and stabilizes the bottom pattern, while the classical diffusive transport $\langle F_{diff}^{00} \rangle$ is generally directed from troughs to crests and destabilizes the bottom patterns. These two diffusive transports result in a total transport $\langle F \rangle$, which can be either directed from crests to troughs ($n = 0$) or from troughs to crests ($n = 18$), depending on the mode number n , as well as the relative M_2 phase. When mode number $n = 0$, these three sediment transports flow in a longitudinal direction, since there is no lateral structure, while these transports flow laterally when mode number $n = 18$.

The instability mechanism can also be studied using the divergences of these three sediment fluxes, which have the same lateral structure as their corresponding bottom pattern. Fig. C.4a shows these divergences in the longitudinal direction at $y = 0$ for $\Delta\phi_{M_2} = 19^\circ$ and mode number $n = 0$, together with the corresponding bottom pattern, while the ones for $\Delta\phi_{M_2} = 19^\circ$ and mode number $n = 18$ are shown in Fig. C.4b. From these figures it follows that the divergence of the classical diffusive transport $\langle F_{diff}^{00} \rangle$ enhances perturbations of bottom patterns, and the divergence of topographically induced diffusive transport $\langle F_{topo}^{00} \rangle$ reduces the amplitudes of the perturbations. These two sediment transports almost balance each other, resulting in a divergence of the total transport $\langle F \rangle$ with smaller magnitude. When mode number $n = 0$ is considered, $\langle F \rangle$ transports sediment from troughs to crests, while for mode number $n = 18$, $\langle F \rangle$ transports sediment from crests to troughs.

The existence and stability of laterally uniform morphodynamic equilibria depends not only on the relative M_2 phase but also on the M_2 amplitude at inlet I , which is shown in Fig. C.5. In this figure, the region in parameter space where no laterally uniform morphodynamic equilibrium exists, is indicated by the white color. Linearly stable equilibria are found in the black colored area, while linearly unstable equilibria (resulting from the diffusive mechanism) in the light gray colored area.

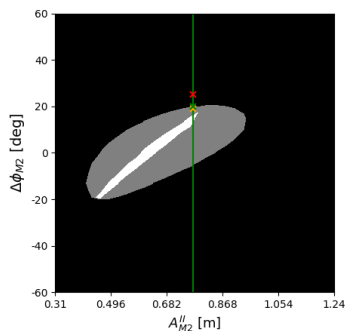


Figure C.5: Existence and linear stability of stable laterally uniform morphodynamic as a function of the M_2 tidal amplitude at inlet II and the relative phases when dominated by diffusive transport. The white, black, and grey regions indicate where no, linearly stable, diffusively unstable morphodynamic equilibria are found. If the underlying equilibrium is unstable, the mechanism resulting in the largest positive growth rate is used as indicative of the instability mechanism. The crosses indicate the experiments discussed in detail in this appendix.

REFERENCES

- [1] X. Deng, C. Meerman, T. Boelens, T. De Mulder, P. Salles, and H. M. Schuttelaars, *Morphodynamic equilibria in double-inlet systems: existence and stability*, *Journal of Geophysical Research* **126**, 2021JF006266 (2021).

D

BIFURCATION DIAGRAM FOR MORPHODYNAMIC EQUILIBRIA BY VARYING FRICTION PARAMETER

To complete the bifurcation diagram for variation of friction parameter c_d shown in Fig. 4.3a, the characteristic values for amplitudes of mode 1, 2 and 3 of the bed profile are shown in Fig. D.1a, D.1b and D.1c, respectively. From Fig. D.1a it follows that only branches $B3 - B6$ have a nonzero amplitude of mode 1. Fig. D.1b shows that $B1 - B6$ have a nonzero amplitude of mode 2, in which the amplitudes of mode 2 for branches $B5$ and $B6$ are positive. Fig. D.1c demonstrates that $B3 - B8$ have a nonzero amplitude of mode 3. The amplitudes of mode 3 for branches $B3$ ($B4$) and $B5$ ($B6$) are positive.

D

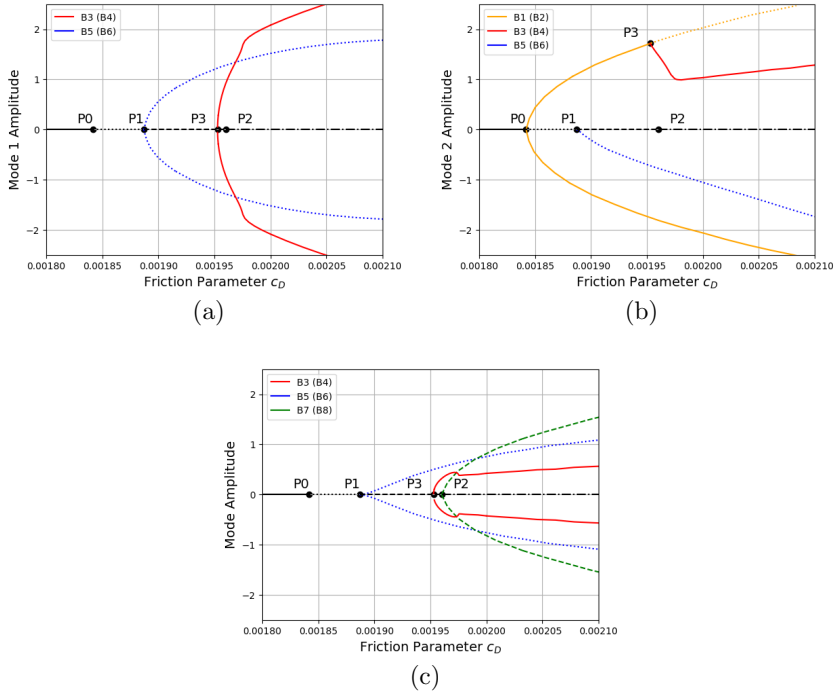


Figure D.1: Bifurcation diagram for morphodynamic equilibria by varying friction parameter c_d . Panel (a), (b) and (c) show the characteristic values of mode 1, 2 and 3 of morphodynamic equilibria, respectively. Solid, dotted and dashed lines indicate the number of positive growth rates : none, 1 and 2. Dash-dotted line indicates regions out of consideration.

E

THE OPERATOR G

In Chapter 2, 3 and 4, the nonlinear operator G is used. The operator works on the solution vector Ψ and has the same dimension as Ψ . The vector Ψ contains the amplitudes of all physical variables, associated with the tidal constituents taken into account. Here we will illustrate how to obtain two of these entries. From this, we consider the scaled leading order continuity equation (2.13a) which reads

$$B\zeta_t^{00} + [B(1-h)u^{00}]_x = 0, \quad (\text{E.1})$$

where the superscript '00' denotes leading order in both ϵ and γ . Now, at leading order, both ζ^{00} and u^{00} only have an M_2 temporal dependency. Using this, it is found that at Eq. (E.1) can be written as

$$-\zeta_{c1} + [(1-h)u_{s1}]_x = 0, \quad (\text{E.2})$$

$$\zeta_{s1} + [(1-h)u_{c1}]_x = 0. \quad (\text{E.3})$$

Now these two equations constitute the first two entries of G :

$$G = \begin{bmatrix} -\zeta_{c1} + [(1-h)u_{s1}]_x \\ \zeta_{s1} + [(1-h)u_{c1}]_x \\ \dots \end{bmatrix}. \quad (\text{E.4})$$

The other entries of G can be obtained by using a similar procedure.

ACKNOWLEDGEMENTS

What I experienced in the past thirty years makes me ask myself a question, is all this real or just a dream?

In the summer vacation of the millennium, I was just a little boy who lived in a small village which I call home in the south of China, ignorant to this world. At the day time, I might run away from my daily duty assigned by my parents, for it was really boring to take care of the grains being dried alone, and I was fond of playing with my friends in neighbouring villages or catching buds. When my parents came home, they always complained about my escaping. At the night time, my brother and I might patiently wait for my father to finish watching news and weather forecasting in the small black and white television, then we were allowed to switch channel to watch one or two hours of drama. Before sleeping, we always had to drive away all the mosquitoes inside our mosquito net.

In the summer vacation of the year 2010, I graduated from my senior high school and had to decide which university I should go. My parents wanted me to stay in Guangxi, and kept persuading me to choose a local university. But I was stubborn and made up my mind to run away from my home as far as I could. Luckily, one of uncles helped me persuade my parents to let me make the choice, so I could finally choose Shanghai University. It is the first and most important choice I have made in these thirty years. I don't know whether this choice is good or bad, but I never regret for that.

After spending a whole day in the train K150 with Tina Ji and YuYing Ou who became my best friends later, I finally arrived at Shanghai. It seems a dream to me, for I just heard of this fabulous city but have never thought that one day I could study there. Everythings in my dream became solid, the Shanghai South Railway Station, the East Nanjing Road, the Oriental Pearl TV Tower and more. The old saying is right, "it is better to see once than to hear a hundred times."

In the summer vacation of the year 2020, I was a PhD student in the third year of my research in Delft University of Technology in the Netherlands. One more time, I have never thought that I could have a chance to study in Europe, all this just likes a dream. Europe is no longer an abstract name to me, it is the colorful windmills under clouds in the Netherlands, it is the sunshine coming through the mosaic windows of the unfinished La Sagrada Familia in Spain, it is the cool breeze of a Puglia beach in Italy.

It seems so unreal that I can experience so much wonderful things in the past thirty years, and I begin to wonder whether all this is just a dream. I believe it is, it is a beautiful long dream that I don't want to and have no need to wake up. I would like to deliver my sincere gratitude to everyone who helped me and will help me to have such a nice dream.

First of all, I would like to express my deepest gratitude to my promoter and daily supervisor Prof. Henk Schuttelaars. Thank you, Henk, you not only offered me the opportunity to do research in Delft, but also you are patient and enthusiastic in helping

and supporting me, especially in my research. Moreover, you also inspire me to be optimistic. The first time we met, you asked me "Everything is good?" I have forgotten how I answered at that time, but I think I know how to answer you now. Yes, everything is good.

I am grateful to my promoter Prof. Tom De Mulder. Thank you for your overall advice and supports in my whole PhD research, especially your help when I was learning FEniCS in Ghent University.

I am also thankful to my Master thesis supervisor Prof. Dajun Zhang. Thank you for not only guiding me through my Master research, but also for introducing me to Henk.

I enjoyed my four years in Delft Institute of Applied Mathematics thanks to my nice colleagues. You guys have created a harmonious and comfortable atmosphere, Prof. Arnold Heemink, Prof. Haixiang Lin, Wim van Horsen, Evelyn Sharabi, Dorothée Engering, Kees Lemmens, Xiwei Wu, Yoeri Dijkstra, Marco Rozendaal, Jie Liu, Haochuan Feng, Henk Jongbloed, Xiangrong Wang, Jianbing Jin, Cong Xiao, Senlei Wang, Renli Liang, Xiaohui Wang, Xiao Li, Jing Wang, Anna Spinosa.

I also want to thank my friends Tao Hou, Shan Jing, Hongpeng Zhou, Jinyang Wang, Qi Tian, Rong Fan, Fanyuan Meng, Xiujie Dou, Wenting Ma, Yawei Du, Biyue Wang, et al.

Finally, I would like to express my utmost gratitude to my family. Your unlimited support and understanding are the most important key to my wonderful dream. In particular, I would like to thank my girlfriend who has never bothered me in these four years and has never told me her name. I also thank anyone who can bring me any news from my girlfriend.

Even though dreams are fragile and easy to turn into nightmares, I deeply believe that I still live in a wonderful long dream, for I have all your help.

I think, in the summer vacation of the year 2030, I will do my research on Mars. What a wonderful dream! Just kidding, not Mars, it must be a better place that I have never thought of.

Xiao Deng
Delft, April 2022

CURRICULUM VITÆ

Xiao DENG

Xiao Deng was born on 9 June 1991 in Wuzhou, Guangxi Zhuang Autonomous Region, China. He studied applied mathematics in College of Science at Shanghai University from 2010, and got his Bachelor degree in 2014 and his Master degree in 2017. His Master thesis is about the semi-discrete Ablowitz-Kaup-Newell-Segur hierarchies. Funded by China Scholarship Council, he went to Delft University of Technology as a PhD student. His research topic is the morphodynamic equilibria in double-inlet systems.

LIST OF PUBLICATIONS

1. **X. Deng**, C. Meerman, T. Boelens, T. De Mulder, P. Salles, and H. M. Schuttelaars. *Morphodynamic equilibria in double inlet systems: their existence and stability*, Journal of Geophysical Research, 126(2021).
2. **X. Deng**, T. De Mulder, and H. M. Schuttelaars. *Initial formation of channel–shoal patterns in double–inlet systems*, Ocean Dynamics, 73(2023),1-21.
3. D. J. Zhang, S. M. Liu, and **X. Deng**. *The nonlinear Schrödinger equation with nonzero backgrounds: Bilinearisation and reduction approach*, Open Communications in Nonlinear Mathematical Physics, 2022, Submitted.